

Transport through graphene quantum point contacts

Von der Fakultät für Mathematik, Informatik und Naturwissenschaften der RWTH Aachen University zur
Erlangung des akademischen Grades einer Doktorin der Naturwissenschaften genehmigte Dissertation

vorgelegt von

Sowmya Spandana, Somanchi

aus

Hyderabad, Indien

Berichter:

Universitätsprofessor Dr. Christoph Stampfer

Universitätsprofessor Dr. Markus Morgenstern

Tag der mündlichen Prüfung: 23. August 2023

Diese Dissertation ist auf den Internetseiten der Universitätsbibliothek online verfügbar.

Abstract

This thesis investigates low temperature transport through graphene quantum point contacts (QPCs) encapsulated in hexagonal boron nitride (hBN) using the van der Waals technique. Single layer graphene (SLG) QPCs are fabricated using electron beam lithography followed by SF_6 based reactive ion etching to define the shape and the width of the QPC. In such devices, we observe that the rough edges due to physical etching play an important role in the quantized conductance characteristics of the QPC particularly around the charge neutrality point (CNP). In order to be able to achieve better control over the charging of these localized edge states, we fabricate local top gates to see if it is possible to control the edges independently from the rest of the QPC channel. In one of the two devices measured, we use a pair of top gates in a split gate geometry that cover only the edges on either side of the QPC. Here, we not only observe quantized conductance kinks on the order of $2 - 3 e^2/h$ but also a non-linear relative gate lever arm. This can be explained using the fact that the edges are very likely to be terminated by Fluorine atoms after etching with SF_6 which results in higher charge accumulation along the edges and consequently, a gate voltage dependent gate lever arm.

In the other device, we employ a single top gate spanning the entire channel of the QPC except the edges. We measure the conductance as a function of both the top and the back gate voltages and observe conductance kinks that result in a linear relative gate lever arm. This dominant linear line denotes the charge neutrality of each individually measured conductance trace and its slope is referred to as the "major" slope. However, interestingly, we also observe several other features that evolve with a smaller "minor" slope. In both experiment and theoretical calculations using the tight binding model, we notice that sweeping the gates simultaneously along a direction with the minor slope results in a much cleaner conductance trace especially around the CNP where the edge disorder is the maximum. This suggests that the features corresponding to the minor slope are due to the effect of the electric field lines of the top gate on the edge states. Since these localized edge states are farther from the top gate as compared to the channel, they are tuned less strongly as compared to the Bloch states in the channel right under the top gate. This is further corroborated by the Landau fan measurements along both the directions with major and minor slope. Here, we observe that (i) the larger Landau level features at higher magnetic field appear to be unaffected by the direction of sweep. (ii) There are number of vertical straight lines that are unaffected by the magnetic field in the low magnetic field, low charge carrier density region around the CNP. These are the localized states due to the edges. (iii) The number of such vertical straight line features is lesser along the minor line than any other direction of sweep of the gates. (iv) In general, the evolution of the conductance kinks from the size quantization to their respective Landau levels is much cleaner along the direction of the minor line without a lot of interference from localized states. Thus, we have been able to use the top gate as a knob to disentangle the features related to edge disorder from size quantization.

We then move to bilayer graphene (BLG) where we apply voltage on a pair of split gates to define the width of the QPC. We create a displacement field using the combination of the split gates and a graphite back gate. This depletes the charge carriers underneath the side gates, thereby creating a 250 nm wide channel

in between the source and the drain. Using a layer of graphite as the back gate instead of the doped Si as in the case of the single layer QPCs ensures that the gate is much closer to BLG resulting in a far better tuning besides also screening any impurities from the surrounding SiO₂ or hBN. We include three other finger gates along the length of the QPC channel to tune the charge carrier density locally. Conductance traces exhibit clear $4 e^2/h$ steps that split into intermediate kinks at higher values of parallel magnetic field indicating spin degeneracy lifting. From the crossing points of spin-up and spin-down branches of successive sub-bands, we extract the values of sub-band spacing. More importantly, in the transconductance plots as a function of the finger gate voltage and the magnetic field, we observe discontinuities in the applied voltage at (i) 0 T between the spin-up and spin-down levels of the first sub-band. This is manifested in the form of a step at $2 e^2/h$ that remains unaffected by the magnetic field. (ii) Another gap in voltage is observed at a higher value of magnetic field at the crossing point of the spin up level of the first sub-band and the spin-down level of the second sub-band. This is evident in the form of step at around $1.5 \times 4 e^2/h$ that travels down $4 e^2/h$ which was observed earlier in GaAs heterostructures and referred to as the 0.7 analog, similar to the 0.7 anomaly at 0 T as a result of exchange/electron - electron (e-e) interactions. In our device, we attribute the voltage gap at 0 T to a spin-orbit (SO) coupling of the Kane - Mele type that dominates the e-e interactions. While at higher magnetic field, this situation is reversed and the Zeeman effects quenches the SO interaction. Both these voltage gaps seem to evolve linearly with the displacement field.

Zusammenfassung

Diese Dissertation untersucht den Tieftemperaturtransport durch Graphen-Quantenpunktkontakte (QPCs), die in hexagonalem Bornitrid (hBN) verkapselt sind, unter Verwendung der Van-der-Waals-Technik. Single-Layer-Graphen (SLG)-QPCs werden unter Verwendung von Elektronenstrahlolithographie hergestellt, gefolgt von SF_6 -basiertem reaktivem Ionenätzen, um die Form und die Breite des QPC zu definieren. Bei solchen Vorrichtungen beobachten wir, dass die rauen Kanten aufgrund des physikalischen ätzens eine wichtige Rolle bei den quantisierten Leitfähigkeitseigenschaften des QPC spielen, insbesondere um den Ladungsneutralitätspunkt (CNP). Um eine bessere Kontrolle über das Aufladen dieser lokalisierten Kantenzustände zu erreichen, stellen wir lokale Top-Gates her, um zu sehen, ob es möglich ist, die Kanten unabhängig vom Rest des QPC-Kanals zu steuern. Bei einem der beiden gemessenen Geräte verwenden wir ein Paar Top-Gates in einer Split-Gate-Geometrie, die nur die Kanten auf beiden Seiten des QPC bedecken. Hier beobachten wir nicht nur quantisierte Leitwertknice in der Größenordnung von $2 - 3 e^2/h$, sondern auch einen nichtlinearen relativen Gate-Hebelarm. Dies kann mit der Tatsache erklärt werden, dass die Kanten nach dem ätzen mit SF_6 sehr wahrscheinlich von Fluoratomen abgeschlossen werden, was zu einer höheren Ladungsakkumulation entlang der Kanten und folglich zu einem von der Gatespannung abhängigen Gate führt Hebelarm.

Bei der anderen Vorrichtung verwenden wir ein einzelnes oberes Gate, das den gesamten Kanal des QPC mit Ausnahme der Kanten überspannt. Wir messen die Konduktanz als Funktion sowohl der Top- als auch der Back-Gate-Spannung und beobachten Konduktanzknice, die zu einem linearen relativen Gate-Hebelarm führen. Diese dominante lineare Linie bezeichnet die Ladungsneutralität jeder einzelnen gemessenen Leitfähigkeitsspur, und ihre Steigung wird als "major"-Steigung bezeichnet. Interessanterweise beobachten wir jedoch auch mehrere andere Merkmale, die sich mit einer kleineren "minor" Steigung entwickeln. Sowohl in experimentellen als auch in theoretischen Berechnungen unter Verwendung des engen Bindungsmodells stellen wir fest, dass das gleichzeitige überstreichen der Gates entlang einer Richtung mit der kleineren Steigung zu einer viel saubereren Leitwertspur führt, insbesondere um den CNP herum, wo die Kantenstörung maximal ist. Dies deutet darauf hin, dass die Merkmale, die der kleineren Steigung entsprechen, auf die Wirkung der elektrischen Feldlinien des oberen Gates auf die Randzustände zurückzuführen sind. Da diese lokalisierten Randzustände im Vergleich zum Kanal weiter vom oberen Gate entfernt sind, werden sie im Vergleich zu den Bloch-Zuständen im Kanal direkt unter dem oberen Gate weniger stark abgestimmt. Dies wird weiter durch die Landau-Fächermessungen entlang beider Richtungen mit großer und kleiner Neigung bestätigt. Hier beobachten wir, dass (i) die größeren Merkmale des Landau-Niveaus bei einem höheren Magnetfeld von der Richtung des Sweeps unbeeinflusst zu sein scheinen. (ii) Es gibt eine Anzahl vertikaler gerader Linien, die durch das Magnetfeld in dem Bereich mit niedrigem Magnetfeld und niedriger Ladungsträgerdichte um den CNP herum unbeeinflusst bleiben. Dies sind die lokalisierten Zustände aufgrund der Kanten. (iii) Die Anzahl solcher vertikaler gerader Linienmerkmale ist entlang der Nebenlinie geringer als in jeder anderen Richtung der Pfeilung der Tore. (iv) Im Allgemeinen ist die Entwicklung der Konduktanzknice von der Größenquantisierung zu ihren jeweiligen

Landau-Niveaus viel sauberer entlang der Richtung der Nebenlinie ohne viel Interferenz von lokalisierten Zuständen. Somit konnten wir das obere Tor als Knopf verwenden, um die Merkmale im Zusammenhang mit der Kantenunordnung von der Größenquantisierung zu entwirren.

Wir wechseln dann zu zweischichtigem Graphen (BLG), wo wir Spannung an ein Paar geteilter Gates anlegen, um die Breite des QPC zu definieren. Wir erzeugen ein Verdrängungsfeld unter Verwendung der Kombination der Split-Gates und eines Graphit-Back-Gates. Dadurch werden die Ladungsträger unterhalb der Seitengates verarmt, wodurch ein 250 nm breiter Kanal zwischen Source und Drain entsteht. Die Verwendung einer Graphitschicht als hinteres Gate anstelle des dotierten Si wie im Fall der einschichtigen QPCs stellt sicher, dass das Gate viel näher an BLG liegt, was zu einer weitaus besseren Abstimmung führt und außerdem Verunreinigungen von der Umgebung abschirmt SiO_2 oder hBN. Wir schließen drei weitere Finger-Gates entlang der Länge des QPC-Kanals ein, um die Ladungsträgerdichte lokal abzustimmen. Leitfähigkeitsspannen zeigen klare $4 e^2/h$ -Schritte, die sich bei höheren Werten des parallelen Magnetfelds in Zwischenknicken aufteilen, was auf eine Aufhebung der Spinentartung hindeutet. Aus den Kreuzungspunkten von Spin-up- und Spin-down-Zweigen aufeinanderfolgender Teilbänder extrahieren wir die Werte des Teilbandabstands. Noch wichtiger ist, dass wir in den Steilheitsdiagrammen als Funktion der Finger-Gate-Spannung und des Magnetfelds Diskontinuitäten in der angelegten Spannung bei (i) 0 T zwischen den Spin-up- und Spin-down-Pegeln des ersten Teilbands beobachten. Dies äußert sich in Form einer Stufe bei $2 e^2/h$, die vom Magnetfeld unbeeinflusst bleibt. (ii) Eine weitere Spannungslücke wird bei einem höheren Wert des Magnetfelds am Kreuzungspunkt des Spin-Up-Niveaus des ersten Teilbands und des Spin-Down-Niveaus des zweiten Teilbands beobachtet. Dies zeigt sich in Form einer Stufe bei etwa $1.5 \times 4 e^2/h$, die sich um $4 e^2/h$ nach unten bewegt, was früher beobachtet wurde in GaAs-Heterostrukturen und wird als 0.7-Analog bezeichnet, ähnlich der 0,7-Anomalie bei 0 T als Ergebnis von Austausch/Elektron-Elektron (e-e)-Wechselwirkungen. In unserem Gerät schreiben wir die Spannungslücke bei 0 T einer Spin-Orbit (SO)-Kopplung des Kane-Mele-Typs zu, die die e-e-Wechselwirkungen dominiert. Bei einem höheren Magnetfeld kehrt sich diese Situation um und der Zeeman-Effekt löscht die SO-Wechselwirkung. Diese beiden Spannungslücken scheinen sich linear mit dem Verschiebungsfeld zu entwickeln.

Contents

1. Introduction	15
1.1. Quantum point contacts in Mesoscopic physics	15
1.2. Quantum computation	16
1.3. Graphene as a host material for electronic devices	17
1.4. Outline of this thesis	18
2. Quantum point contacts	21
2.1. Introduction	21
2.2. History of quantum point contacts	22
2.2.1. Point contacts in metals	22
2.2.2. Point contacts in semiconductor 2DEGs	22
3. Quantum point contacts in graphene	27
3.1. Graphene	27
3.2. Graphene nanostructures	28
3.3. Characteristic length scales and gate couplings in graphene nanodevices	30
3.4. Electronic transport in graphene nanoribbons and nanoconstrictions	33
3.4.1. Graphene nanoribbons/constrictions on SiO ₂	34
3.4.2. Suspended graphene nanoribbons/constrictions	35
3.4.3. Graphene nanoribbons/constrictions based on hBN	36
3.4.4. Encapsulated graphene nanoribbons/constrictions	37
4. Quantum point contacts in bilayer graphene	39
4.1. Gate defined BLG nanoconstrictions on SiO ₂	40
4.2. Gate defined suspended BLG nanoconstrictions	40
4.3. Gate defined encapsulated BLG nanoconstrictions	41
5. Fabrication of graphene and bilayer graphene quantum point contact devices	45
5.1. Introduction	45
5.2. Substrate preparation	45
5.3. Exfoliation of graphene	45
5.4. Selection of graphene flakes	46
5.5. Exfoliation of hBN	47
5.6. Selection of hBN flakes	48
5.7. van der Waals stacking method/dry transfer technique	49
5.7.1. Step 1	49
5.7.2. Step 2	49

5.7.3.	Step 3	50
5.7.4.	Step 4	50
5.8.	Characterizing the stacked heterostructure	51
5.9.	Patterning the heterostructure and, adding contacts and gates	52
5.9.1.	Single-layer graphene - Patterning the constriction	52
5.9.2.	Single-layer graphene - Contacts	53
5.9.3.	Single-layer graphene - Definition of top gates	53
5.9.4.	Bilayer graphene - contacts	53
5.9.5.	Bilayer graphene - Definition of top (split) gates	55
5.9.6.	Bilayer graphene - Definition of finger gates	55
6.	Single-layer and bilayer graphene quantum point contact device geometry	57
6.1.	Single layer graphene QPC devices	57
6.1.1.	Single top gated graphene constriction devices	58
6.1.2.	Dual top gated graphene constriction devices	59
6.2.	Bilayer graphene QPC devices	59
6.3.	With split and finger gates	60
7.	Edge disorder in etched top gated graphene quantum point contacts	61
7.1.	Introduction	61
7.2.	Measurement set-up	62
7.3.	Theory of conductance through an ideal QPC	63
7.4.	Conductance through a QPC with a single top gate	65
7.4.1.	Conductance as a function of back gate and top gate	65
7.4.2.	Extraction of gate lever arm from quantum Hall measurements	67
7.4.3.	Effect of localized states on conductance	68
7.4.4.	Effect of the top gate on localized states	70
7.5.	Conductance of a QPC with two top gates	73
7.5.1.	Non-constant gate lever arm measurements	73
7.6.	Theoretical simulations of conductance in a graphene QPC with a single top gate	77
7.7.	Conclusion	78
8.	Crossover from size quantization to Landau quantization in etched graphene quantum point contacts	81
8.1.	Introduction	81
8.2.	Experimental magnetic field measurements - Evolution of conductance kinks in an etched graphene QPC with a single top gate	81
8.3.	Theoretical simulations - Evolution of conductance kinks with magnetic field	85
8.3.1.	Simulations of magnetic field measurements using the nanoribbon model	85
8.3.2.	Analysis of different Eigen states in the graphene nanoribbon	86
8.3.3.	Rescaling the theoretical simulations to fit the experimental data	87
A.	Convert the energy axis in simulation to the charge carrier density axis in experimental data	87
B.	Readjust the magnetic field axis in simulation to fit the experimental data	88

C. Summary of the rescaling procedure	88
8.3.4. Simulations of magnetic field measurements using the constriction model	89
8.4. Comparison between experiment and theory	90
8.4.1. Conclusion	92
9. Spin states in gate defined bilayer graphene quantum point contacts	95
9.1. Introduction	95
9.2. Measurement configuration	96
9.3. Formation of a 1D channel	97
9.4. Formation of sub-bands in the QPC: Quantized conductance	98
9.5. Spin splitting of sub-bands	99
9.6. Extraction of sub-band spacing	99
9.7. Identification of peaks	101
9.7.1. Smoothing the data	103
9.7.2. Horizontal amplification of peaks	103
9.7.3. Interpolation of peaks	103
9.8. Sub-band spacing as a function of displacement field	106
9.9. The 0.7 analog structure	106
9.10. Conclusion	109
10. Conclusion and Outlook	111
10.1. Conclusion	111
10.2. Current research and outlook	114
10.2.1. Scanning gate microscopy	114
10.2.2. Split gate QPCs in single layer graphene	115
10.2.3. Quantum dots in bilayer graphene	115
Appendices	117
A. Process parameters	117
B. Transport through an etched graphene QPC with a single top gate	123
C. Transport through gate defined bilayer graphene QPC	125
D. List of samples	129
A. Directory of figures	131
Publications	134
Bibliography	137
Curriculum Vitae	154

Eidesstattliche Erklärung

Sowmya Spandana Somanchi

geboren in Indien, erklärt hiermit, dass diese Dissertation und die darin dargelegten Inhalte die eigenen sind und selbstständig, als Ergebnis der eigenen originären Forschung, generiert wurden.

Hiermit erkläre ich an Eides statt

1. Diese Arbeit wurde vollständig oder grösstenteils in der Phase als Doktorand dieser Fakultät und Universität angefertigt;
2. Sofern irgendein Bestandteil dieser Dissertation zuvor für einen akademischen Abschluss oder eine andere Qualifikation an dieser oder einer anderen Institution verwendet wurde, wurde dies klar angezeigt;
3. Wenn immer andere eigene- oder Veröffentlichungen Dritter herangezogen wurden, wurden diese klar benannt;
4. Wenn aus anderen eigenen- oder Veröffentlichungen Dritter zitiert wurde, wurde stets die Quelle hierfür angegeben. Diese Dissertation ist vollständig meine eigene Arbeit, mit der Ausnahme solcher Zitate;
5. Alle wesentlichen Quellen von Unterstützung wurden benannt;
6. Wenn immer ein Teil dieser Dissertation auf der Zusammenarbeit mit anderen basiert, wurde von mir klar gekennzeichnet, was von anderen und was von mir selbst erarbeitet wurde;
7. Teile dieser Arbeit wurden zuvor veröffentlicht und zwar in:

- **From diffusive to ballistic transport in etched graphene constrictions and nanoribbons**

S. Somanchi, B. Terrés, J. Peiro, M. Staggenborg, K. Watanabe, T. Taniguchi, B. Beschoten, and C. Stampfer

Annalen der Physik 529, 1700082 (2017)

- **Observation of the Spin-Orbit Gap in Bilayer Graphene by One-Dimensional Ballistic Transport**

L. Banszerus, B. Frohn, T. Fabian, S. Somanchi, Epping, M. Müller, D. Neumaier, K. Watanabe, T. Taniguchi, F. Libisch, B. Beschoten, F. Hassler, and C. Stampfer

Phys. Rev. Lett. 124, 177701, 2020

27.09.2023

List of abbreviations

Abbreviation	Explanation
1D	one dimensional
2D	two dimensional
2DEG	two dimensional electron gas
AFM	atomic force microscopy
ALD	atomic layer deposition
BLG	bi-layer graphene
CNP	charge neutrality point
CVD	chemical vapour deposition
EBL	electron beam lithography
FET	field effect transistor
FQHE	fractional quantum hall effect
GNC	graphene nanoconstriction
GNR	graphene nanoribbon
FWHM	full width at half maximum
hBN	hexagonal boron nitride
IT	information technology
NEMS	nano electro mechanical systems
PMMA	polymethylmethacrylate
PVA	polyvinylalcohol
QHE	quantum hall effect
QPC	quantum point contact
RIE	reactive ion etching
SGM	scanning gate microscopy
SEM	scanning electron microscopy
SLG	single-layer graphene
SOC	spin-orbit coupling

1. Introduction

The last 50 years of mankind have witnessed a huge surge in the development of information technology (IT), thanks to the tremendous breakthroughs in the field of electronics coupled with an enormous market demand for fast and efficient devices. For example, in the case of computers that originally took up the size of a small room, a rapid evolution of technology has allowed us to manufacture laptops, tablets and smart phones that fit the size of our palms. This decrease in size was complemented with a corresponding increase in processing power over time. This, along with the development of low cost fabrication technology has led to an inevitable use of transistors in every walk of human life. Such an ever increasing demand for faster and smaller electronic devices means that we need to look for new ways towards miniaturization of devices. In 1965, Gordon Moore, a computer scientist and co-founder of the IT giant, Intel, observed that the number of transistor components of a micro-chip doubled every two years [1], which later came to be known as the Moore's law. In order to keep up with this law, it is therefore necessary to manufacture even smaller and faster transistors that could be incorporated into a smaller volume. Intel has already introduced a 14 nm transistor [2, 3] into the market and has further laid down the road towards 10 nm technology [4, 5]. However, there seem to be significant problems with regard to the yield, time needed for improving defects and the cost of production which could be a result of the fast increasing market demand as we push the limits of attainable transistor densities. For example, as the size of the transistor decreases to make more compact devices, high amount of energy dissipation is inevitable. All these point towards the fact that there is a natural physical limit to the process of miniaturization - the size of the atom ($\sim 1 \text{ \AA}$). As we go down to such a minuscule level, quantum mechanics inevitably comes into the picture pushing the humankind to come up with innovative ideas to design electronic devices at such a small scale. The ultimate level of miniaturization is achieved when single molecules or atoms are employed as the building blocks of electronic devices. Several research groups have already reported on the transport mechanisms through single molecule [6] and single atom [7] based transistors already. However, the scalability and integration of such devices in complex circuits is still a problem. Besides the technical difficulties involved in the fabrication of these devices, it is also important to understand the transport of electrons when they are confined to such small nanostructures which can, in fact, be significantly different when compared to their bulk counterparts.

1.1. Quantum point contacts in Mesoscopic physics

Mesoscopic physics refers to the study of physical systems whose size falls in between the macroscopic bulk three dimensional (3D) materials and the microscopic world of atoms and molecules [8, 9]. Macroscopic implies visible to the naked eye such as a piece of solid material that contains a large number of atoms and molecules. Therefore, macroscopic properties are properties of the bulk matter, for example, density, volume, viscosity, stress, strain, temperature, surface tension etc. While the material properties can be described using the the laws of classical mechanics in the case of macroscopic systems, mesoscopic

objects need the concept of probability and quantum mechanics to describe their properties. In such a case, quantities such as energy and momentum are allowed to have only discrete values instead of a continuum as in the case of macroscopic objects. For example, when discussing the band structure of a solid, we speak about the probability of the energy levels being occupied by an electron.

Thus, mesoscopic physics deals with the change in fundamental properties that occurs when a macroscopic object is miniaturized, as in the case of transistors in semiconductor electronics. In doing so, as the number of atoms on the surface becomes smaller and smaller, a change in the dimension of confinement of electrons in the system occurs resulting in low dimensional systems as described below [10, 11].

When electrons (or holes) are confined, say along the z -axis, but are free to move along the x - y plane, it results in a quantum well. Electrons confined in such a system form what is known as the two dimensional electron gas (2DEG). Similarly, when the electrons are confined along two directions (say, z and y), it forms a one dimensional (1D) system called a quantum wire. A carbon nanotube is an example of such 1D system where the motion is only along the tube axis and limited along the diameter. Another example of such a 1D system is a quantum point contact (QPC) where a narrow one dimensional bottle-neck is connected to two electron reservoirs on both sides. There are also zero dimensional systems called quantum dots where the motion of electrons is confined in all three dimensions, thereby resulting in small, isolated, dot like regions.

In this thesis, we will focus on quantum point contacts. 1D quantum confinement in these systems occurs when their size is of the same magnitude as the Fermi wavelength of electrons. A direct and perhaps, the most important consequence of quantum confinement is seen in the conductance of a QPC. For example, while the conductance of a macroscopic wire increases continuously with its diameter, in contrast, for a QPC in the ballistic transport regime, the conductance increases in discrete steps of $2e^2/h$ [12]. An interesting result of this quantization is that this effect depends only on fundamental constants e , the charge of an electron $= 1.602 \times 10^{-19}$ C, and h , the Planck's constant $= 6.626 \times 10^{-34}$ m²kg s⁻¹ and is independent of the material properties. However, the exact energy values at which the quantization occurs is dependent on the material as the size of the potential well or the width of the QPC for a particular gate voltage is determined by the type of the material. Another reason for the interest in QPCs is that the density of electrons in the QPC can be controlled by the use of the external gates or electric fields. Moreover, at such small length scales, disorder also plays a huge role in the conductance or transmission of electrons through the device. Thus, QPCs are considered to be the foundation blocks for the study of mesoscopic electrical transport experiments such as the Aharonov - Bohm effect [13–15], Fabry - Perot interference [16], quantum decoherence [17] etc.

1.2. Quantum computation

While miniaturization forces us to look for ways to improve the design and fabrication of mesoscopic systems, it also compels us to look for alternate computational techniques. For instance, in very small devices, due to quantum tunnelling, it is possible for electrons to effectively cross a physical barrier, thereby, making it difficult to define a definite on or off state that is essential for electronics. Quantum computers store information in quantum states called qubits instead of the ordinary classical bits in traditional electronics. The fundamental difference between the two is that while the classical bit can assume only one value, either 0 or 1 (off or on state equivalent of an electrical switch), a qubit can be in any superposition of these two states. Harnessing this property of a quantum state along with others such as interference and entanglement between multiple qubits allows a quantum computer to perform various tasks that are difficult or impossible

for a classical computer. Any quantum mechanical two level system allows the possibility of designing a qubit. For instance, D. Loss and D. P. DiVincenzo first proposed that the spin of an electron, which has a spin down (0) or a spin up (1) state could be used as a qubit in a quantum computer as opposed to using the charge of the electron like in the case of traditional electronics [18].

Quantum point contacts are an integral component of such electronic and quantum computation experiments. They can be used to read out the state of a charge [19–22] or spin [23–28] in a nearby capacitively coupled quantum dot. As the conductance of a QPC increases in a step like manner, it becomes extremely sensitive to any electrostatic changes in the surrounding environment. Thus, it becomes a very effective tool in detecting the charge on the dot i.e. it acts as a charge detector.

1.3. Graphene as a host material for electronic devices

While most of the traditional electronic devices are based on semiconductors such as GaAs and Si, over the last two decades, other substitute materials with a higher electron mobility or those with a higher spin life time have received a huge attention both by the scientific community and the industry. Materials such as graphene, molybdenum disulphide (MoS_2), tungsten diselenide (WSe_2) and other transition metal dichalcogenides have been vastly explored. Indeed, this shift in research in terms of exploring new materials was also recommended by Intel recently [29].

Specifically, graphene is a unique material that offers several advantages [30]. Its Dirac Hamiltonian is responsible for various physical phenomena such as Klein tunneling [31], half-integer Hall quantization [32] etc. It is expected to have high electron mobility on the order of $100,000 \text{ cm}^2 \text{V}^{-1} \text{s}^{-1}$ at room temperature [33] and large spin life-times of up to $1 \mu\text{s}$ [34, 35]. Trauzettel et al. proposed the use of electron spin in graphene as a qubit owing to its long spin decoherence life-time which is desirable in qubits [36]. This is attributed to the low atomic weight of carbon leading to small spin-orbit coupling along with the nuclear spin-free C_{12} isotope in graphene that leads to negligible hyperfine interaction. Achieving a qubit in graphene involves identifying spin states and manipulating electron spin, for which, it is first essential to confine electrons to a small space. In case of semiconductors, electrons are confined to the valence band until they are supplied with energy equivalent to the band gap which allows them to move to the conduction band. This allows us to define two states - one in which there is no flow of electrons when the electrons are in the valence band and the other in which there is current flow as the electrons move to the conduction band, thereby providing a way of controlling and stopping the flow of electrons. However, graphene suffers from the lack of an intrinsic band gap which is the most important prerequisite for its use in the current semiconductor based electronic industry. Thankfully, the possibility of confining charge carriers using devices such as graphene nanoribbons (GNRs) or constrictions (GNCs) is predicted to open an energy gap [37]. GNRs and GNCs are 1D systems carved out of a two dimensional graphene sheet similar to how QPCs in semiconductors are 1D dimensional channels in a 2DEG, thus confining the electrons in a single direction. Therefore, many research groups started to explore graphene in this particular direction.

However, the early devices did not show very high values of mobility. One reason for this was that the nanodevices were fabricated on substrates like Si/SiO_2 which resulted in a significant amount of disorder due to substrate roughness and electron - hole charge puddles [38, 39]. The other reason was that the fabrication technique involved electron beam lithography and etching or cutting the graphene flake in the shape of narrow ribbon or constriction. The rough edges with dangling bonds result in edge disorder and increased scattering of electrons during transport, thus giving low values of mobility ranging from 10,000 to a max-

imum of $50,000 \text{ cm}^2\text{V}^{-1}\text{s}^{-1}$ at cryogenic temperatures. Suspending the constriction removes the problem of substrate induced disorder and brought a significant increase in device quality [40]. However, the devices are extremely fragile and susceptible to high voltage loads. In 2010, Dean et al. showed that this problem may be circumvented by using hexagonal boron nitride (hBN), an atomically flat insulator with nearly the same lattice constant as graphene as a suitable substrate [41]. The last and most significant breakthrough came when researchers realized that encapsulating graphene between two layers of hBN results in even higher experimental values of mobility of around $150,000 \text{ cm}^2\text{V}^{-1}\text{s}^{-1}$ and ballistic QPCs [42]. However, the performance of even such high quality nanostructures is heavily influenced by disorder arising from rough edges which can tamper the conductance and wash out any confinement effects potentially. A proper understanding of how exactly the disorder related localized edge states participate in transport and whether their influence can be tuned by some external means stands as an important unanswered question.

On the other hand, the bilayer equivalent of graphene, although still has no intrinsic band gap, presents the possibility of opening a band gap when an electric field is applied perpendicular to its layers [43–47] and therefore, acts as a semiconductor. Thus, the problem of edge disorder in bilayer graphene (BLG) based devices may be completely circumvented by using additional gates to create a soft wall confinement of electrons similar to semiconductors.

The aim of this thesis is to confine charge carriers in hBN encapsulated single and bilayer graphene quantum point contacts. In the case of single-layer graphene, we fabricate quantum point contacts by physical etching and investigate whether it is possible to tune the influence of localized edge states on the electron transport using external top gates. Indeed, we see that using top gates presents a unique opportunity to be able to dissociate the effect of confinement such as conductance quantization from the features arising due to edge disorder.

By encapsulating bilayer graphene (BLG) with hBN and then defining a QPC using electrostatic gates, we achieve a device where we can confine electrons far from the edges of the BLG flake and also enjoy all the design benefits offered by lithography. The high quality of the device is investigated through the observation of quantized conductance due to a gate tunable spin orbit (SO) coupling. This is manifested in the form of an additional kink at $2 e^2/h$ at zero magnetic field. Controlling the SO coupling in BLG may allow us to use these devices in spin based field effect transistors or in spin-orbit valves. Another major discovery is the evidence of spin states at higher magnetic fields which have not been achieved in such devices until now. Moreover, we also observe splitting of spin-up states at higher magnetic field reminding us of the 0.7 analog in GaAs heterostructures due to electron - electron interactions. The existence of six fully spin polarized modes in magnetic field measurements open up the possibility of using these devices as spin polarizers and detectors in BLG based transport experiments.

1.4. Outline of this thesis

In the following chapter 2, a brief introduction to a quantum point contact and its historical development starting from point contacts in metals to QPCs in semiconductor based 2DEGs is presented. In chapter 3, quantum point contacts in single layer graphene and the technological developments are presented in the form of a brief literature review. This chapter also discusses some important length scales such as mean free path, how it determines the size of the devices to be fabricated to see ballistic transport, and how this is affected by the presence of disorder. Similarly, chapter 4 consists of some previous research in bilayer graphene QPCs and the experiments related to band gap opening. Chapter 5 describes the fabrication of

hBN encapsulated single and bilayer graphene QPC devices measured in this thesis using the van der Waals stacking technique followed by electron beam lithography and reactive ion etching. All the specific details regarding the geometry of the devices measured in this thesis are presented in chapter 6. In chapter 7, we explore the influence of top gates (a single global top gate and also a pair of dual top gates) on edge disorder while measuring the transport properties through etched single layer graphene QPCs. Along the same lines, in chapter 8, we investigate the effect of edge disorder using a parallel magnetic field to see how the conductance quantization steps evolve. Next, in chapter 9, we focus on the formation of gate defined QPCs in bilayer graphene, formation of sub-bands along with the observation of spin states in a parallel magnetic field. Finally, the thesis concludes with Chapter 10 with a short overview of other current and possible future experiments in graphene QPCs.

2. Quantum point contacts

2.1. Introduction

A quantum point contact is a one dimensional channel (length l and width w) formed in a two dimensional electron or hole system [48–50]. Fig. 2.1 shows the schematic of one such gate defined QPC in a semiconductor 2DEG. Alternatively, it is also referred to as a constriction since the flow of charge carriers is "constricted" along a specific dimension geometrically. When the width of the constriction is comparable to the Fermi wavelength (λ_F) and the length is much smaller than the mean free path (l_m) of charge carriers, it forms a system that is ideal to study quantum mechanical effects such as quantized conductance.

Transport through such a one dimensional ballistic conductor where $l_m(> l) \gg \lambda_F(\sim w)$ is analogous to the problem of transmission or scattering of electrons in a wave guide with a certain number of modes. Due to the quantum confinement of charge carriers, the valence and the conduction bands in the bulk system are now replaced by a series of discrete one dimensional energy bands called sub-bands. The energy spacing between two successive sub-bands is called the sub-band spacing. In such a case, the number of modes or 1D sub-bands occupied is given by $N = n \frac{2w}{\lambda_F}$ [48, 51] where $n \in \mathbb{Z}_0$ and the dispersion relation is given by

$$E_n(k) = E_n + \frac{\hbar^2 k^2}{2m} \quad (2.1)$$

where E_n is the energy of an electron in the n^{th} sub-band and k is the wave number for propagation inside the conductor. A voltage difference (V) between the two reservoirs on either side of the constriction induces a current (I) through it. For a 1D system with a degeneracy g , the density of states is given by $\rho_n = g \left(2\pi \frac{dE_n}{dk} \right)^{-1}$ and the group velocity is given by $v_n = \frac{1}{\hbar} \frac{dE_n}{dk}$. The current carried by the n^{th} sub-band is given by the product of these two i.e.

$$I_n = \int_0^{eV} e v_n \rho_n dE = \frac{ge^2}{h} V. \quad (2.2)$$

As obtained in the above equation, it is the cancellation of density of states with group velocity that leads to an equipartition of current amongst all the N modes of the system. The current carried by all the N modes together is therefore, given by

$$I = N \frac{ge^2}{h} V. \quad (2.3)$$

The total conductance through the device is then given by

$$G = \frac{I}{V} = N \frac{ge^2}{h}. \quad (2.4)$$

This shows that the conductance increases by a factor of $\frac{ge^2}{h}$ as we move from one sub-band to the next. Thus, we see that the equipartition of current i.e. the equal distribution of current among all the propagating modes in the constriction is the main reason for conductance quantization.

Note that the pre-factor g depends on the degeneracy of the system under consideration. In case of graphene, it is 4, if the four fold degeneracy is preserved and 2, if the valley degeneracy is lifted and 1, if both spin and valley degeneracies are lifted. Additionally, we shall see in section 7.3 that in the presence of disorder such as rough edges in etched QPCs, the conductance in eq. 2.4 is affected by another factor c_0 called the transmission coefficient. As the name suggests, c_0 is related to the finite probability of transmission of electrons through the constriction as they are scattered at the rough edges and may, therefore, vary anywhere between 0 and 1 [42].

2.2. History of quantum point contacts

In this section, a brief history of the research conducted in metal and semiconductor based QPCs is discussed. The experimental progress achieved in these systems serves as an important prelude and a source of inspiration for many analogous discoveries in single layer graphene and bilayer graphene QPCs including formation of sub-bands, quantized conductance, spin states, 0.7 analog etc. as we shall see in the following chapters. Therefore, having a knowledge of the type of experiments and the results obtained in such devices would help us predict the results in graphene as well.

2.2.1. Point contacts in metals

The history of ballistic transport started with point contacts based on metals that were fabricated by simply pressing a metal needle or a wedge on a metallic single crystal, followed by spot-welding. Ballistic transport in such a device was first examined by Yuri Sharvin in 1965 [52]. His longitudinal electron focusing experiment used point contacts to inject and detect electrons in a metal. Later on, in 1974, Tsoi further developed this idea for transverse electron focussing [53]. Point contacts have also been used to study a wide range of interaction mechanisms such as electron-phonon interaction [54], electron-magnon interaction [55], Kondo scattering [56] etc. Using such point contact spectroscopy in superconductors, several interesting important phenomena such as Josephson effect [57] and Andreev reflections [58] have been studied. This geometry proved very useful in the investigation of superconducting energy gap in several materials [58, 59]. Finally, quantum mechanical tunnelling experiments using scanning tunnelling microscopy (STM) in which the metallic microscope tip acts an atomic point contact have also been extremely useful in surface characterization [60]. However, excluding the case of STM in which the size of the tip is on the order of atomic length, transport in metal point contacts would be only classical or semi-classical since the Fermi wavelength of conduction electrons is too small ($\lambda_F \approx 0.5$ nm) as compared to the size of the point contact. Further, in these metallic QPCs, the resistance is solely determined by the geometry of point contact and cannot be varied.

2.2.2. Point contacts in semiconductor 2DEGs

Unlike metals, in semiconductor 2DEGs such as the interface in a GaAs/AlGaAs heterostructure, point contacts cannot be formed by the technique described in previous section, since the electron gas lies inside the interior of the planar heterostructure. In this case, point contacts are formed by fabricating two split gate electrodes on top of the heterostructure. By applying a suitable negative voltage to these gates, the area below the gates is completely depleted of any charge carriers and thus, no longer electrically conductive. The only connection between the two reservoirs on either side of the gates is the narrow channel between the

gates which now becomes a constriction as shown in Fig. 2.1. The width of this constriction can be modified and the transport can be completely pinched off by changing the voltage on the split gates. This method of "electrostatic squeezing" of a 2DEG to form a 1D transport channel was first developed by Thornton et al. [61] and Zheng et al. [62] in 1986.

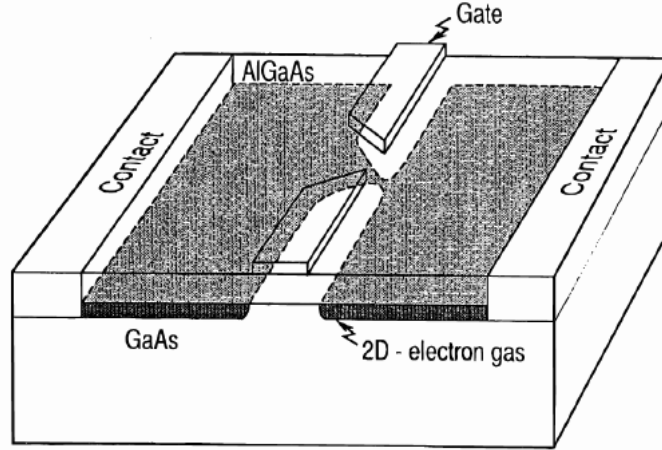


Figure 2.1.: Schematic cross-sectional view of a quantum point contact in a GaAs-AlGaAs based 2D electron gas. When a negative voltage is applied to gate electrode, the region underneath is depleted of charge carriers, thus, forming a constriction. Figure reprinted from Ref. [48].

Using this technique in GaAs/AlGaAs heterostructures, the first experimental evidence for quantum mechanical size effects was observed in the form of zero field size quantization by two independent groups, van Wees et al. [12] and Wharam et al. [63] in devices with a size much smaller than the mean free path of electrons. By sweeping the gate voltage, the measured conductance trace showed a series of steps with a height of $2e^2/h$ (see Fig. 2.2) [12]. Moreover, as the voltage is gradually decreased, the width of the point contact also decreases until the conductance is completely pinched off. As explained in section 2.1, a simple explanation for this observation is provided using the formation of 1D subbands with a change in the gate voltage. As the width increases by an amount corresponding to half the Fermi wavelength, an additional channel i.e an additional sub-band is added to the conductance in a step like manner. The authors of Ref. [63] further showed how the steps evolve in the presence of an external parallel magnetic field: the magnetic field lifts the spin degeneracy which now gives rise to additional intermediate plateaus corresponding to the spin split energy levels [64].

Another important feature of QPCs that attracts a lot of attention even until date is the additional step at $0.7 \times 2e^2/h$ besides the usual the $2e^2/h$ quantization [65–73]. This is called 0.7 conductance anomaly and is sensitive to both temperature and magnetic field. Several plausible explanations for this phenomenon were offered including spontaneous spin polarization of electrons [70, 71] or the presence of a magnetic impurity leading to Kondo effect [68, 69]. Several other accompanying effects such as an enhancement of Lande g factor at low charge carrier density suggest that a form of electron-electron interaction could be responsible for both these features [72]. More recent studies have attributed this to a van Hove ridge or an enhanced density of states at the top of the QPC barrier resulting in strongly enhanced electron - electron interactions [74, 75]. It is also interesting to note that anomalies at other non-integer values of conductance such as 0.5, 0.6 etc. besides 0.7 were observed not only in GaAs [73] but also in other semiconductor systems such as

InAs [67] and Si [66].

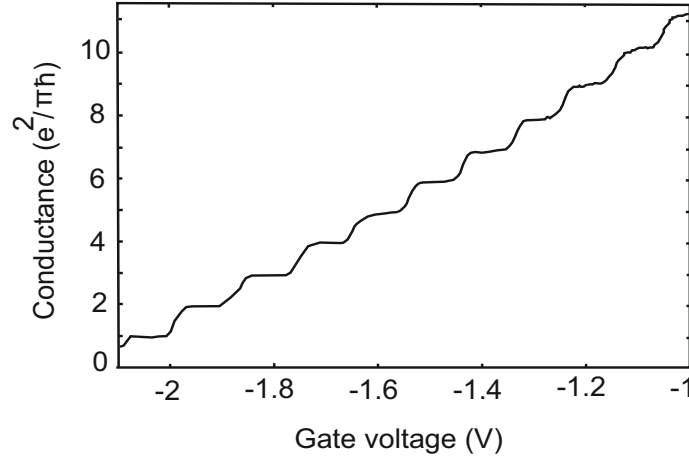


Figure 2.2.: Conductance of a quantum point contact similar to Figure 2.1. Multiple plateaus at intervals of $2e^2/h$ are visible. Figure adapted from Ref. [12].

Owing to the fact that QPCs show such clear characteristics of electron confinement in 1D, they can be immensely powerful tools as electron interferometers. Yang et.al devised an electrical analogue of the Mach-Zehnder interferometer in optics where QPCs act as electron beam splitters [76]. This utilizes the edge transport in the quantum Hall regime which is therefore quite sensitive and more robust in high magnetic fields as compared to earlier double slit electron interferometers. Other groups have reported on various other interference patterns exhibited by QPCs including Aharnov Bohm effect [13, 14] and Fabry Perot oscillations [16]. In general, QPCs have played a key role in understanding several interesting electronic transport phenomena.

The ultimate goal of spintronics is to create devices called spin valves which can control the orientation of the spin of the electrical currents passing through them. In this sense, QPCs are extremely useful and with the ascertainment of high quality through phenomena such as ballistic transport and quantized conductance, control and manipulation of spin was the next big goal. Several efforts have been made towards the generation of spin polarized currents in QPCs even without the means of an external magnetic field i.e. by all electrical means using side gates and lateral spin orbit coupling. Recently, an all-electric spin valve was demonstrated by Chuang et.al in asymmetrically biased GaAs QPCs [77].

Ever since the proposal of Loss and DiVincenzo on quantum computing using quantum dots [18], numerous efforts have been made to study the spin of an electron using quantum dots. The next subsequent step was to explore the possibility of making electron spin qubits. QPCs have been used together in conjunction with quantum dots in several semiconductor spin qubit experiments. A major breakthrough in the field of spin based quantum computing was the use of a QPC to read out the individual electron spin in a quantum dot in a GaAs/AlGaAs 2DEG [23]. In another related ground breaking experiment, coherent manipulation of electron spin was shown again in GaAs quantum dots. Here, QPC charge sensors were used as local electrometers [24]. Several other publications also used a QPC placed in the close vicinity of a quantum dot due to their charge sensitivity and have shown spin manipulation using various techniques [25–28].

Besides GaAs, another highly explored material is Si. Si based 2DEGs have relatively lower carrier mobility and therefore, most of the conductance investigation experiments were initially performed usually

on GaAs heterostructures until the early 90s. Another reason could have been a difficulty in confining charge carriers with an effective gating. Nonetheless, eventually, technological improvements gave significant results such as the observation of the 2D metal-insulator transition at zero magnetic field [78] and the measurement of spin and valley splitting in Si based systems [79]. Further experiments in QPCs included the detection of 1D ballistic transport along with steps on the order of $4 e^2/h$ in Si inversion layers [80] and Si/SiGe 2DEG [81] while another study reported e^2/h steps suggesting full degeneracy lifting along with the 0.5 anomaly in a strongly confined SiGe 2DEG [82]. Recently, electrical control of a spin qubit was demonstrated in a Si/SiGe quantum dot where a QPC is used as a charge sensor [83]. The performance of this device was even better than those based on GaAs in terms of the spin coherence time. In general, in III-V semiconductor systems, a high degree of spin control has been achieved.

While GaAs has been the most popular material to fabricate 2DEGs, InAs has also shown promising results particularly in terms of one dimensional transport. Besides quantized conductance, conductance anomalies such as 0.5 or $0.7 e^2/h$ have also been frequently observed [67, 84–86]. Results similar to Ref. [77] were also achieved in InAs QPCs with in-plane side gates which can be used as robust spin injectors and detectors [85]. In fact, side gating is much easier to achieve in InAs as compared to GaAs due to smaller surface depletion. Efforts towards achieving an all-electric spin valve have also yielded pretty encouraging results where lateral gates have been used to create a strongly spin polarized current by purely electrical means without the help of any external magnetic field [84, 87].

The above literature is not exhaustive but already provides an idea of how metal and semiconductor 2DEG based QPCs have evolved from simple spectroscopic tools to spin qubits over the last 3-4 decades.

3. Quantum point contacts in graphene

This chapter has been published in parts in:

From diffusive to ballistic transport in etched graphene constrictions and nanoribbons

S. Somanchi, B. Terrés, J. Peiro, M. Staggenborg, K. Watanabe, T. Taniguchi, B. Beschoten, and C. Stampfer *Ann. Phys. (Berlin)* 529, 1700082 (2017). ©2017 by WILEY - VCH Verlag GmbH & Co. KGaA, Weinheim. Reprinted with permission.

3.1. Graphene

Ever since its isolation in 2004 by A. Geim and K. Novoselov [88], the carbon allotrope, graphene has received a lot of attention in both fundamental research and industrial applications. Its unique two dimensional hexagonal honey comb crystal structure confers it with unique characteristics unlike traditional semiconductors [30, 89–91]. For example, graphene exhibits a linear dispersion relation (at low energies) instead of the usual quadratic relation unlike other semiconducting materials. This is, in fact, the reason for its excellent electronic, optical and other physical properties. Consequently, the electrons in graphene behave like massless chiral Dirac fermions [92]. This peculiar property of chirality in graphene is responsible for finite transmission of electrons through an electrostatic barrier, a phenomenon known as Klein tunnelling [31, 93]. Graphene is known to exhibit an exceptionally high values of mobility even at room temperature which has been used in high frequency electronics to achieve cut off frequencies of about 100 GHz and even higher [94, 95]. Further, graphene also has a high saturation velocity as compared to conventional semiconductors due to the higher energy of optical phonons [96]. Along with this, graphene can also withhold high current densities on the order of 10^8 A/cm^2 which is much higher than that of copper [97]. The high current carrying capacity makes graphene an attractive material of choice for interconnects in integrated circuits [98]. While, in semiconductors, doping with n- or p-type materials is used to achieve the desired nature of the charge carriers, in graphene, this is possible simply by applying an electric field using a gate. The nature of charge carriers can then effectively be tuned from holes to electrons as they cross the Dirac point, a property which can be used in field effect transistors and sensor applications [99]. The linear dispersion relation also gives graphene, an energy dependent density of states and an anomalous (half integer) quantum hall effect visible even at room temperature [100]. Besides these, graphene also has a very high thermal conductivity (4840 - 5300 W/mK) at room temperature [101]. This is an added advantage when using graphene in electronic circuits as it ensures good distribution of heat, increases the longevity and make more compact devices.

In terms of optical properties, graphene has an absorption coefficient of 2.3% and a reflection coefficient of 0.1% [102]. Thus, graphene's high transparency and low reflectance combined with a high charge carrier

mobility make it a promising material in the field of opto-electronics, for example, in transparent conducting electrodes, light emitting diodes etc [103–105]. Moreover, with a theoretical value of Young’s modulus of ≈ 1 TPa, graphene can be integrated into several nanoelectromechanical (NEMS) applications [106]. Finally, graphene, being ultra thin (thickness ≈ 0.345 nm) also has a huge advantage when designing electronic devices since it is much easier to bring the top gates closer to the electron transport channel as compared to traditional 2DEGs where the channel lies inside a heterostructure with a thickness around 5 - 50 nm. This results in an enhanced gate coupling to graphene and hence, more electrostatic control over the charge carrier density.

Graphene is also considered to be a promising candidate for future spintronics based devices. This is owing to the low mass of carbon, due to which graphene has a very low spin-orbit coupling. Added to this, almost 99% of graphene consists of nuclear spin free carbon isotope C^{12} resulting in a small hyper-fine interaction which promises a long spin life time on the order of $1 \mu s$ [107]. Particularly, as discussed in chapter 1, with the miniaturization of electronic devices quickly reaching a saturation, graphene based spintronics could serve as an alternative to extend the Moore’s law. Graphene with its planar geometry and mono-atomic thickness is a viable alternative to Si in traditional CMOS based technology to overcome the scaling issues without affecting the performance. Thus, overall, graphene could potentially be an ideal choice of material to explore scalable, patternable ultra-thin, light weight, strong yet flexible, high performance electronic, opto-electronic and spintronic devices.

3.2. Graphene nanostructures

In spite of all the above mentioned virtues, graphene lacks one crucial property when realizing many electronic device concepts - a band gap. Along with this, graphene also exhibits a finite minimum conductivity even at the Dirac point where the charge carrier density vanishes [108]. This has a huge impact when integrating graphene into nanoelectronic devices since it can result in leakage currents and low on-off current ratios. Therefore, many research groups have been concentrating on engineering a band gap in graphene. One elegant means of doing so is by confinement of charge carriers in devices such as graphene nanoribbons (GNRs) or constrictions (GNCs) (see Fig. 3.1).

A GNR is obtained by etching or cutting a graphene sheet/flake along two parallel lines with a nanometer width resulting in different edge geometries such as zig-zag and armchair [109, 110]. Atoms along a zig-zag edge come from the same sub-lattice while those along an armchair edge come from two different sub-lattices in the graphene sheet. Thus, different boundary conditions of these ribbons may result in them displaying different electronic properties. Typically, the length of a GNR l is longer than its width w [111–115]. On the other hand, finite termination of a graphene sheet/flake along both the x and y directions results in a GNC where the length is comparable to or less than the width i.e. $l < \sim w$ [42, 116–118]. Although, physically, both the ribbon and the constriction are obtained by cutting the graphene sheet along a desired direction, their properties differ significantly depending upon the width, length, the number of edge states and the type of edge termination. For example, narrow and long nanoribbons are likely to contain more edge states than their relatively shorter and wider counterparts fabricated in the same manner.

In such nanostructures, theory predicts that it is, in principle, possible to open a band gap of nearly 1 eV in a nanoribbon of width 1 nm [37]. For arm-chair nanoribbons, the smaller the width of the ribbon, the larger the band gap while zig-zag nanoribbons are gapless and thus, cannot be used in field effect transistors

(FETs) [119]. On the other hand, according to Ref. [37], both zig-zag and arm chair nanoribbons with hydrogen passivated edges have a non-zero, direct band gap.

GNR-based FETs have already shown a band gap of about 0.14 eV in 10 nm wide nanoribbons [120] and a gap of nearly 0.2 meV for a width of 15 nm in another study [121] (band gap of narrow GNRs is sensitive to its environment). Successful demonstration of high performance short channel (20 nm) graphene field effect transistors (FETs) with an on-off ratio of 10^5 and a predicted band gap of more than 2 eV has also been achieved [122]. In general, we see that the results obtained experimentally and theoretically, both strongly rely on the width, morphology and the type of edges of the nanoribbon along with the method of fabrication. Importantly, as we go towards much narrower ribbons to achieve larger energy or band gaps, edges show an even more considerable influence on the electronic transport of such devices.

From a fundamental point of view, these narrow strips of graphene provide a platform to confine electrons causing an energy gap near the charge neutrality point (CNP) leading to Coulomb blockade which will be discussed in a bit more detail in the next sections [121, 123, 124]. Furthermore, like in the case of semiconductor 2DEGs, these nanoribbons and constrictions can be used together in conjunction with graphene quantum dots as charge detectors and also tunneling barriers [114, 125, 126].

With the advent of improved fabrication technologies, ballistic transport has already been achieved at room temperature in high quality micron-scale encapsulated graphene devices [127]. More recently, ballistic transport and size quantization effects in encapsulated graphene nanoconstrictions or QPCs have also been reported [42]. Such graphene quantum point contact devices could be exploited to construct valley filters and valley valves in analogy with spin filters and spin valves [128]. Moreover, with engineered electrostatic gating, these ballistic constrictions could also function as collimated point-like sources allowing us to explore a wealth of electron optics experiments based on Veselago lensing, beam splitters or waveguides [129, 130]. Interestingly, graphene QPCs have also been used as sensors even in the field of biology for DNA detection and characterization thanks to their ability to carry large sheet currents and the sensitivity of conductance to the edges [131]. In general, what makes graphene QPCs really exotic is that they display a range of properties depending on their width, edge morphology, orientation, doping etc. that can be tuned on an atomic scale for different applications.

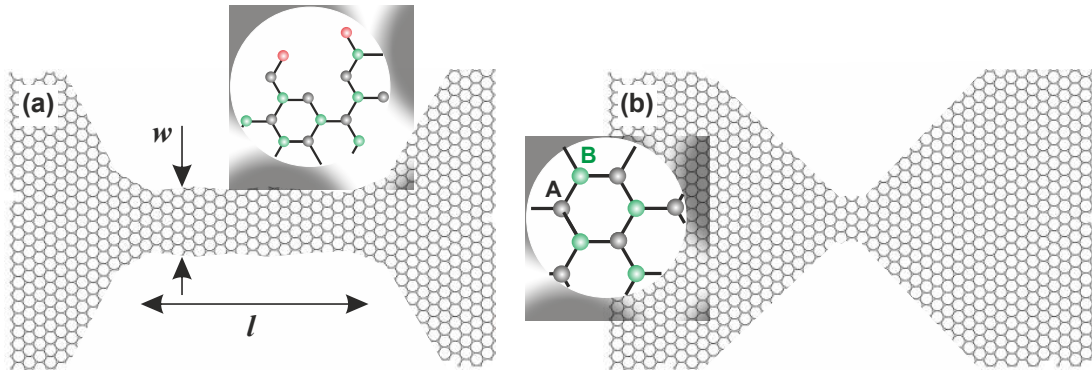


Figure 3.1.: Schematic illustration of a graphene nanoribbon (a) and nanoconstriction (b) of length l and width w . Inset in (a) indicates rough edges and dangling bonds (red dots) along the edge of the nanoribbon. Inset in (b) shows the hexagonal lattice structure of graphene with carbon atoms in the two sub-lattices A (grey dots) and B (green dots).

3.3. Characteristic length scales and gate couplings in graphene nanodevices

In this section, we discuss the properties of graphene nanostructures which depend crucially on (i) the surrounding environment, giving rise to charge carrier inhomogeneities as well as on (ii) the edge termination or edge roughness that is likely to give rise to localized edge states as in the case of etched devices. In particular, the flatness of graphene or the suppression of nanometer-scale strain variations has been shown to be crucial for high carrier mobility [132, 133]. All these have important consequences on the charge transport length scales such as the mean free path as well as on the gate couplings in realistic graphene nanodevices.

Fig. 3.2 (b) shows how the quantity k_F^2/π where k_F is the Fermi wave number varies as a function of back gate voltage V_{bg} in an etched graphene nanoribbon or constriction (see the schematic in Fig. 3.2 (a)) and how it depends on the disorder induced residual charge carrier density n^* according to the following equation.

$$n = \frac{k_F^2}{\pi} = \sqrt{(\alpha \Delta V_{bg})^2 + (n^*)^2} \quad (3.1)$$

Here, n is the net charge carrier density and $\Delta V_{bg} = V_{bg} - V_{bg}^0$ where V_{bg}^0 is the back gate voltage at the CNP. We assume that 1. $V_{bg}^0 = 0$ V such that $\Delta V_{bg} = V_{bg}$ and 2. graphene is placed on a $d = 285$ nm thick SiO_2 layer deposited on a highly p-doped Si substrate that serves as the back gate (BG) resulting in a gate lever arm $\alpha = \frac{\epsilon_0 \epsilon_r}{ed} = 7.2 \times 10^{10} \text{cm}^{-2} \text{V}^{-1}$, where ϵ_0 is the dielectric constant of air and $\epsilon_r = 3.9$ is the value for SiO_2 . The residual charge carrier density n^* reflects the presence of electron-hole puddles near the CNP most likely due to charge impurities in the near vicinity [38]. In cleaner systems exhibiting low values of n^* such as the red trace in Fig. 3.2 (b), there is less smearing of the charge carrier density around the CNP and a lower overall carrier density can be achieved. Thus, in an ideal device, $n^* = 0$.

In Fig. 3.2 (c) and (d), we consider a system where $n^* = 0$ but introduce another disorder related term, the trap state density n_T which arises due to the localized states near the edges of a graphene nanostructure. In this case, we follow Ref. [42] and use

$$n = \frac{k_F^2}{\pi} + n_T(k_F) = \alpha \Delta V_{bg}. \quad (3.2)$$

The localized states arise from the rough edges of a nanoribbon or constriction, for example, by using top-down fabrication such as etching leading to imperfections like dangling bonds (see Fig. 3.1) consequently resulting in edge disorder. Studies have shown that edge disorder can play a huge role in limiting the transport through graphene nanostructures especially in narrower ribbons and constrictions where the edges are much closer to the bulk transport channel [42, 134].

The density of these localized trap states ρ is estimated using a Gaussian (see Fig. 3.2 (c)) where the width and the amplitude together (area under the Gaussian curve) determine the trap state density n_T as shown in Fig. 3.2 (d). We see that as the trap state density increases, the term k_F^2/π which arises due the conduction of non-localized charge carriers smears out along the gate axis in Fig. 3.2 (e). In particular, we observe a gate dependent broadening of k_F^2/π near the CNP. At higher values of V_{bg} , the density of states in the bulk dominates and the transport is not affected by the localized states anymore. The black dashed line is a linear fit using Eq.3.2 to the blue trace assuming $n_T = 0$. Note that this line is parallel to all other traces at higher values of V_{bg} but deviates from the expected value as the gate voltage approaches zero. Thus, the

localized states contribute only to the total density of states and thus, to the charging characteristics of the system but not to the charge transport itself.

From the above discussion, we arrive at the following general relation between n and k_F .

$$n = \frac{k_F^2}{\pi} + n_T(k_F) = \sqrt{(\alpha \Delta V_{bg})^2 + (n^*)^2} \quad (3.3)$$

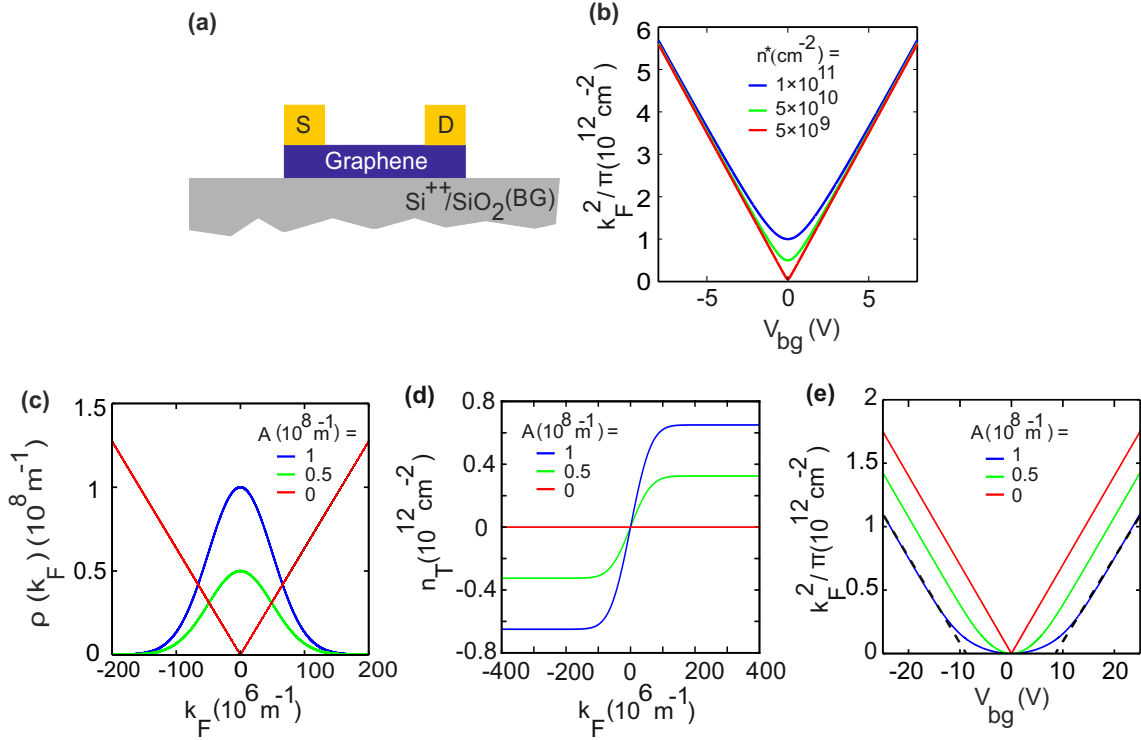


Figure 3.2.: (a) Schematic of a graphene nanoribbon resting on the surface of Si⁺⁺/SiO₂ substrate that serves as the back gate (BG). Source (S) and drain (D) electrodes are used to apply a bias voltage across the ribbon. (b) Density of the non-localized charge carriers k_F^2/π in the bulk channel of the device in (a) as a function of the back gate voltage V_{bg} for different values of residual charge carrier density n^* . (c) Density of localized trap states ρ as a function of the Fermi wave number k_F . Blue and green traces correspond to Gaussian distribution functions with different amplitudes A . Red trace denotes the ideal linear density of states of graphene. (d) Trap state charge carrier density n_T as a function of k_F for different values of A as shown in (c). (e) k_F^2/π as a function of V_{bg} for different values of trap state carrier density n_T . The black dashed line is a straight line fit using the ideal relation $k_F^2/\pi = \alpha \Delta V_{bg}$. As n_T increases, we observe a deviation from the linear behavior of the charge carrier density around the CNP.

Keeping this in mind, in Fig. 3.3 (a), an important length scale for ballistic transport - the mean free path l_m is plotted as a function of applied gate voltage for different carrier mobilities μ . The mean free path is given by

$$l_m = \frac{\hbar \mu}{e} k_F. \quad (3.4)$$

where e is the elementary charge and \hbar , the Planck's constant [127]. For comparison, the Fermi wavelength λ_F is also included.

$$\lambda_F = \frac{2\pi}{k_F} \quad (3.5)$$

For this plot, we assume an ideal disorder-free system where $n^* = n_T = 0$. The Fermi wavelength has to be significantly smaller than the mean free path ($\lambda_F \ll l_m$) for ballistic transport. Fig. 3.3 (a) shows that for high carrier mobility devices e.g. for $\mu = 300,000 \text{ cm}^2\text{V}^{-1}\text{s}^{-1}$, it is possible to have ballistic transport beyond $V_{bg} = 0.15 \text{ V}$ (see region 'A' consisting of both the light and dark gray shaded areas. This includes the region enclosed in between the green and the pink curves to the right side of their point of intersection.). This allows us to obtain long mean free paths on the order of $1 \text{ }\mu\text{m}$ in such a system at very low n ($n = 7 \times 10^{10} \text{ cm}^{-2}$ for $V_{bg} = 1 \text{ V}$).

Further, the window in which it is possible to observe ballistic transport becomes smaller as we move to a mobility of $40,000 \text{ cm}^2\text{V}^{-1}\text{s}^{-1}$ (see region 'B', the dark gray shaded area. This includes the region enclosed in between the green and the orange curves to the right side of their point of intersection). Consequently, for a device with a low mobility to be ballistic, its width should be around $100 - 200 \text{ nm}$ in the voltage range under consideration (see horizontal black dashed line at 130 nm). Whereas, in the case of high mobility devices, it is possible to design devices, for example, with a width of $0.5 \text{ }\mu\text{m}$ for $\mu = 150,000 \text{ cm}^2\text{V}^{-1}\text{s}^{-1}$ and $1.5 \text{ }\mu\text{m}$ for $\mu = 300,000 \text{ cm}^2\text{V}^{-1}\text{s}^{-1}$ to allow ballistic transport (see horizontal black dashed lines at $0.5 \text{ }\mu\text{m}$ and $1.5 \text{ }\mu\text{m}$). Thus, achieving a higher mobility relaxes the restriction on the size of the devices to observe ballistic transport.

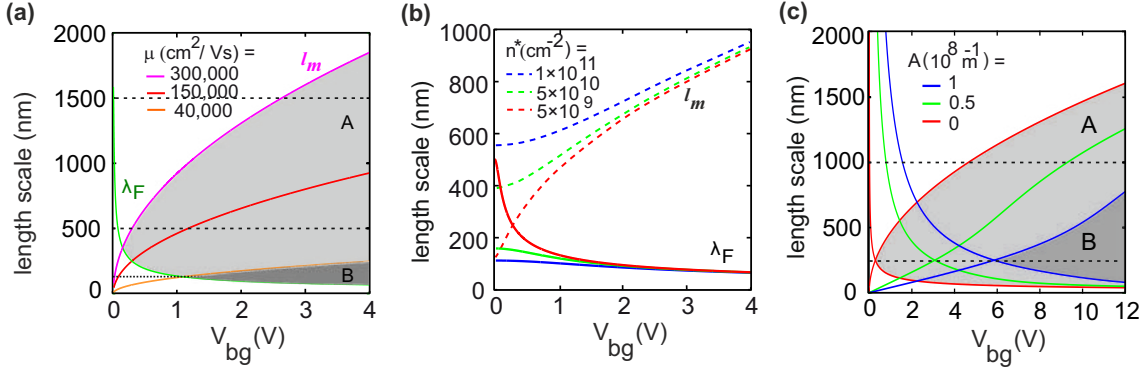


Figure 3.3.: (a) Fermi wavelength λ_F (green trace) and mean free path l_m (orange, red and pink traces) as a function of V_{bg} for different mobilities in an ideal system with no disorder i.e. $n^* = n_T = 0$. (b) Similar to (a) for different values of n^* (see Fig. 3.2 (b)) for the red trace in (a). (c) Similar to (a) for different values of n_T (see Fig. 3.2 (e)) for the red trace in (a).

We, now, introduce the disorder related term n^* back into the system (refer to Fig. 3.2 (b)). Fig. 3.3 (b) shows how the length scales vary for different values of n^* for the red trace in Fig. 3.3 (a) with $\mu = 150,000 \text{ cm}^2\text{V}^{-1}\text{s}^{-1}$. Interestingly, we observe that as n^* increases, the system becomes more conducive to observe ballistic transport - the red traces meet at a voltage of 0.3 V while the blue traces do not meet at all in the given voltage range.

Similarly, in Fig. 3.3 (c), we observe the effect of n_T (refer to Fig. 3.2 (e)) on the length scales. For larger values of trap state density such as the blue traces, a voltage greater than 6 V (see 'B', the dark gray

region in between the two blue traces) is required to observe ballistic transport in devices with dimensions between 200 - 400 nm (see the horizontal black dashed line at 250 nm). This restriction on both the applied voltage and the width of the device relaxes as we go to traces with lower values of n_T - see the region 'A' consisting of both the light and the dark gray shaded areas between the two red traces which allows us to design a device with dimensions greater than 1 μm to observe ballistic transport in the given voltage range (see the horizontal black dashed line at 1 μm).

It is important to note that for the narrow top-down etched nanoribbons and constrictions (roughly $w < 200$ nm), the influences of the rough edges play a dominant and unfortunately, limiting role [135–137]. For such devices, localized states and statistical Coulomb blockade open a mobility gap making the mean free path in Fig. 3.2 (e) - (f) nearly meaningless. For the state-of-the-art etching technology, this puts a lower limit on the nanoribbon and constriction width for observing quantum ballistic transport. In the case of gate defined nanostructures, the quantity $n_T(k_F)$ is no longer relevant since there are no rough edges while n^* can be lessened by using suspended or encapsulated graphene to reduce the influence of charge puddles in the substrate.

The following sections of this chapter describes efforts made in the field of electron confinement in both single layer graphene QPCs followed by bilayer graphene QPCs in the next chapter. In the case of SLG QPCs, we mostly discuss the technique of lithographic confinement of electrons by etching where the broken lattice symmetry introduces an effective mobility gap. While in the case of BLG QPCs, an external out-of-plane electric field can be used to break the inversion symmetry, resulting in the opening of a band gap. The focus is on the technological challenges involved in the fabrication of high quality devices, how disorder due to both substrate and edges as described above, affect the device characteristics and the advancements made so far to understand and control the edge physics.

3.4. Electronic transport in graphene nanoribbons and nanoconstrictions

A common method employed to produce graphene nanoribbons is the lithographic patterning of graphene. On one hand, this method offers huge control over the design and geometry of the sample. However, due to technical limitations, making arbitrarily small nanoribbons with a stronger energy of confinement is difficult to achieve. The use of etching always results in rough edges which act as sources of scattering thereby decreasing the mobility and the overall performance of the device as discussed in the previous section. Other fabrication methods include unzipping of carbon nanotubes [138], bottom-up fabrication from molecules [139], growth along the edges of SiC steps [140], and epitaxial growth [141]. A comprehensive outline of various fabrication techniques and the relevant literature is mentioned in Refs. [125, 142]. While bottom-up synthesized atomically precise GNRs are the most promising for controlling the electronic properties, their maximum length sets some limitations for advanced transport studies and device integration. This makes, at present, top-down lithographically defined GNRs and GNCs, the most common and straight forward approach for fabricating quantum transport devices and is also used for making the graphene nanoconstrictions/ quantum point contact devices in this thesis. Therefore, in the next sections of this chapter, a short literature review consisting of the research conducted in the field in GNRs and GNCs that have mostly been fabricated by etching is presented.

3.4.1. Graphene nanoribbons/constrictions on SiO₂

In the early days of graphene research, the most commonly used substrate for the fabrication of GNRs and GNCs is a highly doped Si/SiO₂. This is thanks to its wide availability, good dielectric properties of SiO₂ and the potential integration of graphene-based devices with the existing Si-based semiconductor technology. Most early experiments involved deposition of graphene on such Si/SiO₂ substrates either by direct exfoliation or by some other transfer method. GNRs or GNCs were then fabricated using a series of electron beam lithography (EBL) and reactive ion etching (RIE) steps [38, 113–116, 124, 132, 133, 143–149]. An example of such a graphene nanoribbon (length $l = 2 \mu\text{m}$ and width $w = 80 \text{ nm}$) is shown in Fig. 3.4 (a). Lateral confinement of electrons in lithographically patterned GNRs is usually characterized by suppressed conductance particularly near the CNP leading to a so-called "transport gap" in back gate voltage characteristic [113–116]. Fig. 3.4 (b) shows an example of conductance as a function of the back gate voltage highlighting the transport gap ΔV_{bg} , centered around the CNP at V_0 . In particular, statistical Coulomb blockade is observed in this region of suppressed conductance similar to the experiments based on quantum dots. Subsequently, transport in such disordered nanoribbons on SiO₂ was explained by treating the nanoribbon as a series of charged islands of varying sizes that exhibit local resonances due to statistical Coulomb blockade in the transport gap region [114]. Moreover, it has also been successfully demonstrated, that the addition of a single electron to the nanoribbon can be monitored by a nearby single electron transistor with a combination of lateral gates [150–153]. Associated with the region of suppressed conductance are two energy scales - one $\Delta E_F \propto \sqrt{\Delta V_{bg}}$ that depends on the extent of the gap in the back gate voltage direction which is a measure of the disorder potential and the other, E_g is the extent of bias voltage (in bias spectroscopy) which gives the charging energy of individual charged islands (see Fig. 3.4 (c)). The transport gap ΔE_F is a result of both the confinement of electrons due to etching and a bulk/edge disorder potential together resulting in the formation of charged islands and quantum dots. While the source-drain gap, E_g is related to the size and charging energy of the associated quantum dots and therefore, scales inversely with the width of the nanoribbon (narrower nanoribbons consist of smaller charge islands with larger charging energy) [113]. This is in agreement with earlier theoretical calculations which suggest that the origin of energy gaps comes from both the confinement and disorder potential due to rough edges [154]. Further, scanning gate microscopy measurements also confirmed the existence of multiple quantum dots in such devices [155].

Similar scaling of the energy gap E_g as a function of the ribbon width was, indeed, also earlier observed by Han et al. [121] in nanoribbons with width ranging from 10-100 nm and lengths of 1-2 μm (i.e. $w < l$). In another closely related study of aspect ratios in etched nanoconstrictions particularly in the regime of $w \sim l$ and also $w > l$ (smallest width = 50 nm, largest length = 1 μm) [156], shorter constrictions showed a much smaller transport gap. This is because shorter constrictions consisted of fewer charge islands and hence, less charging events. Although the width dependent charging energy was nearly independent of the length, the minimum conductivity in the transport gap region itself was strongly length dependent with shorter constrictions having a much higher conductance level ($0.1 - 1 e^2/h$).

A temperature dependent study of the transport gap in nanoribbons with similar dimensions ($20 \text{ nm} < w < 120 \text{ nm}$ and $0.5 \mu\text{m} < l < 2 \mu\text{m}$) revealed that the transport through the nanoribbon is dictated by thermal activation of charge carriers at higher temperatures and variable range hopping at lower temperatures. Electric field-based transport measurements indicate that the transport gap in disordered GNRs is governed by hopping through localized states [157] or co-tunneling processes [158].

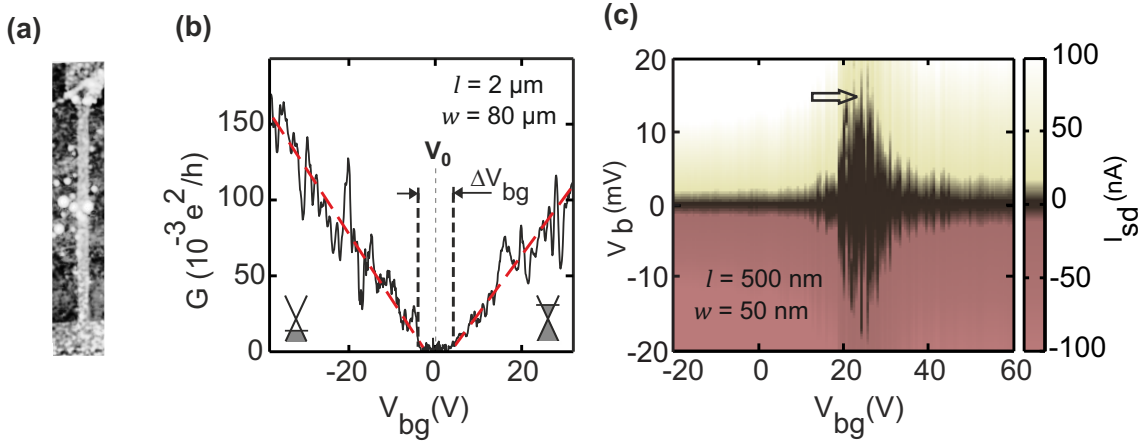


Figure 3.4.: (a) Scanning electron microscopy image of graphene nanoribbon with $l = 2 \mu\text{m}$ and $w = 80 \text{ nm}$. (b) Two-terminal back gate characteristics of the graphene nanoribbon shown in panel (a). The hole and electron transport are highlighted in the insets and red dashed lines mark the overall linear increase of conductance. V_0 denotes the CNP of the conductance trace. (c) Color plot of the source-drain current I_{sd} as a function of the back gate voltage V_{bg} and the bias V_b for a constriction with $w = 50 \text{ nm}$ and $l = 500 \text{ nm}$. The arrow indicates the region of suppressed current which comprises of Coulomb diamonds. Figure adapted from Ref. [156].

Etched graphene nanoribbons were also synthesized using oxygen plasma reactive ion etching with a patterned hydrogen silsesquioxane HSQ layer as protective mask [112]. The transport properties were found to be heavily dependent on the proper removal of the HSQ layer using HF. In these devices having $w = 30 \text{ nm}$ width and $l = 1.7 \mu\text{m}$ channel length, first experimental evidence of sub band formation in 1D channels was noted [112]. However, these devices are not ballistic which is due to a combination of high edge disorder (long channel length implies a stronger influence of edges) and also substrate-induced disorder. More recently, it has been shown that this edge disorder can be reduced by treating the etched graphene constrictions with a low concentration of hydrofluoric (HF) acid for a very short duration of 20 s [146]. This suppresses the transport gap significantly and shifts the CNP close to zero volts. However, the effective energy gap remains unaltered.

3.4.2. Suspended graphene nanoribbons/constrictions

One straight forward approach to reduce substrate-induced disorder is to remove or to replace the SiO_2 substrate. The substrate could be either completely removed to form "suspended" nanoribbons or replaced by another more suitable material. The first significant improvement in device quality was observed by Bolotin et al. in micron-sized suspended and current annealed devices [159]. While the carrier mobility of devices before current annealing remained rather low ($28,000 \text{ cm}^2\text{V}^{-1}\text{s}^{-1}$ at $n = 2 \times 10^{11} \text{ cm}^{-2}$), the mobility of current annealed devices was as high as $230,000 \text{ cm}^2\text{V}^{-1}\text{s}^{-1}$ at similar charge carrier density at a temperature of 4 K. This is attributed to the fact that current annealing removes residual dopants and other fabrication impurities thus resulting in a sharper resistance peaks at the CNP and, correspondingly, to a higher mobility and a lower charge inhomogeneity. Owing to the superior quality of such devices, many interesting phenomena such as ballistic transport [160], snake states [130] and fractional quantum Hall effect [161] which were earlier limited by device quality are now observed.

Signatures of quantized conductance in graphene nanoconstrictions were first observed by Tombros et al. in devices suspended above the surface of a SiO₂/Si substrate [40]. These devices were current annealed which leads to a carrier mobility as high as 600,000 cm²V⁻¹s⁻¹ at a charge carrier density of 5×10^9 cm⁻² at 77 K resulting in an electron mean free path of several hundred nanometers (200 - 450 nm) [162]. Conductance steps were observed at intervals of around $2e^2/h$ suggesting that the valley degeneracy is lifted. The transition from quantized conductance at zero magnetic field to the quantum Hall regime for magnetic fields above 60 mT was observed which confirms the high quality of these devices [40]. This work was further corroborated by calculations performed by S. Ihnatsenka and G. Kirczenow [163] which provide a theory for the observation of integer and fractional quantized conductance with a comparison between zigzag and arm-chair edges. However, in devices produced by the same fabrication method and current annealing but with much smaller device width, Coulomb blockade was observed at 0 T similar to disordered nanoribbons fabricated on SiO₂. The Coulomb blockade becomes strongly suppressed beyond a relatively low magnetic field of nearly 2 T and shows a completely insulating state [164]. This shows that even for high quality samples, edge disorder is most likely inevitable and plays a key role in the determination of the observed physical phenomena. In similarly fabricated devices, formation of p-n junctions was also well studied. Characteristic Fabry-Perót interferences and ballistic transport with a mean free path of nearly 2 μ m were observed, thus, also paving the way for more advanced electron optics experiments in the future [165, 166].

Suspended devices, however, suffer from severe inherent limitations. Crucial to note is that this process does not allow for control over the dimensions of the devices. Also, the maximum applicable back gate voltage is in most cases limited to a few volts due to the straining of graphene. Furthermore, it is difficult to incorporate top gates and fabricate multi-terminal devices.

3.4.3. Graphene nanoribbons/constrictions based on hBN

Most graphene nanodevices that rest directly on SiO₂ suffer from inherent substrate induced disorder in the form of dangling bonds, substrate roughness, charge puddles [38, 39] and surface phonons [167] which cause serious limitations to the mobility of charge carriers in such devices. Later on, hBN has received a great deal of attention as an alternative substrate for graphene owing to its atomically smooth surface that suppresses rippling in graphene, a lattice constant similar to that of graphene and planar structure that is expected to be free of any dangling bonds or surface charge traps [41, 168]. Scanning tunneling microscopy studies also confirmed that graphene on hBN has significantly less pronounced electron-hole puddles as compared to SiO₂ [169].

However, incorporating a new substrate alone cannot improve the quality of nanostructure devices as reported by Bischoff et al. [143]. It was seen that the micron sized graphene devices on hBN have significantly higher mobility (more than 45,000 cm²V⁻¹s⁻¹ at $n = 10^{10}$ cm⁻²) and lower disorder density (n^* less than 10^{10} cm⁻²) than devices fabricated on SiO₂ [158]. However, the transport behavior of nanoribbons remained the same. In both cases, transport seems to be dominated by localized states and charge puddles similar to Ref. [114]. Further, nanoribbons of similar width etched from the same graphene flake showed strong variations in the quality and evolution of conductance. This is a strong indication that edge disorder plays an important role in the transport properties of reactive ion etched graphene nanostructures irrespective of the substrate. In order to reduce the influence of edges, the authors of Ref. [158] also fabricated ultra-short constrictions with a width of only 30 nm [170]. Analysis of transport gap revealed an interesting

result - it is possible that the area over which the charge is localized can be almost 10 times larger than the constriction itself. This is allowed only if these localized states extend along the edges of the constriction into the graphene leads. In such a case, a small wave function overlap between the localized state in the edge and the delocalized state in the lead should allow electron tunneling. These findings further indicate the importance of the influence of edges on transport.

3.4.4. Encapsulated graphene nanoribbons/constrictions

The most successful approach to completely isolate graphene from its surroundings for preventing contamination is by encapsulating it within two flakes of hBN, thus forming a hBN-graphene-hBN "sandwich" structure (see Fig. 3.5 (a)). While the carrier mobility of graphene on SiO₂ was in the range of 10,000 to a maximum of 50,000 cm²V⁻¹s⁻¹, the mobility of such sandwich structures reached the highest values of several hundred thousand [171], which is comparable to values obtained from suspended devices [159, 162]. This was shown to be the case even at room temperature. This technology, therefore, allows us to achieve high mobility devices along with a good control over their geometry and size. Furthermore, it also allows to fabricate high performance multi-terminal devices with an efficient gate coupling [127, 172, 173].

In particular, dry transfer processes [172, 174] for making hBN-graphene-hBN sandwiches together in combination with a metal (Al) hard mask and SF₆ or CHF₃ based reactive ion etching allows us to achieve well controlled constrictions with high quality [42]. Evidence of size quantization in nanoconstrictions with widths in the range of 200 - 380 nm, made from this technique of encapsulating graphene was first observed by Terrés et.al [42]. Conductance kinks with a step height of 2 - 4 e²/h were observed. This height was seen to be dependent on how strongly the electrons were likely to get scattered at the rough edges of the QPC, which in turn, depends on the width of constriction. Conductance trace of one such QPC with a width of 280 nm is shown in Fig. 3.5 (b) and (c). We see clear kinks on the order of 2 e²/h. A detailed analysis of the conductance kinks shall be presented in the following chapters.

Size quantization was further confirmed by the application of magnetic field, upon which the kinks at zero magnetic field evolved into their respective Landau levels at higher magnetic fields [42].

Interestingly, narrower ($w = 35$ and 40 nm) and relatively longer nanoribbons ($l = 100$ and 150 nm respectively) fabricated in the same manner show a transport gap at zero magnetic field similar to etched graphene nanoribbons on SiO₂ (or hBN as discussed in section 3.4.1 and 3.4.3), although the extent of the gap was much smaller due to the reduction of substrate induced disorder [111]. However, a larger magnetic fields, an insulating state, as in the case of high mobility graphene, appears due to the breaking of valley symmetry by the perpendicular magnetic field.

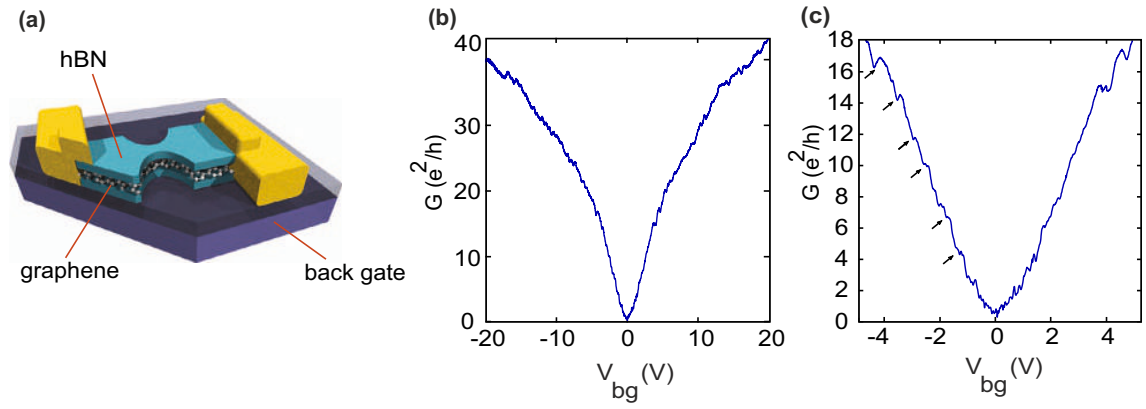


Figure 3.5.: (a) Schematic of a hBN encapsulated graphene nanostriction. Figure adapted from Ref. [42]. (b) Conductance trace of a 280 nm wide encapsulated graphene QPC as a function of the back gate voltage. (c) Close-up of the trace in (b) around the CNP. Conductance kinks on the order of around $2 e^2/h$ are denoted by the black arrows.

4. Quantum point contacts in bilayer graphene

As discussed in the previous chapter, confinement of electrons by etching graphene into nanostructures makes them suffer from an inherent edge disorder. In case of semiconductor systems, as seen in Fig. 2.1, confinement is achieved by the use of additional split gates in a 2DEG, thus, forming a quantum well. The advantage of this method is that the confinement potential is much smoother as compared to the rough edges in the etched graphene samples. However, similar split gate geometry cannot be realized in single layer graphene based devices because it lacks a band gap. In this case, Klein tunnelling occurs between n- and p-doped regions thereby preventing electrostatic gating. In this context, Bernal stacked bilayer graphene presents a great advantage as compared to its single layer counterpart. Bilayer graphene, unlike single layer has a parabolic dispersion relation (at low values of energy) where the charge carriers have an effective mass of about $0.033 m_e$ where m_e is the mass of an electron [175–178]. Although Bernal AB stacked bilayer graphene is also a zero gap metal in its pristine form, it offers the possibility of opening a band gap when a transverse electric field is applied causing a difference in the electrostatic potential between the two layers [175–180]. The gap is a result of the layer asymmetry such that its magnitude can be tuned by the applied gate voltage up to 0.4 eV [179–181]. Therefore, bilayer graphene can be readily combined with the split gate technology of semiconductor 2DEGs for fabricating an edge disorder free system along with a band gap in graphene.

Indeed, an experimental evidence for this band gap was first provided in Ref. [182] using BLG on a SiC substrate. In this experiment, doping is provided to BLG by the adsorption of potassium atoms. This resulted in a maximal band gap of 0.2 eV as observed using ARPES technique. Likewise, for graphene grown epitaxially on SiC, both theory and experiment show a consistent band gap of 0.25 eV. Several groups used bilayer graphene FETs for band gap engineering [135, 136]. Oostinga et.al. used a double gated configuration to induce an insulating state that could be controlled by the applied gate voltages [137]. With this configuration, it is possible to control both the band gap and the carrier concentration independently which was previously not possible with Ref. [182]. In one theoretical work based on tight binding simulations [183], it was seen that it is not quite possible to achieve the International Technology Roadmap for Semiconductors (ITRS) requirements (band gap of 0.4 eV and current on-off ratios over 10^4) [184, 185] for designing a FET with bilayer graphene due to the weak suppression of band to band tunnelling resulting in a small band gap. However, in the same year, using a dual gated geometry for bilayer graphene on SiO_2 , Zhang et.al showed a gate controlled, field tunable band gap of up to 0.25 eV [43]. Moreover, theoretical studies show that bilayer graphene could be a promising candidate for tunnel FETs where even a small band gap of the order of a few hundreds of meV is already enough to achieve the required on/off current ratio [186]. More recently, CVD based Bernal bilayer graphene RF transistors showed an exceptional performance with a forward power gain of up to 5.6 GHz and a conversion gain of -7 dB [187].

The following sections of this chapter focus on the efforts towards the confinement of electrons and

microscopic control of band gap using split gates in bilayer graphene nanoconstrictions.

4.1. Gate defined BLG nanoconstrictions on SiO₂

Similar to etched constrictions, gate defined constrictions also first began on Si/SiO₂ substrate. In one such device with a bilayer graphene flake exfoliated on top of a Si/SiO₂ substrate, Dröscher et.al used a pair of split gates separated by a narrow opening ($w = 80$ nm) and probed the transport through the channel or the constriction between them [188]. This was done by comparing the transport characteristics of the constriction formed due to the split gates to that of region under the continuous top gate in another area of the bilayer graphene flake. The opening of a band gap was seen in the form of an insulating state with an increase in resistance by a factor of 1000 below the top gated region. It was observed that the charge carriers are forced to flow through narrow channel under the split gates for higher displacement fields. This suggested that a perpendicular electric field i.e. a displacement field can confine charge carriers to a restricted area. However, since this device is built on SiO₂, charge puddles and the associated disorder potential led to diffusive transport. The oscillations observed in the lever arm maps were attributed to universal conductance fluctuations instead of quantized conductance. Identical results were noted by Goossens et. al on Si/SiO₂ substrate [189]. Their geometry also involved a continuous "strip gate" which was used to prove that it is possible to open a band gap in bilayer graphene and a split gate geometry to form a narrow channel. Here as well, the constriction ($w \approx 20$ nm) did not show any signs of quantized conductance. The dominant mechanism was deduced to be variable range hopping type and led to a mean free path of only 10 nm at a charge carrier density of 10^{12}cm^{-2} . However, these results were still encouraging enough to show that it is possible to achieve quantum confinement in gated graphene nanostructures which could then be extended to suspended graphene or graphene on hBN to decrease the influence of disorder as we will see in the next sections.

4.2. Gate defined suspended BLG nanoconstrictions

The first evidence of band gap control in bilayer graphene QPCs was demonstrated by Allen et.al. in 2012 in suspended structures [190]. QPCs without both substrate and edge disorder were achieved by local gating. This geometry involved a combination of split gates directly on top of the suspended graphene which depletes the charge carriers in the region underneath leading to the formation of the constriction. The suspension of another central gate (finger gates) on top of these split gates is used to control the charge carrier density of the channel locally. The constrictions ($w \approx 200$ nm) showed quantized conductance with a step height of $2 e^2/h$ at zero magnetic field indicating valley degeneracy lifting. Similar gating technique was used to fabricate dots with varying geometry (circular, elliptical), size (150 - 450 nm) and number of gates. Band gap is induced by application of voltage or a perpendicular electric field to the top gates thereby forming tunnel barriers. The formation of quantum dots is confirmed by the formation and analysis of periodic Coulomb blockade oscillations.

4.3. Gate defined encapsulated BLG nanoconstrictions

Analogous to the chronological order of research in etched SLG devices, once quantized conductance and evidence of band gap opening were observed in suspended BLG devices, the next step was to look for a similar behaviour on BLG constrictions on a cleaner substrate. Graphene encapsulated in hBN was a natural choice based on previous developments and this method was first successfully utilized by Goossens et.al [191]. Using multiple top gates along with the silicon back gate, both one dimensional sub-bands showing signatures of quantized conductance and zero dimensional quantum dots showing Coulomb blockade were demonstrated. The transport gap was only around 50 meV but was sufficient enough to achieve quantum confinement. However, due to this relatively small band gap, the channel showed a minimum conductance of e^2/h and it was not possible to completely pinch it off. Further, the conductance step height was on the order of $2 e^2/h$ instead of $4 e^2/h$ as expected for gate defined bilayer graphene. On the other hand, by inducing double barriers using appropriate gate voltages, a region of strongly suppressed conductance with diamond like features of Coulomb blockade was observed.

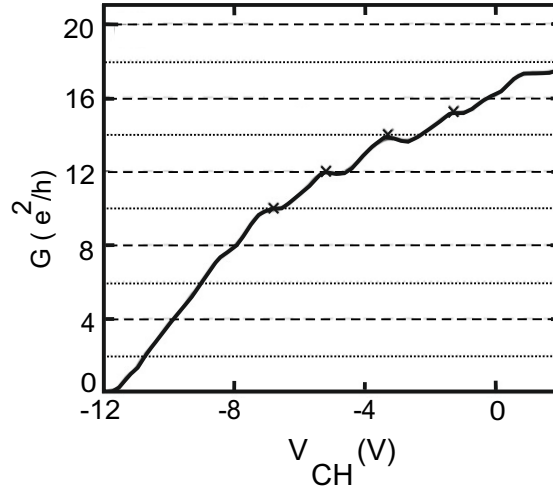


Figure 4.1.: Conductance of a gate defined encapsulated bilayer graphene QPC sample with a graphite back gate at zero magnetic field as a function of the channel gate voltage V_{CH} . Quantized conductance steps on the order of $2 e^2/h$ are clearly visible as indicated by the \times symbols. Figure adapted with permission from Nano Lett. 2018, 18, 1, 553-559. Copyright (2018) American Chemical Society.

More recently, a similar top gate and split gate geometry was used in encapsulated graphene QPCs along with a graphite back gate [192]. This small change had a tremendous impact on the resistance of the channel below the depletion gates- almost $1 \text{ G}\Omega$ as compared to $10 - 100 \text{ k}\Omega$ in the previous works [193–195]. With this addition, a resistance of almost $10^5 \text{ h}/e^2$ was achieved while depleting the region under the top gate. Two different QPC samples were investigated by this group. One of them showed quantized conductance with a step height of $2 e^2/h$ while in case of the other, it was $4 e^2/h$. This difference in the expected step height is attributed to the different residual disorder or strain patterns in both the devices. This could be due to the fact that the hBN layer separating top or split gate from the graphene is relatively thinner compared to GaAs heterostructures and may lead to changes in the confinement potential. A band gap of about 47 meV could be opened below the split gates which is consistent with the value achieved in previously discussed publications as well. Finally magnetic field measurements demonstrated a complete degeneracy lifting and

expected quantum Hall plateaus for bilayer graphene (see Fig. 4.1). The important point to take home from this work is that the use of graphite back gate has the potential to achieve large on-off resistance ratios (on the order of $G\Omega$) which was previously not possible with bilayer graphene on a substrate. This is due to the fact that graphite helps in screening charge impurities from underlying Si, hBN and even graphene itself thereby resulting in a large reduction in disorder. A great improvement in sample quality using graphite back gate was already demonstrated earlier by Ref. [196].

While high quality samples with robust conductance steps have been devised, deviations from the expected step height of $4 e^2/h$ have been commonly observed. It is not usual to observe valley degeneracy lifting even at zero magnetic field due to confinement. Control and breaking of valley degeneracy is a crucial requirement for both spintronics and valleytronics. Very recently, clear quantization steps on the order of $4 e^2/h$ and their peculiar splitting into steps on the order of e^2/h , $2 e^2/h$ and $4 e^2/h$ in the presence of a magnetic field was observed [197]. In this case, the back gate and the side gates on one hand are used to locally deplete the charge carriers and create a band gap in the region of the QPC. The global top gate on the other hand is fabricated right on top of the side gates (separated by a layer of oxide) and can tune the Fermi level in QPC directly. Further, a small perpendicular magnetic field of 20 mT was also applied on the leads in their normal state. When a magnetic field is applied perpendicular to the plane of graphene, a complete lifting of the four fold degeneracy is visible in the first two Landau levels. However, in case of higher sub-bands, the degeneracy of $4 e^2/h$ seems to be restored at high magnetic fields. In the intermediate fields, steps on the order of $2 e^2/h$ were also visible. Such peculiarities of the system in the presence of a magnetic field are explained by the formation, splitting and mixing of magneto-electric sub-bands. Thus, this particular study allows us to study and control the transition of sub-bands from full degeneracy to full splitting and forms an important step towards the development of valleytronics.

Similar results were indeed also observed by the authors from the same research group as Ref. [192]. Full four fold degeneracy at zero magnetic field, two fold degeneracy at intermediate magnetic fields and restoration of the four fold degeneracy in complete quantum Hall regime was noticed in three bilayer quantum point contacts of similar geometry but varying widths as in Ref. [198]. A theory for the observed mode splittings and crossings was provided using both k.p theory and tight binding simulations, both of them in agreement with each other. At zero magnetic field, the Berry curvature induces a non-zero orbital magnetic moment in the states occupied by the QPC. This leads to a vertical magnetic field splitting lines at low magnetic fields. At high magnetic fields, the system evolves into the Landau levels of gapped bilayer graphene which is manifested in the step height once again.

Finally, it is worth mentioning that the split gate technology has also been used to achieve confinement in zero dimensional quantum dots as well. Authors of Ref. [199] used a similar fabrication technique (i.e. including a graphite back gate) to prepare quantum dots of superior quality comparable to those in semiconductors. Using opposite voltages on the source/drain and the dot that they connect, both n- and p- type dots were formed, thus, demonstrating the ambipolar nature of the charge transport. Next, like the experiments based on etched quantum dots, a perpendicular magnetic field was applied to extract single particle level spectrum, shelling filling and show orbital degeneracy as well from the coulomb resonances. Thereafter, using a parallel magnetic field, a Zeeman splitting with a g-factor around 2 was observed, which is as expected for carbon based systems. This method of fabrication and device operation was further extended by Banszerus et.al. [200] to define single, double and triple dots in bilayer graphene using three finger gates on top of the split gates. In fact, this device is designed such that it could be used to define both quantum point contacts and quantum dots by careful selection of appropriate side and finger gate voltages.

For the schematic of the device, please refer to Ref. [200] or Fig. 5.7. Different features expected in traditional etched quantum dots such as coulomb peaks, excited states, double and triple dot formation are all possible and highly reproducible in this configuration. These experiments serve as the first step towards realization of spin relaxation experiments in bilayer graphene quantum dots. One can then combine such a quantum dot with a quantum point contact for spin qubit based experiments.

5. Fabrication of graphene and bilayer graphene quantum point contact devices

Contributions to this chapter:

All single layer graphene and hBN samples including optical images were made by Sowmya Somanchi. The bilayer graphene samples have been fabricated and the corresponding images have been provided by Luca Banszerus from RWTH Aachen University. All the schematics are made by Sowmya Somanchi.

5.1. Introduction

In this chapter, details regarding the fabrication of the devices discussed in this thesis are described. To begin with, isolation of graphene and hBN is introduced as the very first step to make any device. In the following section, the stacking technique used to assemble these 2D materials into van der Waals heterostructures or "sandwiches" is described. These sandwiches are processed further using standard electron beam lithography, reactive ion etching and metal evaporation to form the final device.

5.2. Substrate preparation

For all our devices, we used a substrate consisting of a $7\text{ mm} \times 7\text{ mm}$ size chip made from a $\text{Si}^{++}/\text{SiO}_2$ wafer, where the thickness of the oxide is about 285 nm. Here, Si^{++} is intended to be used as the back gate and therefore, the wafer is p-doped to ensure that the back gate is indeed conducting at cryogenic temperature. Using electron beam lithography (EBL), which is later followed by metal evaporation, Cr/Au based cross shaped markers (for example, see yellow + in Fig. 5.2 (b)) are designed on this wafer. Later, the wafer is diced into small chips of desired size. These markers are useful to identify the position of the graphene or hBN flake when exfoliated. This position is then utilized while designing the mask for EBL of the actual device. Before exfoliation, the chip is cleaned in Acetone/IPA and also exposed to oxygen plasma for a brief period to clean any residues of the dicing resist or other contaminants. This also increases the adhesion of the flake to the chip while exfoliation.

5.3. Exfoliation of graphene

Although, graphene was first isolated using the process of simple mechanical exfoliation [201], several other methods have been developed to optimize the quality, size and yield of graphene flakes for various ap-

plications. Some of these include chemical vapour deposition (CVD) based growth of graphene on catalytic metal substrates such as copper and nickel, epitaxial growth on silicon carbide, electrochemical exfoliation and synthesis using organic molecular precursors [202]. However, out of all these, mechanical exfoliation seems to be the simplest and the most straight forward process which also yields a high quality of graphene in terms of high electron mobility particularly when encapsulated with hBN as discussed in section 3.4.4. In the recent years, CVD on copper has also produced devices with exceptionally great performance. However, the high quality of graphene which is usually manifested in the form of features such as ballistic transport, quantized conductance etc. seems to be more dependent on the process of encapsulation with hBN rather than the origin of graphene i.e. exfoliated or CVD [42, 171, 174]. Hence, all the state-of-the-art graphene based devices mentioned in this thesis are encapsulated in hBN where both hBN and graphene are fabricated by using the technique of mechanical exfoliation.

Graphene is exfoliated by placing the natural graphite flakes on a sticky scotch tape (Nitto Denko model no. BT-150E-CM or Minitron Ultron 1008R and 1009R tape). The tape is then folded around 5-6 times until it is entirely covered with graphite. Exfoliating too many times can lead to smaller flakes. Then a Si/SiO₂ chip is pressed onto the tape with an adequate amount of force and then released to pick up the flakes. The thickness of the silicon oxide layer provides an optical contrast that is sufficient for the determination of single and bilayer graphene using an optical microscope (see Fig. 5.1 (a) and (c)).

5.4. Selection of graphene flakes

In case of SLG based devices used in this thesis, the size of the final device which consists of the constriction along with the leads is around $12 \times 6 \mu\text{m}$ (see Fig. 6.1 (d) and Fig. 6.2 (a)). Since the transfer process might lead to the formation of bubbles, graphene flakes with dimensions of about at least $20 \times 10 \mu\text{m}$ are chosen such that there is enough space to fit at least one device while avoiding the areas with bubbles. Similarly, for BLG, flakes with a size of at least $10 \times 10 \mu\text{m}$ are chosen to fabricate all the gates later on. Using a fresh tape for exfoliation ensures minimum residues on the flakes. This can also be verified using light and dark field microscopy.

After exfoliation, Raman spectroscopy (using a laser with an excitation wavelength of 532 nm) is used to confirm the number of layers in the exfoliated graphitic flake. Raman spectroscopy serves as a non-destructive tool to obtain a wealth of information about the quality of graphene such as the number of layers [203, 204], doping [205, 206], strain [207, 208] etc.

In particular, the Raman 2D peak can be used to distinguish between single and bilayer graphene [209]. The 2D peak is a consequence of a double resonance process wherein the excitation and the recombination of an electron-hole pair results in the emission of two transverse optical (iTO) phonons near the K point [210, 211]. In case of single layer graphene, the 2D peak is usually described by fitting a single Lorentzian curve [212]. Although it is sometimes observed that a Voigt model i.e. a combination of both Lorentzian and Gaussian curves fits the peak better especially around the tails of the curve for graphene on SiO₂. This could be a result of charge inhomogeneties and physical corrugations in SiO₂. These are known to be responsible for nanometer scale strain variations which follow a Gaussian distribution [132]. Typically, for graphene on SiO₂, the full width at half maximum (FWHM) is around $22\text{-}23 \text{ cm}^{-1}$. From single to bilayer, the band structure evolves from a linear, single valence and conduction bands to a parabolic, double valence and conductance bands. As a result, the number of bands that participate in the double resonance process and the possible scattering mechanisms increases. Therefore, in case of bilayer graphene, the 2D

peak consists of four Lorentzian peaks corresponding to different Raman processes [213] and the FWHM is usually between 90 - 100 cm^{-1} .

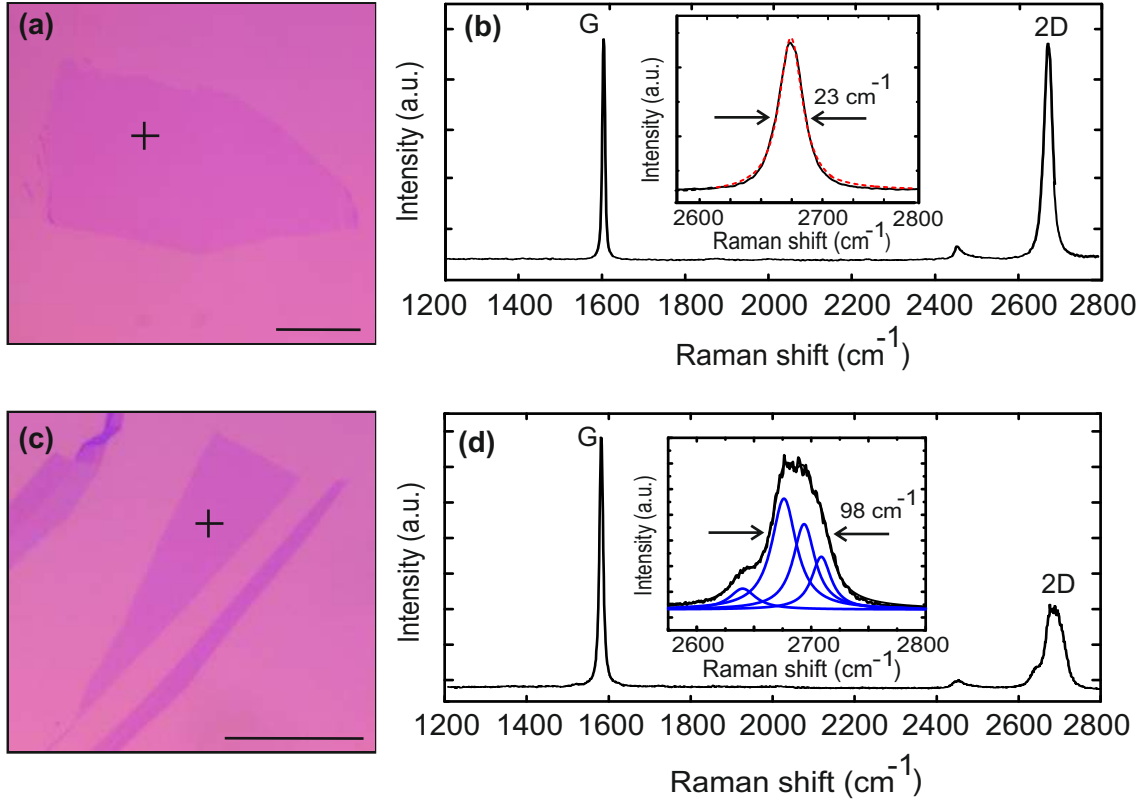


Figure 5.1.: (a) Optical microscopy image of a single layer graphene flake exfoliated on the surface of a Si⁺⁺/SiO₂ chip. (b) Raman spectrum of the flake in (a) at the point indicated by the black cross. The G and 2D peaks are indicated. Inset: Single Lorentzian curve (red dashed line) fitted to the 2D peak with a FWHM of 23 cm^{-1} . (c) Optical microscopy image of a bilayer graphene flake exfoliated on the surface of a Si⁺⁺/SiO₂ chip. (d) Same as (b) at the point indicated by the black cross in (c). Inset: Four Lorentzian curves (dashed blue lines. Solid black line is the cumulative sum of all the four blue dashed lines and the red dashed line is a Lorentzian fit to the solid black line.) Here, the FWHM is taken as the sum of the widths of individual Lorentzians. Scale bar in (a) and (c) is 20 μm .

5.5. Exfoliation of hBN

hBN is exfoliated from high quality crystals provided by K. Watanabe and T. Taniguchi from the National Institute for Material Science in Japan. In this case, two different types of substrates are used for exfoliation. One is a Si⁺⁺/SiO₂ substrate as in the case of graphene exfoliation. hBN flakes exfoliated in this way are typically used as the bottom layer during the fabrication of graphene-hBN sandwiches. We refer to such a flake as "bottom hBN". The other one is called "top hBN" and is obtained by exfoliating hBN crystals on a Si⁺⁺ wafer that is coated with a layer of polyvinyl alcohol (PVA)/polymethyl methacrylate (PMMA). The top hBN is then used to pick up graphene and deposit on the bottom hBN, the details of which are elucidated further in section 5.7.

The thickness of the resist layers is optimized such that the contrast of hBN on $\text{Si}^{++}/\text{PVA}/\text{PMMA}$ is similar to that of hBN on $\text{Si}^{++}/\text{SiO}_2$.

5.6. Selection of hBN flakes

While flakes with a thickness of around 15 nm are easily identifiable with a standard optical microscope, thinner hBN flakes particularly single and bilayer flakes are more easily identified using some special optical filters, thinner SiO_2 wafers etc. As seen in Fig. 5.2 (a)-(d), the thickness of the hBN flakes can be approximately guessed from the optical contrast with the substrate but is also confirmed later with AFM. Additionally, dark field microscopy which is possible with most optical microscopes is also quite useful to determine and choose cleaner flakes without any contamination such as bubbles, impurities from the sticky tape, PMMA residues or even micro-cracks which may not be very apparent in light field microscopy (see Fig. 5.2 (e)-(h)).

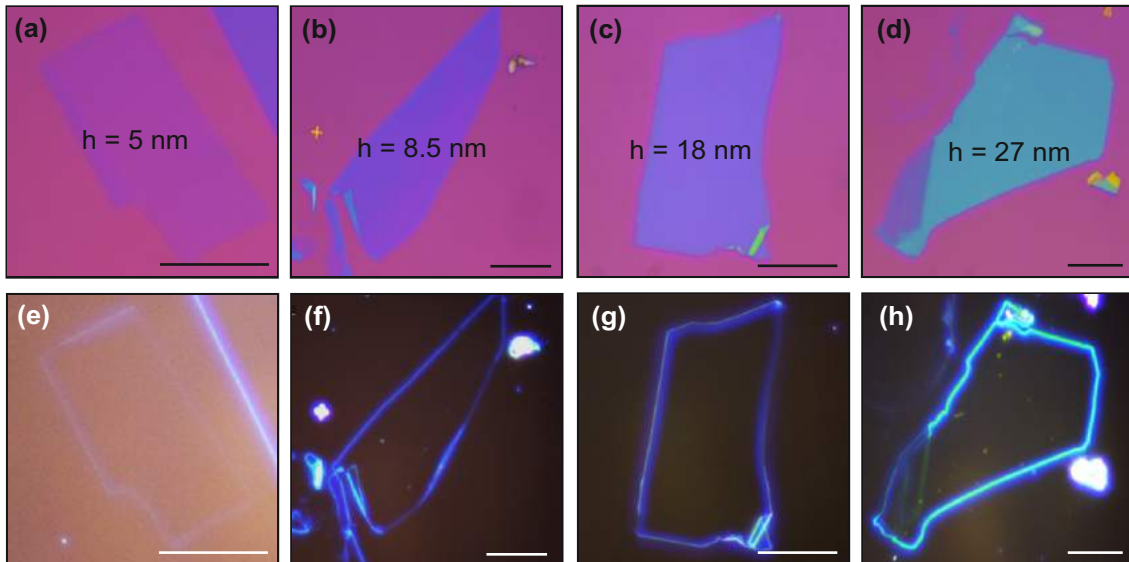


Figure 5.2.: (a)-(d) Light field optical microscope images of hBN flakes with different thickness or height h . (a)-(b) hBN flakes exfoliated directly on Si/SiO_2 substrate. ((c)-(d)) hBN flakes exfoliated on a Si substrate that is spin coated with PVA/PMMA. Observe that the optical contrast is identical in both the cases. (e)-(h) Dark field microscope images corresponding to (a)-(d) respectively. In case of very thin hBN such as in (e), more light may be needed to observe the flake with a better contrast. Impurities are more easily identified in dark field images as compared to their light field counterparts. Scale bar in all the panels is $20 \mu\text{m}$.

The size of the top hBN should be larger than size of the graphene flake to pick it up successfully. Otherwise, the graphene flake might break or fold up during the pick-up process. The thickness of the top hBN is also important while fabricating a top gate since the hBN acts a gate oxide. If it is too thin ($< 15 \text{ nm}$), high voltages can easily break the gate. If it is too thick ($> 50 \text{ nm}$), metallization of contacts during subsequent device fabrication can become a hassle.

Similar to top hBN, the size of the bottom hBN should also be big enough to encapsulate the entire graphene flake while the thickness should not be too low (usually between 20-40 nm) to prevent the hBN from cracking after the final step of transfer. In general, it is desirable to have the total height of the stack below ≈ 80 nm for the ease of fabrication. Finally, similar to graphene, we ensure that the hBN flakes are also freshly exfoliated just before transfer. In such cases, making a stack is successful almost all the time. If the flakes are allowed to rest on the substrate for too long, we observed that we laid down the top hBN on top of graphene instead of picking it up. Or the graphene flake does not get picked up by the hBN at all. This could be due to the increase of van der Waals adhesive forces between the flake and the substrate.

5.7. van der Waals stacking method/dry transfer technique

The method used to transfer graphene in this thesis utilizes the van der Waals interaction forces between graphene and hBN. Here, a PMMA membrane with exfoliated hBN on top is used to pick up and transfer graphene onto another hBN flake.

5.7.1. Step 1

In step 1, all the flakes are prepared for transfer. Once a top hBN flake is selected as explained above, a circle of about 5 mm radius is scratched around the flake on the $\text{Si}^{++}/\text{PVA}/\text{PMMA}$ wafer using a pair of tweezers. Then, a drop of water is released carefully along the circumference of the scratch. Since water dissolves PVA, a circular PMMA membrane consisting of the pre-selected hBN flake is slowly separated. Then, the wafer is dipped into a beaker filled with distilled water which releases the hBN/PMMA membrane. This membrane is then fished using a metal ring attached to holder. The membrane is allowed to dry on top of the ring after which the top hBN is ready for transfer (see schematic Fig. 5.3 (a)). Simultaneously, graphene and bottom hBN are also exfoliated on a Si/SiO_2 chips.

To stack these flakes, we use a transfer system (built by the University of Manchester) which includes an optical microscope, a vacuum holder for the fishing metal ring, and a rotatable sample stage with vacuum to hold the substrate and a heater to heat the stage. Both the stage and the vacuum holder are equipped with a set of micrometer screws to move them along x and y directions. These are useful to adjust the relative positions of graphene and hBN. Additionally, the vacuum holder can move vertically along z axis and is used to bring the membrane in contact with the substrate on the stage.

5.7.2. Step 2

In step 2 of the transfer process as shown in Fig. 5.3 (b), the metal ring with the top hBN is attached to the vacuum holder with the membrane facing downwards towards the stage. The chip with the graphene flake is placed on stage and held down by vacuum. Using the optical microscope attached, the position of the hBN is aligned relative to the graphene flake. Then the ring is lowered onto the stage until the meniscus of the membrane touches the surface of the chip. To aid this, a nitrogen gun can be used to blow the gas onto the membrane such that it touches the graphene flake. At this stage, the heater temperature can be increased to about 40°C to increase the adhesion between graphene and hBN. A change in contrast is visible once they are in contact and one can see the hBN laid on top of the graphene. Once this is observed, the membrane is slowly lifted upwards picking up the graphene flake along with it. This is due to the fact the graphene

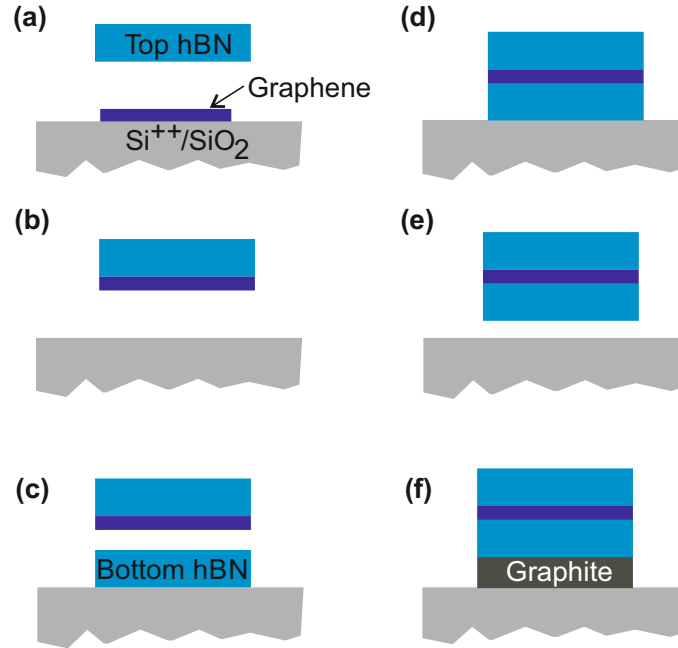


Figure 5.3.: Schematic figures of the van der Waals stacking method- **(a)** The top hBN is exfoliated on top of a PVA/PMMA layer and the graphene flake is exfoliated on SiO₂ substrate. **(b)** The top hBN is used to pick up the graphene flake. **(c)** The bottom hBN is exfoliated on top of another Si⁺⁺/SiO₂ substrate chip. **(d)** The membrane consisting of top hBN/graphene can be completely melted onto the substrate. This is used for single layer graphene devices where the Si⁺⁺ acts as the back gate. **(e)** On the other hand, the top hBN/graphene membrane can also be used to pick up the bottom hBN. **(f)** In case of bilayer devices, this stack deposited on top of a graphite flake exfoliated on another substrate chip.

adheres more strongly to the hBN than to the chip thanks to the van der Waals forces present between the two. Note that if the temperature is too high, the membrane might just melt and collapse onto the chip and cannot be used to pick up graphene.

5.7.3. Step 3

In step 3 (see Fig. 5.3 (c)-(d)), the substrate with graphene is replaced by another chip with bottom hBN. Once again, the membrane, now consisting of both top hBN and graphene is lowered onto this chip as described in step 2. Now, the heater is set to a temperature of about 120°C to fully melt the membrane onto the chip. Once in contact and fully melted, the membrane does not move any further and can be torn off by simply moving the stage laterally.

5.7.4. Step 4

Finally, in step 4 (see Fig. 5.3 (e)-(f)), the PMMA membrane on the chip can be dissolved in acetone and further cleaned in IPA. The end product is a hBN-Gr-hBN stack or sandwich. In general, this process can be repeated to pick up as many as flakes as one desires and lay them all down on a suitable substrate. For example, in case of BLG based devices where a graphite back gate is desired, instead of melting the membrane in step 3, the hBN on the chip is lifted off and the entire stack is placed on a layer of graphite

exfoliated on a SiO₂ chip. For detailed images of this and other different transfer processes, please check Ref. [214].

The transfer technique that we use here, in which the graphene flake does not come into contact with any potential contaminants such as organic solvents (Acetone, IPA etc.) or liquid polymers (PVA, PMMA etc.) is called the van der Waals pick up transfer or the dry transfer method and was introduced by Wang et.al. [172] and further developed by Zomer et.al [215]. Both these techniques utilize glass slide/PDMS/polymer stacks to pick up crystals. On the other hand, the method described above replaces this with a simple polymer membrane. Such a modification facilitates higher visibility of graphene and hBN and therefore a better alignment for a local transfer. Dry transfer produces high quality samples with enhanced electronic properties such as high charge mobility, lower residual charges etc. It also eliminates the need for any further annealing which was earlier necessary to remove any impurities.

5.8. Characterizing the stacked heterostructure

Once the hBN/graphene/hBN sandwich is fabricated, it is immersed in solution of acetone for around 10-15 minutes in acetone to dissolve the PMMA membrane on top of the sandwich. This is followed by leaving in isopropyl alcohol (IPA) for 5 min to finish the process of cleaning. Fig. 5.4 (a) shows the optical image of such a sandwich resting on a Si/SiO₂ substrate. Graphene is indicated by the dashed lines (solid lines indicate the rest of the few layer graphene flake). One can also see the bubbles indicated by solid black circles. Since these bubbles have contaminants and are not properly encapsulated, they tend to have low mobility. Therefore, these regions are avoided while designing devices.

After cleaning the sandwich, Raman spectroscopy is once again used to determine which area of the stack is clean, free from cracks and bubbles for patterning the device. The cracks can arise while stacking different layers while the bubbles are formed due to the agglomeration of hydrocarbon residues [216]. Fig. 5.4 (b) shows the map of the FWHM of the 2D peak across the hBN/graphene/hBN sample. Through encapsulation of graphene with hBN, strain fluctuations are reduced and this leads to a narrower 2D peak of around 17-18 cm⁻¹ [132]. The 2D peak is connected to the mobility of the sample - the smaller the width, the higher the mobility [133]. Therefore, in order to fabricate high mobility devices, regions with 2D width in the range of 17 - 21 cm⁻¹ are chosen to fabricate devices.

Fig. 5.4 (c) shows the optical image of a bilayer graphene sandwich deposited on a graphite flake (solid black line). The dashed line indicates the position of the bilayer graphene flake. Similar to single layer, the peak width once again reduces as compared to that on SiO₂ and the entire peak width is typically around 55-65 cm⁻¹. In order to verify this, one could, in principle, look at the peak width of individual Lorentzian curves such as those in the inset of Fig. 5.1 (d) and ensure that it is less than 21 cm⁻¹. However, this would be difficult to do for a complete 2D peak FWHM map shown in Fig. 5.4 (d) as it consists of different regions consisting of only the graphene flake, graphite flake and the region of overlap between the two. These could be distinguished from the intensity scale. The area of overlap is the region where we build devices (shown in the next sections) and is already above 70 cm⁻¹ due to contribution of both graphite and graphene. We can, however, ensure that the bilayer flake is rather homogeneous (except around its edges) and without any big bubbles or cracks, thus, suitable for building devices.

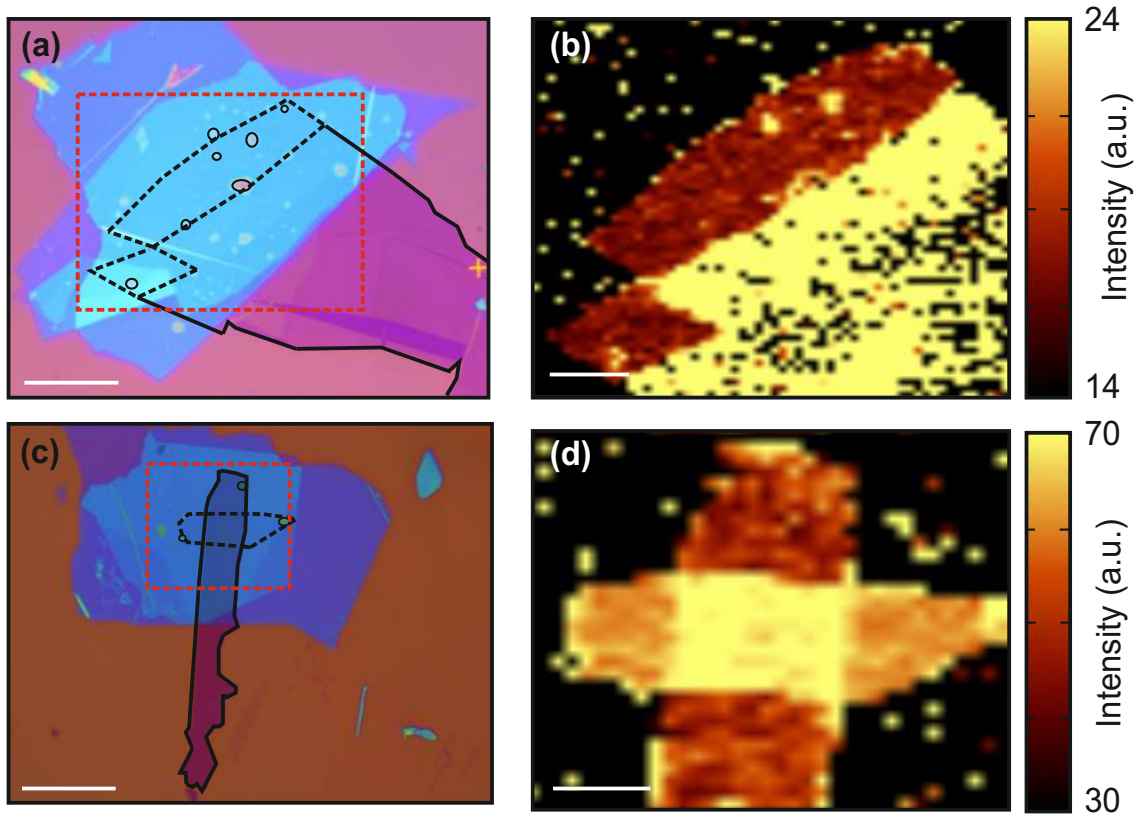


Figure 5.4.: (a) Optical image of a hBN-SLG-hBN stack on a Si/SiO₂ substrate. The single layer region is denoted by the black dashed lines while the rest of the few layer graphene is denoted by the black solid line. Bubbles are indicated by the black solid line circles. (b) Raman map showing the FWHM of the 2D peak across the region enclosed by the red dashed line in (a). (c) Optical image of hBN- BLG- hBN stack on graphite/Si/SiO₂. Black dashed line indicates the bilayer flake while the solid black line indicates the graphite flake. (d) Raman map showing the FWHM of the 2D peak across the region enclosed by the red dashed line in (c). Scale bars in (a) and (c) correspond to 20 μm . Scale bar in (b) is 10 μm while it is 6 μm in (d).

5.9. Patterning the heterostructure and, adding contacts and gates

In general, we employ a series of standard EBL and RIE procedures followed by metal evaporation to form contacts. The detailed process parameters are elucidated in the Appendix A.2 (for SLG) and A.3 (for BLG).

5.9.1. Single-layer graphene - Patterning the constriction

In order to pattern the device, a double layer resist stack consisting of PMMA 50K and PMMA 950K is spin coated on the Si/SiO₂ chip containing the sandwich to serve as an EBL mask. Such a double layer resist stack provides a better under-cut. Upon development of the resist after EBL (Fig. 5.5 (a)), a thin layer of Al (20 nm) is evaporated as an etch mask. After metal lift-off in acetone, there is metal remaining only in the areas designated for the QPC as shown in Fig. 5.5 (b). In the subsequent steps, the sample is exposed to Ar/SF₆ plasma. Ar is used to etch graphene while SF₆ has good selectivity towards hBN. All the areas

unprotected by the metal are etched away (see Fig. 5.5 (c)). Finally, the remaining metal is removed using Cr etchant resulting in a hBN-Gr-hBN QPC (see Fig. 5.5 (d)).

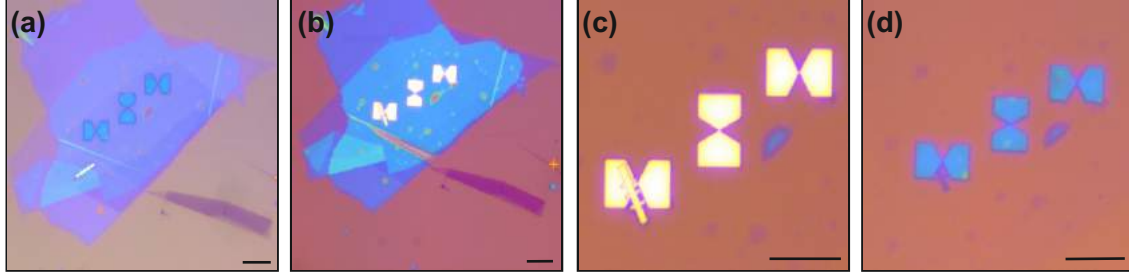


Figure 5.5.: (a) Optical image of the sample in Fig. 5.4 (a) after the development of the EBL mask. (b) Optical image after the deposition and lift-off of Al hard mask. Note that the hall bar was metallized already in a previous step and might have rolled over onto one of the QPC devices due to bad adhesion of the metal. This is not seen very often as the metallization and lift-off procedure is optimized quite well and may be treated as an exception. (c) Sample after reactive ion etching in Ar/SF₆. (d) QPC devices after stripping the remaining metal in a Cr etchant solution. Scale bar in all the panels is 10 μm .

5.9.2. Single-layer graphene - Contacts

After defining the QPC, one dimensional contacts are fabricated as explained in Ref. [172]. Here, we use a resist stack consisting of two layers of PMMA 50K followed by a final layer of PMMA 950K (Fig. 5.6 (a)). After another EBL step, evaporation of Cr/Au (5/100 nm) and subsequent lift off results in edge contacts (Fig. 5.6 (b)). The thickness of the metal deposited must be larger than the height of the stack for making proper contacts.

5.9.3. Single-layer graphene - Definition of top gates

After contacting graphene, a layer of hBN (between 20-40 nm thickness), is transferred onto the entire device as shown in Fig. 5.6 (b)). This, along with the top hBN of the hBN-Gr-hBN stack together serves as a gate oxide for the top gate. Deposition of a layer of hBN is much easier and less time consuming (can be done in a single step using the same transfer system) as compared to using other forms of gate oxides such as Al₂O₃ which requires layer to layer deposition of metal and subsequent oxidation. Further, hBN has also been proven to be a good choice of dielectric for graphene based devices [217, 218]. For the top gate, once again, we follow the above procedure for EBL and evaporate Cr/Au (5/90 nm) (Fig. 5.6 (c) and (d)).

5.9.4. Bilayer graphene - contacts

In case of BLG based devices, a graphite back gate is used. This enables us to have a huge control over device statistics since the gate is significantly closer to graphene (30 nm or less) as compared to Si⁺⁺ (285 nm). It also helps in screening any potential fluctuations from Si/SiO₂ (please see section 4.3). In these devices, the back gate is also electrically connected to the rest of the device by one dimensional contacts. A schematic and an AFM image of a bilayer graphene device used in this thesis are presented in Fig. 5.7.

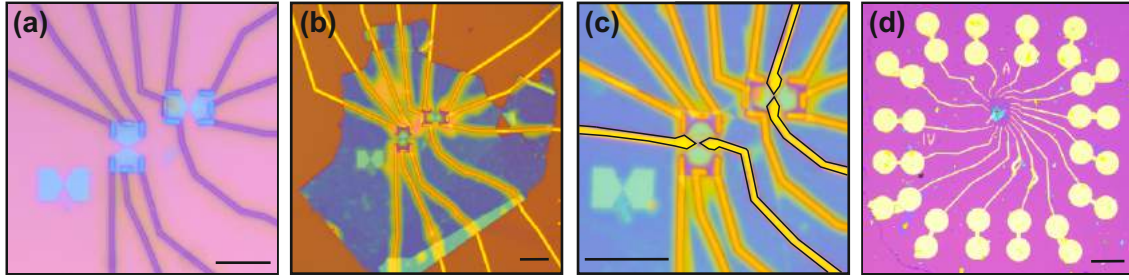


Figure 5.6.: (a) QPC devices from Fig. 5.5 after EBL of contacts and subsequent development. (b) After deposition of Cr/Al metal and lift-off. Afterwards, another layer of hBN (height ≈ 30 nm) is deposited on top of these devices to act as a gate oxide. (c) After deposition and metal lift-off of top gates (indicated by the black lines). (d) Final image of the device with side contacts, top gates and bond pads that is ready to be measured. Scale bar in (a)-(c) is $10\ \mu\text{m}$ and $200\ \mu\text{m}$ in (d).

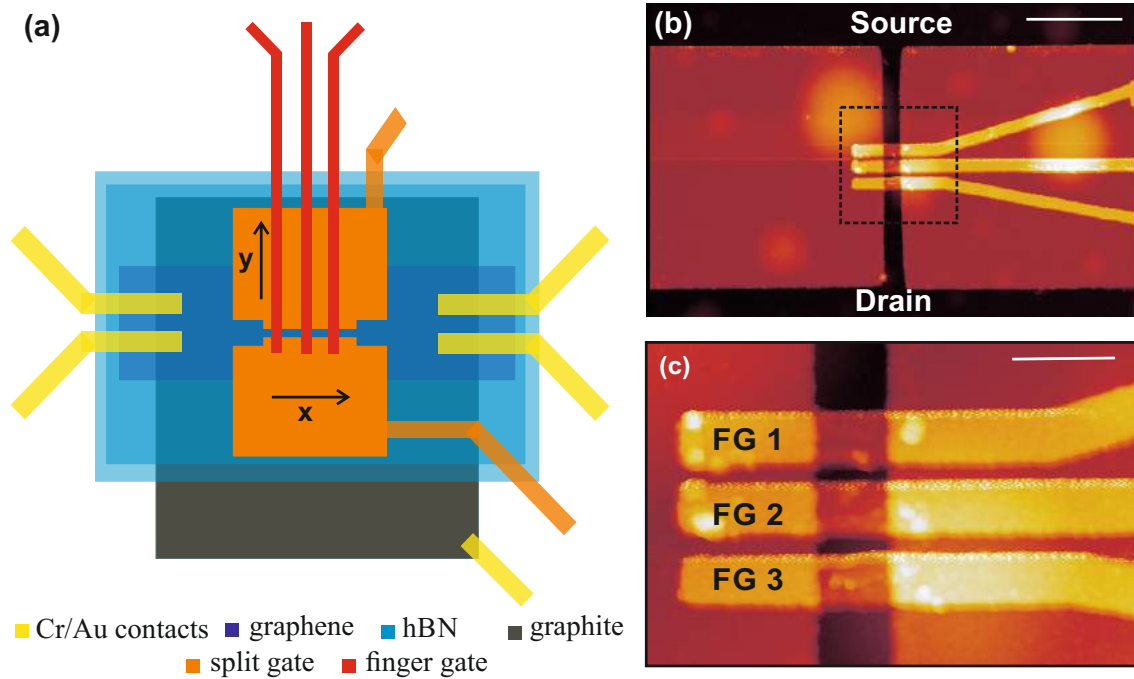


Figure 5.7.: (a) Schematic top view of a split gated BLG QPC. All the various parts of the device are depicted using different colors. (b) AFM image of the final device showing the split gates and finger gates. Scale bar corresponds to $2\ \mu\text{m}$. (c) AFM image of the device in the region enclosed by the black dashed line in (b). Scale bar corresponds to $0.5\ \mu\text{m}$.

In this case, the van der Waals technique described in section 5.7 is used to stack a hBN-bilayer graphene-hBN sandwich on top of a layer of graphite on SiO_2 . The size of the graphite layer is chosen in such a way that it protrudes out of the sandwich making it clearly visible and accessible to make contact (see Fig. 5.4 (c) and schematic Fig. 5.7 (a)). The graphene and graphite flake are oriented perpendicular to each other for ease of making contacts and preventing short circuit. After the deposition of the sandwich, contacts to graphite back gate and graphene are once again made using reactive ion etching followed by EBL based on a PMMA mask. The contacts act the source and drain at which voltage/current is induced or detected. A mixture of CF_4 (40 sccm) / O_2 (4 sccm) is used to etch the device. O_2 is used to remove any organic

contaminants from the sample while CF_4 is used to etch through hBN (see Fig. 5.8 (b)). Standard light field microscopy and Raman spectroscopy are employed periodically to check if the top hBN has been etched thoroughly and if the bottom hBN is still intact. After successful etching, Cr/Au (5nm/70 nm) were evaporated to make contacts. It is worth mentioning that several tests have also been performed with other fluorine based gases such SF_6 and CHF_3 . SF_6 turned out to be too strong for our purpose i.e. it completely etched away the Si wafer, probably due to higher molecular weight of SF_6 as compared to CF_4 . On the other hand, experiments with CHF_3 showed no significant difference. If anything, the process seemed to be not very reproducible after repeated trials. Therefore, for the sample in this thesis, we have used CF_4 , which showed good selectivity towards hBN along with a controllable etch rate.

5.9.5. Bilayer graphene - Definition of top (split) gates

After the metallization of the contacts, the next step is to fabricate the split gates and their corresponding leads. After following a similar procedure for lithography on top of the upper hBN, two Cr/Au (5/45 nm) based split gates are designed (see Fig. 5.8 (c)). The split gates produced in this step are $5\mu\text{m}$ wide and are separated by approximately 250 nm as seen in the AFM images in Fig. 5.7 (b)).

5.9.6. Bilayer graphene - Definition of finger gates

In this step, atomic layer deposition (ALD) is used to fabricate a 25 nm thick dielectric layer (Al_2O_3) on the structure prior to the fabrication of the finger gates (see Fig. 5.8 (d)).

Then, finger gates consisting of Cr/Au (5 nm/ 70 nm) are fabricated similar to the other gates and contacts (see Fig. 5.8 (e)). Fig. 5.7 (c) shows the final image of a device with three finger gates (FG1-FG3) crossing the channel defined by the split-gates. These finger gates have a width of around 200 nm and are separated by around 60 nm.

During the process of ALD, the oxide is deposited throughout the entire sample including the bond pads. This must be removed in order to bond the sample later on. For this purpose, a wet chemical etching process was used. The samples were first placed in a solution consisting of a Tetra-Methyl Ammonium Hydroxide (TMAH) based optical developer for two minutes followed by water for five minutes before drying them with nitrogen gas.

In some cases, where a finer finger gate pattern is desired, a slightly smaller electron beam dose ($115\mu\text{C}/\text{cm}^2$ instead of the standard $120\mu\text{C}/\text{cm}^2$) is used. In addition, a methyl isobutyl ketone (MIBK) based developer was used instead of isopropanol for the development of the finger gates which seemed to improve the resolution of lithography greatly.

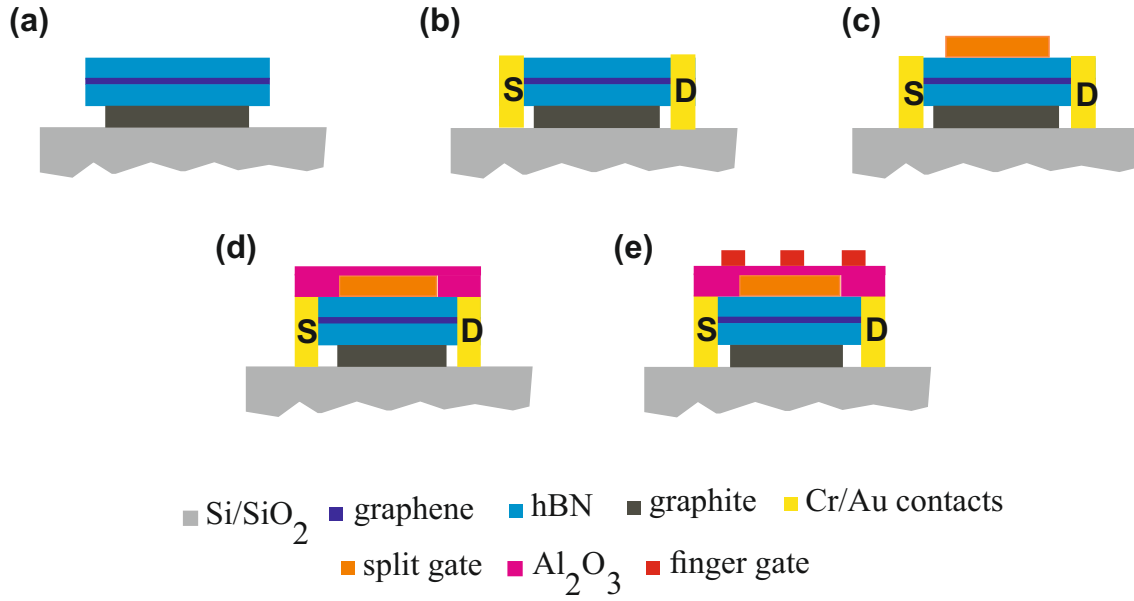


Figure 5.8.: Schematic cross section of bilayer graphene nanoconstriction device at different stages of processing along the x direction indicated in Fig. 5.7. Colors used for various components are also the same. **(a)** hBN-graphene-hBN sandwich deposited on graphite/Si⁺⁺/SiO₂. **(b)** Side contacts deposited on the sandwich while ensuring that they do not short the device (graphene) with back gate (graphite). These act the source (S) and the drain (D). **(c)** Fabrication of split gates. **(d)** Al₂O₃ (pink) is deposited on top of the entire device. **(e)** Finger gates are deposited on top of the gate oxide.

6. Single-layer and bilayer graphene quantum point contact device geometry

This chapter has been published in parts in:

From diffusive to ballistic transport in etched graphene constrictions and nanoribbons

S. Somanchi, B. Terrés, J. Peiro, M. Staggenborg, K. Watanabe, T. Taniguchi, B. Beschoten, and C. Stampfer *Ann. Phys. (Berlin)* 529, 1700082 (2017). ©2017 by WILEY - VCH Verlag GmbH & Co. KGaA, Weinheim. Reprinted with permission.

Author contributions:

S. Somanchi fabricated the single layer graphene samples while the bilayer graphene samples were fabricated by L. Banszerus.

In this chapter, we describe the exact geometry- device dimensions, thickness of individual hBN or graphite flakes, the design of the gates (top/split/finger) and other such minute but important details that have been taken into consideration during the fabrication of the specific devices used in this thesis.

6.1. Single layer graphene QPC devices

In sections 3.3 - 3.4, we discussed how edges play an important role in electron transport through nanostructures, particularly, in narrow ribbons or constrictions where edges account for an appreciable fraction of the total device area [121, 219]. As long as the devices are fabricated using the traditional method of etching (reactive ion or plasma etching) resulting in random edge termination, edge disorder is always present and can potentially hamper the overall conductance even in high quality sandwich devices that show ballistic transport. Although there is enough experimental evidence to prove that edges play an important role in transport [42, 125], manipulating the influence of such localized edge states on the transport has not been achieved in such devices.

One standard component that can be added to several graphene devices to gain extra control over the transport characteristics is a top or a side gate using graphene leads. For example, side gated graphene FETs have been used to study several characteristics such as the modulation of conductance, transconductance [149, 220, 221] etc. In case of quantum dots, plunger gates are used to control the barrier strength and the electron tunnelling rate to study electron-hole crossover, ground and excited states etc. [143, 151–153,

222]. Top and side gates have already been demonstrated as useful in controlling the electronic transport of the channel, for example, by forming a p-n junction that creates a potential barrier [129, 130]. They provide additional knobs to tune the electron density locally in the specific region of the device they are incorporated into. Therefore, in this chapter, we employ additional metallic top gates in the region of the constriction with a goal of shedding more light on the charging characteristics of these localized edge states and to see if their detrimental influence on the transport can be tuned using the gates.

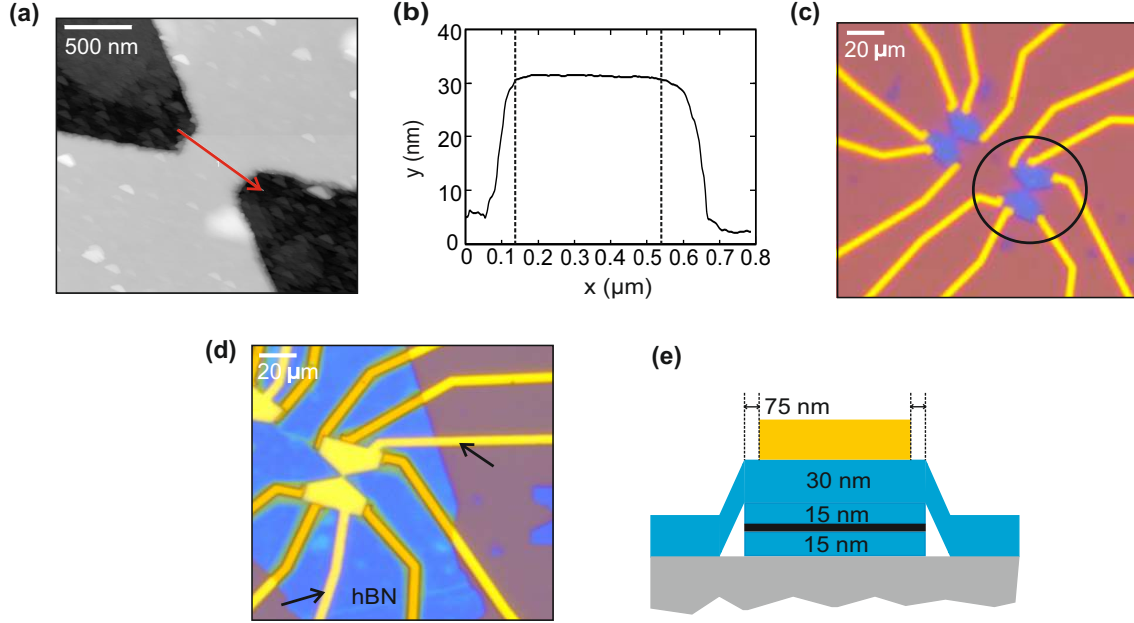


Figure 6.1.: (a) AFM image of a 380 nm wide etched constriction built using hBN encapsulated graphene. (b) Height profile of the constriction along the solid red line in (a). The distance between the two black dashed lines gives the approximate width of the constriction. (c) Optical microscopy image of the constriction after fabrication of Cr/Au contacts. Each device has six contacts (in yellow), three on either side of the constriction. (d) Optical microscopy image of the device encircled in the (c) after the deposition of a 30 nm thick hBN and the fabrication of the Cr/Au top gate. Note that the two contacts to the top gate as indicated by the black arrows are short to one another during experiment ensuring that there is only global top gate applying a symmetric potential over the constriction. (e) Cross-sectional schematic of the final device in (d) along the red line in (a). The Si⁺⁺/SiO₂ surface is represented in gray, hBN in blue, graphene in black and the top gate in yellow. We indicate different length scales including the width of the different hBN layers and the separation between the top gate and the edge of the constriction (see the black dashed lines).

6.1.1. Single top gated graphene constriction devices

Fig. 6.1 (a) shows an AFM image of a 380 nm wide (see the line cut in Fig. 6.1 (b)) and 150 nm long constriction fabricated using a hBN-graphene-hBN sandwich that is built using the van der Waals pick-up technique described in section 5.7. The entire device rests on the surface of a p-doped Si substrate with an oxide thickness of 285 nm (t_{SiO_2}) which acts as the back gate. The thickness of the bottom (t_{bottom}) and the

top hBN (t_{top}) is about 15 nm each. The design and fabrication process used here is similar to the devices described in Ref. [42] which have shown a mobility of nearly $150,000 \text{ cm}^2\text{V}^{-1}\text{s}^{-1}$ and a mean free path exceeding 1 μm . However, one major difference in the geometry of the device is that size of the leads is much larger as compared to the width of the constriction - 6 μm in this case as compared to 1.5 - 2 μm in Ref. [42].

This ensures that the leads are significantly larger than the mean free path and the phase coherence length making the transport through the leads effectively diffusive. This allows us to attribute any features of ballistic transport to the constriction only. Further, it might also prevent any stray interference effects such as Fabry- P  ot oscillations from masking the features related to quantized conductance [42]. Since the Cr/Au based side contacts rest on top of the sandwich as shown in Fig. 6.1 (c), another layer of hBN with a thickness $t_{gateoxide} \approx 30 \text{ nm}$ is placed on top of the entire sandwich constriction which along with the top hBN of the sandwich acts a dielectric for the top gate. On top of this, a Cr/Au based top gate that also mimics the shape of a constriction with a width of 230 nm is deposited (see Fig. 6.1 (d)) in such a way that the top gate covers everything (including the leads) except the edges of the constriction. It is designed to be symmetric such that distance between the top gate and the edge of the QPC is around 75 nm on either side of the QPC as shown in the schematic in Fig. 6.1 (e).

The idea behind this geometry is to use the top gate to tune the conductive channel predominantly and to a lesser extent, the edge regions while the back gate tunes the entire device globally. If this is achieved, then we can disentangle the influence of the edges on the channel and see how the conductance of this device compares now with those in Ref. [42]. We would then have a device in which the contribution of the localized edge states can somehow be separated from transport through the central region in the device using an additional gate. This could be used to extract important information on the how the localized edge states participate in transport.

6.1.2. Dual top gated graphene constriction devices

Fig. 6.2 (a) shows an AFM image of a 300 nm wide and 150 nm long graphene constriction device with two top gates. The fabrication of this device is similar to the one described in the previous section i.e. it includes etching a hBN-graphene-hBN sandwich to form a constriction with wide leads, 1D side contacts and an additional layer of hBN as the top gate dielectric (see Fig. 6.2 (b)-(c)). The thicknesses t_{bottom} and t_{top} are about 17 nm and 15 nm respectively while $t_{gateoxide}$ is around 30 nm. The only difference as compared to the device in the previous section is that the sample now consists of two top gates that are designed to be about 30 nm inside on either side of the constriction. They fall directly over the constriction and also extend along the edges of the leads on either side of the constriction (see the schematic in Fig. 6.1 (d)).

6.2. Bilayer graphene QPC devices

In the previous sections of this chapter, we have discussed the confinement of electrons in constrictions that are fabricated by top-down lithography techniques and reactive ion etching of single layer graphene. As discussed in chapter 4, it is possible to open a band-gap in bilayer graphene in the presence of an external electric field, thereby allowing us to overcome the problem of edge roughness. In such a sample, a

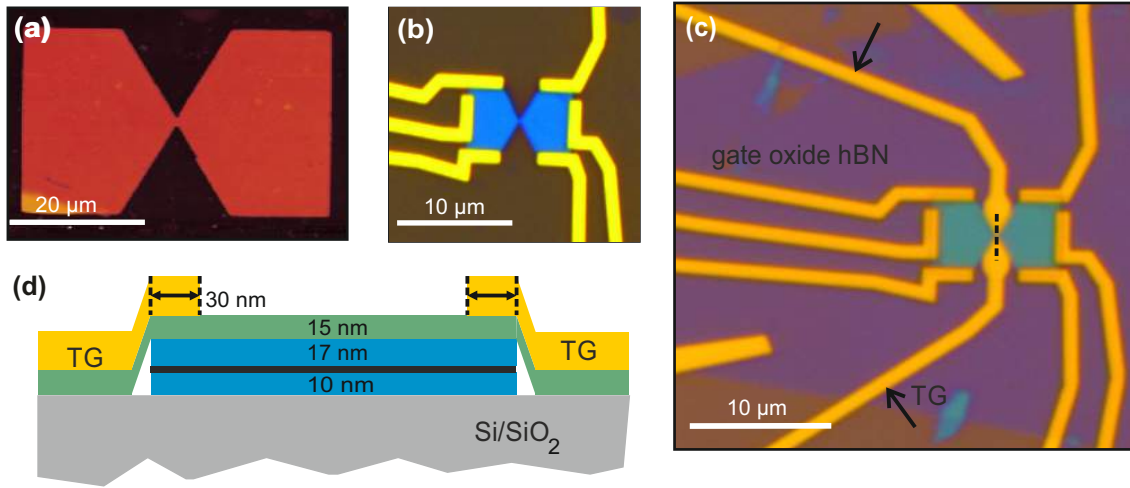


Figure 6.2.: (a) AFM image of an etched 300 nm wide hBN encapsulated graphene constriction. (b) False colored optical microscope image of the constriction with six Cr/Au based 1D side contacts, three on either side of the constriction. The sandwich is blue and the contacts are yellow in color. (c) False colored optical microscope image of the final device with top gates (TG). An additional layer of hBN on top of the constriction (in purple color) is used as the top gate dielectric. (d) Schematic cross-sectional illustration of the device along the dashed line in (c) highlighting the top gate geometry. Here, Si/SiO₂ substrate is gray, hBN in the sandwich is blue, graphene is black, hBN laid on top of the contacts is green and the top gates are yellow in color. Thicknesses of different layers in the device is indicated. The top gate is designed to be around 30 nm (the distance between the black dashed lines) inside the constriction and overlap the edges of the leads as well.

constriction can be formed by the use of external gates. In the following section, we discuss the fabrication of such a gate defined BLG nanoconstriction.

6.3. With split and finger gates

The device consists of BLG encapsulated in hBN sandwich as described in section 5.7. The thicknesses of the bottom (t_{bott}) and the top hBN (t_{top}) are approximately 30 nm and 20 nm respectively. This is then placed on top of a graphite flake (thickness ≈ 10 nm) resting on the surface of a Si⁺⁺/SiO₂ substrate and acts the back gate. All further details about the fabrication of this device have already been described in section 5.9.4 (see Fig. 5.8). Electron beam lithography and reactive ion etching followed by metal evaporation are used to form one dimensional Cr/Au contacts and two split gates which are 5 μ m wide and separated from each other by a 250 nm wide channel. ALD is used to deposit a 28 nm thick layer of Al₂O₃ that acts the gate oxide for the finger gates as shown in Fig. 5.7. These three finger gates are also fabricated using the same technique as the split gates and side contacts. The finger gates FG1 - FG3 are fabricated at equal interval spacing along the length of the channel. Each finger gate is around 200 nm wide and separated from the adjacent one by a distance of 60 nm. In the following chapters, we shall see how the combination of these split and finger gates is used to form a QPC in this device.

7. Edge disorder in etched top gated graphene quantum point contacts

This chapter has been published in parts in:

From diffusive to ballistic transport in etched graphene constrictions and nanoribbons

S. Somanchi, B. Terrés, J. Peiro, M. Staggenborg, K. Watanabe, T. Taniguchi, B. Beschoten, and C. Stampfer *Ann. Phys. (Berlin)* 529, 1700082 (2017). ©2017 by WILEY - VCH Verlag GmbH & Co. KGaA, Weinheim. Reprinted with permission.

Contributions to this chapter:

Fabrication of all the etched top gated devices and the experimental measurements were performed by S.Somanchi. Theoretical simulations were performed by T. Fabian and F. Libisch from Vienna University of Technology.

7.1. Introduction

In this chapter, we study the effect of a top gate on the conductance of the etched single layer graphene nanoconstrictions discussed in section 6.1 of the previous chapter.

While the overall substrate induced disorder and as a result, the residual charge carrier density n^* is much lesser for hBN encapsulated graphene nanoconstrictions, edge disorder due to the device fabrication technique of etching graphene flakes is still present. Indeed, authors of Ref. [42] have used back gated encapsulated graphene constrictions and still observed a strong influence of the localized edge states or trap states n_T on the conductance of their devices especially as the constriction width was reduced down to 230 nm. This presents a need for designing experiments through which it is possible to manipulate the influence of edge disorder on the conductance of the QPC.

In this context, addition of a external gates provides a way of tuning the charge carrier density and the doping profile in the QPC. The in-built back gate is universal. It uses the substrate Si as the gate and the SiO₂ on top of the substrate as the gate dielectric. It applies an electric field to not only the channel but also the leads connecting the channel to the source and drain metal contacts. As a result, the contact resistance may change during device operation. To avoid the influence of contact resistance, four terminal configuration is used measure the sample.

The advantage with implementing an additional top gate is that it is possible to bring the gate much closer to the graphene layer underneath. In the current devices, the top gate dielectric is hBN with a thickness of

around 30 - 40 nm which is much smaller than the SiO_2 thickness that is around 300 nm. Considering the fact that the dielectric constants for SiO_2 and hBN are nearly the same (≈ 4), the capacitive coupling of the top gate is around 7 - 10 times stronger than that of the back gate as the top gate is much closer to the graphene structure. As explained earlier in the previous chapter, the geometry of the etched graphene QPC device consists of one global top gate that covers the entire channel except the edges in one case as shown in Fig. 6.1 and two top gates that cover just the edges in the other case as shown in Fig. 6.2. The idea behind such a geometry is to see if the top gate can be used as a means to manipulate the localized states along the edges and the bulk states in the channel with different strengths. However, whether it is one or two top gates, one should keep in mind that there will always be fringe fields from the top gate that affect the regions that the top gate does not cover especially considering the short distances between the edges and the channel (see Fig. 6.1 (e) and Fig. 6.2 (d)). Therefore, while the top gate may not be used to exclusively tune just the edges or the channel, it can still be used to allow a different tuning or coupling strength between the edges and the channel. This discussion will form the crux of many results discussed below.

7.2. Measurement set-up

All the measurements are performed in a $^3\text{He}/^4\text{He}$ dilution refrigerator. The single layer graphene based experiments described in this chapter and also Chapter 8 are performed at a temperature of around 4 K. The measurement set-up is equipped with superconducting magnetic field coils that can apply a magnetic field of up to ± 9 T to the sample. The chip carrier socket is fixed using a set of screws and can be rotated to fix the sample either perpendicular or parallel to the magnetic field.

To connect the sample on the Si/ SiO_2 chip to the measurement equipment, the chip is fixed down on a commercial chip carrier (Kyocera C-QFN PB-C88084) using a conductive silver glue (Beru RLS001). Thereafter, the bondpads are connected to the chip carrier using an Al-Si 1% based TPT HB06 wedge bonder. The sample can then be mounted into the set-up and is ready to be measured. Standard lock-in amplifiers (Stanford Research SRS 830) are used to measure differential conductance and resistance. To apply a fixed DC bias across the sample, an I-V convertor is used. The DC bias is further complemented with an AC voltage $V_{AC} = 300 \mu\text{Vp-p}$ that is generated by a standard lock-in (Stanford Research SRS 830). Hence, both these sources of voltage together contribute to the bias V_b across the constriction. The resulting current I_{sd} between the source and drain terminals is measured using a multimeter (Agilent 34401). All the gate voltages including back gate V_{bg} and top gate V_{tg} voltages are applied using a standard voltage source, Yokogawa 7651. A high resistance ($1\text{M } \Omega$ or greater) is connected in series with all the gates to prevent the sample and the equipment from damage due to any sudden high voltage/current break-down. The resulting differential I-V curves are measured using another lock-in. The voltage drop across of the sample V_{sd} is measured using Agilent 34401 for four terminal conductance measurements to avoid contact resistance. The four terminal (or differential) conductance across the QPC is given by $G(= dI/dV) = I_{sd}/V_{sd}$. All the electrical equipment was controlled by a python based measurement software called Labber [223].

Fig. 7.1 (a) shows the scanning electron microscopy (SEM) image of the device shown in Fig. 6.1 (d). In the close-up in Fig. 7.1 (b), we see a single top gate with a width of ≈ 230 nm mimicking the shape of the constriction underneath. Fig. 7.1 (c) shows a false color AFM image of the etched dual top gated QPC device described in Fig. 6.2 (c). As such, there is no electrical contact between the two top gates 1 and 2 i.e. there is no current along the black dashed line, but in this particular configuration, they are short to each

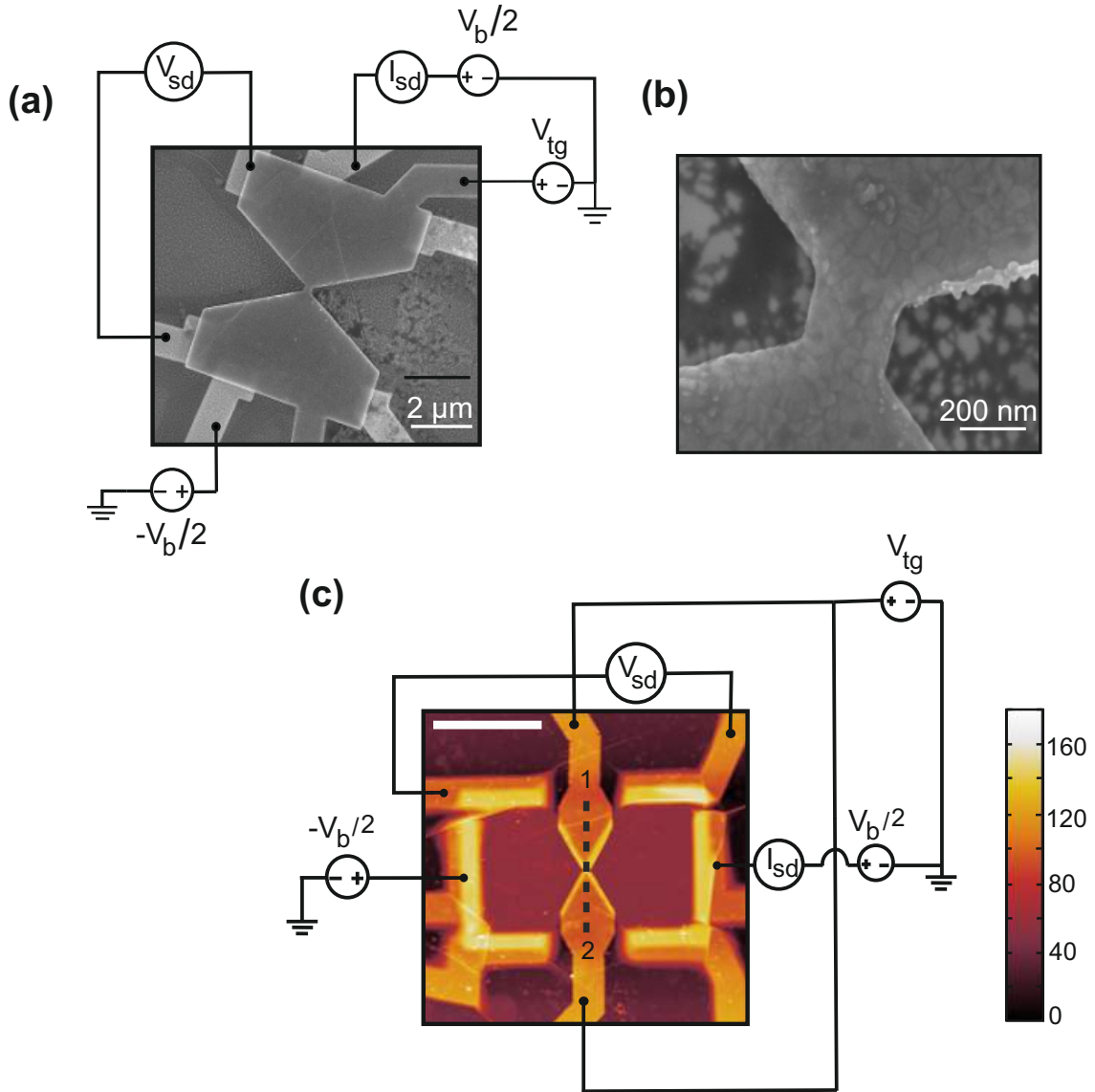


Figure 7.1.: (a) SEM image of the final 380 nm etched QPC device with a single top gate shown in Fig. 6.1 (d) including the top gate in the same shape as that of the constriction underneath. (b) Close-up of the top gate in (a) around the center. (c) False color AFM image of the etched, top gated 300 nm wide encapsulated graphene constriction with two top gates 1 and 2 as shown in Fig. 6.2 (c). The gates are electrically isolated from one another, so there is no current along the black dashed line unless they are shorted to one another as depicted here.

other externally such that a symmetric voltage is applied on both the gates.

7.3. Theory of conductance through an ideal QPC

In section 2.1, we saw how the conductance in a QPC system with degeneracy g and width w is quantized in units of ge^2/h . Since ballistic transport in such a system is analogous to a wave guide problem, the number of modes m or channels of transport is given by $m = \frac{k_F w}{\pi}$ where $m \in \mathbb{Z}_0$. Therefore, as the Fermi wave

number k_F reaches a value of $m\pi/w$, there is a jump in the value of conductance by a factor of ge^2/h as seen in Fig. 7.2.

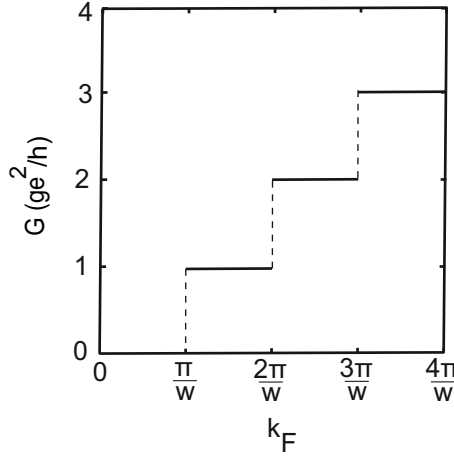


Figure 7.2.: Schematic of the conductance G as a function of the Fermi wave number k_F in a QPC of width w . The degeneracy of the system is given by g .

This information can now also be specifically applied to a graphene QPC using the following Landauer formula

$$G = \frac{4e^2}{h} \sum_{m=1}^{\infty} \theta\left(\frac{wk_F}{\pi} - m\right), \quad (7.1)$$

where $\theta(x)$ is the Heavy side step function and the factor 4 accounts for the spin and valley degeneracy of graphene [12, 40, 63]. Therefore, the conductance increases in a series of steps, by a quantum of $4e^2/h$ whenever the factor wk_F becomes a multiple of π . Fourier series expansion of this equation gives

$$G = \frac{4e^2}{h} \frac{c_0 wk_F}{\pi} + \frac{4e^2}{h} \left[\sum_{j=1}^{\infty} c_j \sin(2jwk_F - \phi_j) - \frac{c_0}{2} \right]. \quad (7.2)$$

The factor c_0 , called the tranmission coefficient is the average transmission per mode i.e. it indicates the amount of electrons that actually travel from the source to the drain through the QPC after being scattered at the rough edges of the constriction. In the case of an ideal constriction, $c_0 = 1$, $\phi_j = 0$ and $c_j = 1/(j\pi)$ for $j > 0$. However, c_0 is reduced to a value between 0 and 1 in the presence of rough edges that limit the transmission of charge carriers through the QPC [42]. The mean conductance $G^{(0)}$ is given by the zeroth order component in this expansion i.e.,

$$G^{(0)} = \frac{4e^2 c_0}{h} \left(\frac{wk_F}{\pi} - \frac{1}{2} \right) = \frac{4e^2}{h} \frac{c_0 w}{\pi} \sqrt{\pi \alpha (V_g - V_g^0)} - \frac{2e^2}{h} c_0 \quad (7.3)$$

Here, we have used the fact that ideal graphene has a linear density of states and thus,

$$n = \frac{k_F^2}{\pi} = \alpha (V_g - V_g^0), \quad (7.4)$$

where V_g^0 is the gate voltage at the CNP. Thus, in contrast to diffusive transport, where $G \propto V_g$, here, in the case of transmission via quantum modes in graphene, we expect to see $G \propto k_F \propto \sqrt{n} \propto \sqrt{V_g}$ dependence.

Table 7.1.: Sub-band spacing and Fermi velocity for three different steps shown in the bias spectroscopy measurements in Fig. 7.3 (d)

Step no.	ΔG (step height)	ΔE (meV)	v_F (10^6 m/s)
A	2.08	6.2 ± 1.0	1.14 ± 0.18
B	2.58	5.0 ± 0.6	0.92 ± 0.11
C	3	4.9 ± 0.7	0.90 ± 0.13

7.4. Conductance through a QPC with a single top gate

7.4.1. Conductance as a function of back gate and top gate

Fig. 7.3 (a) shows the conductance through the 380 nm wide QPC device with a single top gate (see Fig. 7.1 (a)) as a function of both the top gate V_{tg} and the back gate V_{bg} voltages. This map is obtained by measuring the conductance $G(V_{tg})$ as V_{tg} is varied from -2 to 2 V for a fixed value of V_{bg} . Thus, several conductance traces are obtained as the value of V_{bg} is varied from -20 to 20 V. The solid white line corresponds to the CNP of each such individual conductance trace $G(V_{tg})$ measured as a function of V_{tg} for a fixed value of V_{bg} . Thus, this feature, the CNP is tuned both by the top and back gate along this solid white line.

In Fig. 7.3 (b), we see the conductance trace (in black) measured by sweeping both V_{tg} and V_{bg} simultaneously according to the equation $V_{bg} = 0.143 \times V_{tg} + 3.6$ along the direction of the white dashed arrow in Fig. 7.3 (a). This direction is perpendicular to the solid white CNP line. Besides the CNP of the QPC, as denoted by the vertical blue dashed line, we find another minor kink in conductance (see the red arrow) leading to an asymmetry in the conductance profile of the QPC. Due to this, we stick to the holes side for all future measurements and data analysis.

We observe conductance kinks with a step height on the order of 2 - 3 e^2/h in the close-up in Fig. 7.3 (c) starting from as low as 4 - 6 e^2/h and going up to 24 e^2/h . This indicates the confinement of charge carriers in the QPC in accordance with eq. 7.1. However, we see that the observed features are more like kinks rather than steps. This is a consequence of the fact that the charge carriers are bound to scattering at the rough edges of the QPC resulting in a decay in the magnitude c_j of higher order Fourier components and the accumulation of random phases i.e. $\phi_j \neq 0$ in eq. 7.2 [42]. As a result, the expected sharp quantization steps now appear as periodic modulations. Authors of Ref. [224] explained this using back-scattering at energies close to the opening of a new mode which results in a reduction in transmission causing the slight dips in conductance as we move one kink to another.

The confinement of the charge carriers can be further supported by performing bias spectroscopy measurements in the holes side of the conductance trace as shown in Fig. 7.3 (d). We consider three kinks A, B and C at $\approx 4, 13.5, 17.5 e^2/h$ which show very nice signs of quantization (see red dashed boxes in Fig. 7.3 (d) and the corresponding kinks denoted by the red double-edged arrows in Fig. 7.3 (c)). The dense regions along the source - drain bias voltage axis V_{sd} (see the right end of blue double edged arrows in Fig. 7.3 (d)) where the traces seem to bunch together correspond to the plateaus/kinks in conductance. The source-drain bias across the QPC is used to extract the sub-band spacing ΔE directly for the three kinks and summarized in Table 7.1. Using the sub-band spacing and the width of the QPC $w = 380$ nm, one can calculate the Fermi velocity v_F using the relation $v_F = 2w\Delta E/h$. This matches well with the value expected for graphene ($\approx 10^6$ m/s).

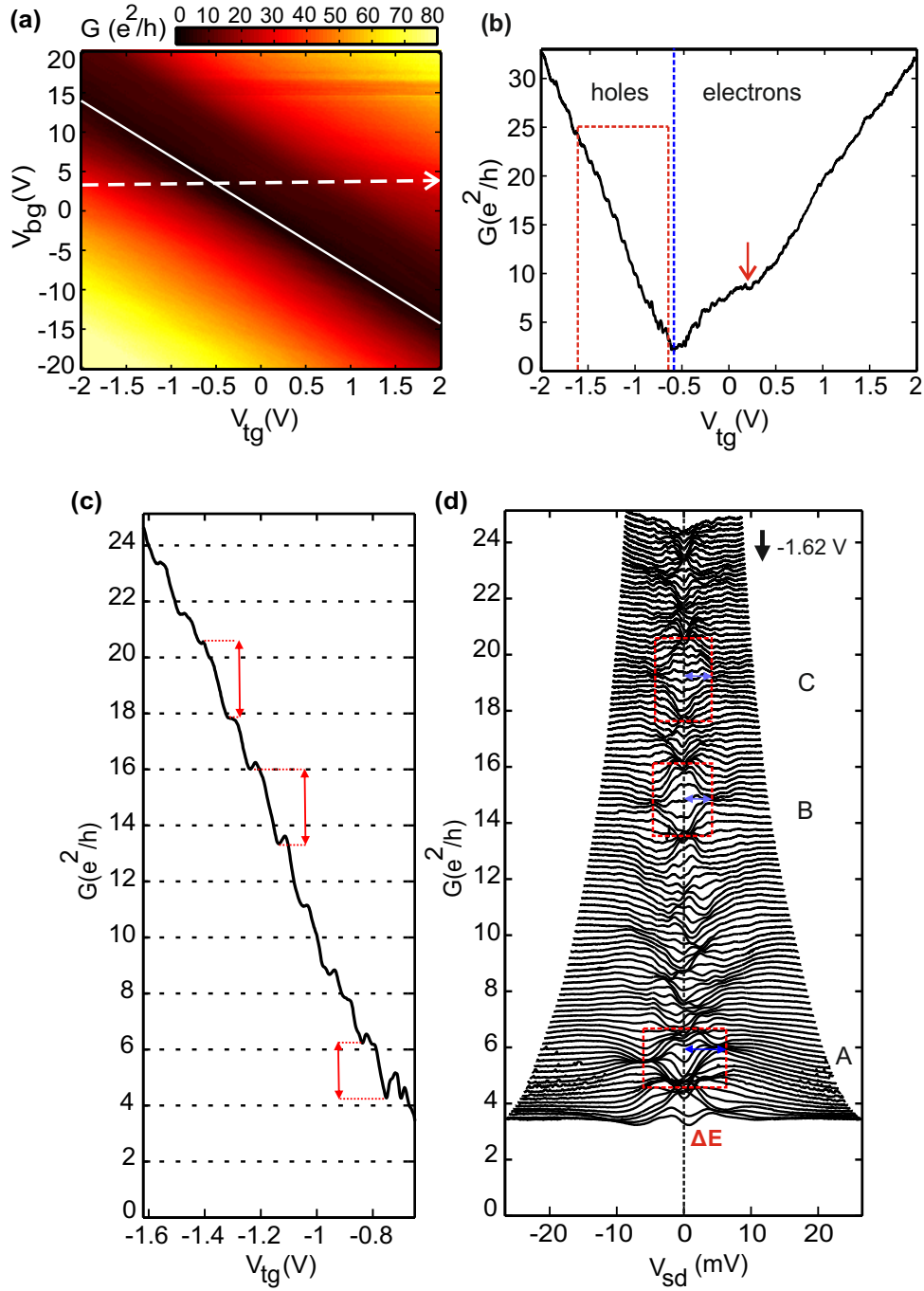


Figure 7.3.: (a) Four terminal conductance G through the 380 nm wide QPC with a single top gate as a function of the top gate voltage V_{tg} and the back gate voltage V_{bg} at a DC bias of 500 μV . The solid white line marks the CNP of each individual conductance trace $G(V_{tg})$ at a fixed V_{bg} . (b) Conductance trace along the white dashed arrow in (a). Here, V_{tg} and V_{bg} are varied simultaneously such that $V_{bg} = 0.143 \times V_{tg} + 3.6$. The blue dashed line denotes the CNP. (c) Close-up of the trace shown in (b) in the region enclosed by the red dashed lines. (d) Zero magnetic field differential conductance G as a function of the bias across the QPC V_{sd} measured using a lock-in with an AC excitation voltage of 300 μV p-p. For each trace, V_{tg} is varied from -0.65 V to -1.62 V in steps of 9 mV (see label on the upper right corner). The blue double edged arrows indicate the sub-band spacing ΔE for the kinks denoted A, B and C (See corresponding red double edged arrows in (c). Also refer to table 7.1).

7.4.2. Extraction of gate lever arm from quantum Hall measurements

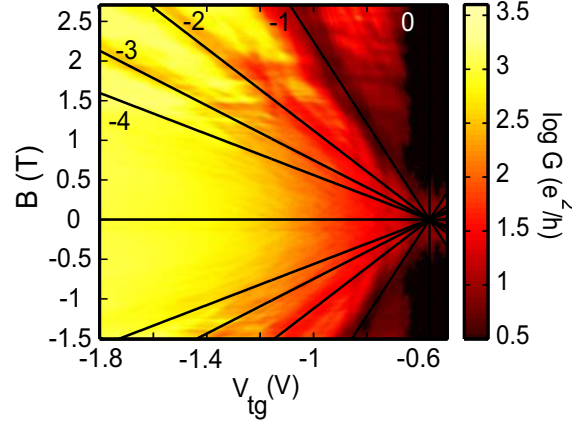


Figure 7.4.: Measurement of Landau levels in the 380 nm wide QPC with a single top gate. Longitudinal differential conductance G as a function of the top gate voltage V_{tg} and the perpendicular magnetic field B . The conductance trace at $B = 0$ T is shown in Fig. 7.3 (b). The solid black lines indicate the evolution of Landau levels with the indices $m = 0$ to -4 .

The strength of a gate i.e. how well it tunes the device can be estimated by calculating the lever-arm (α) which is simply the capacitance per unit area of the gate to the graphene structure. The slope of the solid white line in Fig. 7.3 (a) is a measure of the relative lever arm α_{tg}/α_{bg} i.e. the ratio of the capacitive coupling of the back and top gate to the constriction. Thus, $\alpha_{tg}/\alpha_{bg} = \Delta V_{bg}/\Delta V_{tg} \approx 7$.

Indeed, this value fits well with the value calculated using the thicknesses of dielectric materials, hBN and SiO_2 . The back gate lever arm can be calculated by assuming a simple parallel plate capacitor model and is given by $\alpha_{bg} = \epsilon_0 / [(e t_{\text{SiO}_2} / \epsilon_{\text{SiO}_2}) + (e t_{\text{bottom}} / \epsilon_{\text{hBN}})]$ where ϵ_0 is the dielectric field constant of vacuum, e is the elementary charge, t_{SiO_2} and t_{bottom} (see section 6.1.1) are the values of thickness and ϵ_{SiO_2} ($= 3.9$) and ϵ_{hBN} ($= 4$) are the dielectric constants of the gate dielectrics SiO_2 and hBN respectively [43]. This gives us a value of $\approx 7.2 \times 10^{10} \text{V}^{-1} \text{cm}^{-2}$. Likewise, the lever arm of the top gate is given by $\alpha_{tg} = \epsilon_0 \epsilon_{\text{hBN}} / e(t_{\text{top}} + t_{\text{gateoxide}}) \approx 49.12 \times 10^{10} \text{V}^{-1} \text{cm}^{-2}$ where t_{top} and $t_{\text{gateoxide}}$ refer to the thickness of the top hBN layer of the hBN-graphene-hBN sandwich and the gate oxide hBN (see Fig. 6.2 (d)) respectively. Using these values, we obtain the relative lever arm $\alpha_{tg}/\alpha_{bg} = 6.82$.

Experimentally, the gate lever arm can be extracted from quantum Hall measurements. We, now, discuss the measurement of Landau levels in the QPC as a function of the top gate voltage V_{tg} and a perpendicular magnetic field B . The energy of Landau level with index m in graphene is given by

$$E_m(B) = \text{sgn}(m) v_F \sqrt{\hbar |e| 2 |m| B}, \quad m \in \mathbb{Z}_0. \quad (7.5)$$

On the other hand, the energy dispersion relation for massless Dirac fermions in graphene is given by

$$E = \hbar v_F k_F. \quad (7.6)$$

Comparing these two results, we get

$$B_m = \frac{\hbar}{4me} \frac{k_F^2}{\pi}. \quad (7.7)$$

Using eq. 7.4, we get

$$B_m = \frac{h}{4me} n = \frac{h}{4me} \alpha_{\text{eff}} \Delta V_{\text{tg}} \quad (7.8)$$

where α_{eff} is the effective gate lever arm [42, 134] such that

$$n = \alpha_{\text{eff}} \Delta V_{\text{tg}} = \alpha_{\text{tg}} \Delta V_{\text{tg}} + \alpha_{\text{bg}} \Delta V_{\text{bg}}. \quad (7.9)$$

Thus, the Landau levels form straight lines with a slope $C_m = \frac{h}{4me} \alpha_{\text{eff}}$ in the $B - V_{\text{tg}}$ plane. Fig. 7.4 shows the Landau fan map of the QPC where the conductance trace at $B = 0$ T is same as the black trace in Fig. 7.3 (b)). As mentioned earlier, in order to measure this trace, the back gate and the top gate are swept simultaneously according to the equation $V_{\text{bg}} = 0.143 \times V_{\text{tg}} + 3.6$ such that it is perpendicular to the solid white CNP line in Fig. 7.3 (a). Thus, $\frac{\Delta V_{\text{bg}}}{\Delta V_{\text{tg}}} = 0.143$. Using this and the fact that $\alpha_{\text{tg}}/\alpha_{\text{bg}} = 7$ in eq. 7.9, we obtain the relation

$$\alpha_{\text{eff}} = \alpha_{\text{tg}}(1 + 0.143^2) \quad (7.10)$$

The solid black lines in Fig. 7.4 correspond to different Landau levels with the index $m = 0$ to -4 fitted according to eq. 7.8. Taking the average of the slopes of all these lines, we get an effective lever arm $\alpha_{\text{eff}} = \text{average slope} \times 4me/h = 50.03 \times 10^{10} \text{V}^{-1} \text{cm}^{-2}$.

Using this value in eq. 7.10, we extract the value of the top gate lever arm as $\alpha_{\text{tg}} = 49.03 \times 10^{10} \text{V}^{-1} \text{cm}^{-2}$ which matches excellently with the value obtained through pure geometry in the beginning of this section. Further, the back gate lever arm $\alpha_{\text{bg}} = \alpha_{\text{tg}}/7 = 7.01 \times 10^{10} \text{V}^{-1} \text{cm}^{-2}$.

7.4.3. Effect of localized states on conductance

After identifying the series of quantized conductance kinks, we now proceed to investigate how the mean conductance in eq. 7.3 behaves for this device. In Fig. 7.5 (a), the same trace shown in Fig. 7.3 (b) is measured for a larger range of V_{tg} (see the black trace). Using the gate lever arms extracted in the previous section, we now convert V_{tg} into n using eq.7.9 (see the top axis). The blue trace is a square root fit to the holes side of the experimental trace using the Landauer- Büttiker formula in eq.7.3. This is obtained by first squaring the conductance as shown in Fig. 7.5 (b) and then fitting a straight line to the data as depicted by the blue trace. The first fit parameter gives the slope $(= 16c_0^2 w^2 \alpha_{\text{tg}}/\pi)$ of this straight line which is used to extract the transmission coefficient $c_0 \approx 0.7$ for a QPC of width $w = 380$ nm. The other fit parameter V_0^h which is the x - intercept of the blue straight line in Fig. 7.5 (b), along with the slope is used to obtain the blue square root fit in Fig. 7.5 (a). Note that the constant c_0 , in fact, determines the actual height of the kinks shown in Fig. 7.3 (c). The step height is given by $c_0 \times 4e^2/h \approx 2.8 e^2/h$ which fits well the observed $2 - 3 e^2/h$ height of these kinks.

Thus, we clearly see that the measured trace follows the expected $G \propto \sqrt{V_{\text{tg}}} \propto \sqrt{n}$ at higher gate voltages and deviates as we approach the CNP i.e. for absolute values of $V_{\text{tg}} < 2.5$ V or $n < 1 \times 10^{12} \text{cm}^{-2}$ (see orange shaded region and also refer to Fig. 3.2) (e)). This is a primary indication of the fact that the ideal relation between n and k_F i.e. $n = k_F^2/\pi$ is not enough to explain the experimentally measured trace and needs to be modified to eq. 3.2 to include the additional trap state charge carrier density n_T .

The density of trap states ρ is estimated using a Gaussian as shown by the black trace in Fig. 7.6 (a) as opposed to the linear density of states in ideal graphene (see the red line). The factor V_0^h as well as the

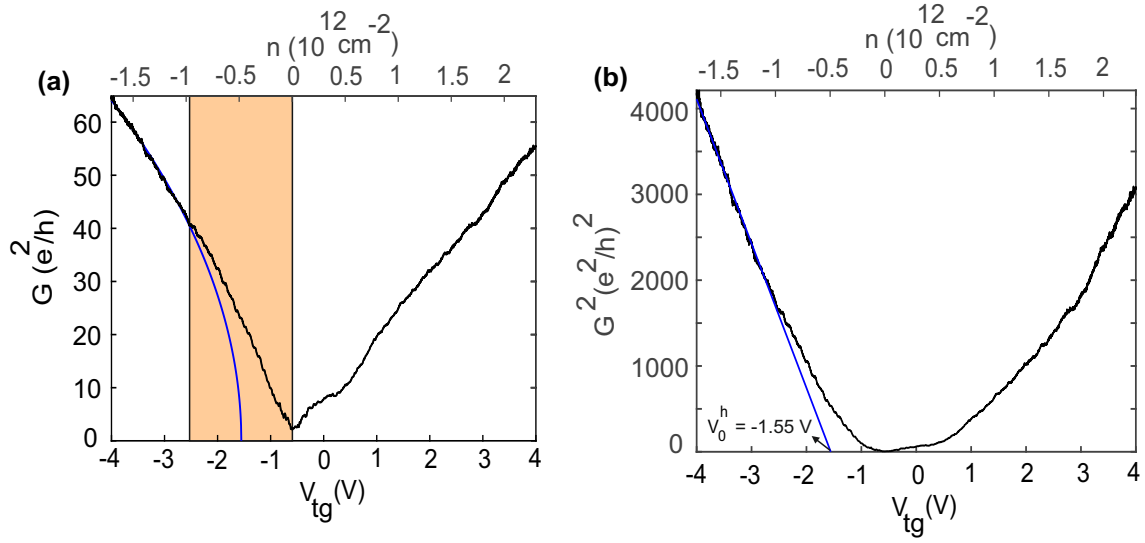


Figure 7.5.: (a) Conductance trace shown in Fig. 7.3 (b) as a function of V_{tg} and also the charge carrier density $n(V_{tg})$ (see top x axis). Blue trace is a fit using eq. 7.3 i.e. $G \propto \sqrt{V_{tg}} \propto \sqrt{n}$. Orange shaded region denotes the deviation of G from the square root fit. (b) Square of the conductance in (a) is shown by the black trace. Blue line is a straight line fit using eq. 7.3.

difference in the conductance between the measured trace and the square root fit (black and blue traces in Fig. ?? (a)) are used to estimate the centre, width and the height of the Gaussian. The larger the width of the orange shaded region, the larger the area under the Gaussian in Fig. 7.6 (a). Thus, the trap states play a significant role only around the CNP. As k_F approaches zero close to CNP, it is clear from the equation $n = \frac{k_F^2}{\pi} + n_T(k_F) = \alpha \Delta V_{tg}$, that the charge carrier density is dominated by n_T . Far away from the CNP, when $k_F^2 \gg \pi n_T$, the ideal relation between n and k_F and consequent square root behavior of the conductance is restored as ρ approaches the tail end of the Gaussian. Thus, the deviation of G from its ideal behavior provides us a way to extract n_T experimentally.

The trap states contribute only to the charging characteristics i.e. they act like electron traps and reduce the overall transmission of the channel but do not contribute to the electron transport itself [42]. Such trap states can be found at the rough edges of samples like the present device which are fabricated by cutting or etching the graphene flake resulting in a number of localized states [170, 225]. Therefore, one would expect that in narrower constrictions where the edges are much closer to the bulk of the QPC, their influence is much stronger. While the suppression of conductance due to rough edges was earlier shown via simulations for example, in Ref. [224], this was observed experimentally in hBN encapsulated graphene QPCs by the authors in Ref. [42] where back-scattering of electrons at the rough edges was much higher in narrower constrictions with a width of 230 nm and was significantly reduced as the width increased. As a result, the value of c_0 was close to 0.5 in a 230 nm wide constriction and the consequent step height was approximately $2 e^2/h$ ($c_0 \times 4e^2/h$) while it was close to 1 with evident $4 e^2/h$ height kinks in a 310 nm wide constriction. Moreover, when the same device (width = 230 nm) was measured once again after exposing it to air for several days, it showed the nearly the same transport characteristics at higher values of n or k_F . But, the second cool-down of sample resulted in a larger spread of conductance at smaller values of n around the CNP implying more trap states. As the graphene was sandwiched between two layers of hBN, the bulk was protected while only the edges were exposed to air and likely experienced some chemical modifications.

This, further, proves that the edges contribute to trap state density i.e. the charging characteristics of the sample.

With the trap state density taken into consideration, the Landauer - Büttiker model now fits the measurement pretty well (red trace in Fig. 7.6 (b)). Further, it is now possible to express the conductance as a linear function of rescaled k_F using eq. 3.2 as shown by the black trace in Fig. 7.6 (c) which overlaps quite well with the expected linear mean conductance trace denoted by the red dashed line.

Once the conductance is linearized, this provides us an alternate method to verify the width of our device besides AFM or SEM measurements. By subtracting the zeroth order term i.e. the mean conductance G^0 from the measured conductance i.e. the red dashed line subtracted from the black trace in Fig. 7.6 (c), we are left with the superimposed conductance modulations as seen in Fig. 7.7 (a). If these modulations are indeed signatures of size quantization, then the first peak in the Fourier transform of this quantity $\delta G = G - G^0$ should give us the width of the QPC. From Fig. 7.7 (b), we see that the first peak occurs at around 386 nm which is quite close to the width of the QPC from AFM measurements (≈ 380 nm) in Fig. 6.2 (a).

7.4.4. Effect of the top gate on localized states

Since the top gate covers only the bulk of the channel, it is expected to have stronger coupling to the channel as compared to the edges that only experience fringe field effects. Therefore, the measurements described in this section are performed to check if tuning the top gate allows us to control the influence of localized edge states on the channel conductance.

For this purpose, we consider the derivative of the conductance, dG/dV_{bg} in the V_{tg} - V_{bg} plane as shown in Fig. 7.8 (a). Note that the solid black "major line" is same as the one shown in Fig. 7.3 (a) i.e. it denotes the CNP of each individual conductance trace $G(V_{tg})$ measured at a particular value of V_{bg} . Therefore, the slope of this line, the "major slope" corresponds to the ratio of gate lever arms. We find that there are several features evolving parallel to this line (see solid black lines in the close-up in Fig. 7.8 (b)).

Fig. 7.8 (c) shows conductance traces measured perpendicular to the major line, similar to the measurement of the trace discussed in Fig. 7.8 (b), i.e. according to the equation $V_{bg} = 0.143 \times V_{tg} + k^0$ where $k^0 = 1.20, 2.24, 2.96, 3.60, 4.24$ (see section 7.4.2) as we move towards the left from the orange to the pink trace. Note that the black trace in Fig. 7.8 (c) is the same as the black trace shown in Fig. 7.3 (b). All the traces show highly robust quantized conductance steps on the order of $2-3 e^2/h$ that move parallel to the major line as we move from one trace to the next (see blue arrows). These features that develop parallel to the major line are a result of the evolution of quantized conductance kinks with the top gate voltage.

Besides these larger features, there are several other features that evolve parallel to the so-called "minor line" (see the black dashed lines in Fig. 7.8 (a) and (b)).

Since the top gate is confined only to the inner channel of the QPC leaving the edges free, extended states that exist over the entire sample including the bulk region under the top gate (orange region with a width of 230 nm in Fig. 7.8 (d)) are tuned quite strongly by the top gate resulting in the quantized conductance features evolving parallel to major line with a slope of 7. However, the localized states closer to and along the edges of the QPC (red dots) are influenced by the stray field emerging from the top gate. These states are only weakly tuned by the top gate i.e. their capacitive coupling to the top gate is much weaker than the extended states which results in the minor lines with a much smaller slope of about 1.4. Naturally,

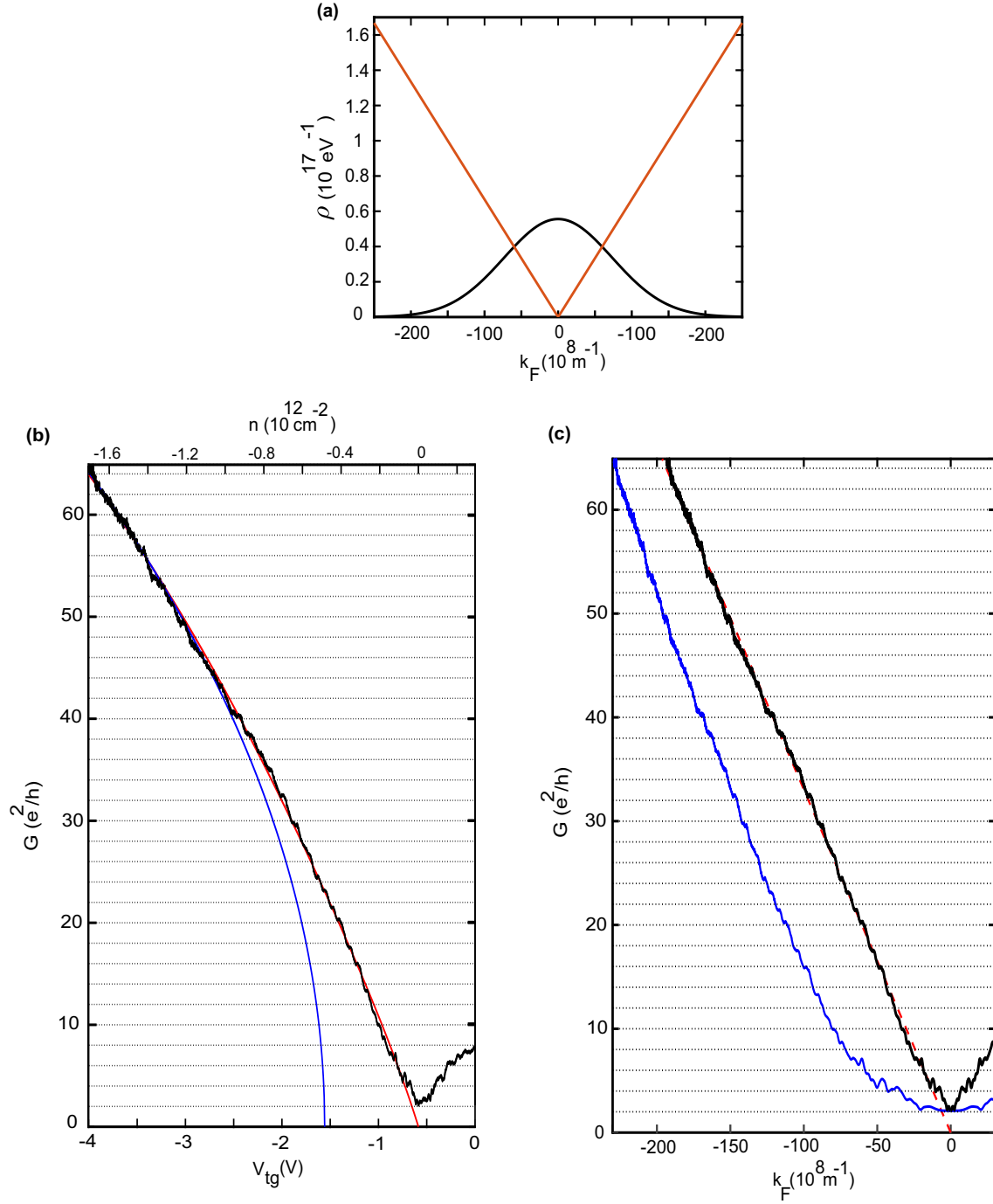


Figure 7.6.: (a) Density of trap states (black curve) estimated using a Gaussian. Red trace denotes the ideal linear density of states of graphene. (b) Conductance trace (in black) for the holes in (a). Red trace is a square root fit to the black conductance trace after accounting for the density of trap states shown in (a). Thus, once the trap states are taken into consideration, $G(V_{tg})$ follows the expected square root relation. Blue trace is same as the one shown in Fig. 7.5 (a) i.e. it is the fit to the experimental data without including the trap state density and deviates from the expected square root relation. (c) Conductance as a function of k_F . Blue trace is obtained from the corresponding blue trace in (b). Black trace denotes the conductance trace after rescaling k_F using the eq. 3.2, $n = \frac{k_F^2}{\pi} + n_T(k_F) = \alpha \Delta V_{tg}$. Red dashed line shows the expected ideal linear conductance such that $G \propto k_F$.

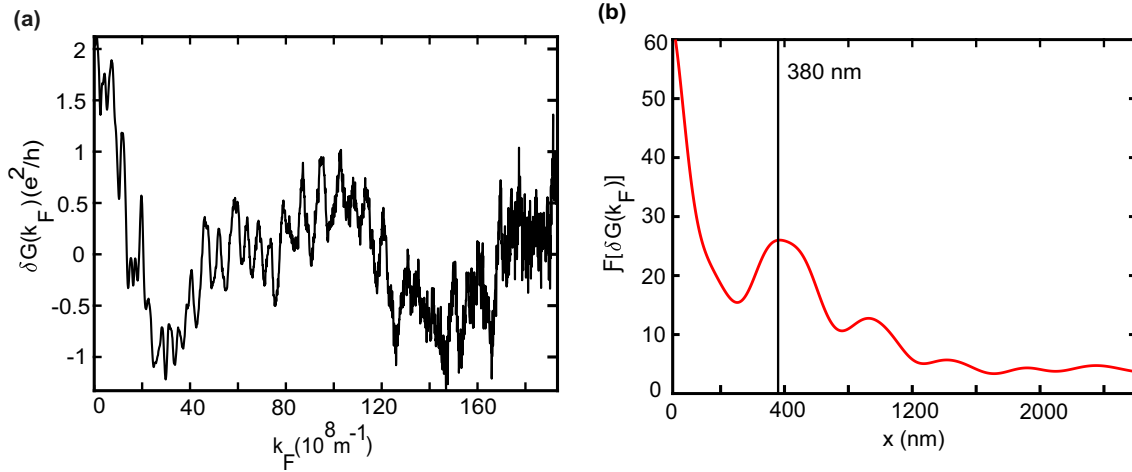


Figure 7.7.: (a) Modulations in hole conductance $\delta G = G - G^0$ as a function of k_F . G, G_0 refer to the conductance and mean conductance traces after including the trap state density, n_T i.e. the solid black and dashed red traces in Fig. 7.6 (c) respectively. (b) Fourier transform of the conductance in (a). The first prominent peak appears at 386 nm which is nearly equal to the width of the QPC i.e. 380 nm.

both extended and localized edge states are tuned with the same capacitive strength by the back gate as they are the same distance away from the gate.

In this scenario, it should be possible to reduce the influence of these localized edge states by sweeping the gates along the minor line. The resulting conductance would then be mostly a result of size quantization with minimal influence of edge disorder. To check this prediction, we sweep the top and back gate voltages simultaneously along two lines with different slopes (marked 1 and 2 in Fig. 7.9 (a)). The conductance trace 1 has already been shown and discussed in Fig. 7.3 (b) and is perpendicular to the major line. Here, both V_{tg} and V_{bg} are varied simultaneously according to the equation $V_{bg} = 0.143 \times V_{tg} + 3.6$. The sweep direction 2 is parallel to the minor line and the gate voltages are swept such that $V_{bg} = 3.74 - 1.4 \times (V_{tg} + 1.32)$ (see Appendix B.1). The kinks in the conductance traces in Fig. 7.9 (b) can be correlated with the corresponding conductance derivative maxima in Fig. 7.9 (a) (see black arrows in Fig. 7.3 (a)). The kinks are highly robust and occur at the same value of conductance independent of the sweep direction.

For instance, we see a series of clear $2-3 e^2/h$ steps starting from $16 e^2/h$ down to up to $8 e^2/h$ (marked ✕, ▲, ★ and ■) in both traces although occurring at different gate voltages.) Further, we notice that as we go closer to the CNP (below $6 e^2/h$, see ◆, ●), the conductance behaves quite differently in both traces. Since it has been established that disorder due to trap states manifests strongly around the CNP [42], this corroborates the argument that the influence of these localized trap states depends on the sweep direction.

Similar results were obtained in another data set shown in Fig. 7.10 (a) where the sweep directions "3" and "4" are parallel to "1" and "2" discussed above. Therefore, the gate voltages are swept according the equation $V_{bg} = 0.143 \times V_{tg} + 2.722$ for trace 3 and $V_{bg} = 3.2 - 1.4 \times (V_{tg} + 1.32)$ for trace 4. Once again, we see that the conductance kinks (see different symbols from $6 - 16 e^2/h$) in Fig. 7.10 (b) are quite robust irrespective of the sweep direction, thus, proving the size confinement of electrons.

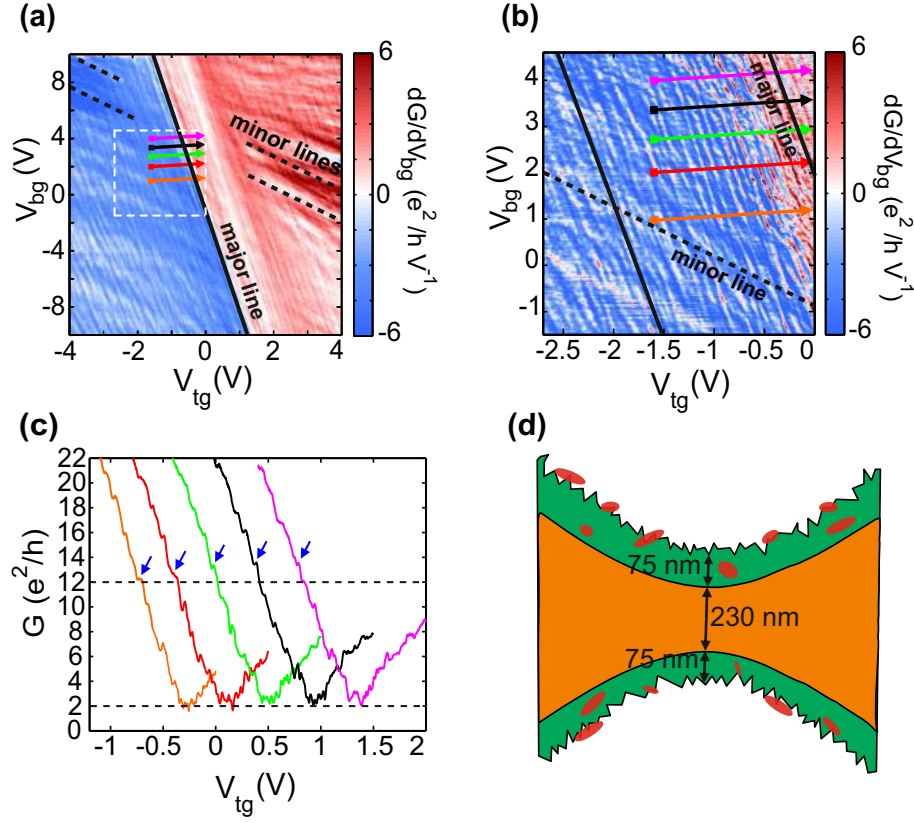


Figure 7.8.: (a) Transconductance dG/dV_{bg} of the QPC as a function of V_{tg} and V_{bg} at a DC bias voltage $V_b = 500 \mu V$ along with an AC bias of $300 \mu V_{\text{peak-to-peak}}$. The solid black "major line" indicates the CNP of each individual conductance trace in top gate $G(V_{tg})$ at a fixed value of V_{bg} (similar to Fig. 7.3 (a)). Besides this dominant feature, several other structures are seen to evolve parallel to the "minor line", as indicated by the black dashed lines. (b) Close-up of the region enclosed by the white dashed lines in (a). (c) Individual conductance traces measured along the corresponding coloured arrows in (a) and (b). Starting from the left, each trace is offset horizontally by 0.5 V with respect to its previous trace for clarity. Note that the black trace is the same as the one measured in Fig. 7.3 (b). (d) Schematic of the rough-edged QPC (green) along with the top gate (orange). The width of the top gate (the QPC) is 230 nm (380 nm). Red dots mark localized states along the edges of the QPC.

7.5. Conductance of a QPC with two top gates

7.5.1. Non-constant gate lever arm measurements

Similar measurements on the behavior of conductance were also performed on the 300 nm wide QPC with two top gates as shown in Fig. 7.1 (c). Similar to the discussion in section 7.4.2, the value of α_{bg} estimated using the parallel plate capacitor model is $7.32 \times 10^{11} V^{-1} cm^{-2}$. The fact that the back gate has a nearly constant lever arm has also been shown previously in Ref. [37] using quantum Hall measurements in a perpendicular magnetic field.

Fig. 7.11 (a) shows a plot of the four terminal conductance G through the constriction as a function of V_{bg} and V_{tg} voltages. The solid white line indicates the CNP of each individual back gate trace $G(V_{bg})$ measured at a particular value of V_{tg} . However, unlike the earlier device with a single top gate, here, we

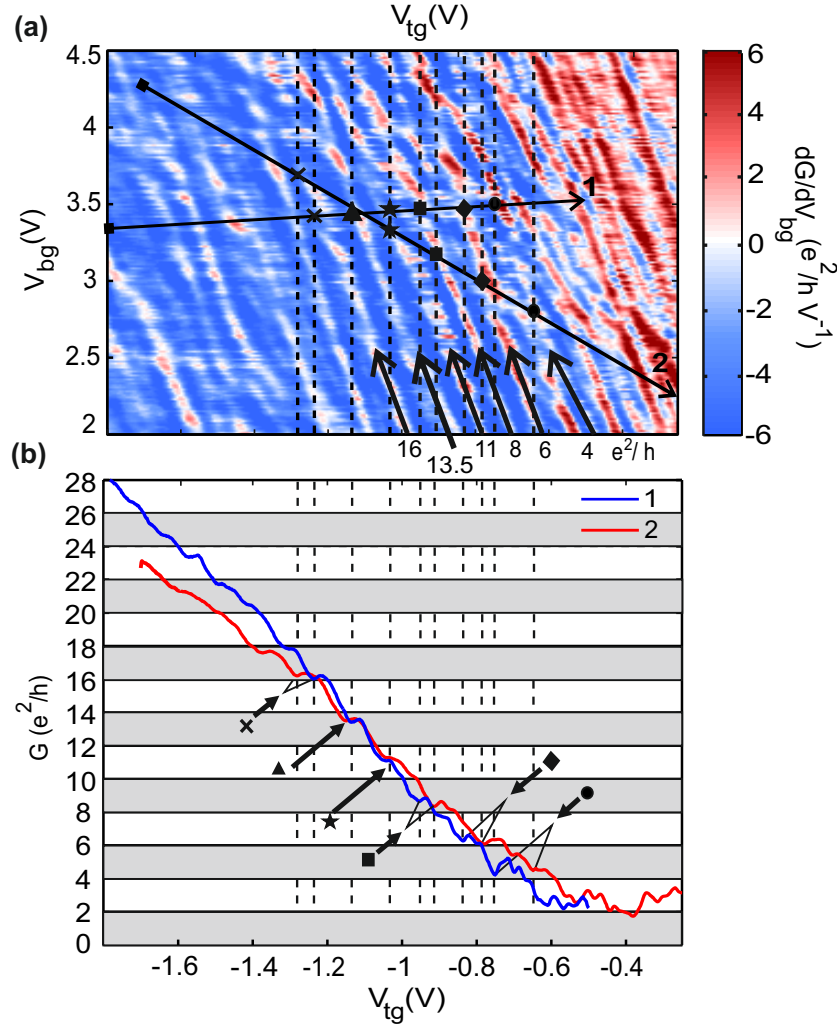


Figure 7.9.: (a) Close-up of the conductance map shown in Fig. 7.3 (b). The black arrows indicate different directions of sweep "1" and "2" of V_{bg} and V_{tg} . (b) Conductance traces corresponding to the arrows shown in (a). "1" corresponds to the trace that is measured along a line (slope = 0.143) which is perpendicular to major line in Fig. 7.8 (a) from $V_{tg} = -1.8$ V to -0.5 V. Here, V_{tg} is varied such that $V_{bg} = 0.143 \times V_{tg} + 3.6$. "2" corresponds to the trace that is measured along a line (slope = -1.4) that is parallel to the minor line Fig. 7.8 (a) as V_{tg} is varied from -1.7 V to -0.25 V. Here, V_{tg} is varied such that $V_{bg} = 3.74 - 1.4 \times (V_{tg} + 1.32)$. The symbols indicate different conductance kinks and can be correlated to the derivative maxima in the conductance map in (a) using the black dashed lines.

observe that the slope of this line is continuously changing implying a non-constant relative lever arm (in the voltage range under consideration). Interestingly, this effect is comparable to the previous experiments on side gated HF-dipped graphene nanoribbons on SiO_2 [220]. In those devices, the non-constant lever arm is attributed to edge modification due to their treatment with HF. Such a modification resulting in Fluorine terminated graphene edges is also possible with the presented top gated devices since the hBN-graphene-hBN sandwiches were etched using SF_6 during fabrication. Calculations also suggest that replacing -OH and -O by -F termination leads to significant reduction in density of states along the graphene edges resulting in back gate dependent top gate coupling [226]. Similar to the single top gate device discussed earlier, this

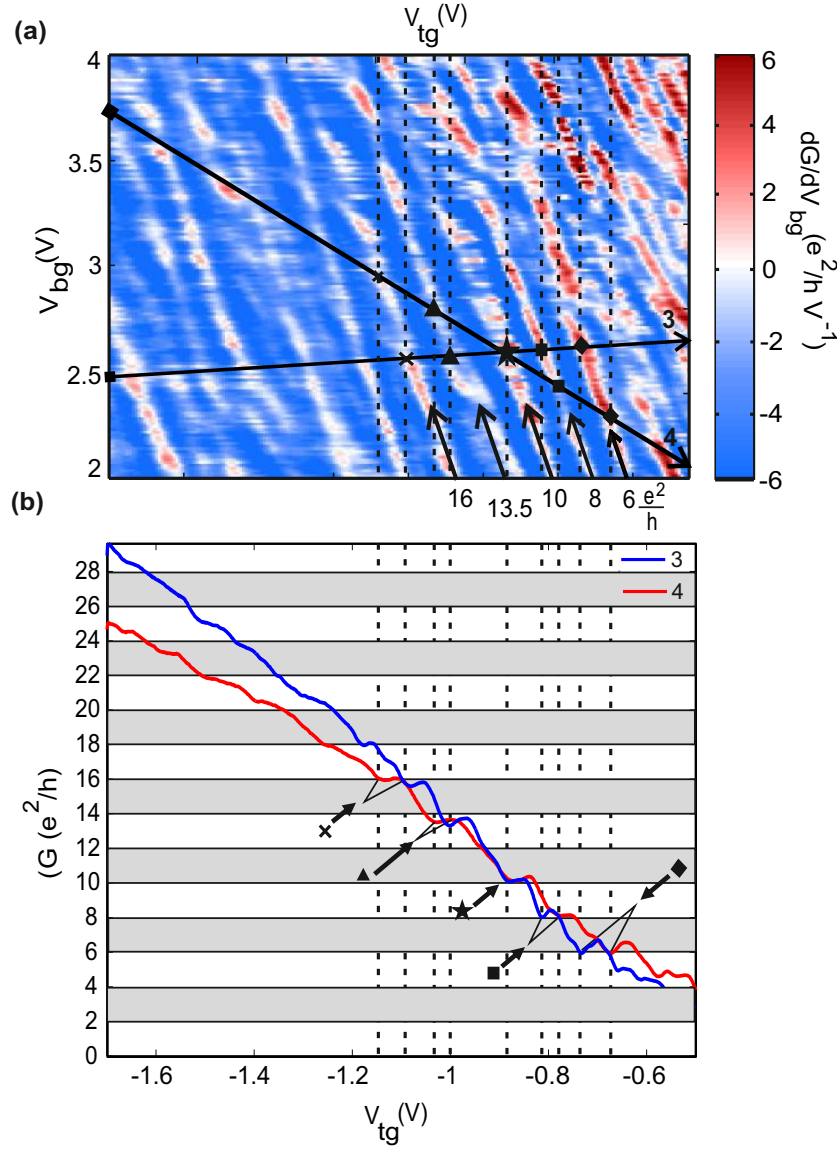


Figure 7.10.: (a) Similar to Fig. 7.9 (a). The black arrows indicate different directions of sweep of V_{bg} and V_{tg} - the arrows marked "3" and "4" are similar to "1" and "2" respectively in Fig. 7.9 (a). (b) Conductance traces corresponding to the arrows shown in (a). Trace "3" is measured along a line (slope = 0.143) perpendicular to major line in Fig. 7.8 (a). Here, V_{tg} is varied such that $V_{bg} = 0.143 \times V_{tg} + 2.722$. While "4" corresponds to the trace that is measured along a line (slope = -1.4) that is parallel to the minor line in Fig. 7.8 (a) as V_{tg} is varied from -1.7 V to -0.5 V. Here, V_{tg} is varied such that $V_{bg} = 3.2 - 1.4 \times (V_{tg} + 1.32)$. The symbols indicate different conductance kinks and can be correlated to the derivative maxima in the conductance map in (a) using the black dashed lines.

is most likely a result of the proximity of the top gates to the channel due to which the entire constriction is tuned and not just the edges.

Fig. 7.11 (b) shows individual conductance traces (horizontal line cuts from Fig. 7.11 (a)) as a function of the back gate voltage. Each trace is shifted horizontally by V_0 which is the value of V_{bg} at the CNP such that the CNP is now at zero. Similarly, each trace is offset by $4 e^2/h$ vertically with respect to its previous trace. In the inset, we show the transmission coefficient c_0 which has been extracted by fitting the conductance of

individual back gate traces to a square root function as explained in Fig.7.5. For a constriction with a width of 300 nm, we observe that the overall transmission through the constriction can be slightly tuned and levels off at a value of nearly 0.5.

Fig. 7.11 (c) shows a close up of the same traces as in Fig. 7.11 (b) shifted horizontally by a constant value of V_{bg} . Importantly, we observe that the conductance kinks on the order of $2\text{--}3\ e^2/h$ are indeed independent of V_{tg} . Thus, the top gates can be used to prove that these kinks are, indeed, very stable signatures of quantized conductance and occur solely due to the effect of size confinement in the constriction.

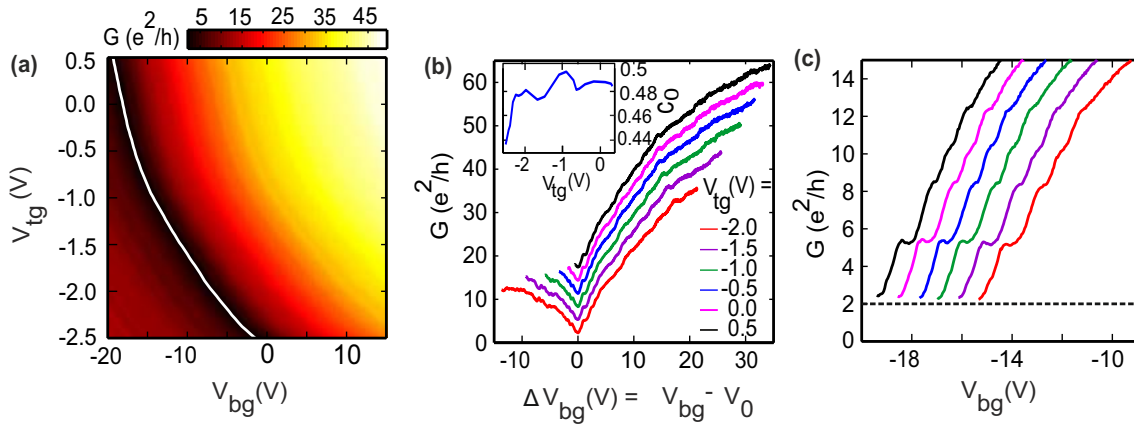


Figure 7.11.: (a) Four terminal conductance G of the 300 nm wide QPC with two top gates shown in Fig.7.1 (c) as a function of the back gate V_{bg} and the top gate voltage V_{tg} . Here, both top gates TG1 and TG2 are short to one another such that a symmetric gate voltage is applied on both the top gates. Solid white line indicates the CNP of each conductance trace in back gate $G(V_{bg})$ measured at a fixed value of V_{tg} . (b) Horizontal line-cuts across the plot in (a). Individual curves represent back gate traces at different values of V_{tg} with the CNP shifted to zero. The curves are offset vertically by $4\ e^2/h$ for clarity. Inset shows the transmission coefficient calculated from individual back gate traces as a function of V_{tg} using the same method as in Fig.7.5. (c) Close-up of the traces in (b). The black trace is at a fixed value of V_{tg} ($= 0.5\text{ V}$) and all the other traces to its right are shifted by 0.85 V relative to the preceding trace.

Independent tuning of each of the two top gates also yielded similar results i.e. a non uniform lever arm (see Fig. 7.12). Unfortunately, this sample did not remain stable enough to conduct further measurements. For future study in this direction, it would be highly informative to tune the two top gates independently from one another in both a symmetric and an asymmetric manner to understand the influence of tuning multiple gates on the trap state density [221, 227].

However, a constant problem that we encountered with such dual top gated devices was that if one of the gates did not work, it led to an asymmetric gate potential and a conductance profile through the QPC. For this reason, the single top gate design of the previous sample was far more useful and stable to study the conductance of the device.

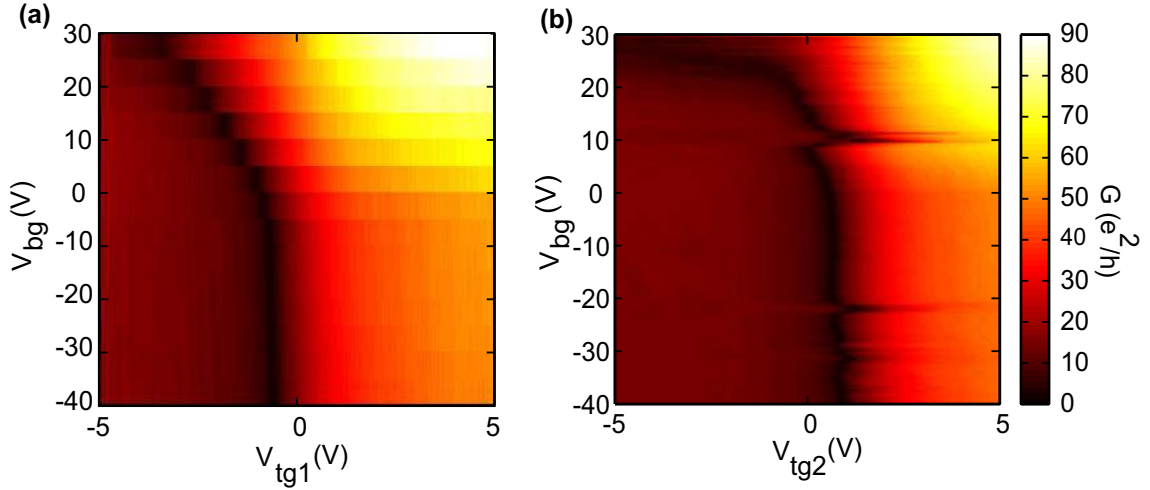


Figure 7.12.: Four terminal conductance G of a 300 nm wide QPC with two top gates shown in Fig.7.1 (c) as a function of the back gate V_{bg} and the top gate voltage V_{tg} . **(a)** The top gate TG1 is swept continuously along with the back gate while the other top gate TG2 is grounded. **(a)** TG2 is swept continuously while TG1 is grounded.

7.6. Theoretical simulations of conductance in a graphene QPC with a single top gate

Features similar to the experiment described in section 7.4 including different major and minor slopes in the lever arm map have also been attained using theoretical simulations using an idealized scattering structure. We employ a tight-binding Hamiltonian [224],

$$H = \sum_i V_i \Phi_i \Phi_i - \sum_{(i,j)} \gamma_{ij} \Phi_i \Phi_j + \text{h.c.}, \quad (7.11)$$

where i are lattice sites with on-site potential V_i , and (i,j) are pairs of lattice sites with hopping matrix elements γ_{ij} . We include coupling up to the third-nearest-neighbor and omit physical spin. The sample geometry is quite simple and minimal - it consists of a 50 nm long and 20 nm wide ribbon (I) cut out of a large graphene flake as shown in Fig. 7.13 (a). We simulate 200×200 atoms in an ≈ 20 nm wide zig-zag ribbon. A small amount of disorder in the form of edge roughness with an amplitude of about 4 \AA is included to account for patterning of the device. As contacts, we use semi-infinite leads within the Landauer-Büttiker formalism [228, 229].

Similar to the experiment, we tune not only the Fermi energy E but also the potential near the edge of the ribbon via a side gate U . We can thus independently tune the localized states and the bulk states. The side gate potential U tunes the energy of localized edge states and slightly decreases the width of the transmission channel. The Fermi energy E affects the on-site potential on all the atoms, including the edges. The differential conductance dG/dE thus features two slopes on the $U-E$ plane, just as in the experiment: the first emerges due to conductance quantization (parallel to the black dashed lines in Fig. 7.13 (b)). The second (parallel to the purple line) is given by the edge-localized states, which are more strongly tuned by U . We compare the conductance along two line cuts in the $U-E$ plane in all our simulations. The first is at fixed side gate $U = -0.2 \text{ eV}$ (green line) and the other one is parallel to the slope due to the edge-states (purple line in Fig. 7.13 (b) and (c)). These are equivalent to the two cuts perpendicular to the "major slope"

and parallel to the "minor slope" considered in the experiment. The "minor slope" avoids resonances of localized states, leading to cleaner quantization signatures than at fixed U . Indeed, the purple conductance trace in Fig. 7.13 (c) shows slightly better steps as compared the green trace.

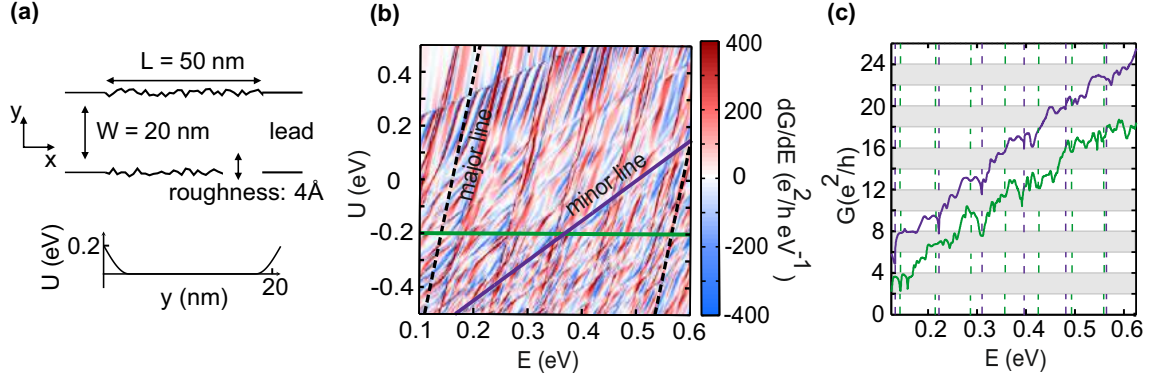


Figure 7.13.: (a) Schematic of the ribbon model (I) consisting of a 50 nm long and 20 nm wide graphene ribbon with an edge roughness of 4 \AA . The potential near the edge is tuned with the side-gate potential U . (b) Differential conductance as a function of the Fermi energy E and side gate potential U . Black dashed line denotes the evolution of the conductance kinks. Therefore, it is comparable with the "major line" in Fig. 7.8 (a). The green line is at a fixed side gate $U = -0.2$ eV and can be compared with the measurements perpendicular to the major line i.e. line "1" in Fig. 7.9 (a). The purple line $U(E) = 3/2 E - 0.75$ eV denotes the evolution of the edge states and corresponds to the "minor line" in the experiment in Fig. 7.8 (a) and is comparable with line "2" in Fig. 7.9 (b). (c) Conductance along the two sweep directions in purple and green in (b). The purple curve is offset vertically by $+ 4 e^2/h$ for clarity. Dashed lines mark the energies of the conductance steps.

7.7. Conclusion

In this chapter, we have used additional top gates on an encapsulated graphene constriction where the idea was to have another knob besides the back gate to tune the transmission of the quantum point contact. Two different geometries of top gate - the first one with a single global top gate covering the entire channel except the edges and the second type with two top gates, one on either side of the constriction and covering only its the edges symmetrically. In the case of the constriction with two top gates, we observe a non-constant, non-linear gate lever arm. This is attributed to the fluorine terminated rough edges resulting from reactive ion etching which lead to a back gate dependent top gate coupling. We see quantized conductance kinks on the order of $2 - 3 e^2/h$ that shift nicely with the back gate voltage, further corroborating the argument that these kinks are a result of size quantization occurring within the constriction.

In the case of the device with the global top gate, we can clearly see two different slopes in the measurement of lever arm - a stronger "major" slope due to quantized conductance kinks and a relatively smaller "minor" slope due to the localized edge states, something that we also see in the theoretical tight binding simulations. By sweeping the back and top gates along two directions - along the minor slope and perpendicular to the major slope, we show that the influence of edge disorder on the channel conductance can be varied. This is visible in the corresponding conductance traces which show significant differences in the

features observed around the CNP where the effect of edge disorder is maximum. Away from the CNP, the conductance kinks are independent of the direction of sweep.

Thus, employing an additional top gate is a successful technique to not only shed light on the contribution of the edge states but also to control their influence on the transport through a QPC.

8. Crossover from size quantization to Landau quantization in etched graphene quantum point contacts

Contributions to this chapter:

S.Somanchi fabricated and performed measurements on the etched top gated graphene QPC device. The theoretical simulations were performed by T. Fabian and F. Libisch from Vienna University of Technology.

8.1. Introduction

In this chapter, we discuss the conductance of the etched graphene QPC device with a single top gate discussed in section 6.1.1 as a function of a perpendicular magnetic field. The magnetic field offers another possibility to distinguish the bulk states in the QPC channel from the localized edge states through the difference in the effect it produces on them. We observe this difference in evolution between the localized edge and bulk states as the device moves from a size quantization regime at zero magnetic field to Landau quantization as the field increases.

8.2. Experimental magnetic field measurements - Evolution of conductance kinks in an etched graphene QPC with a single top gate

In Fig. 8.1 (a) and (c), we look at how the conductance kinks in the trace "1" (measured perpendicular to the major line) and trace "2" (measured parallel to the minor lines and is therefore, expected to have lesser influence of edge disorder on the conductance) are affected by a perpendicular magnetic field B . As explained already using Fig.7.9 (b), conductance trace "1" is measured by sweeping both V_{tg} and V_{bg} simultaneously according to the equation $V_{bg} = 0.143 \times V_{tg} + 3.6$ while for trace "2", we use $V_{bg} = 3.74 - 1.4 \times (V_{tg} + 1.32)$.

The transition from the size quantization regime (see different symbols in Fig. 8.1 (a) - (f) denoting various conductance kinks) at low B field to Landau level quantization at higher magnetic fields occurs when the cyclotron radius of the charge carriers becomes half the width w of the QPC. For a semiconductor with conventional parabolic bands, we can use the relation $r_c = m^*v/eB$ where the effective mass of the electron m^* is constant as it moves in a magnetic field B with a velocity v and cyclotron radius r_c . In the case of graphene with conical bands at the Dirac point, the momentum of an electron with Fermi velocity

v_F is given by $P = \hbar k_F = m^* v_F$. Therefore, the dynamical mass of the electron $m^* = \hbar k_F / v_F$ varies as a linear function of k_F or \sqrt{n} in the case of graphene [230, 231].

Thus, the cyclotron radius is given by

$$r_c = \frac{\hbar k_F}{eB} < \frac{w}{2}. \quad (8.1)$$

Using the above equation at the boundary where the system moves from quantized conductance kinks to Landau levels, we get the following relation.

$$B_c = \frac{h}{\pi e} \frac{\sqrt{\pi n}}{w}. \quad (8.2)$$

Therefore, the critical magnetic field B_c at the boundary is proportional to the square root of the charge carrier density n . In the magnetic field measurements shown in Fig. 8.1 (b) and (e), the green curve marks this line of transition for the present QPC device with a width of 380 nm. At magnetic fields above this trace, we see that the transconductance in both the traces "1" and "2" displays near-identical features in the form of Landau levels from the index $m = 0$ to -4. However, below the green trace, around zero B field region in Fig. 8.1 (c) and (f) i.e. where the conductance is still dominated by size quantization, the features evolve quite differently for these two traces. This region is highly influenced by the amount of edge disorder in the device, which changes for different directions of sweeping the gate voltages V_{bg} and V_{tg} in traces "1" and "2". We already understood from the discussion on Fig. 7.9 in the previous chapter, that the conductance kinks further away from the CNP look nearly identical for both sweep directions 1 and 2. The difference occurs as we get closer to the CNP. Indeed, the largest discrepancies appear at zero magnetic field and near the CNP, where the disorder is strongest. For example, see the difference in features around ■, ◆, ● in Fig. 8.1 (c) and (f).

Similar results are also observed for the second data set involving the conductance traces "3" and "4" shown in Fig. 7.10 (b). As explained in the previous chapter, trace "3" is measured similar to trace "1" in accordance with the equation $V_{bg} = 0.143 \times V_{tg} + 2.722$ while trace "4" is measured similar to trace "2" in accordance with the equation $V_{bg} = 3.2 - 1.4 \times (V_{tg} + 1.32)$. In Fig. 8.2 (a) - (c), we see the evolution of the conductance kinks in trace "3" with magnetic field and in Fig. 8.2 (d) - (f), we see the same results for trace "4". Nearly-identical quantum Hall features for both these traces as seen in Fig. 8.2 (b) and (e). Upon careful observation of the corresponding close-up Landau fan maps in Fig. 8.2 (c) and (f), we see that there are features which seems to be unaffected by the magnetic field. For example, observe the vertically straight features (black lines) to the right of ◆ in both Fig. 8.2 (c) and (f) (also see the black straight lines in Fig. 8.1 (c) and (f)). Interestingly, we see that the straight line around the ◆ in Fig. 8.2 (c) gets modified to a more curved feature in in Fig. 8.2 (f) which joins the Landau level $m = -3$ going upwards. Thus, this straight line feature seems to be somehow related to the direction of sweep i.e. whether we sweep the gate voltages such that the trace is measured perpendicular to the major line or parallel to the minor line. In the next sections, we delve deeper into such differences at low magnetic field between the two directions of sweep and try to explain them using theoretical simulations in section 8.4.

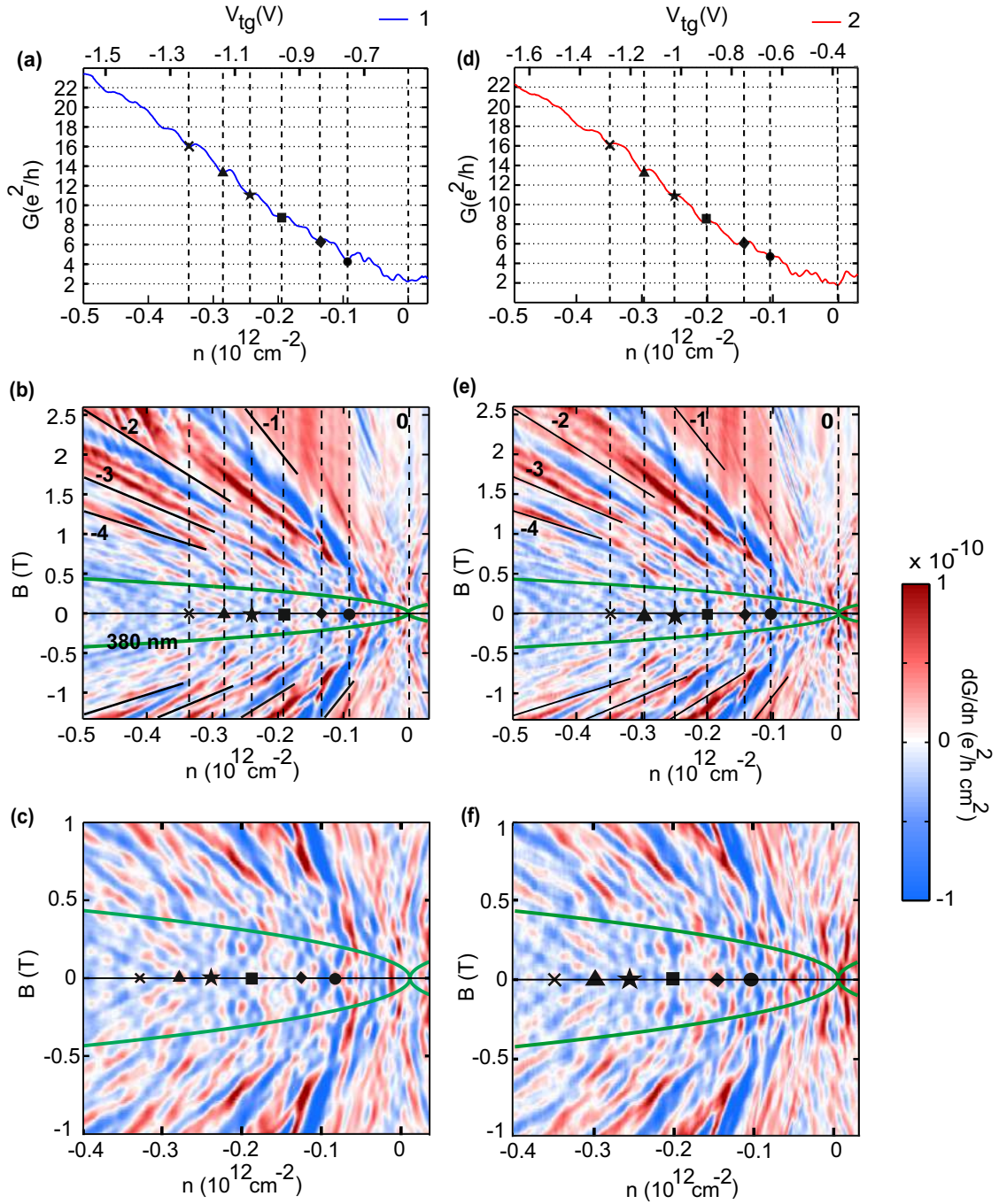


Figure 8.1.: (a) Conductance trace "1" from Fig. 7.9 (b) as a function of the charge carrier density n . This trace is obtained by sweeping the top and back gate voltages simultaneously along a direction perpendicular to the major line as discussed in Fig. 7.8 (a). Here, V_{tg} is varied such that $V_{bg} = 0.143 \times V_{tg} + 3.6$. (b) Differential conductance (offset by the mean $\langle dG/dn \rangle$) of the trace in (a) as a function of the magnetic field B . The green curve marks the region of transition between the size quantization regime at lower B field and quantum Hall regime at higher B field for a QPC with a width of 380 nm, in accordance with eq.8.2. Landau levels with the index $m = 0$ to -4 are visible at B field above the green curve. (c) Close-up of the trace in (b) in the low magnetic field region. (d,e,f) Same as (a,b,c) for the conductance trace "2" in Fig. 7.9 (b). The conductance trace "2" in (d) is obtained by sweeping the top and back gate voltages simultaneously along a direction parallel to the minor line as discussed in Fig. 7.8 (a). Here, V_{tg} is varied such that $V_{bg} = 3.74 - 1.4 \times (V_{tg} + 1.32)$.

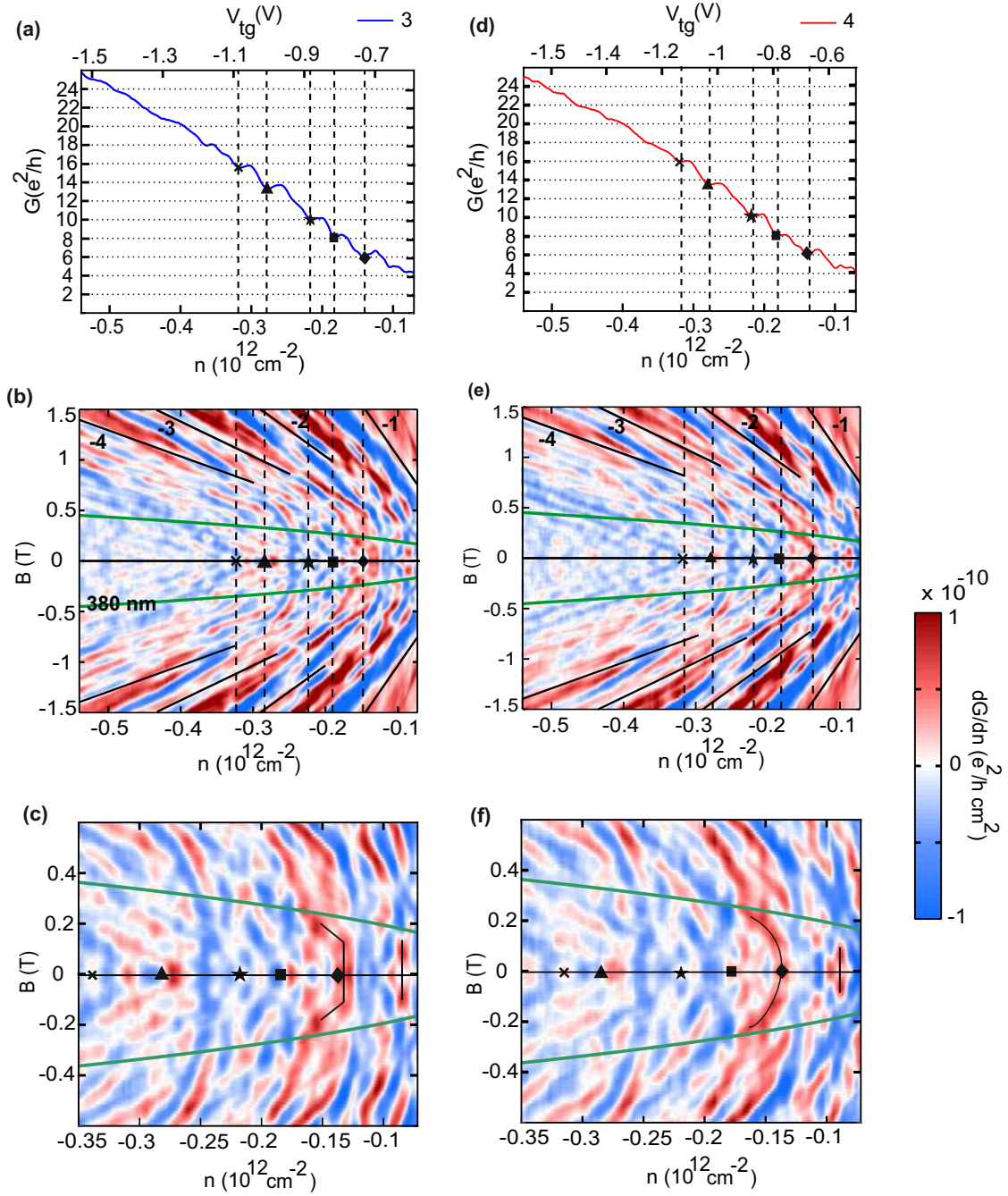


Figure 8.2.: (a) Conductance trace "3" from Fig. 7.10 (b) as a function of the charge carrier density n . This trace is obtained by sweeping the top and back gate voltages simultaneously along a direction perpendicular to the major line as discussed in Fig. 7.8 (a). Here, V_{tg} is varied such that $V_{bg} = 0.143 \times V_{tg} + 2.722$. (b) Differential conductance (offset by the mean $\langle dG/dn \rangle$) of the trace in (a) as a function of the magnetic field B . The green curve marks the region of transition between the size quantization regime at lower B fields and quantum Hall regime at higher B fields for a QPC with a width of 380 nm, in accordance with eq.8.2. Landau levels with the index $m = -1$ to -4 are visible at B field above the green curve. (c) Close-up of the trace in (b) in the low magnetic field region. (d,e,f) Same as (a,b,c) for the conductance trace "4" in Fig. 7.10 (b). The conductance trace "4" in (d) is obtained by sweeping the top and back gate voltages simultaneously along a direction parallel to the minor line as discussed in Fig. 7.8 (a). Here, V_{tg} is varied such that $V_{bg} = 3.2 - 1.4 \times (V_{tg} + 1.32)$.

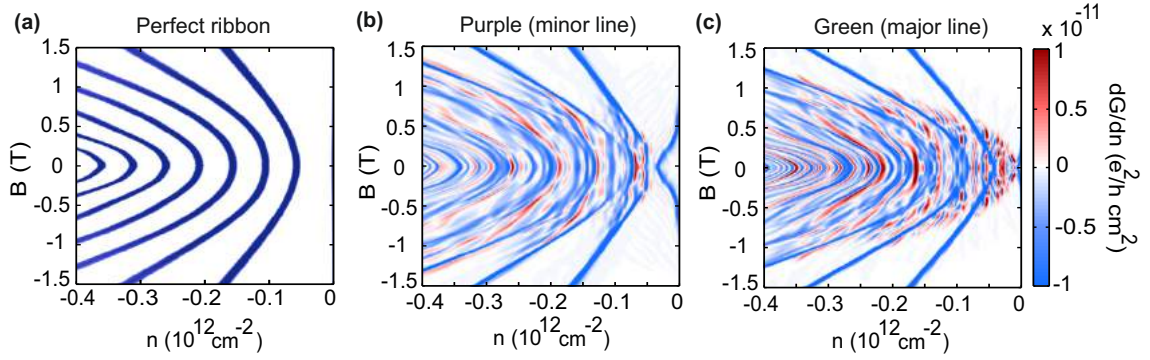


Figure 8.3.: (a) Theoretical differential conductance in a perfect graphene nanoribbon with no edge disorder. In this ideal system, spin and valley degrees of freedom remain degenerate as the holes evolve from size quantization to Landau quantization. (b) Theoretical differential conductance in a ribbon with an edge roughness of 4 \AA as shown in Fig. 7.13 (a). The conductance trace at zero B -field is the purple trace shown in Fig. 7.13 (c). Here, both the Fermi energy of the ribbon E and the side gate potential U are varied simultaneously. This is equivalent to sweeping the back and the top gate voltages simultaneously in a direction parallel to the minor lines as shown in Fig. 7.13 (b). (c) Same as (b) but for the green trace shown in Fig. 7.13 (c). Here, the side gate potential is fixed and only the Fermi energy is varied. This is comparable to sweeping the gates in a direction perpendicular to the major line. Compared to (c), (b) shows a cleaner pattern implying lesser influence of edge disorder in (b).

8.3. Theoretical simulations - Evolution of conductance kinks with magnetic field

8.3.1. Simulations of magnetic field measurements using the nanoribbon model

We now look into the evolution of the two theoretical conductance traces shown in Fig. 7.13 (c) in the presence of a perpendicular magnetic field. It is useful, however, to first consider the ideal case of a translationally invariant ribbon geometry (I) discussed in section 7.6 without edge disorder. In this case, in Fig. 8.3 (a), conductance steps evolve adiabatically from the size-quantization at low magnetic field to the Landau levels in quantum Hall regime, as expected. In the case of the purple trace in Fig. 7.13 (c) which is obtained by sweeping the gates parallel to the minor slope, we see that edge roughness distorts the ideal quantization at low B field although the underlying pattern of the conductance steps remains is still quite clearly visible (see Fig. 8.3 (b)). The number of additional features in the zero magnetic field increases further for the green trace in Fig. 7.13 (c) as shown in Fig. 8.3 (c). As explained earlier, green trace is similar to the case of sweeping the back and top gates in a direction perpendicular to the major line. Important to note is that not all the interferences due to the localized edge states can be avoided with the side gate, since the states show different degrees of localization. Thus, a single additional gate cleans the transmission spectrum only partially.

8.3.2. Analysis of different Eigen states in the graphene nanoribbon

In this section, we investigate the factors responsible for the magnetic field interference patterns discussed in the previous sub-section. To gain insight into this, we consider quasi-bound states of our scattering geometry, i.e. the Eigen states (and complex Eigen energies) of the Hamiltonian of the graphene ribbon. The imaginary part Γ of the Eigen energies $E = \varepsilon + i\Gamma$ describes the coupling of the Eigen states to the leads. This Γ determines the width of each resonance in the transmission spectrum such as in Fig. 8.1 and Fig. 8.2. States with vanishing Γ show up as sharp peaks in the transmission while the others mainly contribute to a broad background signal [232]. We show these Eigenstates in the upper half of Fig. 8.4 (a) as green and yellow lines such that green (yellow) corresponds to the states with minimum (maximum) strength of coupling to the leads Γ . Features in the transmission spectrum often arise from some Eigen state with weak coupling to the leads - see the effect of green lines in the lower half of Fig. 8.4 (a) which is a close-up of Fig. 8.1 (c).

We can group the Eigen states into three rough categories according to their dependence on B and their imaginary part Γ [Fig. (8.4)]:

- (i) Eigenstates with weak coupling to the leads (green lines, $\Gamma \ll 1$) with their Eigen energies almost independent of the magnetic field. They show strong localization near the edge of the ribbon as seen in Fig. 8.4 (b) and (c).
- (ii) Eigen states with weak coupling to the leads which shift to larger i.e. more negative n with increasing magnetic field. These are the extended Eigen states of the system with rather weak coupling to the leads as seen in Fig. 8.4 (d).
- (iii) Eigen states with strong coupling to the leads (yellow lines, $\Gamma \gg 1$) which move towards lower or less negative n with increasing field. These are states of the semi-infinite lead which extend slightly into the system as shown in Fig. 8.4 (e). They evolve towards the zeroth Landau level in this energy range.

The evolution in magnetic field of these Eigen states and interference between them results in the complex transmission pattern. Features which do not depend on B typically arise from strongly localized states - due to their small area, their Eigen energies are (almost) independent of the magnetic field [233]. A transmission feature which can be attributed to such a single Eigen state (i) is the conductance peak at $n = -0.076 \times 10^{12} \text{cm}^{-2}$ in the lower half of Fig. 8.4 (a). Its largest probability amplitude is near the edge of the ribbon and Eigen state in Fig. 8.4 (b) and scattering state in Fig. 8.4 (c) at this energy are very similar.

On the other hand, the interaction of two different Eigen states is responsible for the peak that develops at $B \approx -76 \text{ mT}$ at $n \approx -0.105 \times 10^{12} \text{cm}^{-2}$, and is marked by a + in Fig. 8.4 (a). At this point, two localized states (in green, in the upper half of the figure) approach each other starting from $B = 0 \text{ T}$ with increasing magnetic field. When their Eigen energies are at the same value, the (hole) transmission increases (appears as blue in the transmission spectrum in the lower half as the current tunnels sequentially over both Eigenstates). This, however, is one of the few very obvious interference effects, while there are apparently many more of them in the experiment.

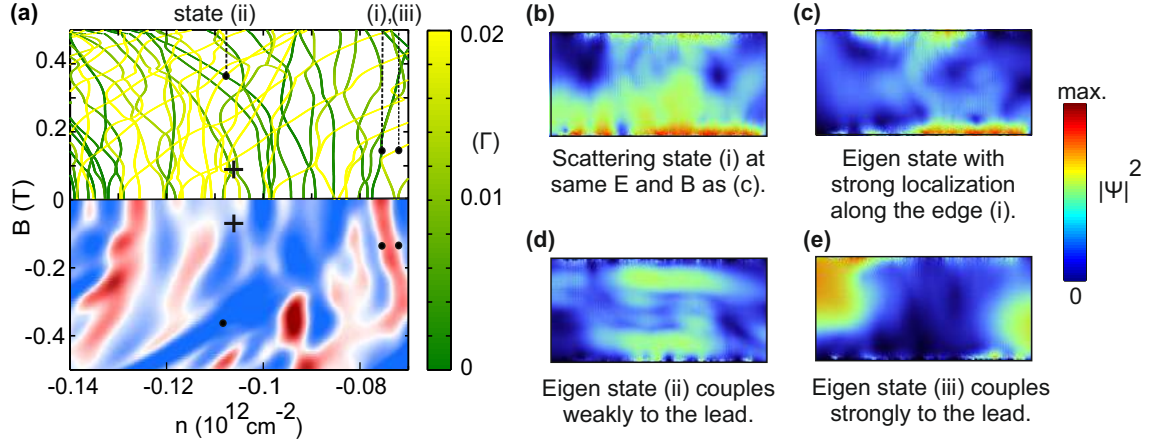


Figure 8.4.: (a) Lower half of the figure is a close - up of the Fig. 8.1 (c). Therefore, this is the map of the differential conductance dG/dn as a function of the charge carrier density n and the perpendicular magnetic field B . The corresponding conductance trace $G(n)$ at $B = 0$ T is the conductance trace "1". Upper half represents the Eigen states of the open system color coded according to their strength of coupling to the leads (Γ). Thus, green lines represent the states with the weakest coupling to the leads while yellow lines represent the states with the strongest coupling. The + symbol marks the resonance formed by the intersection of two green Eigen states. (b-e): Probability of the wave function Ψ at the • in (a). (b,c) Scattering state and Eigen state at the position marked (i), i.e. at $B = 0.15$ T, $n = -0.076 \times 10^{12} \text{ cm}^{-2}$ in the upper of (a). Both of them show a strong localization along the edge. They also show only a weak dependence on B (dark green line denoted as state (i) in the upper half of (a) or the corresponding red-blue feature in the lower half of (a)). (d) Eigen state at position (ii) i.e. at $B = 0.36$ T, $n = -0.11 \times 10^{11} \text{ cm}^{-2}$ in (a). This Eigen state (green line at state (ii) in the upper half in (a)) follows a conductance step (blue features in the lower half) and moves towards more negative n values with increasing B . (e) Eigen state at position (iii) i.e. at $B = 0.15$ T, $n = -0.072 \times 10^{11} \text{ cm}^{-2}$, denoted by a yellow line in the upper half in (a). In this case, the yellow line moves towards less negative n values with increasing B , thus, its energy decreases with increasing B .

8.3.3. Rescaling the theoretical simulations to fit the experimental data

A. Convert the energy axis in simulation to the charge carrier density axis in experimental data

All the theoretical simulations described until now are originally calculated as a function of the energy of the conducting quasiparticles E . Before we can compare this data to the experiment, we have to rescale the data to the correct n and B axis. As discussed in section 7.4.3, the charge carrier density including the contribution of trap states is given by eq. 3.2, $n = \frac{k_F^2}{\pi} + n_T(k_F)$. Using the knowledge that n_T is estimated using a Gaussian, the charge carrier density can be rewritten in terms of energy as

$$n = \int_0^{E_F} \left(a e^{-E^2/2\sigma^2} + bE \right) dE, \quad (8.3)$$

where a , b and σ are fit parameters. Here, a determines the amount of trap states and σ , their distribution around the charge neutrality point. The overall scaling from the calculated energy to the measured charge carrier density is given by the parameter b .

With these parameters, we can compare the conductance kinks in theory with experiment. This procedure is as follows: First, we fit b to the level spacing for large charge carrier density n in the experiment. This scaling accounts for the difference in width and edge disorder strength in experiment and theory. Automatically, the zero field conductance traces agree well. Then, we adjust the trap state density parameters a, σ to recover the experimental conductance step spacing at low n . The parameter a controls how much the spacing of the lower levels is increased and σ determines how many of the lowest levels are affected. Since a and σ also somewhat affect the higher n region, we re-adjust the parameter b . With this, we attain excellent agreement of all spacings at $B = 0$ T. This is shown as the overlay (black curves) in Fig. 8.7 (b).

B. Readjust the magnetic field axis in simulation to fit the experimental data

After we have adjusted the n -axis, we also rescale the B axis to account for the smaller size of the ribbon in theory (20 nm) as compared to the experiment (380 nm). Here, there are two different options: The energy E_m of the Landau level with index m scales according to eq. 7.5 i.e. $E_m \propto \sqrt{B}$. This means that once the energy axis is fixed, the B axis is also fixed. However, rescaling the B axis to fulfill eq. 7.5, $E_m(B) = \text{sgn}(m)v_F\sqrt{\hbar|e|2|m|B}$ does not correctly account for the transition from size to Landau quantization. This is because Landau quantization sets in once the Landau wave function is smaller than the constriction width according to eq. 8.1. To correctly model the low B regime, one should, thus, rescale the B -axis according to

$$E = v_F \hbar k = ev_F w B \propto B. \quad (8.4)$$

Now, the energy spacing of the Landau levels (LL) given by eq. 7.5) for a given value of B would be much too narrow. It is impossible to fit both eq. 7.5 and eq. 8.4 with a single linear rescaling of the B axis. Rescaling the n -axis in the low field region and the high field region separately solves this problem. For fitting the high field region, we first arbitrarily choose some fixed "high" B field value. We take the value of B where it equals two times the field of the Landau level onset. The onset happens when $2r_C < w$ (see eq. 8.1). Since the experimental Landau fan shows straight lines in the n - B plane at this B field, a minimal $n \propto E_F^2$ model is sufficient and we account for only the trap states by an appropriate offset.

We interpolate smoothly between the two regimes by making b in eq. 8.3] dependent on B : We define a function $\alpha(B)$ as a product of Fermi functions $\tilde{F}(B, \mu, T) = 1 - 1/(\exp((B - \mu)/T) + 1)$

$$\alpha(B) = \tilde{F}(B, 0.52, 0.35) \tilde{F}(B, 0.26, 0.09) \tilde{F}(B, 0.05, 0.02). \quad (8.5)$$

which smoothly decreases from 1 at $B = 0$ T to 0 as B increases. Both functional form and values (B, μ, T) are an arbitrary choice. We use α to smoothly rescale n for changing B such that

$$n = \alpha(B) \int_0^{E_F} \left(a e^{-E^2/2\sigma^2} + b_{B=0} E \right) dE, \quad (8.6)$$

$$+ (1 - \alpha(B)) \left(\int_0^{E_F} b_{B=LL} E dE + \Delta \right). \quad (8.7)$$

C. Summary of the rescaling procedure

The rescaling procedure is summarized in Fig. 8.5. Differential conductance of a pristine graphene nanoribbon without edge roughness as a function of energy E_F and magnetic field B as shown in Fig. 8.5 (a). The Landau fan shows no straight lines since $E_m(B) \propto \sqrt{B}$ according to eq. 7.5. A linear density of states with

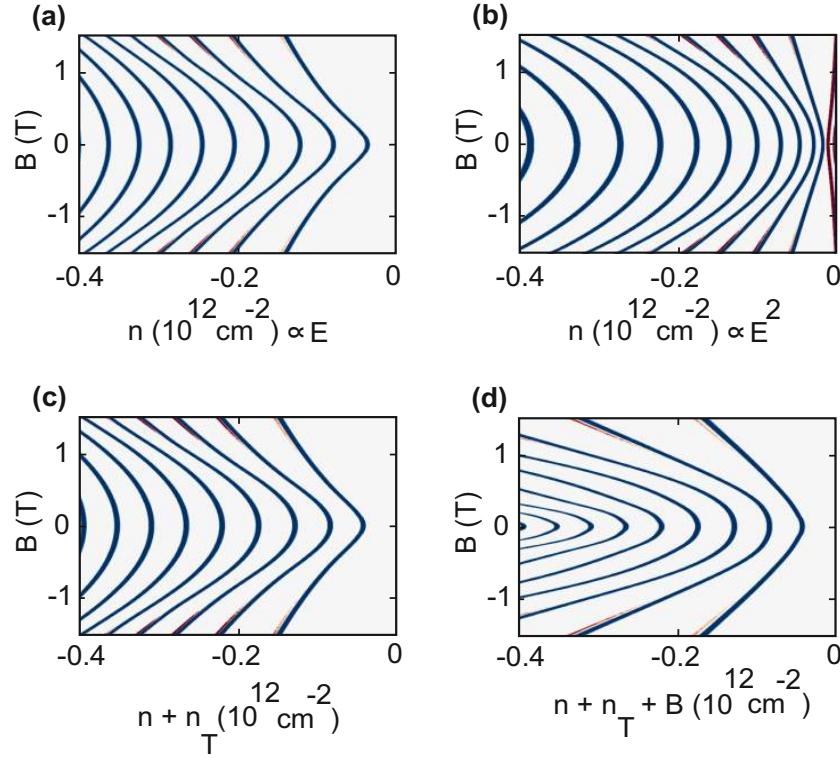


Figure 8.5.: Pristine ribbon as in Fig. 8.3 (a) with different rescalings. (a) The x -axis is a function of the Fermi energy E_F (instead of the charge carrier density n). (b) assuming $n \propto E_F^2$. (c) trap states included. (d) interpolation between fits for both $B = 0$ T and high field regime.

$n \propto E_F^2$ produces the usual linear Landau Fan in Fig. 8.5 (b) with $n_m \propto B$. However, quantization steps at low n are too narrowly spaced compared to the experiment. Trap states fix the spacing of quantization energies at low n in Fig. 8.5 (c), but distort the Landau fan since the additional density at low n results in an almost linear $n \approx E_F$ in this regime. Different scalings in the high and low B -field regime in Fig. 8.5 (d) resolve this last issue and agree best with the experiment.

8.3.4. Simulations of magnetic field measurements using the constriction model

The simple ribbon ($w \approx 20$ nm) model (I) agrees qualitatively with the experimental Landau level measurements. The larger size of the experimental structure ($w \approx 380$ nm) implies many more Eigen states, which also interfere more strongly in the transport measurements due to their smaller energy spacing. Next, the constriction geometry includes broad leads that reach the Landau regime earlier than the center of the constriction, which is not included in our simple ribbon model (I). Furthermore, there are certain key features in the experimental data at high energies that are absent in the simulation results - the set of diagonal lines quickly evolving towards higher (absolute) or more negative charge carrier densities with increasing magnetic field (see Fig. 8.7 (g) - (i)). We, therefore, set up a more accurate model (II) of the experimental geometry (see Fig. 8.6), including four contact points, a constriction with a width of the order of 250 nm between wider graphene regions of $1 \mu\text{m}$ in width. These model dimensions substantially increase the numerical cost, yet provide much better agreement with the experiment as we shall in the next section. We

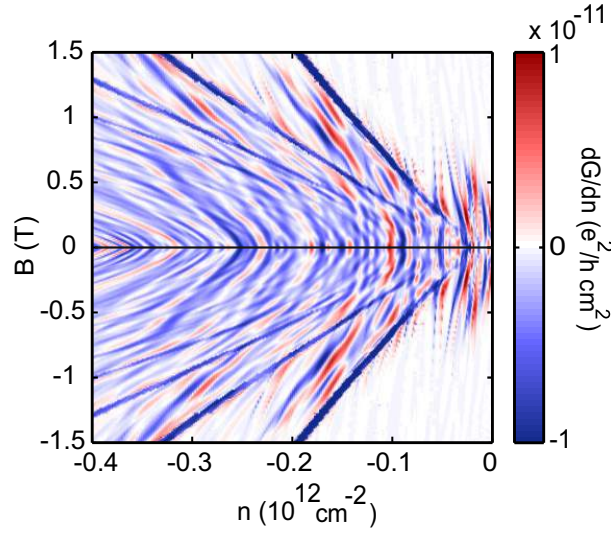


Figure 8.6.: (a) Theoretical derivative of the conductance through a nanoconstriction as a function of the charge carrier density n and the magnetic field B measured in a four-terminal configuration. The width of the constriction is 250 nm constriction while that of the leads is 1 μm . We include a random edge roughness on the order of 5 nm in this geometry.

observe more complicated, richer interference patterns which are one step closer to the experiment. We conclude that bulk and localized edge states are the basic ingredients of the signatures in the experiment.

8.4. Comparison between experiment and theory

Experiment and theory not only agree quantitatively but also share many similar features in differential conductance on the B - n plane when we compare Fig. 8.7 (b) (experimental result from Fig. 8.1 (a)) with Fig. 8.7 (a) (Simple ribbon model (I) from Fig. 8.3 (c)) and Fig. 8.7 (c) (Constriction model from Fig. 8.6).

Firstly, the overall structure of the evolution of conductance kinks into Landau levels fits well between theory and experiment. This pattern of evolution in theoretical ribbon model (I) (with no disorder in Fig. 8.3 (a)) is shown on top of the experimental data (black curves) in Fig. 8.7 (b). There is an excellent agreement in the position of Landau levels at higher B field between experiment and the theory.

Further, at lower B field, both the number of kinks and their spacings in the charge carrier density range under consideration agree. In the case of the constriction model (II) in Fig. 8.7 (c) as well, the zero field quantization steps are found by an independent calculation without disorder in the region of the QPC. This independent calculation results in a slight uncertainty in the absolute position, but once again, the number, spacing and the evolution of conductance steps agree with experiment (not shown).

Next, in the low n region around $B = 0$ T, vertical features (marked by the dashed lines) appear due to localized states in the close-ups in Fig. 8.7 (d) - (f). These features vary little with B in the ribbon model (I) while additional oscillations in amplitude emerge for the constriction model (II) and the experiment. For example, observe the 'D'-like shape in the experiment in Fig. 8.7 (e) which is recognizable as a combination of a conductance step (● at $4 e^2/h$) / Bloch state that depends strongly on B (curved dashed line) and a localized state (straight dashed line) with weak B dependence. Here, the 'D' is broken into several

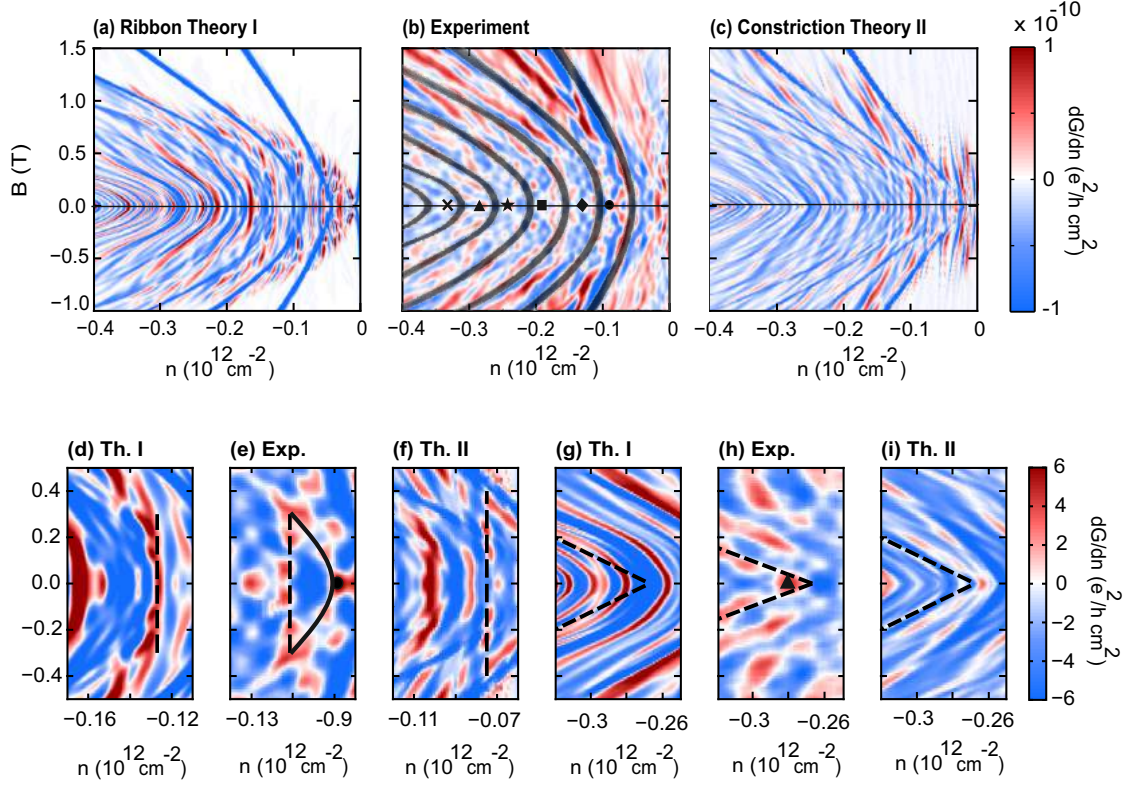


Figure 8.7.: Comparison of features in differential conductance between experiment shown in **(b)** (from Fig. 8.1 (b)) and theoretical ribbon model (I) shown in **(a)** (from Fig. 8.3 (c)) and theoretical constriction theory model (II) shown in **(c)** (from Fig. 8.6). All these measurements take into account the edge disorder. However, the black overlay on the experiment in **(b)** is the evolution of conductance kinks in an ideal ribbon without any edge roughness based on the ribbon theory (I) in Fig. 8.3 (a). Notice how the evolution of states from size quantization at $B = 0$ T to quantum Hall level quantization at higher B matches quite well between the experiment in **(b)** and the overlay. The lower panels feature close-ups around the low n and high n regime in the upper panels. In the low n regime in **(d,e,f)**, straight line features (dashed lines) that are independent of B dominate the interference patterns in both theory and experiment. While in the high n regime in **(g,h,i)**, 'V'-shaped patterns emerge. Here, size quantization features evolve rapidly into the respective Landau levels.

dots probably due to interferences with other states. Only when all of involved Eigen states are brought energetically close to each other by the magnetic field, do they form a resonance as discussed in section 8.3.2. We also observe such broken features in the constriction model in Fig. 8.7 (f) that is closer to the experimental dimensions while these are rather straight lines in the nanoribbon model in Fig. 8.7 (e).

Here, we must note that since the edge disorder determines the finer details of the interference pattern, we do not expect to see the identical features at the same value of n in both theory and experiment. However, the type and the quality of features observed matches quite well.

At higher n , 'V'-like shapes dominate the differential conductance as seen in Fig. 8.7 (g) - (i). Densely spaced quantization steps at $B = 0$ T evolve into much larger spaced Landau Levels at higher values of B . For the smaller ribbon model (I) in Fig. 8.7 (g), the high charge carrier density region is dominated by parabolic features, which also show the evolution from size to Landau quantization. In this case, the parabolicity is caused by the rescaling procedure we use to match the experiment (see section 8.3.3). On the other hand, for the constriction model (II) in Fig. 8.7 (i), quantization steps at zero field become more closely spaced and rescaling is much weaker. For this model we observe 'V'-like shapes similar to those seen in experiment in Fig. 8.7 (h).

Using the above knowledge on the factors responsible for the observation of different features in differential conductance, we can now also explain the differences with regard to the conductance kink \blacklozenge at $6 e^2/h$ between the "major" and "minor" voltage sweep directions shown in Fig. 8.2 (c) and (f). On the left side, we observe a straight vertical line. This gets converted to a more curved line which is how one expects a size quantization feature to evolve into a Landau level. This is once again an indicator of the fact that the system in Fig. 8.2 (c) experiences a stronger contribution of localized states due to the fact that the gates are swept along a direction perpendicular to the major line.

8.4.1. Conclusion

We have measured the conductance through a graphene nanoconstriction with a back and top gate in the presence of a perpendicular magnetic field.

In the high field regime, we recover identical Landau level quantization for both "major" and "minor" directions of gate voltage sweep. However, at low B -field, we see several features that evolve differently with the magnetic field. Some of these are typical features that arise due to Bloch states and emerge into the Landau levels. While other features remain nearly unaffected by the magnetic field. These features are located mostly around the CNP and are a result of localized edge states.

Such results are also reproduced theoretically in both a ribbon and a constriction geometry with very small edge roughness as compared to the experiment. This shows that even a very small amount of edge disorder is enough to disrupt the size confinement effects in nanostructures. The behavior of different Eigen states in the ribbon/constriction is used to explain the different features observed in the magnetic field dependent conductance measurements. For example, the minor lines are a result of Eigen states dominating the edges and remain unaffected by the magnetic field.

Thus, using both theoretical and experimental magnetic field measurements, we were able to explain the features evolving with different slopes in the 2D conductance maps seen in the previous chapter (see Fig. 7.8). By combining the usage of top gate with external magnetic field, we were able to disentangle the size quantization features due to extended states in the bulk from the localized states due to edge disorder.

It is further confirmed by the simulations that it is possible to manipulate the influence of edge disorder on conductance by changing the direction of gate voltage sweep (see Fig. 8.3 (b) and (c)).

9. Spin states in gate defined bilayer graphene quantum point contacts

This chapter has been published in parts in:

Observation of the Spin-Orbit Gap in Bilayer Graphene by One-Dimensional Ballistic Transport

L. Banszerus , B. Frohn, T. Fabian, S. Somanchi, Epping, M. Müller, D. Neumaier, K. Watanabe, T. Taniguchi, F. Libisch , B. Beschoten , F. Hassler, and C. Stampfer, Phys. Rev. Lett. 124, 177701, 2020.

Contributions to this chapter:

The fabrication of the sample discussed in the chapter was done by L. Banszerus. The measurements were performed by L. Banszerus and B. Frohn from RWTH Aachen University. All the data presented here have been analyzed by S. Somanchi.

9.1. Introduction

In the previous two chapters, we have discussed the confinement of charge carriers in QPCs which have been fabricated by top-down lithography and reactive ion etching of single layer graphene. Although features like size quantization depicting the high quality of samples have been well established in such devices, observation and study of charge and spin states and their excitation has been difficult to achieve due to the presence of edge disorder. This may be overcome by using bilayer graphene to open a band-gap by using a perpendicular electric field as mentioned already in chapter 4. In this chapter, we use this property of bilayer graphene which allows us to confine charge carriers in a narrow channel using a combination of back gate and split gates. We use additional finger gates and observe the formation of sub-bands in such a gate defined bilayer graphene QPC. Application of a parallel magnetic field results in spin splitting of these sub-bands. BLG is also of particular interest due to its weak intrinsic spin-orbit (SO) interaction [234]. SO interaction also plays an key role in understanding the evolution of the band structure in the presence of an external electric field. Theoretical studies have shown that BLG has an intrinsic SO coupling of around 24 μeV at K points for the low energy valence and conduction bands which are closest to the Fermi level [235, 236]. Another study projected the gap induced by SO coupling at the K point to be on the order of 10^{-3} meV [237]. Kane and Mele first predicted quantum spin Hall effect in graphene due to the spin-orbit interaction [238]. According to their model, SO interaction in graphene is attributed to two reasons - one is the intrinsic SO coupling and the second is extrinsic or Rashbha SO coupling. Though the intrinsic SO coupling is very weak for carbon, typically a few μV or even smaller [239–241], it can be enhanced by using heavy metal adatoms [242] or with proximity effect by using a suitable insulating substrate such as

transition metal dichalcogenides [243–245] or hBN [246, 247]. SO coupling is also crucial in spintronics related experiments such spin life time measurements [248, 249].

Although conventional charge transport in both SLG and BLG is well studied experimentally, spin - orbit interaction coupled electronic transport has not yet been fully explored. Recently, resonance microwave measurements have been used to extract a SO gap of around 40 μeV in the case of single layer graphene [250]. Investigation of such small energy scales becomes feasible only when the energy scales in the system are comparable. In the current device with a sub-band spacing in the range of 0.3 - 0.6 meV, we observe the presence of a SO gap at zero magnetic field and spin split sub-band crossings at a higher magnetic field. The SO gap is manifested as a step at $2 e^2/h$ due to the splitting of the first sub-band at zero magnetic field and may be interpreted as substrate induced proximity enhancement of the SO coupling of the Kane - Mele type [238]. This device also allows to explore electron - electron interactions at higher magnetic field manifesting in the so-called 0.7 analog feature, similar to the 0.7 anomaly which was earlier observed not only in semiconductor heterostructures such GaAs 2DEGs [251–254] but also in suspended SLG QPCs [40].

9.2. Measurement configuration

The set-up of the dilution refrigerator used for measuring this device has already been discussed in section 7.2. The measurements were made at a temperature of 30 mK. Similarly, all the details about the fabrication and geometry of the QPC discussed in this chapter have been described in section 6.2.

The sample consists of a BLG flake encapsulated in hBN placed on top of a graphite flake (thickness ≈ 10 nm) resting on a $\text{Si}^{++}/\text{SiO}_2$ substrate. The graphite flake acts as the back gate (bg) to which a voltage V_{bg} is applied. A symmetric DC bias voltage V_{DC} superimposed by an AC voltage $V_{AC} = 300 \mu\text{V}_{\text{peak-to-peak}}$ across the entire BLG channel together constitute the bias voltage V_b between the source and the drain contacts (see the schematic of the measurement set-up in Fig. 9.1). Depending upon the resistance of the channel, a current I_{sd} is measured. Using the voltage across the channel V_{sd} , the differential conductance $G = dI/dV = I_{sd}/V_{sd}$ in a four probe configuration can be measured using standard lock-in techniques. The two split gates (sg) are 5 μm wide, are short to one another and a split gate voltage V_{sg} is applied to them. This results in a perpendicular displacement field such that the region underneath the side gates is depleted of charge carriers, thereby forming a 250 nm (separation between the two split gates) wide channel between the source and the drain. However, sg and bg alone are not enough to observe quantized conductance. For this purpose, three finger gates fg1 - fg3, each 200 nm wide, are designed on top of the sg across the BLG channel. The distance between two adjacent finger gates is approximately 60 nm.

The voltage applied to each of these finger gates, $V_{fg1} - V_{fg3}$, while keeping V_{bg} and V_{sg} constant (see section 9.4 for more details), can be used to locally tune the strength of confinement i.e. the Fermi energy and adjust the number of modes in a particular region of the channel and if necessary even pinch off the transport underneath a particular gate entirely. Previously, in the same device, it was possible to achieve different configurations of quantum dots - single, double, triple by varying the voltages applied to the three finger gates [200]. This shows the importance of the finger gates in the confinement of charge carriers. In this chapter, we use the side and the finger gates to form a quantum point contact.

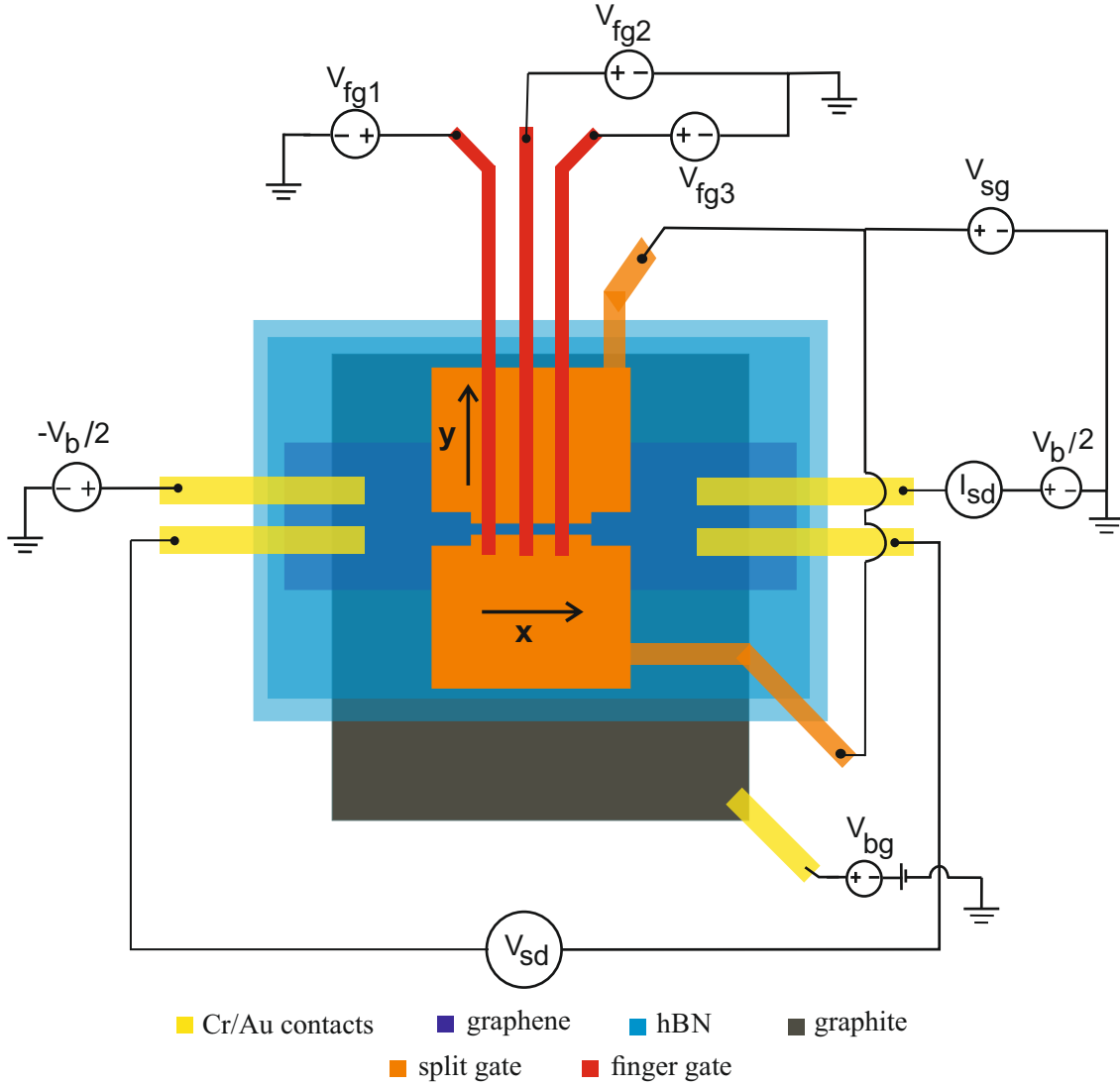


Figure 9.1.: Schematic: Top view of the sample (also see Fig. 5.7) and the measurement set-up

9.3. Formation of a 1D channel

In this section, we discuss the formation of a QPC in this device by applying a voltage to the split gates such that the region underneath the SGs is depleted leading to the formation of a narrow channel or a QPC between the source and the drain contacts. In Fig. 9.2 (a), a symmetric DC bias of $300 \mu\text{V}$ is applied between the source and drain and the two terminal resistance is measured as a function of the side gate voltage V_{sg} and the back gate voltage V_{bg} while all the other finger gates are grounded. The white dashed line represents the CNP of the each individual conductance trace in back gate voltage $G(V_{bg})$ at a fixed value of V_{sg} . The slope of this line is the relative lever arm $\alpha_{bg}/\alpha_{sg} \approx 0.8$. As explained in section 7.4.2, one can also calculate the gate lever arms using the thickness of the gate dielectrics i.e. the thickness of the bottom t_{bottom} and the top hBN t_{top} of the hBN-graphene-hBN sandwich used for making the device (see section 6.2). In this case, since the gate dielectric (hBN) is the same for both the back and the split gates, the relative lever arm may be calculated using the ratio $\alpha_{bg}/\alpha_{sg} = t_{top}/t_{bottom} = 20\text{nm}/30\text{nm} \approx 0.7$. This

agrees quite well with the experimental value obtained above.

The application of the voltages V_{bg} and V_{sg} together results in an increase of resistance as we go towards higher gate voltages away from zero along the diagonal dashed white line. The larger the resistance, the larger the gate induced band gap opened in the bilayer graphene region under the side gates. Any point along this diagonal line corresponds to a displacement field arising due to voltage applied to both the gates. The displacement field due to the back (split) gate is given by $D_{bg(sg)} = +(-)\epsilon_{bg(sg)}(V_{bg(sg)} - V_{bg(sg)}^0)/t_{bg(sg)}$ where $\epsilon_{bg(sg)}$ is the dielectric constant of the back (split) gate oxide which in this case is hBN with a value of 4. $V_{bg(sg)}^0$ is the gate voltage which leads to an initial carrier doping. This is the CNP i.e. the point of intersection of the black dashed lines where $V_{bg}^0 = V_{sg}^0 = 0$ V. The average of the two $D = (D_{bg} + D_{sg})/2$ gives the net displacement field that is responsible for opening the band gap. Therefore, in the present device, there is no net charge carrier doping at zero displacement field.

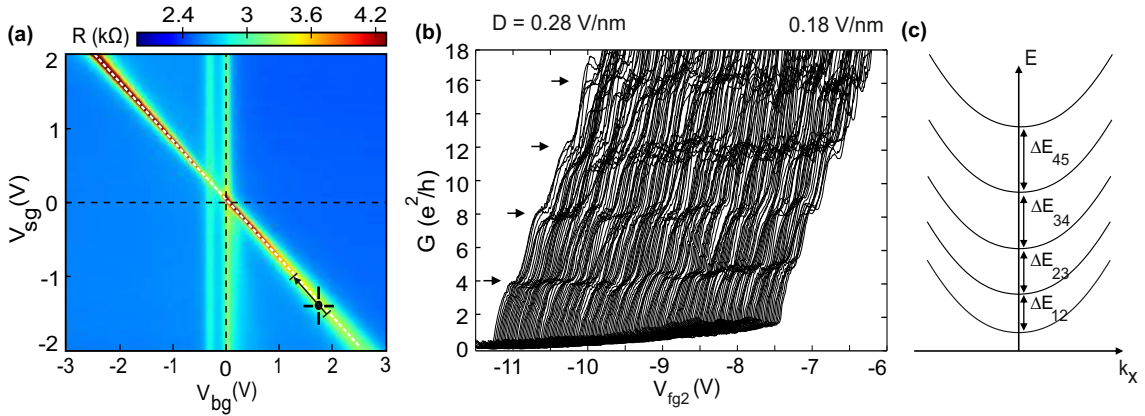


Figure 9.2.: (a) Measurement of the two terminal resistance R as a function of V_{bg} and V_{sg} at $V_b = 300 \mu\text{V}$ while all the fingers gates fg1-fg3 are set to ground. Figure adapted from Ref. [200]. (b) Four terminal conductance G through the device as a function of V_{fg2} while the displacement field varies along the direction of the black arrow in (a). The other two finger gates are set at a constant voltage of -4 V. (c) Schematic representation of the formation of various sub-bands as indicated by the arrows in (b). The figure shows the dispersion relation of bilayer graphene. ΔE_{ij} is the difference in energy between the i^{th} and the j^{th} sub-bands.

9.4. Formation of sub-bands in the QPC: Quantized conductance

Fig. 9.2 (b) shows the four terminal conductance as a function of the finger gate voltage V_{fg2} for different values of displacement field ranging from 0.28 to 0.18 V/nm i.e. for different combinations of V_{sg} ($= -1.5$ to -1 V) and V_{bg} ($= -1.256 \times V_{sg}$) along the direction of the black arrow in Fig. 9.2 (a). The other two finger gates are fixed at a constant voltage of -4 V. For calculating the four terminal conductance, a series resistance of 760Ω is subtracted from the actual data. This is to account for the resistance of the regions in the $5 \mu\text{m}$ long channel which are not directly tuned by the finger gate fg2. Note that the value of this

resistance also depends on the value of the side gate voltage besides V_{fg1} and V_{fg3} . Therefore, it can vary slightly by around 100 - 200 Ω for different measurements and is adjusted accordingly.

Clear quantized conductance steps at values of 4, 8, 12, 16 e^2/h as expected for ideal bilayer graphene are observed (see black arrows). This indicates four-fold degeneracy and a transmission of unity through the QPC. Similar to the results obtained in single layer graphene as discussed in section 7.4.1 and 7.5.1, these steps in conductance indicate the confinement of charge carriers in the QPC resulting from the formation of sub-bands in bilayer graphene as shown in the schematic in Fig. 9.2 (c). With a decrease in displacement field as we move from the left to the right in Fig. 9.2 (b), we observe an increase in the background or residual conductance. This is a result of the current leaking from the channel to the region underneath the side gates as the finger gate voltage increases. Nevertheless, the height of the steps still remains nearly the same at 4 e^2/h .

9.5. Spin splitting of sub-bands

Next, we investigate the evolution of the conductance steps at a fixed displacement field as a function of an external parallel magnetic field $B_{||}$ as shown in Fig. 9.3 (a). The conductance trace is measured at a displacement field of 0.26 V/nm (see black dot in Fig. 9.2 (a) where $V_{bg} = 1.76$ V, $V_{sg} = -1.397$ V) and its evolution from zero to up to a field of 6 T is shown. At 0 T, once again, we see conductance steps at a height of 4 e^2/h . At higher magnetic fields, intermediate steps at 2, 6, 10, 14... e^2/h become visible (see the black arrows) indicating a spin degeneracy lifting of the sub-bands.

9.6. Extraction of sub-band spacing

The appearance of intermediate plateaus is better understood using the the transconductance dG/dV_{fg2} plot as a function of the parallel magnetic field and the finger gate voltage as shown in Fig. 9.3 (b). As the magnetic field increases, each sub-band (indicated by the ■ symbol) splits into two branches- one with a positive and the other with a negative slope (corresponding to the solid and dashed black lines emerging out of each ■) indicating the spin-up and spin-down sub-bands respectively.

The evolution of the sub-bands with the magnetic field is elucidated further in the schematic of Fig. 9.3 (c). At $B_{||} = 0$ T, the sub-bands are spin and valley degenerate and at a finite magnetic field split into spin-up and spin-down states. Consider the first and the second sub-band with energies E_1 and E_2 respectively. As the magnetic field increases, at a certain point, the spin-up branch of the first sub-band $1\uparrow$ crosses the spin down branch of the second sub-band $2\downarrow$. At this point (≈ 3.1 T, see the black dot "•" marked ΔE_{12} in Fig. 9.3 (b) and (c)), the Zeeman energy of sub-band splitting is equal to the sub-band spacing ΔE_{12} . Therefore, we can use $E_{Zeeman} = g\mu_B B_{||} = \Delta E_{12}$ at this crossing point to calculate the sub-band spacing ($B_{||} = 3.1$ T and assuming $g = 2$ for BLG). Similarly, using the other crossing points ($\Delta E_{23}, \Delta E_{34}$ etc.), the spacing between the next consecutive sub-bands can also be extracted as shown in Table 9.1. Other higher order crossing points such as the black dots at ΔE_{13} and ΔE_{24} are also visible in Fig. 9.3 (b). These appear as a result of the crossover of the spin-up state of one sub-band $n\uparrow$ with the spin-down state of the next consecutive sub-band $n+1\downarrow$. For example, ΔE_{13} is the crossing point of the spin-up state of the first sub-band $1\uparrow$ with energy E_1 and spin-down state of the third sub-band $3\downarrow$ with energy E_3 (see Fig. 9.3 (c)).

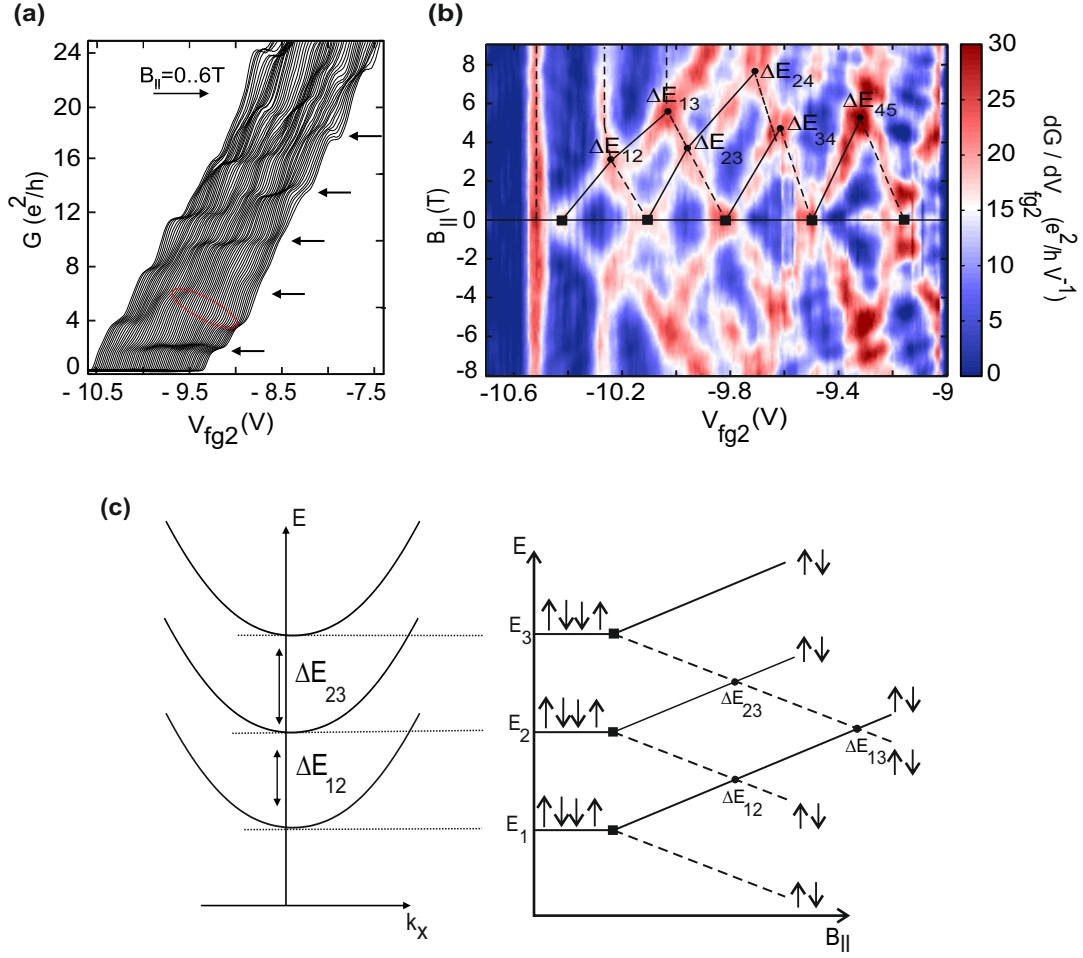


Figure 9.3.: (a) Conductance G as a function of V_{fg2} measured at \bullet in Fig. 9.2 (a). The parallel magnetic field $B_{||}$ is varied from 0 to 6 T. (b) Transconductance dG/dV_{fg2} as a function of V_{fg2} and $B_{||}$. The black squares '■' denote the sub-bands formed at zero magnetic field (also shown in (c)). As the magnetic field increases, each sub-band splits into a spin-up and spin-down sub-band (see the solid (spin-up) and dashed (spin-down) black lines emerging out of each ■). At the crossing points indicated by the black dots '•', Zeeman energy of spin splitting is equal to the sub-band spacing. (c) Schematic representation of the Zeeman splitting of sub-bands in the presence of a parallel magnetic field. Each sub-band splits into a spin-up and a spin-down sub-band. At the crossing points, the spin-up (down) of one sub-band crosses with the spin-down (up) of the next (previous) sub-band.

Once again, we use the values of magnetic field at which these crossing points occur in Fig. 9.3 (b) and compare them to the expected values in Table 9.2.

The exact method in which the values of the gate voltage and the magnetic field at these crossing points are extracted is explained in Appendix 9.7.

Note that in Fig. 9.3 (b), there are features such as the vertical black dashed lines which seem to be independent of magnetic field. For example, observe the spin-down state of the first sub-band. The Fermi level is pinned at a value of ≈ -10.5 V due to quantum capacitance effects. As we go to higher values of magnetic field beyond the crossing point at ΔE_{12} , the $2\downarrow$ level also appears as a vertical straight line since it must travel parallel to the $1\downarrow$ (also shown in the sub-plot (c)).

Table 9.1.: Sub-band spacing extracted from the crossing points in Fig. 9.3 (b). Here, the resolution in the measurement of $B_{||}$ is 100 mT i.e. the uncertainty in $B_{||}$, $\delta B_{||} = 50$ mT. Thus, the uncertainty in the measurement of sub-band spacing $\delta(\Delta E) = g\mu_B\delta B_{||} = 6 \mu\text{eV}$ (assuming $g = 2$ for graphene). Using the single particle model, the width w of the QPC for a given sub-band spacing ΔE_{ij} is given by $w = A\sqrt{\frac{j^2 - i^2}{\Delta E_{ij}}}$ where the constant $A = \frac{\hbar\pi}{\sqrt{2m^*}}$. The standard deviation of the width of QPC in the last column $s = 44$ nm. The average width of the QPC is 369 nm and the standard error $s/\sqrt{N} = 22$ nm where $N = 4$ is number of values of the width [255]. Thus, the width of the QPC $w = 369 \pm 22$ nm.

$B_{ }$ (T)	Sub-band spacing	$\Delta E = g\mu_B B_{ }$ (meV)	Width (w) of the QPC (nm) from single particle model
3.1	ΔE_{12}	0.359	309
3.7	ΔE_{23}	0.428	365
4.5	ΔE_{34}	0.521	391
5.3	ΔE_{45}	0.614	409

Table 9.2.: Sub-band spacing at the higher order crossing points in Fig. 9.3 (b). As explained in Table 9.1, the uncertainty in the measurement of the sub-band spacing, $\delta(\Delta E) = 6 \mu\text{eV}$.

$B_{ }$ (T)	Sub-band spacing	Extracted from the plot $\Delta E = g\mu_B B_{ }$ (meV)	Calculated (meV)
5.7	ΔE_{13}	0.656	$\Delta E_{12} + \Delta E_{23}$ $= 0.787$
7.6	ΔE_{24}	0.880	$\Delta E_{23} + \Delta E_{34}$ $= 0.949$

Assuming the single particle model with a one dimensional box with a length of confinement w , the energy of the particle in the n^{th} sub-band is given by $E_n = \frac{\hbar^2 n^2 \pi^2}{2m^* w^2}$ where $m^* = 0.033m_e$ is the effective mass of the electron and $n \in \mathbb{Z}^+$. Using the values of the sub-band spacing from Table 9.1 in the above expression, we can calculate the average width of the QPC which is roughly 370 nm. This is on the same order of the width of 250 nm obtained from the AFM measurements in Fig. 5.7 (b) and (c).

9.7. Identification of peaks

In this section, we explain the procedure used to extract the values of the crossing points in the transconductance maps shown in Fig. 9.3 (b). These crossing points correspond to the local maxima or peaks in the transconductance $dG/dV_{bg}(V_{fg2})$ at a particular value of the parallel magnetic field $B_{||}$.

To identify these maxima, we use a 2D peak finder function [256]. This MATLAB code identifies the peak by using the local maxima (there is also another possibility to use the weighted centroids method as well). Each peak is considered to be a Gaussian with a certain width (a smooth point spread function).

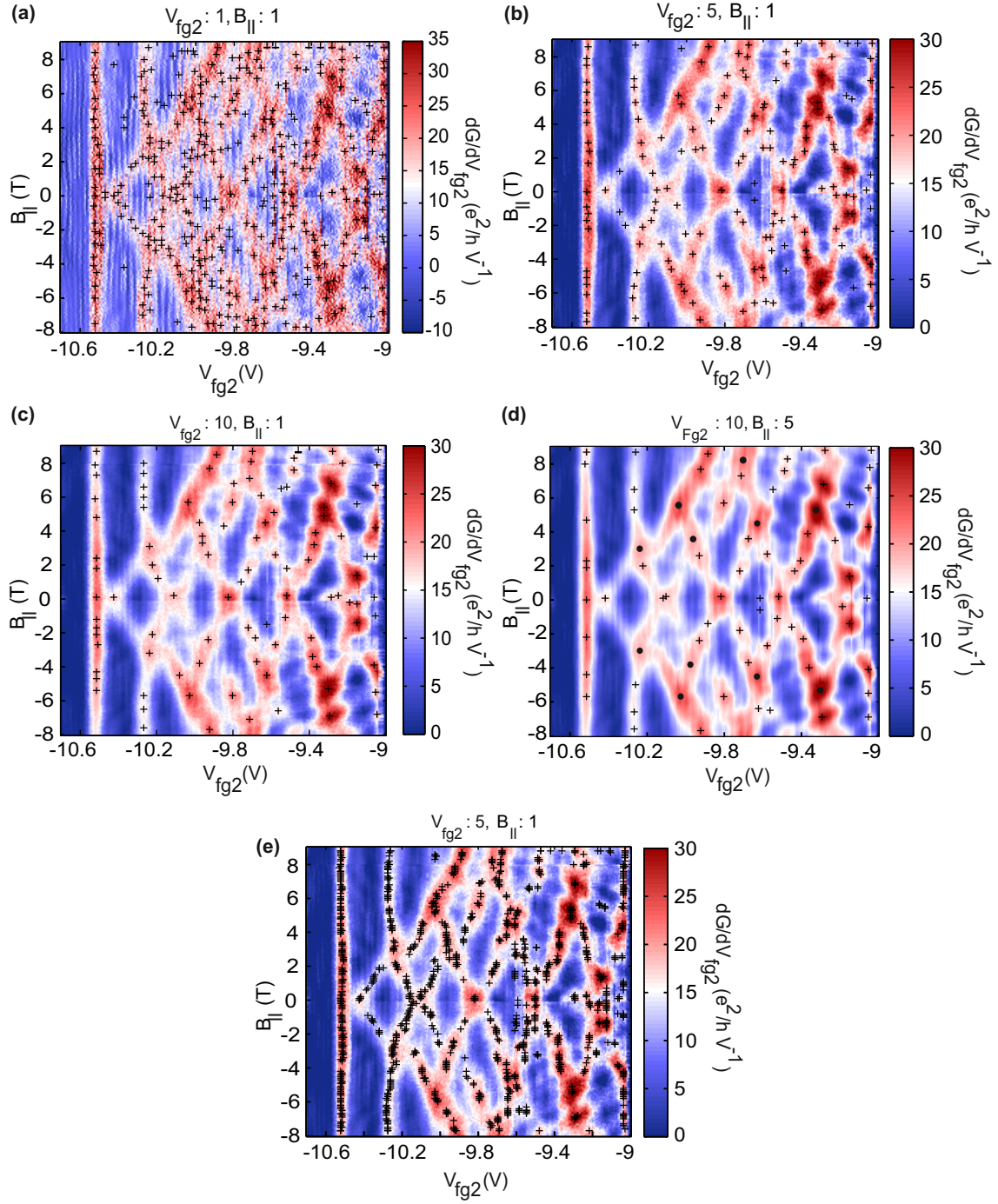


Figure 9.4.: (a) - (d) Transconductance map shown in Fig. 9.3 (b) for different values of span i.e. smoothing along the V_{fg2} and $B_{||}$ axes. Span in (a) is 1 along V_{fg2} and 1 along $B_{||}$ axis. Span in (b) is 5 along V_{fg2} and 1 along $B_{||}$ axis. Span in (c) is 10 along V_{fg2} and 1 along $B_{||}$ axis. Span in (d) is 10 along V_{fg2} and 5 along $B_{||}$ axis. Data points indicated by "+" correspond to the derivative maxima identified by the 2D peak finder function. (e) Same as (b) but with 100 times horizontal amplification of peaks in each trace.

9.7.1. Smoothing the data

First, we smooth the raw data using a moving average with certain span [223, 257]. The span is an integer and refers to the number of data points over which the data is smoothed. Naturally, the number of peaks identified by the 2D peak finder function depends on how much the raw data is smoothed. Smoothing the data to a certain extent reduces the influence of stray peaks such as Coulomb oscillations and ensures that the peak identified by the function is, indeed, the derivative maximum. However, smoothing it way too much can have the opposite effect, decreasing the relative height of some peaks with respect to the background, thereby making it difficult to distinguish all the peaks especially if they are quite close to one another – compare the number of peaks identified by "+" in different sub-plots of Fig. 9.4). Consider Fig. 9.4 (d) where we smooth the data across 10 points along the gate axis i.e. $\text{span} = 10$ along the V_{fg2} axis and is equal to 5 across the $B_{||}$ axis. This is the same amount of smoothing used in the Fig. 9.3 (b). The peak finder function identifies several maxima including the crossing points denoted by "•" symbols. The values of the magnetic field at these points are then used to calculate the sub-band spacings.

However, since this amount of smoothing is a bit too much for determining all the derivative maxima in the entire map, for all the subsequent calculation, we use Fig. 9.4 (b) where the data is smoothed only 5 times along the gate axis and not smoothed at all along the field axis. This seems to work well to identify even more peaks in the transconductance plot as the function scans the data radially without any hindrance from unwanted stray peaks such as in Fig. 9.4 (a).

9.7.2. Horizontal amplification of peaks

From Fig. 9.4 (b), although all the crossing points are identified, all the derivative maxima in every single horizontal line-cut along the gate axis are clearly not identified. In order to achieve this, we employ the following procedure. First, we modify the raw data by amplifying the value of the derivative for each trace $dG/dV_{bg}(V_{fg2})$ at a particular value of $B_{||}$ 100 times. The rest of the traces remain constant at the original intensity. This is to ensure that all the peaks in this trace are much stronger than the peaks in the neighbouring traces such that the 2D peak finder function locates all of them when scanning the data. Subsequently, this procedure is repeated for all traces one-by-one such that almost all the peaks (the black cross symbols) in every single trace are identified as shown in Fig. 9.5 (a).

9.7.3. Interpolation of peaks

Identification of all the peaks in every single trace is important since the differences between the two successive peaks in any given trace is a measure of the Zeeman splitting at that particular value of $B_{||}$ (see Fig. 9.3 (c)). Hence, in order to obtain all the peaks, we develop the following procedure. As an example, consider the spin-up and spin-down states of the first sub-band as shown in Fig. 9.5 (b). As explained earlier, the difference between two peaks on each of these lines at a particular value of magnetic field (denoted by 'A') corresponds to the Zeeman splitting energy of the first sub-band. Now, if the peak finder function has been unable to identify one or more peaks along the spin down state feature at around -10.5 V, we obtain these missing peaks by linear interpolation between the peak at the next lower and the peak at the next higher value of the field (see the green dots). In this way, we locate all the peaks for the feature corresponding to the $1\downarrow$ state. Similar interpolation technique is followed for the $1\uparrow$ state as well. Knowing all the peaks, the

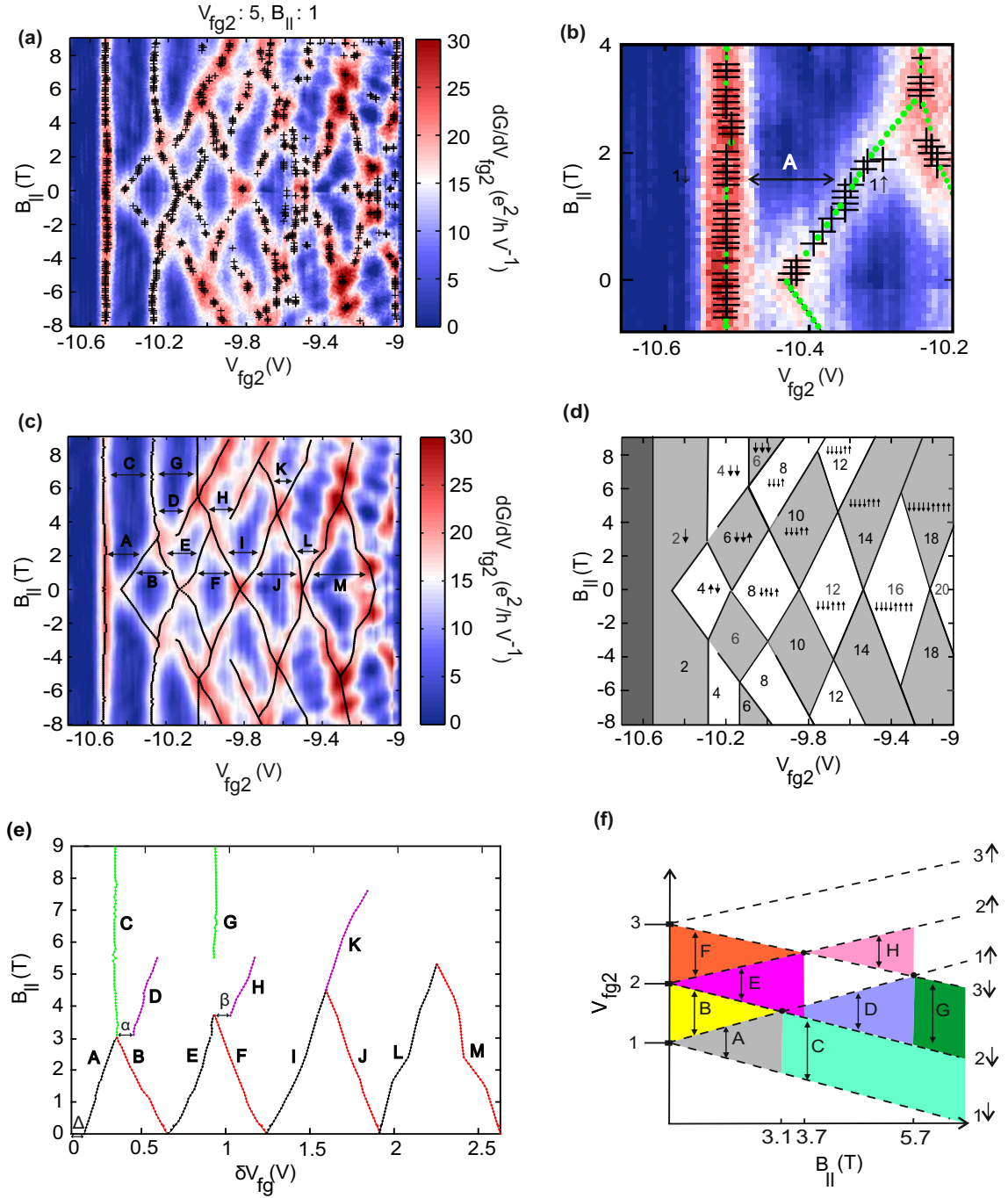


Figure 9.5.: (a) Same transconductance plot as shown in Fig. 9.4 (b) but with 100 times horizontal amplification of peaks (black cross symbols) for each conductance trace $G(V_{fg2})$ at a particular value of $B_{||}$. (b) Green dots show linear interpolation between the peaks. (c) All the peaks in the entire plot identified after the linear interpolation in (b). (d) Schematic representation of the sub-band splitting shown in (c) with the conductance steps (the numbers) in units of e^2/h and the occupancy of each sub-band (see arrows next to the numbers). (e) Difference in finger gate voltage at a given value of $B_{||}$ between two relevant sub-bands δV_{fg} as a function of $B_{||}$ as indicated in (c). (f) Difference in finger gate voltage at a given value of $B_{||}$ between two relevant sub-bands given by A - H as shown in (c) and (e).

difference in the finger gate voltage between two points on the $1\uparrow$ and $1\downarrow$ state features at the same particular value of $B_{||}$ allows us to calculate the amount of sub-band splitting 'A'. Using the same procedure, we obtain all the peaks (denoted by black dots) in the entire plot of Fig. 9.5 (c).

The same data is presented in the schematic in Fig. 9.5 (d) highlighting the different plateaus in conductance in units of e^2/h (see the numbers) and the associated spin structure (see the arrows next to the numbers). The difference in finger gate voltage at a given value of $B_{||}$ between two relevant sub-bands (see the black arrows next to A - M in Fig. 9.5 (c)) is a measure of the Zeeman splitting and is depicted in Fig. 9.5 (e) - the distances or the differences in the finger gate voltage δV_{fg2} as a function of the magnetic field. For example, A is the difference in V_{fg2} , δV_{fg2} between two points on $1\downarrow$ and $1\uparrow$ states at the same value of $B_{||}$ as $B_{||}$ goes from 0 to 3.1 T (when $1\uparrow$ and $2\downarrow$ states meet each other) as seen in Fig. 9.5 (f). B is the difference in V_{fg2} between two points on $1\uparrow$ and $2\downarrow$ states at the same value of $B_{||}$ as $B_{||}$ goes from 0 to 3.1 T. C is the difference in V_{fg2} between two points on $1\downarrow$ and $2\downarrow$ states at the same value of $B_{||}$ as $B_{||}$ goes from 3.1 to 8.3 T. D is the difference in V_{fg2} between two points on $1\uparrow$ and $2\downarrow$ states at the same value of $B_{||}$ as $B_{||}$ goes from 3.1 to 5.7 T (when $1\uparrow$ and $3\downarrow$ states meet each other).

Straight away from Fig. 9.5 (e), one can notice that every branch from A - M falls under one of the three categories based on their slope (see Table 9.3) - those with a positive slope (spin up) corresponding to $g = 2$ such as A, E, I, L, D, H and K, those with a negative slope (spin down) with $g = -2$ such as B, F, J and M and the ones (spin down) which appear as a straight line due to Fermi level pinning such as C and G.

One can observe other small but interesting differences from this plot. As we move from one sub-band to the next higher level, the density of states and consequently, the net charge carrier density of graphene increases. This has a huge influence on the device electrostatics which is clearly visible on the voltage scale along the x axis. For example, notice how the difference in the slopes of A and B in Table 9.3 is much larger than the difference between L and M due to Fermi level pinning of the $1\downarrow$. Similarly, the slopes of A and D, E and H and I and K are also quite close to each other suggesting a similar evolution of these branches.

More importantly, we observe several gaps such as Δ and α in finger gate voltage which are discussed in the following sections.

Table 9.3.: Slopes of the different branches A - M shown in Fig. 9.5 (e).

Branch	slope (T/V)	Branch	slope (T/V)
A	16.3	H	10.7
B	-9.9	I	12.9
C	-	J	-14.37
D	17.63	K	12.8
E	13.8	L	14.74
F	-12.72	M	-14.2
G	-		

9.8. Sub-band spacing as a function of displacement field

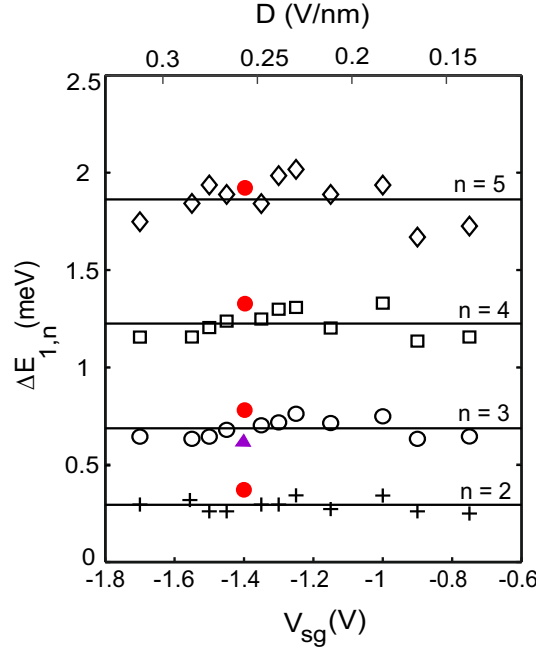


Figure 9.6.: Difference in energy between the first and the n -th sub-band $\Delta E_{1,n} = \sum_{i=1}^{n-1} \Delta E_{i,i+1}$ for $2 \leq n \leq 5$ as a function of the side gate voltage V_{sg} or the displacement field D . The red dots and the purple triangle correspond to the values obtained from Table 9.1 and 9.2 respectively. These data are extracted from Fig. 9.3 (b) while the remaining data points are obtained from the plots shown in Fig. C.1 and C.2 using the procedure described in section 9.7.

The measurements shown in Fig. 9.3 (b) are repeated for several other values of side gate voltage/displacement fields (see Appendix Fig. C.1 and C.2) and the intersection points are once again used to extract the sub-band spacings as explained in section 9.6. Fig. 9.6 shows the energy difference between the first and the n -th sub-band as a function of displacement field. We see that the sub-band energies remain nearly constant in the range of the displacement field under consideration. This suggests that the width of the QPC remains unaffected with changes in the displacement field.

9.9. The 0.7 analog structure

In Fig. 9.5 (e), we observe several gaps in δV_{fg2} such as α and Δ that have been extracted from the transconductance plot of Fig. 9.3 (b). The value of Δ is measured to be around 0.1 V and is visible in the form of a pronounced step at $2 e^2/h$ as seen in the close-up in Fig. 9.7.

Such features were also observed earlier in GaAs heterostructures [254] where the step at $0.7 \times 2e^2/h$ at 0 T gradually evolves down to $0.5 \times 2e^2/h$ with an increase in the parallel magnetic field. This feature was, therefore, called the 0.7 anomaly. However, in our device, we do not observe any step at $0.7 \times 4e^2/h$ but rather, one at $2 \times e^2/h$ that is unaffected by magnetic field. This may be explained as a splitting of the

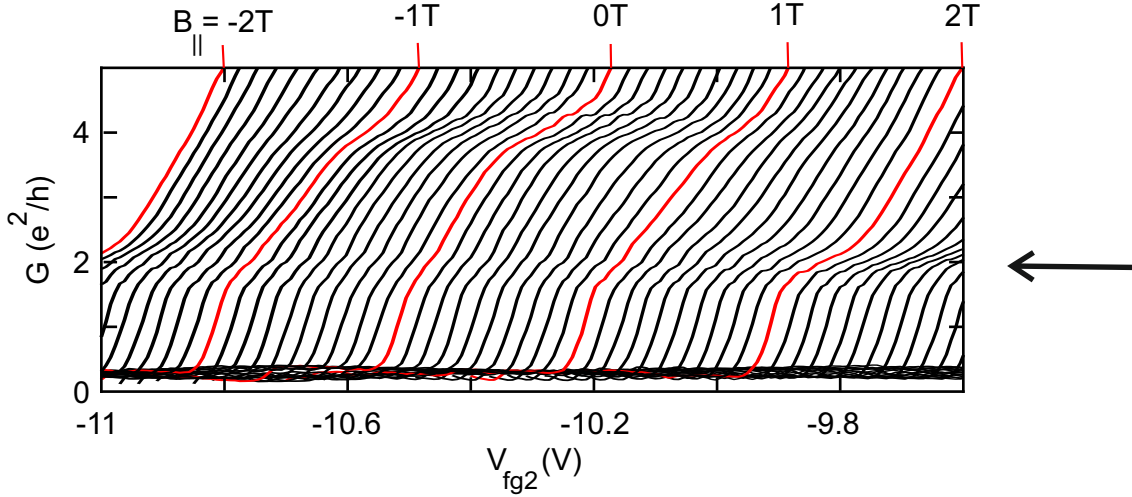


Figure 9.7.: Close-up of Fig. 9.3 (a) at low B_{\parallel} highlighting the presence of the step at $2 e^2/h$ at 0 T that remains constant with magnetic field. (see the black arrow).

first sub-band caused by spin-orbit (SO) coupling of the Kane-Mele type [235, 237, 238, 241, 258] instead of $e-e$ interaction at low B_{\parallel} . The absence of such an effect could be caused by the efficient screening of the graphite back gate [259] which is quite close (≈ 30 nm) to the BLG graphene channel. Thus, at low magnetic field, SO coupling dominates over the $e-e$ interaction.

The splitting of the first sub-band at zero magnetic field is also clearly visible in the transconductance plots shown in Fig. 9.8 (a) - (d) measured at different values of displacement field D . Measurement of Δ in several such measurements (see Fig. C.1 and Fig. C.2) gives us a near linear dependence of Δ on the displacement field in this particular parameter range under consideration as shown in Fig. 9.9 (a). The observed dependence may be attributed to the fact that SO coupling in BLG is enhanced by proximity effects which depends on the overlap between the orbitals of graphene and hBN. Further, since Δ also depends on the band structure of BLG near the Fermi energy, an overall dependence on D is expected [246, 260].

Besides Δ , in Fig. 9.5 (d), one can observe another discontinuous shift in voltage ' α ' of around 0.15 V. This occurs at the crossing point of $1\uparrow$ and $2\downarrow$ levels in Fig. 9.3 (b). Similar behavior was once again observed by the authors of Ref.[254], where they observed an intermediate kink at around $1.5 \times 2e^2/h$ at magnetic field just before the crossing point which eventually went to a step at a height of $2e^2/h$. This discontinuity in the $1\uparrow$ was referred to as the 0.7 analog since its origin and the evolution is similar to that of the 0.7 anomaly at 0 T. This behavior is also observed in the present scenario in Fig. 9.3 (a). Starting from 0 T, as the magnetic field increases, the steps at 4, 8, 12... e^2/h evolve to intermediate steps at 6, 10... e^2/h already at around 2 T. Thereafter, the step at $1.5 \times 2e^2/h = 6 e^2/h$ transforms gradually into a $1 \times 4e^2/h$ as the magnetic field increases towards 6 T (see the red dashed ellipse) indicating a spontaneous spin splitting.

Similar results as seen in other measurements are shown in Fig. 9.8 (e) - (h). Observe how there is a clear step at $6e^2/h$ in the blue trace at 2 T which eventually moves towards a lower step at a height of $4e^2/h$ (see black dashed ellipse) once the levels $1\uparrow$ and $2\downarrow$ intersect in the corresponding transconductance plots in Fig. 9.8 (a) - (d).

In the case of the GaAs heterostructure [254], the 0.7 analog, similar to the 0.7 anomaly was understood as a consequence of strong exchange interactions as theoretical simulations based on simple non-interacting

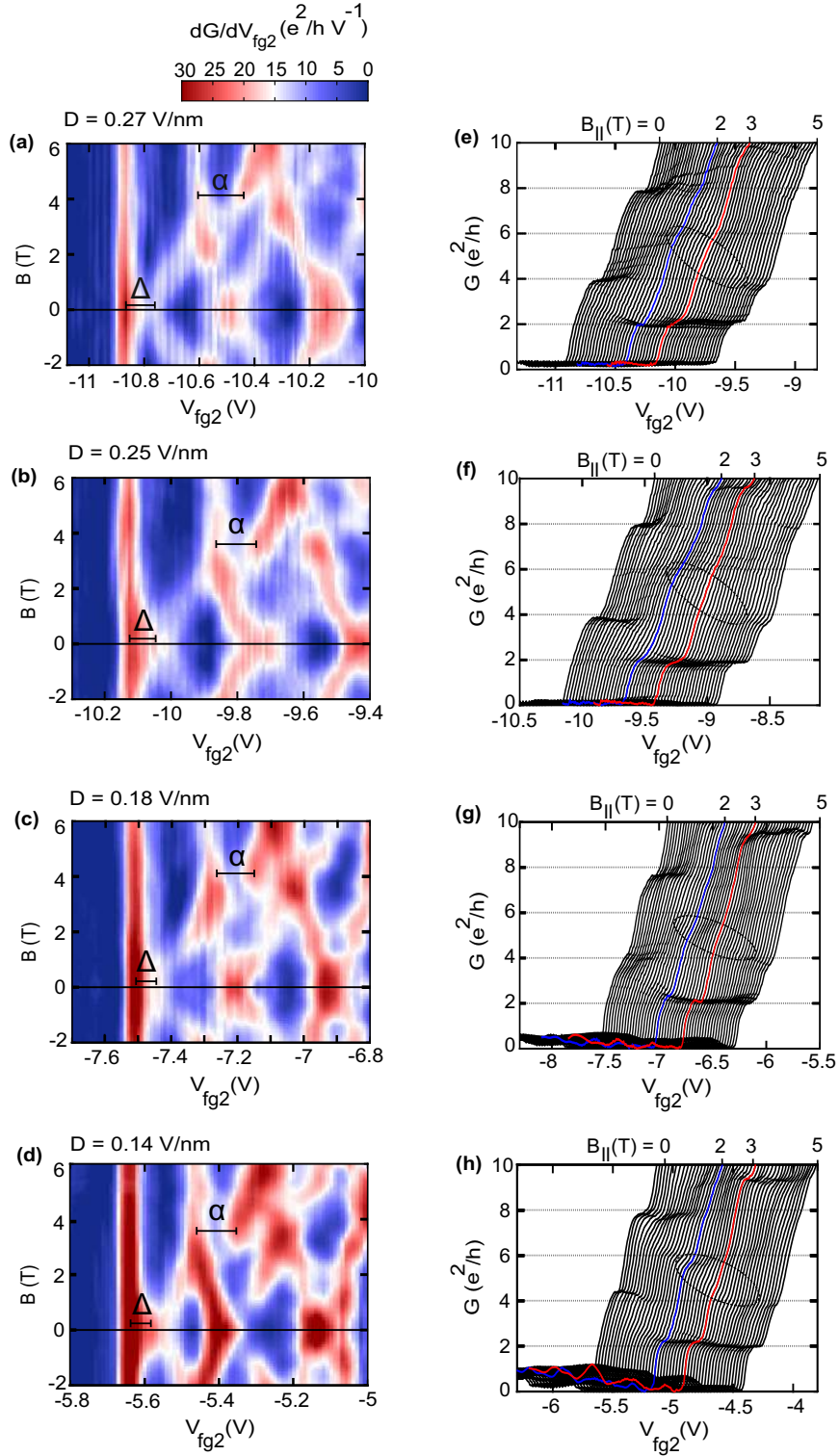


Figure 9.8.: (a - d) Transconductance dG/dV_{fg2} as a function of V_{fg2} and $B_{||}$ for different values of displacement field D . Plots in (a) - (d) are close-ups of Fig. C.1 (d), (e) and Fig. C.2 (i), (k) respectively. (e - h) Corresponding conductance traces from $B_{||} = 0$ to 5 T. Starting from the left, each trace is shifted by 25 mT with respect to its previous trace for the sake of clarity. The 0.7 anomaly is indicated by the black dashed ellipse. The step at $G \approx 1.5 \times 4e^2/h$ (blue trace) at around $B_{||} = 2$ T gradually evolves into $4 e^2/h$ as the magnetic field increases to 5T.

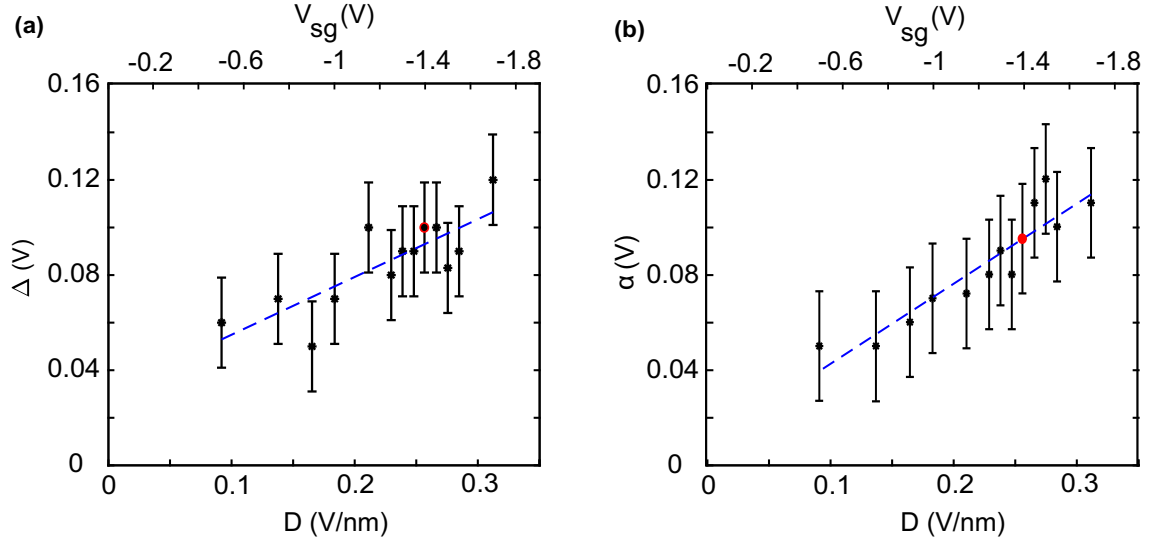


Figure 9.9.: (a,b) Voltage gap Δ and α as a function of D or V_{sg} . Red dots correspond to values extracted from Fig. 9.3 (b). The remaining values have been extracted from the plots in Fig. C.1 and Fig. C.2.

electron model did not show any signs of discontinuities in voltage. Once exchange interactions are included, voltage gaps at the crossing points where the spin-up bands populate twice become visible [261]. The fact that only spin up states show such gaps is explained as a way of the system to increase parallel spin \downarrow electrons at the level crossings which in turn lowers the total energy of the system. This may be also understood as the electrons in $2\downarrow$ being screened by those in $1\uparrow$ [262]. At the crossing point, the energy of $2\downarrow$ is higher than the chemical potential and therefore, empty. Hence, any changes in the ideal behavior of the levels should be coming from the electrons in $1\uparrow$.

In our device, at a finite in-plane magnetic field of around 2 - 3 T, the Zeeman effect dominates the SO coupling making $e-e$ interaction at the 0.7 analog more relevant. Similar to Δ , α shows a linear dependence on the displacement field D as shown in Fig. 9.9 (b) in the given parameter range.

9.10. Conclusion

In summary, we have been able to successfully demonstrate the formation of sub-bands in split gated bilayer graphene QPC resting on a graphite back gate. Conductance steps with a height of $4 e^2/h$ at 0 T split into intermediate kinks with a height of $2 e^2/h$ under the presence of a parallel magnetic field. From the transport measurements, we identify voltage gaps between $1\uparrow$ and $1\downarrow$ states at 0 T and also at the crossing point between $1\uparrow$ and $2\downarrow$ levels. The gap at 0 T is a measure of the spin orbit coupling in BLG and can be tuned by the displacement field. Tuning and controlling the SO gap is useful for spintronic applications such as spin-orbit valves, spin FETs etc [260, 263, 264]. On the other hand, the gap at higher fields is an estimate of the amount of $e-e$ interaction driven spontaneous spin splitting. At this crossing point, we observe 6 fully spin down polarized states. Such a high degree of polarization makes BLG QPCs good spin polarizers and detectors in ballistic spin transport devices [265].

10. Conclusion and Outlook

The goal of this thesis is to achieve confinement of charge carriers in single and bilayer graphene. In the first section of this chapter, we summarize the experiments performed and the results obtained in this direction. In the next section, we provide a short overview of other interesting and relevant experiments on graphene QPCs and an outlook on some possible future experiments.

10.1. Conclusion

Graphene has drawn a lot of attention from both experimentalists and theoreticians since its exotic material and electronic properties confer it a huge potential as the choice of material in electronic and spintronic devices. However, in graphene, unlike traditional semiconducting heterostructures based on GaAs, SiGe etc., there is no band gap which is inevitable for making electronic devices. In this thesis, we explore two different approaches of achieving this : the first one is by etching a graphene flake into narrow strips called constrictions and the other is by using split gates as in the case of its semiconductor counterparts. However, in order to form nanoconstrictions or quantum points which exhibit size quantization, a prerequisite is obtaining high quality samples with high mobility and low scattering of charge carriers. Over the course of time, with the development of new process technology, fabrication of high quality samples was made possible. In chapter 3, we produce graphene and hBN flakes using the technique of mechanical exfoliation. hBN-graphene-hBN sandwiches measured in this thesis were fabricated using the van der Waals pick-up technique developed by Wang et.al. [172]. Using this, it is possible to pick up graphene from the substrate with a layer of hBN by utilizing the van der Waal adhesive force and laying them down on another layer of hBN, all this while ensuring that the surface of graphene is not contaminated by any external agents such as organic solvents. Such samples have shown a significant reduction in the overall doping concentration and strain fluctuations resulting in microscopically clean sample as seen from the Raman spectroscopy measurements. Transport measurements on such samples have also yielded a low residual charge carrier density and high mobility for both single and bilayer graphene.

Indeed, quantum point contacts built from single layer graphene-hBN sandwiches have already shown ballistic transport at a mobility of $150,000 \text{ cm}^2\text{V}^{-1}\text{s}^{-1}$ at the CNP [42]. These state-of-the-art devices were fabricated using a combination of high accuracy electron beam lithography and SF_6 based etching techniques which allow a good control over the constriction size and the edge roughness. These devices showed signatures of ballistic transport and size quantization which testify the high quality of the samples. However, in spite of this, edge disorder was seen to have played an important role in determining the conductance of carriers through the channel and even hampering it. For instance, in narrower constrictions (width $\approx 230 \text{ nm}$), the transmission was limited to only 0.5. This is because the edges are much closer to the channel and have a larger impact on the conductance. Since rough edges are inevitable in etched devices, an understanding of how these edge states function, if and how they can be tuned independently and to what extent still remains an important unanswered question.

With these insights in mind, using the same van der Waals fabrication technique discussed above, in chapter 5, we build a new generation of devices with a similar geometry but much larger leads to ensure that the constriction is indeed ballistic and to remove other interference effects such as Fabry-Pérot oscillations which were previously observed in Ref. [42]. Such interference effects occur due to the coherent reflections of carriers at the finite size leads and therefore, an enlarged size of the lead now ensures that the interference length scale does not obscure the visibility of conductance kinks anymore. Further, the new design now also includes a pair of top (split) gates covering the edges of the constriction to be able to tune the Fermi level at the edges directly and independently from the channel (see Fig. 6.2). In this constriction with a width of 300 nm, a direct manifestation of the localized edge states is visible in the form of a large deviation from the ideal ballistic transport behaviour around the CNP, similar to Ref. [42]. Moreover, robust conductance kinks on the order of $2 - 3 e^2/h$ that are independent of the top gate voltage confirm that they are indeed signatures of size quantization effects occurring in the constriction.

The main result we obtain from this device is the measurement of a non-constant relative gate lever arm α_{tg}/α_{bg} . Since the back gate lever arm is more or less constant, this means that the coupling of the top gate α_{tg} to the constriction changes continuously. This is a consequence of the stray field lines of the top gate such that tuning the top gate influences not only the edges but also the channel. These data are consistent with previously obtained results on graphene nanoribbons whose edges are subjected to treatment with HF acid solution [220]. When the edges of the constriction/ribbon are exposed to Fluorine whether it is the form of HF or SF₆ (during etching), it reduces the disorder potential and increases the charge accumulation near the edges of graphene resulting in a gate tunable gate coupling.

In the other sample discussed in this chapter, we modified the design to now have a single top gate in the shape of a QPC with a width of 230 nm, covering the entire constriction (and the leads as well) except the edges as shown in Fig. 6.1. The global top gate should now provide a uniform field throughout the channel. Only the stray field of the top gate affects the edges while the back gate can be used to tune the entire device. The idea behind incorporating a single top gate instead of a split gate design like in the previous chapter is to exclude the possibility of any asymmetric electric field that may modify the conductance through the 380 nm wide QPC.

The charge carrier density in the QPC can now be tuned by using both the gates independently. Measurement of four terminal conductance as a function of the top gate voltages showed quantized conductance kinks with a step height on the order of $2 - 3 e^2/h$ corresponding to a transmission of 0.7. Bias spectroscopy was used to extract a sub-band spacing of around 5 - 6 meV.

An important result that forms of the crux of this chapter is observed upon close examination of the transconductance maps in Fig. 7.8 (a) - (b). Besides a line with a dominant/major slope which gives the relative lever arm, several other lines with a minor slope are also visible. While the features parallel to the major line come from the evolution of the conductance kinks, the minor slope features are explained as a result of the localized states present along between the top gate and the edges and also along the edges of the QPC. Due to the proximity of the top gate, stray field lines emerging from it tune the edge states but with much lesser strength as compared to the states present right under the top gate in the channel.

We, then, sweep the gates along two different directions - one along the charge carrier density axis perpendicular to the major slope and the other parallel to the minor slope with the hope that the latter suppresses the contribution of edges to the conductance. Right away, we see that the kinks, especially those away from the CNP, remain undisturbed regardless of the direction of sweep. But, the features closer to the CNP, where disorder plays an important role, differ based on the direction of sweep (see Fig. 7.9 (b)).

Similar results are also reproduced in theory using tight binding simulations for a nanoribbon model where cleaner quantization features are seen when we sweep the gates along the minor slope (see the purple line in Fig. 7.13 (b) and (c)).

Another knob that can be used to tune the density of states is a magnetic field applied perpendicular to the QPC. This forces the electrons to move from the size quantization regime to the Landau levels as seen in Fig. 8.1. Experimentally, we observed that the features at higher magnetic fields remain the same for both the directions of sweep. However, since the low field region especially close to the CNP is dominated by edge disorder, the features vary greatly between the two measurements.

The features observed in the transmission spectrum are explained using different types of eigen states and their interference (see Fig. 8.4). For example, the straight line feature close to the CNP that moves almost independent of the magnetic field is an eigen with a very weak coupling to the leads i.e. a strongly localized state. Similarly, the extent of localization of each eigen state determines its dominance in the transmission spectrum - some show up as sharp resonances while others contribute to the background signal. Thus, this basic nanoribbon model (width ≈ 20 nm), after the necessary rescaling to be comparable to the experimental data, explains several experimental features particularly, those close to the CNP. Nevertheless, we also use another accurate constriction model (width ≈ 200 nm) with leads where the dimensions are much closer to reality as shown in Fig. 8.6. Consequently, we observe a lot more interference features as compared to the nanoribbon model. Particularly in the high charge carrier density regime, similar to the experiment, we observe "V" like features due to the rapid evolution of the quantized conductance steps into Landau levels in Fig. 8.7. Thus, we have been able to successfully tune the edges using the top gate. By sweeping along the minor slope, we have been able to reduce the influence of edge disorder which is manifested in the form of cleaner conductance kinks, fewer localized states in the transmission spectrum and relatively well defined Bloch states that move towards their respective Landau levels as expected.

In the next chapter, we study quantum point contacts that are defined by split gate technology on a hBN - bilayer graphene - hBN sandwich resting on a layer of graphite. Using the graphite layer as the back gate, it is possible to achieve stronger confinement of charge carriers as compared to using the traditional Si back gate [200]. The voltage applied to the split gates along with the back gate is used to create a QPC with a width of 250 nm. While the finger gates are used to tune the charge carrier density of the channel locally (see Fig. 9.1). We observe quantized conductance with a step height of $4 e^2/h$ as expected for graphene with full four fold degeneracy. The spin degeneracy is broken with the application of an external parallel magnetic field. Spin splitting of sub-bands is visible in the form of intermediate plateaus in conductance at higher magnetic field values and crossing points in the transconductance map due to the crossover of different spin-up and spin-down states. From these points, where the Zeeman energy matches the sub-band spacing, we extract the sub-band spacings. These values seem to be independent of the displacement field implying the width of the QPC remains unchanged. The most important result of this chapter is the presence of discontinuities in finger gate voltage in the plots of transconductance as a function of finger gate voltage and the magnetic field as described in section 9.9. These are present both at a magnetic field of 0 T between the spin-up and spin-down levels of the first sub-band and at a higher value of more than 3 T at the crossing point of the spin up level of the first sub-band and the spin-down level of the second sub-band. The voltage gap at low magnetic field is attributed to SO coupling that is dominating due to a weak Zeeman effect. On the other hand, at a high magnetic field, $e - e$ interactions dominate the SO coupling as the Zeeman energy increases. Accordingly, we observe a step at $2 e^2/h$ at 0 T which remains constant with magnetic field. While at the crossing point, we observe that there is a step at $6 e^2/h$ that gradually evolves

into $4 e^2/h$ as the magnetic field increases similar to GaAs heterostructures.

Thus, we have realized our goal of charge carrier confinement using high quality hBN encapsulated graphene based QPCs.

10.2. Current research and outlook

10.2.1. Scanning gate microscopy

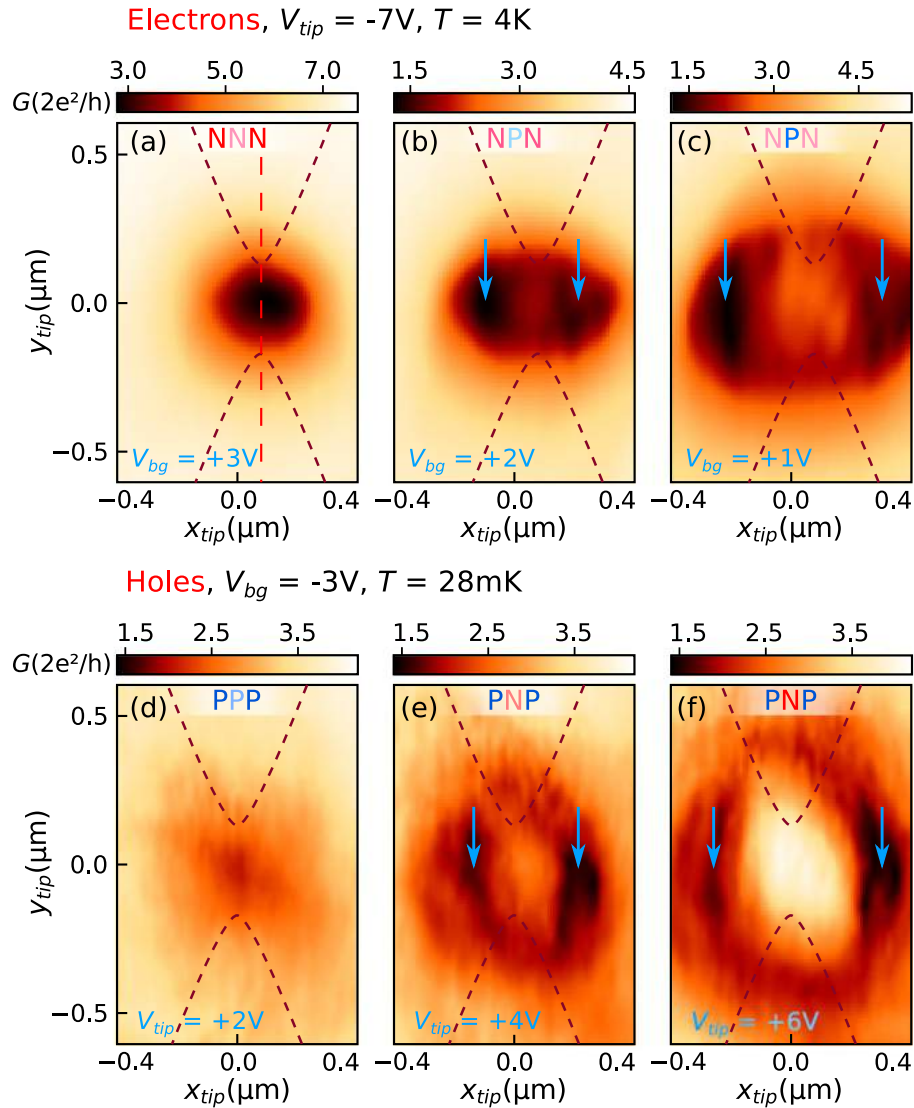


Figure 10.1.: SGM images: Conductance G as a function of the charge carrier density for different values of temperature T . (a) - (c) The tip is at a distance of 120 nm (d_{tip}) from the sample and induces a charge carrier density $\Delta n = -0.23 \times 10^{10} \text{cm}^{-2}$. (a) Bulk density $n = 0.3 \times 10^{10} \text{cm}^{-2}$ (b) $0.22 \times 10^{10} \text{cm}^{-2}$ (c) $0.15 \times 10^{10} \text{cm}^{-2}$ (d) - (f) Here, $n = -0.15 \times 10^{10} \text{cm}^{-2}$ and $d_{tip} = 120$ nm for different values of the tip voltage V_{tip} corresponding to $\Delta n_{max} =$ (d) $0.12 \times 10^{10} \text{cm}^{-2}$ (e) $0.25 \times 10^{10} \text{cm}^{-2}$ and (f) $0.37 \times 10^{10} \text{cm}^{-2}$. Figure reprinted from Ref. [266].

While the transport measurements described in this thesis use external gates to alter the Fermi energy, scanning gate microscopy (SGM) uses the voltage applied to the tip of an atomic microscope to change the local potential of the QPC underneath which produces a change in the conductance [267]. Scanning the tip across the sample is equivalent to having a movable top gate. This technique has already proved useful in the study of localized charge states in graphene quantum dots [268] and nanoconstrictions [155, 269, 270]. In the future, device geometry and experiments may also be modified and developed to study the localized states along the edges. Recently, using the QPC geometry described in chapters 4 and 5 (without the top gates) in single layer encapsulated graphene, we studied the flow of electrons (besides the local density of states), through a circular Veselago lens [266]. We observed a high current density or a high transmission when the tip is placed at the centre of the constriction due to the Klein tunnelling of charge carriers (see the arrows in Fig. 10.1 (b), (c) and (e), (f)). On the other hand, low intensity conductance spots are observed in the SGM images when the tip is placed slightly away from the QPC due to reduced transmission suggesting that the smoothness of the junction plays a crucial role in the electron flow and the corresponding image. Thus, the high quality of our devices has made it possible to study electron optics behaviour in graphene QPCs.

10.2.2. Split gate QPCs in single layer graphene

As explained in chapter 3, in case of monolayer graphene, it is difficult to form a QPC by simply using gates due to the gapless nature of electronic band structure. This is due to the formation of p-n junctions that are conducive for Klein tunneling, effectively leading to short circuit current through the constriction [91]. This stands as a hindrance in the way of QPCs which form an important tool in many transport studies such as quantum Hall interferometry where the electron and hole edge channel mixing in the quantum Hall (QH) regime poses lack of control over QH edge channel transmission. However, it was shown that by using high mobility, encapsulated graphene fabricated using the van der Waals technique, it is possible to separate these edge channels [271]. This technique of fine-tuning the transmission of the QPC in the QH regime can also be exploited in electron optics experiments. Recently, this geometry was used to study the transition of a QPC from a Fabry-Pérot interferometer at a ballistic, low magnetic field regime to a QH regime at high field that is facilitated by snake trajectories [272, 273]. The incorporation of split gates to control edge trajectories was also useful in the study of fractional QHE (FQHE) as well [271, 274, 275]. More recently, graphite top and back gates were also introduced to explore exotic quasi particles such as anyons in the FQHE regime [276].

10.2.3. Quantum dots in bilayer graphene

Realizing a quantum qubit using graphene has been the ultimate goal towards which a lot of experimental research is focused. Recent experiments have used the combination of bilayer graphene and graphite back gate device design similar to the one proposed in chapter 6 to fabricate single quantum dots with clear spin and valley splitting in the presence of a magnetic field [199]. Follow up experiments have been able to reach up to a triple dot regime in fully gate controlled quantum dots [200] where excited states were investigated in the single dot regime. While tunneling barriers in such devices are formed using the ambipolar nature of a graphene p-n junction, they can also be tuned using external gates such that tunnel coupling varies over even two orders of magnitude, in turn making the device vary between the characteristic Coulomb blockade regime and a Fabry-Pérot interferometer [277]. Taking another leap forward, charge

detection has also been established in such devices where another gate defined quantum dot acts as the charge detector instead of using a standard nanoribbon [278]. This gave a degree of charge detection far better than other previous works on graphene quantum dots and even comparable to the quality of other semiconductor quantum dots such as GaAs or Si. This series of development has provided us with a device that is now ready for time resolved measurements [23]. Employing a high frequency read out scheme can then help us to perform spin lifetime measurements in bilayer graphene.

A. Process parameters

A.1. Cleaning the substrate

The $\text{Si}^{++}/\text{SiO}_2$ chips have Cr/Au markers that have been deposited by EBL.

1. 5 min. in acetone in an ultrasound bath
2. 5 min. in IPA in an ultrasound bath
3. Blow dry with N_2 gas
4. Plasma asher (Power = 300 W, flux = 200 sccm, time = 5 min). The chips can now be used for exfoliation of graphene or hBN.

A.2. Fabrication of etched single layer graphene QPCs

A.2.1. Preparing hBN-SLG-hBN sandwiches

1. Break a new un-doped Si wafer into the smaller pieces.
2. Pre-bake it for 1 min at 100°C on a hot plate. Let it cool down before applying any resist to prevent it from forming bubbles.
3. Spin-coat PVA 4% at 3000 rpm for 30 s. (Program no. 3 on the spin coater).
4. Bake the resist for 2 min at 120°C . Let it cool down.
5. Spin-coat PMMA 950K at 3000 rpm for 30 s (Program no. 3).
6. Bake the resist for 6 min at 120°C .
7. Apply PMMA 950 K around the circumference of the ring of the transfer holder using the nozzle of a thin pipette.
8. Place the holder on a cleanroom wipe on top of the hot plate and bake the resist at 120°C for 10 min. Allow it to cool down. Use this holder to fish the top hBN from water as explained in section 5.7.

A.2.2. Processing hBN-SLG-hBN sandwiches

- Cleaning the sandwich
 1. 15 min in acetone
 2. 5 min in IPA

3. Plasma asher: Power = 300 W, flux = 200 sccm, time = 5 min
- Spin coating
 1. Dehydrate the sample at 100°C for 1 min.
 2. Spin coat PMMA 50K at 4000 rpm for 30 s with a pre-acceleration of 500 rpm for 5 s (program no.4).
 3. Bake the resist - first at 100°C for 20 s followed by 160°C for 10 min.
 4. Allow the chip to cool down for a minute.
 5. Spin coat PMMA 950K using program no.4.
 6. Once again, bake the resist - first at 100°C for 20 s followed by 160°C for 10 min.
 7. Allow the sample to cool down for one minute.
 - EBL for hard mask
 1. Dose = $200\ \mu\text{C}/\text{cm}^2$
 2. beam current = 100 pA
 3. beam step size = 1 nm
 - Development of hard mask
 1. 65 s in AR 600-55 developer
 2. 30 s in IPA to stop the development
 3. Blow with N_2 gas.
 - Metallization of hard mask
 1. Evaporation of 20 nm Al at the rate of 0.2 nm/s.
 2. Lift off the metal in acetone for 15 min or until the metal peels away from the surface of the chip.
 3. 5 min in IPA
 4. Blow with N_2 gas.
 - Reactive ion etching
 1. Cleaning the chamber
 - Power = 300 W, Pressure = 1 Pa, Time = 10 min
 - Gas flow: Ar = 20 sccm, O_2 = 20 sccm, SF_6 = 20 sccm
 - Power = 60 W, Pressure = 2.5 Pa, Time = 10 min
 - Gas flow: Ar = 20 sccm, O_2 = 20 sccm
 - Power = 60 W, Pressure = 2.5 Pa, Time = 10 min
 - Gas flow: Ar = 5 sccm, SF_6 = 20 sccm
 2. Etching
 - Power = 60 W, Pressure = 2.5 Pa, Time = 30 s
 - Gas flow: Ar - 5 sccm, SF_6 - 20 sccm

- Stripping the hard mask
 1. 4 min in AZ MIF 319 developer
 2. 1 min in first DI water bath
 3. 9 min in second DI water bath
 4. 5 min in IPA
 5. 10 min in acetone
 6. 5 min in IPA
 7. Blow dry with N₂ gas

A.2.3. Fabrication of contacts

- Spin coating the EBL resist
 1. Dehydrate the sample at 100°C for 1 min.
 2. Spin coat PMMA 50K at 4000 rpm for 30 s with a pre-acceleration of 500 rpm for 5 s (program no.4).
 3. Bake the resist - first at 100°C for 20 s followed by 160°C for 5 min.
 4. Allow the chip to cool down for a minute.
 5. Spin coat the second layer of PMMA 50K using program no.4.
 6. Bake the resist - first at 100°C for 20 s followed by 160°C for 5 min.
 7. Allow the chip to cool down for a minute.
 8. Spin coat PMMA 950K using program no.4.
 9. Once again, bake the resist - first at 100°C for 20 s followed by 160°C for 15 min.
 10. Allow the sample to cool down for one minute.
- EBL of contacts in Juelich
 1. Small contacts (up to 0.5 µm wide)

Dose = 510 µC/cm²

Beam current = 100 pA

Beam step size = 1 nm
 2. Medium contacts (up to 5 µm wide)

Dose = 510 µC/cm²

Beam current = 100 pA

Beam step size = 5 nm
 3. Large Contacts (up to 10 µm wide)

Dose = 510 µC/cm²

Beam current = 150 pA

Beam step size = 50 nm

- 4. Bond pads
 - Dose = 400 $\mu\text{C}/\text{cm}^2$
 - Beam current = 150 pA
 - Beam step size = 50 nm

- Development

1. 60 s in AR 600-55 developer
2. 10 s in 1st IPA bath
3. 20 s in 2nd IPA bath

- Metallization of contacts in Aachen

1. 5 nm Cr at the rate of 0.2 nm/s
2. 90 nm Au at the rate of 0.5 nm/s
3. 30 min in acetone for lifting off the metal
4. 5 min in IPA
5. Blow dry with N_2 gas.

A.2.4. Fabrication of top gate(s)

- Cleaning the sample

After transferring a layer of hBN with a thickness of approx. 20 - 30 nm as the gate dielectric (see section 3.9.3), the sample is cleaned the following way.

1. 10 min in acetone
2. 5 min in IPA

- Spin coating

See the recipe used for fabrication of contacts in section A.2.3

- EBL for top gate in Juelich

See the recipe used for EBL of contacts in section A.2.3

- Development of top gate

See the recipe used for development of contacts in section A.2.3

- Metallization of top gate in Aachen

See the recipe used for metallization of contacts in section A.2.3

A.3. Fabrication of bilayer graphene QPC devices

A.3.1. Preparing hBN-SLG-hBN sandwiches

Same as section A.2.1

A.3.2. Fabrication of contacts

- Cleaning the sample
 1. 5 min in acetone
 2. 5 min in IPA
- Spin coating
See section A.2.3.
- EBL of contacts in Aachen
 1. Dose = $510 \mu\text{C}/\text{cm}^2$
 2. Beam current = 100 pA
 3. Beam step size = 1 nm
 4. Acceleration voltage = 20 kV
 5. Aperture = $7.5 \mu\text{m}$
 6. Write field = $250 \mu\text{m}$
- Development of contacts
See section A.2.3.
- Reactive ion etching
 1. Cleaning the chamber
Power = 300 W, Pressure = 1 Pa, Time = 10 min
Gas flow: Ar = 20 sccm, O₂ = 20 sccm, SF₆ = 20 sccm
Power = 60 W, Pressure = 2.5 Pa, Time = 10 min
Gas flow: Ar = 20 sccm, O₂ = 20 sccm
Power = 60 W, Pressure = 2.5 Pa, Time = 10 min
Gas flow: Ar = 5 sccm, SF₆ = 20 sccm
 2. Etching
Power = 20 W, Pressure = 8 Pa, Time = 2 min
Gas flow: CF₄ - 40 sccm, O₂ - 8 sccm
- Metallization of contacts
 1. 5 nm Cr at 0.2 nm/s
 2. 50 nm Au at 0.5 nm/s
 3. 30 min in acetone for lifting off the metal
 4. 5 min in IPA
 5. Blow dry with N₂ gas.

A.3.3. Fabrication of split gates

- Spin coating
See section A.2.3.
- EBL in Aachen
See section A.3.2
- Development
See section A.2.3
- Metallization
See section A.2.3

A.3.4. Fabrication of finger gates

- Atomic layer deposition
25 nm Al_2O_3
- Spin coating
See section A.2.3
- EBL of contacts in Aachen
 1. Dose = $120 \mu\text{C}/\text{cm}^2$
 2. Beam current = 13 pA
 3. Beam step size = 7 nm
 4. Acceleration voltage = 20 kV
 5. Aperture = $7.5 \mu\text{m}$
 6. Write field = $250 \mu\text{m}$
- Development
See section A.2.3
- Etching
 1. 2 min in 2% TMAH
 2. Cleaning in 5 min in DI water
- Metallization
 1. 5 nm Cr at 0.2 nm/s
 2. 50 nm Au at 0.5 nm/s
 3. 30 min in acetone for lifting off the metal
 4. 5 min in IPA
 5. Blow dry with N_2 gas.

B. Transport through an etched graphene QPC with a single top gate

B.1. Extraction of gate lever arm from quantum Hall measurements

In this section, we show some additional quantum Hall measurements for the traces shown in Fig. 7.9 (b) and Fig. 7.10 (b).

We have already discussed Landau fan measurements and extraction of alpha using trace "1" in section 7.4.2. We now discuss trace "2" from Fig. 7.9 (b).

In this case, as shown in Fig. B.1 (a), the gates are swept according to the equation $V_{bg} = 3.74 - 1.4 \times (V_{tg} + 1.32)$ such that $\frac{\Delta V_{bg}}{\Delta V_{tg}} = -1.4$. Using this and the fact that $\alpha_{bg}/\alpha_{tg} = 1/7$ in eq.7.9, we obtain the relation $\alpha_{eff} = 0.8 \alpha_{tg}$. Here, we use the value of $\alpha_{tg} = 49.03 \times 10^{10} \text{V}^{-1} \text{cm}^{-2}$ extracted from the Landau fan measurements on trace "1" in section 7.4.2 to calculate $\alpha_{eff} = 39.22 \times 10^{10} \text{V}^{-1} \text{cm}^{-2}$. This value is substituted in eq.7.8 to fit Landau levels with the index $m = 0$ to -4 (see solid black lines) for the present data. We see that the Landau levels coincide with the minima of the longitudinal conductance. Further, we see that the same procedure of fitting Landau levels using the same value of α_{tg} works well for the same trace "2" measured at a larger range of V_{tg} and B as shown in Fig. B.1 (b). Using this value of lever arm, we can now convert the voltage to charge carrier density n in Fig. B.1 (c).

In fig. B.2 (a) and (b), we see the Landau fan measurements where the conductance traces at zero magnetic field are indicated by the blue "3" and red "4" traces in Fig. 7.10 (b). As explained in the main text, trace "3" is obtained by sweeping the gate voltages in a direction perpendicular to the major line similar to trace "1" in accordance with the equation $V_{bg} = 0.143 \times V_{tg} + 2.722$. While trace "4" is swept along the direction of trace "2" according to the equation $V_{bg} = 3.2 - 1.4 \times (V_{tg} + 1.32)$. Therefore, we use the values of α_{tg} , α_{bg} and the ratio $\frac{\Delta V_{bg}}{\Delta V_{tg}}$ from Fig. 7.4 for trace "3" and those obtained above in Fig. B.1 for trace "4" to calculate α_{eff} using eq.7.9 and fit the solid black lines corresponding to the Landau levels for $m = -1$ to -4 . Once again, we see that the Landau levels fit perfectly to the minima of longitudinal conductance.

Overall, we see that this sample is extremely stable and that the value of the lever arm extracted is consistent across several Landau fan measurements.

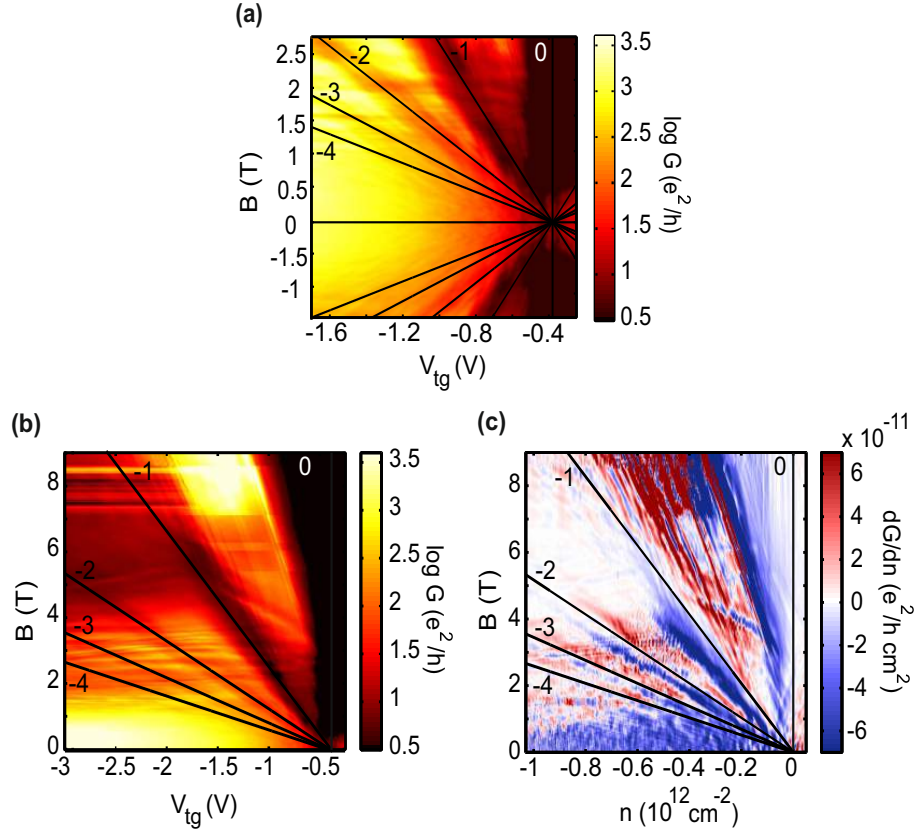


Figure B.1.: (a) Longitudinal differential conductance G as a function of the top gate voltage V_{tg} and the perpendicular magnetic field B . The conductance trace at $B = 0$ T is the red trace "2" shown in Fig. 7.9 (b). The solid black lines indicate the Landau levels from the index $m = 0$ to -4 . (b) Same as (a) but for a larger range of V_{tg} and B . (c) Derivative of differential longitudinal conductance as a function of the charge carrier density n and the magnetic field B .

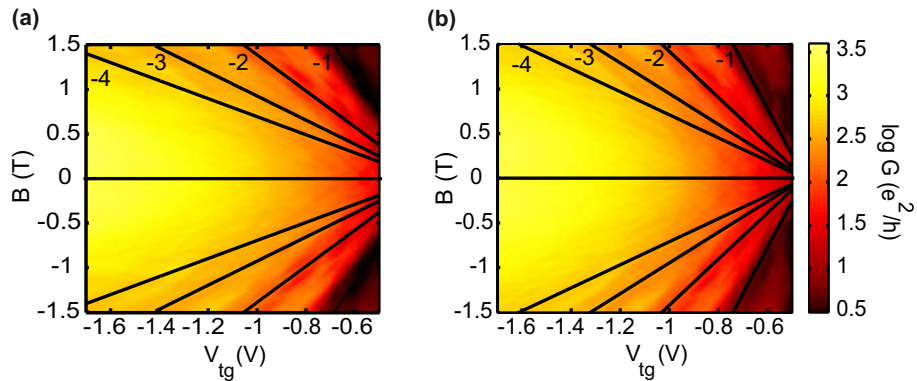


Figure B.2.: Differential longitudinal conductance G as a function of the top gate voltage V_{tg} and the perpendicular magnetic field B . The conductance trace at $B = 0$ T is the blue (red) trace "3" ("4") shown in Fig. 7.10 (b). The solid black lines indicate the Landau levels from the index $m = -1$ to -4 .

C. Transport through gate defined bilayer graphene QPC

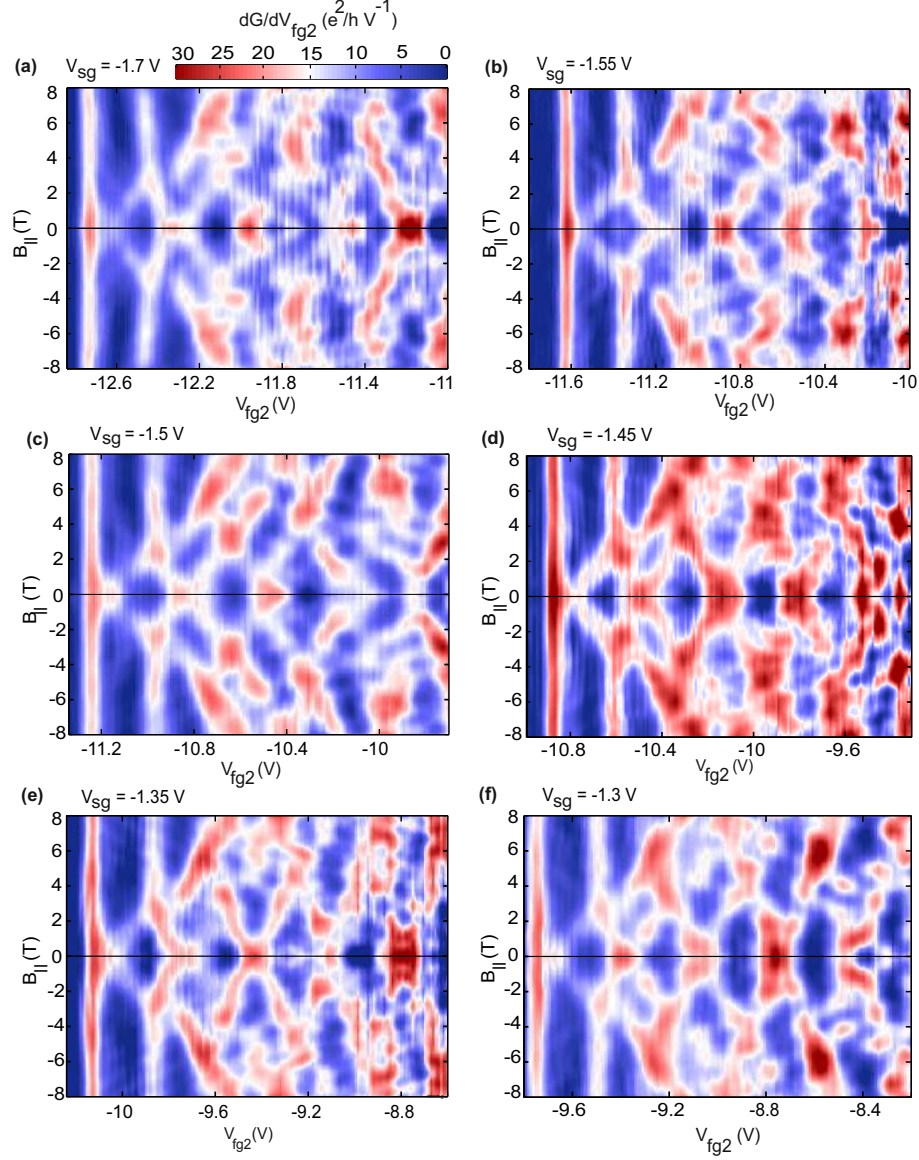


Figure C.1.: Transconductance dG/dV_{fg2} as a function of the side gate voltage V_{fg2} and the parallel magnetic field $B_{||}$ for different values of the side gate voltage V_{sg} . The back gate voltage varies according to $V_{bg} = -1.256 \times V_{sg}$ such that displacement field varies along the black arrow shown in Fig. 9.2 (a). Color scale is the same for all the panels as shown in (a).

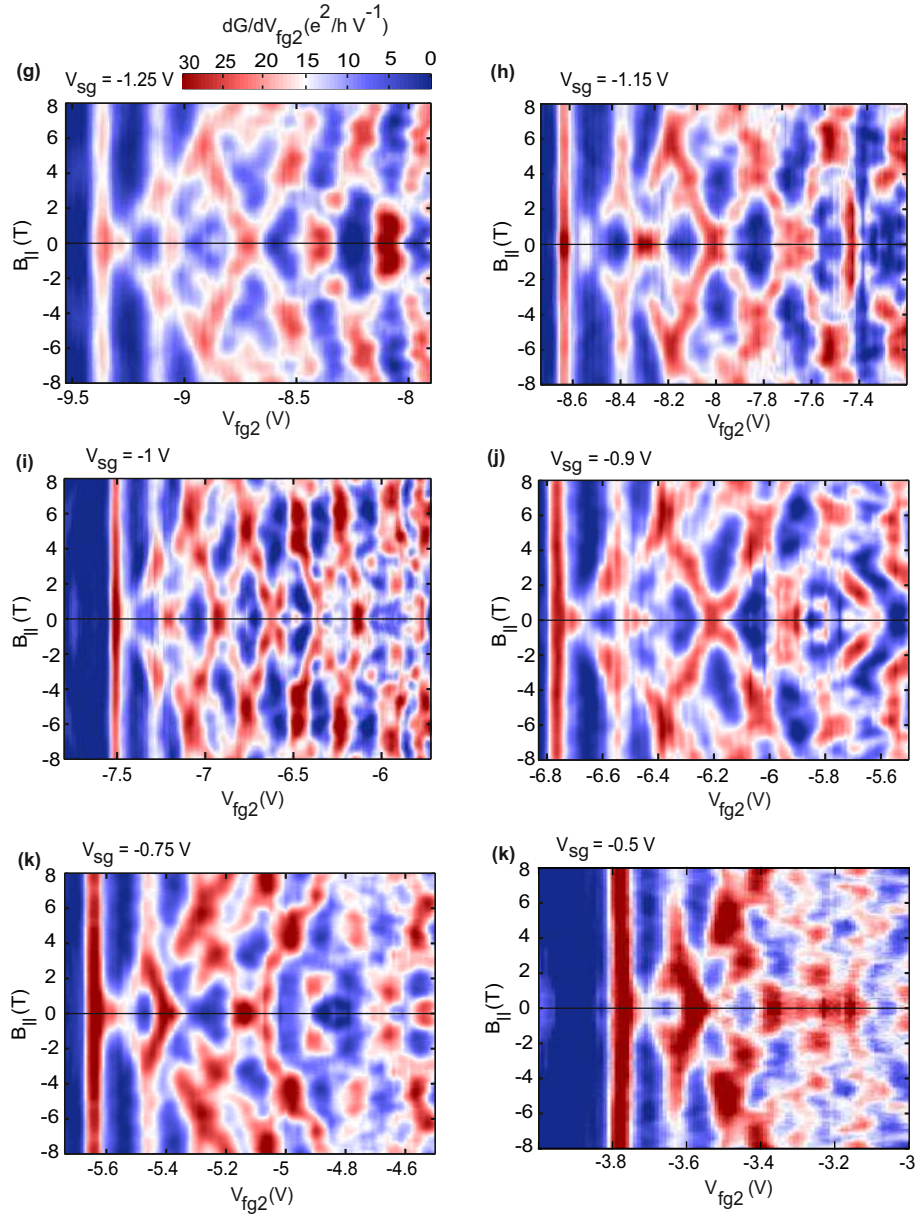
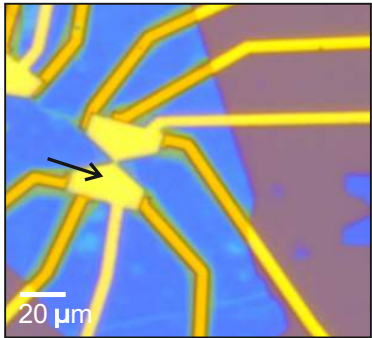
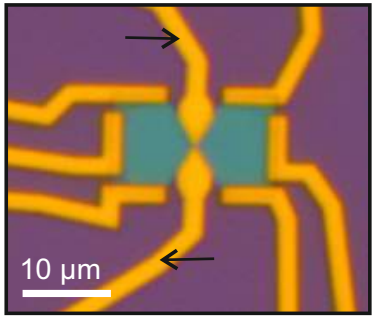
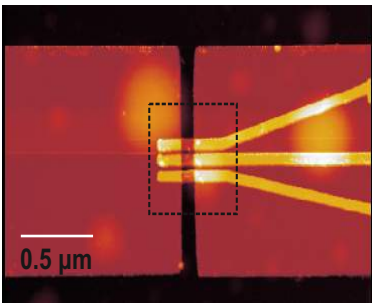
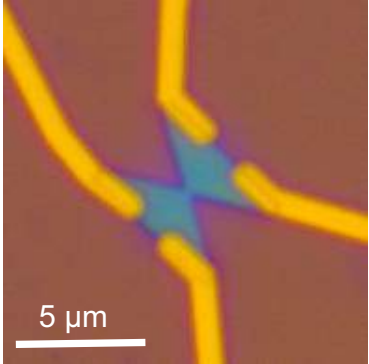
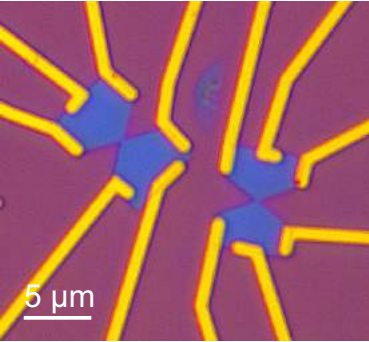


Figure C.2.: Similar to Fig. C.1 for more values of the side gate voltage V_{sg} .

D. List of samples

Device	Specifications	Measurements
	<ul style="list-style-type: none"> • hBN encapsulated graphene nanoconstriction • 6 Cr/Au side contacts • 1 Cr/Au global top gate (see black arrow) 	<ul style="list-style-type: none"> • Observation of quantized conductance kinks due to bulk states (See section 7.4) • Effect of top gate on localized edge states (See section 7.4.3) • Quantum Hall measurements to study the evolution of bulk and localized states (See section 8.2)
	<ul style="list-style-type: none"> • hBN encapsulated graphene nanoconstriction • 6 Cr/Au side contacts • 2 Cr/Au top gates (see black arrows) 	<ul style="list-style-type: none"> • Observation of quantized conductance kinks • Non-linear gate lever arm measurements (see section 7.5.1)
	<ul style="list-style-type: none"> • hBN encapsulated bilayer graphene nanoconstriction on a graphite back gate • 4 Cr/Au side contacts • 2 Cr/Au split gates • 3 Cr/Au finger gates 	<ul style="list-style-type: none"> • Quantized conductance and formation of sub-bands (See section 9.4) • Spin-splitting of sub-bands (See section 9.5) • Observation of 0.7 analog feature (See section 9.9)

Device	Specifications	Measurements
	<ul style="list-style-type: none"> • hBN encapsulated graphene nanoconstriction • 4 Cr/Au side contacts 	<ul style="list-style-type: none"> • Fabry - Pérot interferences in an n-p-n junction formed using the tip of a scanning gate microscope [279]. • Polarized SGM tip is used to create a movable and circular Veselago lens in the graphene QPC [266]. • Detection and manipulation of whispering gallery modes through a circular p-n junction [280].
	<ul style="list-style-type: none"> • hBN encapsulated graphene nanoconstriction • 4 Cr/Au side contacts 	<ul style="list-style-type: none"> • Detrimental influence of antidots along the edges of QPC in quantum Hall regime [281]. • Topological breakdown of graphene quantum Hall edge channels shows electron-hole symmetry [282]. • Probing the interference regime in antidots based graphene nano-quantum hall interferometer [283]

A. Directory of figures

Chapter no.	Figure no.	Location	Matlab file
3	3.2	/Directory/Chapter_3/Chap_3_Fig_2.pdf	Fig. 3.2 (b) - n vs vtg_diff n0.m Fig. 3.2 (c)-(e) - n vs vtg_diff nT.m
	3.3	/Directory/Chapter_3/Chap_3_Fig_3.pdf	Fig. 3.3 (a) - length scales plot_diff mu.m Fig. 3.3 (a) - length scales plot_diff n0.m Fig. 3.3 (a) - length scales plot_diff nT.m
6	6.1	/Directory/Chapter_6/Chap_6_Fig_1.pdf	
	6.2	/Directory/Chapter_6/Chap_6_Fig_2.pdf	
7	7.1	/Directory/Chapter_7/Chap_7_Fig_1.pdf	
	7.2	/Directory/Chapter_7/Chap_7_Fig_2.pdf	
	7.3	/Directory/Chapter_7/Chap_7_Fig_3.pdf	Fig. 7.3 (a) - 035_Lever arm map.m Fig. 7.3 (b) - 057_G vs Vtg_single trace.m Fig. 7.3 (d) - 079_Bias_spec.m
	7.4	/Directory/Chapter_7/Chap_7_Fig_4.pdf	069_Landau_fan.m
	7.5	/Directory/Chapter_7/Chap_7_Fig_5.pdf	057_FFT_single trace.m
	7.6	/Directory/Chapter_7/Chap_7_Fig_6.pdf	057_FFT_single trace.m
	7.7	/Directory/Chapter_7/Chap_7_Fig_7.pdf	057_FFT_single trace.m
	7.8	/Directory/Chapter_7/Chap_7_Fig_8.pdf	Fig. 7.8 (a) - 080_lever_arm.m Fig. 7.8 (b), (c) - 084_Lever arm map.m
	7.9	/Directory/Chapter_7/Chap_7_Fig_9.pdf	084_Lever arm map.m
	7.10	/Directory/Chapter_7/Chap_7_Fig_10.pdf	084_Lever arm map.m
	7.11	/Directory/Chapter_7/Chap_7_Fig_11.pdf	
	7.12	/Directory/Chapter_7/Chap_7_Fig_12.pdf	
	7.13	/Directory/Chapter_7/Chap_7_Fig_13.pdf	Fig. 7.8 (b) - U_vs_E.m Fig. 7.8 (c) - U_vs_E_conductance.m
8	8.1	/Directory/Chapter_8/Chap_8_Fig_1.pdf	Fig. 8.1 (a) - 069_Landau_fan.m Fig. 8.1 (b) - 092 and 095_Landau_fan.m
	8.2	/Directory/Chapter_8/Chap_8_Fig_2.pdf	Fig. 8.2 (a) - 125_Landau_fan.m Fig. 8.2 (b) - 128_Landau_fan.m
	8.3	/Directory/Chapter_8/Chap_8_Fig_3.pdf	Fig. 8.3 (a) - perfect.m Fig. 8.3 (b) - Purple.m Fig. 8.3 (c) - Green.m
	8.4	/Directory/Chapter_8/Chap_8_Fig_4.pdf	Fig. 8.4 (a) - Green_EW.m Fig. 8.4 (a) - Green_EW_lines.m
	8.5	/Directory/Chapter_8/Chap_8_Fig_5.pdf	Fig. 8.5 (a) - Rescaling_A.m
	8.5		Fig. 8.5 (b) - Rescaling_B.m
	8.5		Fig. 8.5 (c) - Rescaling_C.m
	8.5		Fig. 8.5 (d) - Rescaling_D.m
	8.6	/Directory/Chapter_8/Chap_8_Fig_6.pdf	Flo_dat.m
132	8.7	/Directory/Chapter_8/Chap_8_Fig_7.pdf	Fig. 8.7 (a) - Green.m Fig. 8.7 (b) - 069_Landau_fan.m Fig. 8.7 (b) - Perfect_overlay.m Fig. 8.7 (c) - Flo_dat.m

Chapter no.	Figure no.	Location	Matlab file
9	9.1	/Directory/Chapter_9/Chap_9_Fig_1.pdf	
	9.2	/Directory/Chapter_9/Chap_9_Fig_2.pdf	
	9.3	/Directory/Chapter_9/Chap_9_Fig_3.pdf	
	9.4	/Directory/Chapter_9/Chap_9_Fig_4.pdf	120_Luca_draft.m
	9.5	/Directory/Chapter_9/Chap_9_Fig_5.pdf	120_Luca_draft.m
	9.6	/Directory/Chapter_9/Chap_9_Fig_6.pdf	sub_band_spacing.m
	9.7	/Directory/Chapter_9/Chap_9_Fig_7.pdf	120_Luca_draft.m
	9.8	/Directory/Chapter_9/Chap_9_Fig_8.pdf	158_Luca.m 161_Luca.m 173_Luca.m
	9.9	/Directory/Chapter_9/Chap_9_Fig_9.pdf	displacement_field.m
Appendix	B.1	/Directory/Appendix_B/Fig. B_1.pdf	Fig. B.1 (a) - 092 and 095_Landau_fan.m Fig. B.1 (b), (c) - Full_Landau_fan.m Fig. B.1 (b), (c) - Full_Landau_fan_part_2.m
	B.2	/Directory/Appendix_B/Fig. B_2.pdf	125_Landau_fan.m 128_Landau_fan.m
	C.1	/Directory/Appendix_C/Fig. C_1.pdf	Fig. C.1 (a) - 160_Luca.m Fig. C.1 (b), (d), (e) - 173_Luca.m Fig. C.1 (c) - 157_Luca.m
	C.2	/Directory/Appendix_C/Fig. C_2.pdf	Fig. C.2 (g), (h) - 173_Luca.m Fig. C.2 (i) - 157_Luca.m Fig. C.2 (j) - 161_Luca.m Fig. C.2 (k) - 158_Luca.m Fig. C.2 (l) - 159_Luca.m

Publications

Quantum Hall nano-interferometer in graphene

N. Moreau, B. Brun, S. Somanchi, K. Watanabe, T. Taniguchi, C. Stampfer, and B. Hackens
arXiv:2110.07979

Graphene whisperitronics: transducing whispering gallery modes into electronic transport

B. Brun, V.-H. Nguyen, N. Moreau, S. Somanchi, K. Watanabe, T. Taniguchi, J.-C. Charlier, C. Stampfer, and B. Hackens
Nano Lett. 22, 1, 128-134 (2022)

Contacts and upstream modes explain the electron-hole asymmetry in the graphene quantum Hall regime

N. Moreau, B. Brun, S. Somanchi, K. Watanabe, T. Taniguchi, C. Stampfer, and B. Hackens
Phys. Rev. B 104, L201406 (2021)

Upstream modes and antidots poison graphene quantum Hall effect

B. Brun, N. Moreau, S. Somanchi, K. Watanabe, T. Taniguchi, C. Stampfer, and B. Hackens
Nat. Commun. 12, 4265 (2021)

Observation of the Spin-Orbit Gap in Bilayer Graphene by One-Dimensional Ballistic Transport

L. Banszerus, B. Frohn, T. Fabian, S. Somanchi, Epping, M. Müller, D. Neumaier, K. Watanabe, T. Taniguchi, F. Libisch, B. Beschoten, F. Hassler, and C. Stampfer
Phys. Rev. Lett. 124, 177701, 2020

Optimizing Dirac fermions quasi-confinement by potential smoothness engineering

B. Brun, N. Moreau, S. Somanchi, V.-H. Nguyen, A. Mreńca-Kolasinńska, K. Watanabe, T. Taniguchi, J.-C. Charlier, C. Stampfer, and B. Hackens
2D Mater. 7 025037 (2020)

Imaging Dirac fermions flow through a circular Veselago lens

B. Brun, N. Moreau, S. Somanchi, V.-H. Nguyen, K. Watanabe, T. Taniguchi, J.-C. Charlier, C. Stampfer, and B. Hackens

Phys. Rev. B 100, 041401 (2019)

From diffusive to ballistic transport in etched graphene constrictions and nanoribbons

S. Somanchi, B. Terrés, J. Peiro, M. Staggenborg, K. Watanabe, T. Taniguchi, B. Beschoten, and C. Stampfer

Annalen der Physik 529, 1700082 (2017)

Bibliography

- ¹G. E. Moore, “Cramming more components onto integrated circuits”, *IEEE J Solid-State Circuits* **11**, 33–35 (2006).
- ²Intel 14 nm technology, (2022) <https://www.intel.com/content/www/us/en/silicon-innovations/intel-14nm-technology.html>.
- ³M. LaPedus, *Update: intel to build fab for 14-nm chips*, (Feb. 2011) <https://www.eetimes.com/update-intel-to-build-fab-for-14-nm-chips/>.
- ⁴I. newsroom, *Intel technology and manufacturing day in china showcases 10 nm updates, fpga progress and industry’s first 64-layer 3d nand for data center*, (Sept. 2017) <https://newsroom.intel.com/news/intel-technology-manufacturing-day-china/>.
- ⁵D. I. Cutress, *Intel cfo: our 10nm will be less profitable than 22nm*, (Mar. 2020) <https://www.anandtech.com/show/15580/intel-cfo-our-10nm-will-be-less-profitable-than-22nm>.
- ⁶K. Sotthewes, V. Geskin, R. Heimbuch, A. Kumar, and H. J. W. Zandvliet, “Research update: molecular electronics: the single-molecule switch and transistor”, *APL Materials* **2**, 010701 (2014).
- ⁷M. Fuechsle, J. A. Miwa, S. Mahapatra, H. Ryu, S. Lee, O. Warschkow, L. C. L. Hollenberg, G. Klimeck, and M. Y. Simmons, “A single-atom transistor”, *Nature Nanotechnology* **7**, 242–246 (2012).
- ⁸S. Datta, *Electronic transport in mesoscopic systems*, Cambridge Studies in Semiconductor Physics and Microelectronic Engineering (Cambridge University Press, 1995).
- ⁹Y. Imry, “Mesoscopic physics and the fundamentals of quantum mechanics”, *Physica Scripta* **T76**, 171 (1998).
- ¹⁰Y. B. Band and Y. Avishai, “13 - low-dimensional quantum systems”, in *Quantum mechanics with applications to nanotechnology and information science*, edited by Y. B. Band and Y. Avishai (Academic Press, Amsterdam, 2013), pp. 749–823.
- ¹¹C. Beenakker and H. van Houten, “Quantum transport in semiconductor nanostructures”, in *Semiconductor heterostructures and nanostructures*, Vol. 44, edited by H. Ehrenreich and D. Turnbull, Solid State Physics (Academic Press, 1991), pp. 1–228.
- ¹²B. J. van Wees, H. van Houten, C. W. J. Beenakker, J. G. Williamson, L. P. Kouwenhoven, D. van der Marel, and C. T. Foxon, “Quantized conductance of point contacts in a two-dimensional electron gas”, *Phys. Rev. Lett.* **60**, 848–850 (1988).
- ¹³V. Marigliano Ramaglia, F. Ventriglia, and G. P. Zucchelli, “Aharonov-bohm effect in a cavity formed by two quantum point contacts”, *Phys. Rev. B* **52**, 8372–8378 (1995).
- ¹⁴P. Khatua, B. Bansal, and D. Shahar, “Single-slit electron diffraction with aharonov-bohm phase: feynman’s thought experiment with quantum point contacts”, *Phys. Rev. Lett.* **112**, 010403 (2014).

- ¹⁵R. P. Taylor, A. S. Sachrajda, P. Zawadzki, P. T. Coleridge, and J. A. Adams, “Aharonov-bohm oscillations in the coulomb blockade regime”, *Phys. Rev. Lett.* **69**, 1989–1992 (1992).
- ¹⁶S. Maeda, S. Miyamoto, M. H. Fauzi, K. Nagase, K. Sato, and Y. Hirayama, “Fabry-pérot interference in a triple-gated quantum point contact”, *Applied Physics Letters* **109**, 143509 (2016).
- ¹⁷P. Roulleau, F. Portier, P. Roche, A. Cavanna, G. Faini, U. Gennser, and D. Mailly, “Tuning decoherence with a voltage probe”, *Phys. Rev. Lett.* **102**, 236802 (2009).
- ¹⁸D. Loss and D. P. DiVincenzo, “Quantum computation with quantum dots”, *Phys. Rev. A* **57**, 120–126 (1998).
- ¹⁹M. Field, C. G. Smith, M. Pepper, D. A. Ritchie, J. E. F. Frost, G. A. C. Jones, and D. G. Hasko, “Measurements of coulomb blockade with a noninvasive voltage probe”, *Phys. Rev. Lett.* **70**, 1311–1314 (1993).
- ²⁰A. E. Gildemeister, T. Ihn, R. Schleser, K. Ensslin, D. C. Driscoll, and A. C. Gossard, “Imaging a coupled quantum dot-quantum point contact system”, *Journal of Applied Physics* **102**, 083703 (2007).
- ²¹L. M. K. Vandersypen, J. M. Elzerman, R. N. Schouten, L. H. Willems van Beveren, R. Hanson, and L. P. Kouwenhoven, “Real-time detection of single-electron tunneling using a quantum point contact”, *Applied Physics Letters* **85**, 4394–4396 (2004).
- ²²D. Wallin, A. Fuhrer, L. E. Fröberg, L. Samuelson, H. Q. Xu, S. Hofling, and A. Forchel, “Detection of charge states in nanowire quantum dots using a quantum point contact”, *Applied Physics Letters* **90**, 172112 (2007).
- ²³J. M. Elzerman, R. Hanson, L. H. Willems van Beveren, B. Witkamp, L. M. K. Vandersypen, and L. P. Kouwenhoven, “Single-shot read-out of an individual electron spin in a quantum dot”, *Nature* **430**, 431–435 (2004).
- ²⁴T. Obata, M. Pioro-Ladrière, Y. Tokura, Y.-S. Shin, T. Kubo, K. Yoshida, T. Taniyama, and S. Tarucha, “Coherent manipulation of individual electron spin in a double quantum dot integrated with a micromagnet”, *Phys. Rev. B* **81**, 085317 (2010).
- ²⁵E. A. Laird, C. Barthel, E. I. Rashba, C. M. Marcus, M. P. Hanson, and A. C. Gossard, “Hyperfine-mediated gate-driven electron spin resonance”, *Phys. Rev. Lett.* **99**, 246601 (2007).
- ²⁶E. A. Laird, C. Barthel, E. I. Rashba, C. M. Marcus, M. P. Hanson, and A. C. Gossard, “A new mechanism of electric dipole spin resonance: hyperfine coupling in quantum dots”, *Semiconductor Science and Technology* **24**, 064004 (2009).
- ²⁷E. A. Laird, J. M. Taylor, D. P. DiVincenzo, C. M. Marcus, M. P. Hanson, and A. C. Gossard, “Coherent spin manipulation in an exchange-only qubit”, *Phys. Rev. B* **82**, 075403 (2010).
- ²⁸J. R. Petta, A. C. Johnson, J. M. Taylor, E. A. Laird, A. Yacoby, M. D. Lukin, C. M. Marcus, M. P. Hanson, and A. C. Gossard, “Coherent manipulation of coupled electron spins in semiconductor quantum dots”, *Science* **309**, 2180–2184 (2005).
- ²⁹T. Simonite, *Intel puts the brakes on moore’s law*, (Mar. 2016) <https://www.technologyreview.com/s/601102/intel-puts-the-brakes-on-moores-law/>..
- ³⁰D. R. Cooper, B. D’Anjou, N. Ghattamaneni, B. Harack, M. Hilke, A. Horth, N. Majlis, M. Massicotte, L. Vandsburger, E. Whiteway, and V. Yu, “Experimental review of graphene”, *ISRN Condensed Matter Physics* **2012**, 501686 (2012).

-
- ³¹M. I. Katsnelson, K. S. Novoselov, and A. K. Geim, “Chiral tunnelling and the Klein paradox in graphene”, *Nature Physics* **2**, 620–625 (2006).
- ³²V. P. Gusynin and S. G. Sharapov, “Unconventional integer quantum hall effect in graphene”, *Phys. Rev. Lett.* **95**, 146801 (2005).
- ³³E. H. Hwang and S. Das Sarma, “Acoustic phonon scattering limited carrier mobility in two-dimensional extrinsic graphene”, *Phys. Rev. B* **77**, 115449 (2008).
- ³⁴Y. Zhou and M. W. Wu, “Electron spin relaxation in graphene from a microscopic approach: role of electron-electron interaction”, *Phys. Rev. B* **82**, 085304 (2010).
- ³⁵C. Ertler, S. Konschuh, M. Gmitra, and J. Fabian, “Electron spin relaxation in graphene: the role of the substrate”, *Phys. Rev. B* **80**, 041405 (2009).
- ³⁶B. Trauzettel, D. V. Bulaev, D. Loss, and G. Burkard, “Spin qubits in graphene quantum dots”, *Nature Physics* **3**, 192–196 (2007).
- ³⁷Y.-W. Son, M. L. Cohen, and S. G. Louie, “Energy gaps in graphene nanoribbons”, *Phys. Rev. Lett.* **97**, 216803 (2006).
- ³⁸S. Samaddar, I. Yudhistira, S. Adam, H. Courtois, and C. B. Winkelmann, “Charge puddles in graphene near the Dirac point”, *Phys. Rev. Lett.* **116**, 126804 (2016).
- ³⁹J. Martin, N. Akerman, G. Ulbricht, T. Lohmann, J. H. Smet, K. von Klitzing, and A. Yacoby, “Observation of electron-hole puddles in graphene using a scanning single-electron transistor”, *Nature Physics* **4**, 144–148 (2007).
- ⁴⁰N. Tombros, A. Veligura, J. Junesch, M. H. D. Guimarães, I. J. Vera-Marun, H. T. Jonkman, and B. J. van Wees, “Quantized conductance of a suspended graphene nanoconstriction”, *Nature Physics* **7**, 697–700 (2011).
- ⁴¹C. R. Dean, A. F. Young, I. Meric, C. Lee, L. Wang, S. Sorgenfrei, K. Watanabe, T. Taniguchi, P. Kim, K. L. Shepard, and J. Hone, “Boron nitride substrates for high-quality graphene electronics”, *Nature Nanotechnology* **5**, 722–726 (2010).
- ⁴²B. Terrés, L. A. Chizhova, F. Libisch, J. Peiro, D. Jörger, S. Engels, A. Girschik, K. Watanabe, T. Taniguchi, S. V. Rotkin, J. Burgdörfer, and C. Stampfer, “Size quantization of Dirac fermions in graphene constrictions”, *Nature Communications* **7**, 11528 (2016).
- ⁴³Y. Zhang, T.-T. Tang, C. Girit, Z. Hao, M. C. Martin, A. Zettl, M. F. Crommie, Y. R. Shen, and F. Wang, “Direct observation of a widely tunable bandgap in bilayer graphene”, *Nature* **459**, 820–823 (2009).
- ⁴⁴J. B. Oostinga, H. B. Heersche, X. Liu, A. F. Morpurgo, and L. M. K. Vandersypen, “Gate-induced insulating state in bilayer graphene devices”, *Nature Materials* **7**, 151–157 (2008).
- ⁴⁵E. McCann, “Interlayer asymmetry gap in the electronic band structure of bilayer graphene”, *Physica Status Solidi (b)* **244**, 4112–4117 (2007).
- ⁴⁶K. F. Mak, C. H. Lui, J. Shan, and T. F. Heinz, “Observation of an electric-field-induced band gap in bilayer graphene by infrared spectroscopy”, *Phys. Rev. Lett.* **102**, 256405 (2009).
- ⁴⁷A. Ramasubramanian, D. Naveh, and E. Towe, “Tunable band gaps in bilayer graphene heterostructures”, *Nano Lett.* **11**, 1070–1075 (2011).
- ⁴⁸H. van Houten and C. Beenakker, “Quantum point contacts”, *Physics Today* **49**, 22–27 (1996).

- ⁴⁹L.-X. Zhang, J. P. Leburton, R. Hanson, and L. P. Kouwenhoven, “Engineering the quantum point contact response to single-electron charging in a few-electron quantum-dot circuit”, *Applied Physics Letters* **85**, 2628–2630 (2004).
- ⁵⁰Z. Lei, C. A. Lehner, E. Cheah, C. Mittag, M. Karalic, W. Wegscheider, K. Ensslin, and T. Ihn, “Gate-defined quantum point contact in an insb two-dimensional electron gas”, *Phys. Rev. Research* **3**, 023042 (2021).
- ⁵¹H. van Houten, C. Beenakker, and B. van Wees, “Chapter 2: quantum point contacts”, *Semiconductors and Semimetals* **35**, edited by M. Reed, 9–112 (1992).
- ⁵²Y. V. Sharvin, “On the possible method for studying fermi surfaces”, *Zh. Eksperim. i Teor. Fiz.* **48** (1965).
- ⁵³S. I. Bozhko, “Focusing of electrons by a transverse magnetic field”, *JETP Letters* **99**, 487–495 (2014).
- ⁵⁴I. K. Yanson, I. O. Kulik, and A. G. Batrak, “Point-contact spectroscopy of electron-phonon interaction in normal-metal single crystals”, *Journal of Low Temperature Physics* **42**, 527–556 (1981).
- ⁵⁵A. Akimenko, A. Verkin, N. Ponomarenko, and I. Yanson, “Point-contact spectroscopy of magnons in metals”, *Physica B+C* **107**, 369–370 (1981).
- ⁵⁶I. K. Yanson, V. V. Fisun, R. Hesper, A. V. Khotkevich, J. M. Krans, J. A. Mydosh, and J. M. van Ruitenbeek, “Size dependence of kondo scattering in point contacts”, *Phys. Rev. Lett.* **74**, 302–305 (1995).
- ⁵⁷A. Furusaki, H. Takayanagi, and M. Tsukada, “Josephson effect of the superconducting quantum point contact”, *Phys. Rev. B* **45**, 10563–10575 (1992).
- ⁵⁸Y. G. Naidyuk, O. E. Kvitnitskaya, N. V. Gamayunova, D. L. Bashlakov, L. V. Tyutrina, G. Fuchs, R. Hühne, D. A. Chareev, and A. N. Vasiliev, “Superconducting gaps in fese studied by soft point-contact andreev reflection spectroscopy”, *Phys. Rev. B* **96**, 094517 (2017).
- ⁵⁹G. E. Blonder, M. Tinkham, and T. M. Klapwijk, “Transition from metallic to tunneling regimes in superconducting microconstrictions: excess current, charge imbalance, and supercurrent conversion”, *Phys. Rev. B* **25**, 4515–4532 (1982).
- ⁶⁰Y.-h. Zhang, P. Wahl, and K. Kern, “Quantum point contact microscopy”, *Nano Lett* **11**, 3838–3843 (2011).
- ⁶¹T. J. Thornton, M. Pepper, H. Ahmed, D. Andrews, and G. J. Davies, “One-dimensional conduction in the 2d electron gas of a GaAs–AlGaAs Heterojunction”, *Phys. Rev. Lett.* **56**, 1198–1201 (1986).
- ⁶²K. F. Berggren, T. J. Thornton, D. J. Newson, and M. Pepper, “Magnetic depopulation of 1d subbands in a narrow 2d electron gas in a GaAs/AlGaAs Heterojunction”, *Phys. Rev. Lett.* **57**, 1769–1772 (1986).
- ⁶³D. A. Wharam, T. J. Thornton, R. Newbury, M. Pepper, H. Ahmed, J. E. F. Frost, D. G. Hasko, D. C. Peacock, D. A. Ritchie, and G. A. C. Jones, “One-dimensional transport and the quantisation of the ballistic resistance”, *Journal of Physics C: Solid State Physics* **21**, L209–L214 (1988).
- ⁶⁴K.-F. Berggren and M. Pepper, “Electrons in one dimension”, *Philos Trans A Math Phys Eng Sci* **368**, 1141–1162 (2010).
- ⁶⁵K. J. Thomas, J. T. Nicholls, N. J. Appleyard, M. Y. Simmons, M. Pepper, D. R. Mace, W. R. Tribe, and D. A. Ritchie, “Interaction effects in a one-dimensional constriction”, *Phys. Rev. B* **58**, 4846–4852 (1998).

- ⁶⁶Y. Takahashi, A. Fujiwara, and K. Murase, “Quantized conductance in a small one-dimensional si wire on a thin silicon-on-insulator substrate fabricated using SiN-film-masked oxidation”, *Semiconductor Science and Technology* **13**, 1047–1051 (1998).
- ⁶⁷H. Lehmann, T. Benter, I. von Ahnen, J. Jacob, T. Matsuyama, U. Merkt, U. Kunze, A. D. Wieck, D. Reuter, C. Heyn, and W. Hansen, “Spin-resolved conductance quantization in InAs”, *Semiconductor Science and Technology* **29**, 075010 (2014).
- ⁶⁸B. Brun, F. Martins, S. Faniel, B. Hackens, A. Cavanna, C. Ulysse, A. Ouerghi, U. Gennser, D. Mailly, P. Simon, S. Huant, V. Bayot, M. Sanquer, and H. Sellier, “Electron phase shift at the zero-bias anomaly of quantum point contacts”, *Phys. Rev. Lett.* **116**, 136801 (2016).
- ⁶⁹Y. Meir, “The theory of the ‘0.7 anomaly’ in quantum point contacts”, *Journal of Physics: Condensed Matter* **20**, 164208 (2008).
- ⁷⁰H. Lind, I. I. Yakimenko, and K.-F. Berggren, “Electric-field control of magnetization in biased semiconductor quantum wires and point contacts”, *Phys. Rev. B* **83**, 075308 (2011).
- ⁷¹C.-K. Wang and K.-F. Berggren, “Spin splitting of subbands in quasi-one-dimensional electron quantum channels”, *Phys. Rev. B* **54**, R14257–R14260 (1996).
- ⁷²P. Michael and J. Bird, “The 0.7 feature and interactions in one-dimensional systems”, *Journal of Physics: Condensed Matter* **20**, 160301 (2008).
- ⁷³N. Bhandari, P. P. Das, M. Cahay, R. S. Newrock, and S. T. Herbert, “Observation of a 0.5 conductance plateau in asymmetrically biased gaas quantum point contact”, *Applied Physics Letters* **101**, 102401 (2012).
- ⁷⁴F. Bauer, J. Heyder, E. Schubert, D. Borowsky, D. Taubert, B. Bruognolo, D. Schuh, W. Wegscheider, J. von Delft, and S. Ludwig, “Microscopic origin of the ‘0.7-anomaly’ in quantum point contacts”, *Nature* **501**, 73–78 (2013).
- ⁷⁵D. H. Schimmel, B. Bruognolo, and J. von Delft, “Spin fluctuations in the 0.7 anomaly in quantum point contacts”, *Phys. Rev. Lett.* **119**, 196401 (2017).
- ⁷⁶Y. Ji, Y. Chung, D. Sprinzak, M. Heiblum, D. Mahalu, and H. Shtrikman, “An electronic mach-zehnder interferometer”, *Nature* **422**, 415–418 (2003).
- ⁷⁷P. Chuang, S.-C. Ho, L. W. Smith, F. Sfigakis, M. Pepper, C.-H. Chen, J.-C. Fan, J. P. Griffiths, I. Farrer, H. E. Beere, G. A. C. Jones, D. A. Ritchie, and T.-M. Chen, “All-electric all-semiconductor spin field-effect transistors”, *Nature Nanotechnology* **10**, 35–39 (2014).
- ⁷⁸K. Lai, W. Pan, D. C. Tsui, and Y.-H. Xie, “Observation of the apparent metal-insulator transition of high-mobility two-dimensional electron system in a Si/Si_{1-x}Ge_x heterostructure”, *Applied Physics Letters* **84**, 302–304 (2004).
- ⁷⁹M. A. Wilde, M. Rhode, C. Heyn, D. Heitmann, D. Grundler, U. Zeitler, F. Schäffler, and R. J. Haug, “Direct measurements of the spin and valley splittings in the magnetization of a Si/SiGe quantum well in tilted magnetic fields”, *Phys. Rev. B* **72**, 165429 (2005).
- ⁸⁰S. L. Wang, P. C. van Son, B. J. van Wees, and T. M. Klapwijk, “Quantum conductance of point contacts in si inversion layers”, *Phys. Rev. B* **46**, 12873–12876 (1992).

- ⁸¹D Tobben, D. A. Wharam, G Abstreiter, J. P. Kolthaus, and F Schaffler, “Ballistic electron transport through a quantum point contact defined in a Si/Si_{0.7}Ge_{0.3} heterostructure”, [Semiconductor Science and Technology](#) **10**, 711–714 (1995).
- ⁸²G. Frucci, L. Di Gaspare, A. Notargiacomo, D. Spirito, F. Evangelisti, A. Di Gaspare, and E. Giovine, “Conductance anomalies in quantum point contacts”, 190–193 (2009).
- ⁸³E. Kawakami, P. Scarlino, D. R. Ward, F. R. Braakman, D. E. Savage, M. G. Lagally, M. Friesen, S. N. Coppersmith, M. A. Eriksson, and L. M. K. Vandersypen, “Electrical control of a long-lived spin qubit in a si/sige quantum dot”, [Nature Nanotechnology](#) **9**, 666–670 (2014).
- ⁸⁴P. P. Das, K. B. Chetry, N. Bhandari, J. Wan, M. Cahay, R. S. Newrock, and S. T. Herbert, “Understanding the anomalous conductance plateau in asymmetrically biased InAs/In_{0.52}Al_{0.48}As quantum point contacts - A step towards a tunable all electric spin valve”, [Applied Physics Letters](#) **99**, 122105 (2011).
- ⁸⁵P. P. Das, A. Jones, M. Cahay, S. Kalita, S. S. Mal, N. S. Sterin, T. R. Yadunath, M. Advaita, and S. T. Herbert, “Dependence of the $0.5 \times (2e^2/h)$ conductance plateau on the aspect ratio of InAs quantum point contacts with in-plane side gates”, [Journal of Applied Physics](#) **121**, 083901 (2017).
- ⁸⁶S. Heedt, W. Prost, J. Schubert, D. Grützmacher, and T. Schäpers, “Ballistic transport and exchange interaction in inas nanowire quantum point contacts”, [Nano Lett](#) **16**, 3116–3123 (2016).
- ⁸⁷P. Debray, S. M. S. Rahman, J. Wan, R. S. Newrock, M. Cahay, A. T. Ngo, S. E. Ulloa, S. T. Herbert, M. Muhammad, and M. Johnson, “All-electric quantum point contact spin-polarizer”, [Nature Nanotechnology](#) **4**, Article, 759–764 (2009).
- ⁸⁸K. S. Novoselov, A. K. Geim, S. V. Morozov, D. Jiang, Y. Zhang, S. V. Dubonos, I. V. Grigorieva, and A. A. Firsov, “Electric field effect in atomically thin carbon films”, [Science](#) **306**, 666–669 (2004).
- ⁸⁹K. S. Novoselov, V. I. Fal’ko, L. Colombo, P. R. Gellert, M. G. Schwab, and K. Kim, “A roadmap for graphene”, [Nature](#) **490**, 192–200 (2012).
- ⁹⁰A. K. Geim and K. S. Novoselov, “The rise of graphene”, [Nature Materials](#) **6**, 183–191 (2007).
- ⁹¹A. H. Castro Neto, F. Guinea, N. M. R. Peres, K. S. Novoselov, and A. K. Geim, “The electronic properties of graphene”, [Rev. Mod. Phys.](#) **81**, 109–162 (2009).
- ⁹²K. S. Novoselov, A. K. Geim, S. V. Morozov, D. Jiang, M. I. Katsnelson, I. V. Grigorieva, S. V. Dubonos, and A. A. Firsov, “Two-dimensional gas of massless dirac fermions in graphene”, [Nature](#) **438**, 197–200 (2005).
- ⁹³N. Stander, B. Huard, and D. Goldhaber-Gordon, “Evidence for klein tunneling in graphene p - n Junctions”, [Phys. Rev. Lett.](#) **102**, 026807 (2009).
- ⁹⁴Y. Wu, Y.-m. Lin, A. A. Bol, K. A. Jenkins, F. Xia, D. B. Farmer, Y. Zhu, and P. Avouris, “High-frequency, scaled graphene transistors on diamond-like carbon”, [Nature](#) **472**, 74–78 (2011).
- ⁹⁵Y.-M. Lin, C. Dimitrakopoulos, K. A. Jenkins, D. B. Farmer, H.-Y. Chiu, A. Grill, and P. Avouris, “100-ghz transistors from wafer-scale epitaxial graphene”, [Science](#) **327**, 662–662 (2010).
- ⁹⁶V. E. Dorgan, M.-H. Bae, and E. Pop, “Mobility and saturation velocity in graphene on sio₂”, [Applied Physics Letters](#) **97**, 082112 (2010).
- ⁹⁷J. Moser, A. Barreiro, and A. Bachtold, “Current-induced cleaning of graphene”, [Applied Physics Letters](#) **91**, 163513 (2007).

- ⁹⁸P. S. Raja, R. J. Daniel, and R. M. Thomas, “Graphene interconnect for nano scale circuits”, [2014 International Conference on Green Computing Communication and Electrical Engineering \(ICGCCEE\)](#), 1–6 (2014).
- ⁹⁹J. F. Tian, L. A. Jauregui, G. Lopez, H. Cao, and Y. P. Chen, “Ambipolar graphene field effect transistors by local metal side gates”, [Applied Physics Letters](#) **96**, 263110 (2010).
- ¹⁰⁰K. S. Novoselov, Z. Jiang, Y. Zhang, S. V. Morozov, H. L. Stormer, U. Zeitler, J. C. Maan, G. S. Boebinger, P. Kim, and A. K. Geim, “Room-temperature quantum hall effect in graphene”, [Science](#) **315**, 1379–1379 (2007).
- ¹⁰¹A. A. Balandin, S. Ghosh, W. Bao, I. Calizo, D. Teweldebrhan, F. Miao, and C. N. Lau, “Superior thermal conductivity of single-layer graphene”, [Nano Lett](#) **8**, 902–907 (2008).
- ¹⁰²R. R. Nair, P. Blake, A. N. Grigorenko, K. S. Novoselov, T. J. Booth, T. Stauber, N. M. R. Peres, and A. K. Geim, “Fine structure constant defines visual transparency of graphene”, [Science](#) **320**, 1308–1308 (2008).
- ¹⁰³Y.-Y. Choi, S. J. Kang, H.-K. Kim, W. M. Choi, and S.-I. Na, “Multilayer graphene films as transparent electrodes for organic photovoltaic devices”, [Solar Energy Materials and Solar Cells](#) **96**, 281–285 (2012).
- ¹⁰⁴J. Wu, H. A. Becerril, Z. Bao, Z. Liu, Y. Chen, and P. Peumans, “Organic solar cells with solution-processed graphene transparent electrodes”, [Applied Physics Letters](#) **92**, 263302 (2008).
- ¹⁰⁵G. Jo, M. Choe, C.-Y. Cho, J. H. Kim, W. Park, S. Lee, W.-K. Hong, T.-W. Kim, S.-J. Park, B. H. Hong, Y. H. Kahng, and T. Lee, “Large-scale patterned multi-layer graphene films as transparent conducting electrodes for GaN light-emitting diodes”, [Nanotechnology](#) **21**, 175201 (2010).
- ¹⁰⁶W. Wang, C. Shen, S. Li, J. Min, and C. Yi, “Mechanical properties of single layer graphene nanoribbons through bending experimental simulations”, [AIP Advances](#) **4**, 031333 (2014).
- ¹⁰⁷W. Han, R. K. Kawakami, M. Gmitra, and J. Fabian, “Graphene spintronics”, [Nature Nanotechnology](#) **9**, 794–807 (2014).
- ¹⁰⁸Y. Sui, T. Low, M. Lundstrom, and J. Appenzeller, “Signatures of disorder in the minimum conductivity of graphene”, [Nano Lett](#) **11**, 1319–1322 (2011).
- ¹⁰⁹M. Fujita, K. Wakabayashi, K. Nakada, and K. Kusakabe, “Peculiar localized state at zigzag graphite edge”, [Journal of the Physical Society of Japan](#) **65**, 1920–1923 (1996).
- ¹¹⁰S. Dutta and S. K. Pati, “Novel properties of graphene nanoribbons: a review”, [J. Mater. Chem.](#) **20**, 8207–8223 (2010).
- ¹¹¹A. Epping, C. Volk, F. Buckstegge, K. Watanabe, T. Taniguchi, and C. Stampfer, “Insulating state in low-disorder graphene nanoribbons”, [physica status solidi \(b\)](#) **256**, 1900269 (2019).
- ¹¹²Y.-M. Lin, V. Perebeinos, Z. Chen, and P. Avouris, “Electrical observation of subband formation in graphene nanoribbons”, [Phys. Rev. B](#) **78**, 161409 (2008).
- ¹¹³F. Molitor, C. Stampfer, J. Güttinger, A. Jacobsen, T. Ihn, and K. Ensslin, “Energy and transport gaps in etched graphene nanoribbons”, [Semiconductor Science and Technology](#) **25**, 034002 (2010).
- ¹¹⁴C. Stampfer, J. Güttinger, S. Hellmüller, F. Molitor, K. Ensslin, and T. Ihn, “Energy gaps in etched graphene nanoribbons”, [Phys. Rev. Lett.](#) **102**, 056403 (2009).

- ¹¹⁵K. Todd, H.-T. Chou, S. Amasha, and D. Goldhaber-Gordon, “Quantum dot behavior in graphene nanoconstrictions”, *Nano Lett* **9**, 416–421 (2009).
- ¹¹⁶M. Wang, E. B. Song, S. Lee, J. Tang, M. Lang, C. Zeng, G. Xu, Y. Zhou, and K. L. Wang, “Quantum dot behavior in bilayer graphene nanoribbons”, *ACS Nano* **5**, 8769–8773 (2011).
- ¹¹⁷V. Clericò, J. A. Delgado-Notario, M. Saiz-Bretín, A. V. Malyshev, Y. M. Meziani, P. Hidalgo, B. Méndez, M. Amado, F. Domínguez-Adame, and E. Diez, “Quantum nanoconstrictions fabricated by cryo-etching in encapsulated graphene”, *Scientific Reports* **9**, 13572 (2019).
- ¹¹⁸R. Krishna Kumar, D. A. Bandurin, F. M. D. Pellegrino, Y. Cao, A. Principi, H. Guo, G. H. Auton, M. Ben Shalom, L. A. Ponomarenko, G. Falkovich, K. Watanabe, T. Taniguchi, I. V. Grigorieva, L. S. Levitov, M. Polini, and A. K. Geim, “Superballistic flow of viscous electron fluid through graphene constrictions”, *Nature Physics* **13**, 1182–1185 (2017).
- ¹¹⁹A. Zhang, Y. Wu, S.-H. Ke, Y. P. Feng, and C. Zhang, “Bandgap engineering of zigzag graphene nanoribbons by manipulating edge states via defective boundaries”, *Nanotechnology* **22**, 435702 (2011).
- ¹²⁰W. S. Hwang, P. Zhao, K. Tahy, L. O. Nyakiti, V. D. Wheeler, R. L. Myers-Ward, C. R. Eddy, D. K. Gaskill, J. A. Robinson, W. Haensch, H. G. Xing, A. Seabaugh, and D. Jena, “Graphene nanoribbon field-effect transistors on wafer-scale epitaxial graphene on sic substrates”, *APL Materials* **3**, 011101 (2015).
- ¹²¹M. Y. Han, B. Özyilmaz, Y. Zhang, and P. Kim, “Energy band-gap engineering of graphene nanoribbons”, *Phys. Rev. Lett.* **98**, 206805 (2007).
- ¹²²J. P. Llinas, A. Fairbrother, G. Borin Barin, W. Shi, K. Lee, S. Wu, B. Yong Choi, R. Braganza, J. Lear, N. Kau, W. Choi, C. Chen, Z. Pedramrazi, T. Dumslaff, A. Narita, X. Feng, K. Müllen, F. Fischer, A. Zettl, P. Ruffieux, E. Yablonovitch, M. Crommie, R. Fasel, and J. Bokor, “Short-channel field-effect transistors with 9-atom and 13-atom wide graphene nanoribbons”, *Nature Communications* **8**, 633 (2017).
- ¹²³F. Sols, F. Guinea, and A. H. C. Neto, “Coulomb blockade in graphene nanoribbons”, *Phys. Rev. Lett.* **99**, 166803 (2007).
- ¹²⁴Z. Chen, Y.-M. Lin, M. J. Rooks, and P. Avouris, “Graphene nano-ribbon electronics”, *Physica E: Low-dimensional Systems and Nanostructures* **40**, 228–232 (2007).
- ¹²⁵D. Bischoff, A. Varlet, P. Simonet, M. Eich, H. C. Overweg, T. Ihn, and K. Ensslin, “Localized charge carriers in graphene nanodevices”, *Applied Physics Reviews* **2**, 031301 (2015).
- ¹²⁶J. Güttinger, T. Frey, C. Stampfer, T. Ihn, and K. Ensslin, “Spin states in graphene quantum dots”, *Phys. Rev. Lett.* **105**, 116801 (2010).
- ¹²⁷A. S. Mayorov, R. V. Gorbachev, S. V. Morozov, L. Britnell, R. Jalil, L. A. Ponomarenko, P. Blake, K. S. Novoselov, K. Watanabe, T. Taniguchi, and A. K. Geim, “Micrometer-scale ballistic transport in encapsulated graphene at room temperature”, *Nano Lett* **11**, 2396–2399 (2011).
- ¹²⁸A. Rycerz, J. Tworzydło, and C. W. J. Beenakker, “Valley filter and valley valve in graphene”, *Nature Physics* **3**, 172–175 (2007).
- ¹²⁹S. Chen, Z. Han, M. M. Elahi, K. M. M. Habib, L. Wang, B. Wen, Y. Gao, T. Taniguchi, K. Watanabe, J. Hone, A. W. Ghosh, and C. R. Dean, “Electron optics with p-n junctions in ballistic graphene”, *Science* **353**, 1522–1525 (2016).

- ¹³⁰P. Rickhaus, P. Makk, M.-H. Liu, E. Tóvári, M. Weiss, R. Maurand, K. Richter, and C. Schönenberger, “Snake trajectories in ultraclean graphene p-n junctions”, *Nature Communications* **6**, 6470 (2015).
- ¹³¹A. Girdhar, C. Sathe, K. Schulten, and J.-P. Leburton, “Graphene quantum point contact transistor for dna sensing”, *Proceedings of the National Academy of Sciences* **110**, 16748–16753 (2013).
- ¹³²C. Neumann, S. Reichardt, P. Venezuela, M. Drögeler, L. Banszerus, M. Schmitz, K. Watanabe, T. Taniguchi, F. Mauri, B. Beschoten, S. V. Rotkin, and C. Stampfer, “Raman spectroscopy as probe of nanometre-scale strain variations in graphene”, *Nature Communications* **6**, 8429 (2015).
- ¹³³N. J. G. Couto, D. Costanzo, S. Engels, D.-K. Ki, K. Watanabe, T. Taniguchi, C. Stampfer, F. Guinea, and A. F. Morpurgo, “Random strain fluctuations as dominant disorder source for high-quality on-substrate graphene devices”, *Phys. Rev. X* **4**, 041019 (2014).
- ¹³⁴S. Somanchi, B. Terrés, J. Peiro, M. Staggenborg, K. Watanabe, T. Taniguchi, B. Beschoten, and C. Stampfer, “From diffusive to ballistic transport in etched graphene constrictions and nanoribbons”, *Annalen der Physik* **529**, 1700082 (2017).
- ¹³⁵S. Y. Zhou, G.-H. Gweon, A. V. Fedorov, P. N. First, W. A. de Heer, D.-H. Lee, F. Guinea, A. H. Castro Neto, and A. Lanzara, “Substrate-induced bandgap opening in epitaxial graphene”, *Nature Materials* **6**, 770–775 (2007).
- ¹³⁶X. Peng and R. Ahuja, “Symmetry breaking induced bandgap in epitaxial graphene layers on SiC”, *Nano Lett* **8**, 4464–4468 (2008).
- ¹³⁷J. B. Oostinga, H. B. Heersche, X. Liu, A. F. Morpurgo, and L. M. K. Vandersypen, “Gate-induced insulating state in bilayer graphene devices”, *Nature Materials* **7**, 151–157 (2007).
- ¹³⁸D. V. Kosynkin, W. Lu, A. Sinitskii, G. Pera, Z. Sun, and J. M. Tour, “Highly conductive graphene nanoribbons by longitudinal splitting of carbon nanotubes using potassium vapor”, *ACS Nano* **5**, 968–974 (2011).
- ¹³⁹J. Cai, P. Ruffieux, R. Jaafar, M. Bieri, T. Braun, S. Blankenburg, M. Muoth, A. P. Seitsonen, M. Saleh, X. Feng, K. Müllen, and R. Fasel, “Atomically precise bottom-up fabrication of graphene nanoribbons”, *Nature* **466**, 470–473 (2010).
- ¹⁴⁰M. Sprinkle, M. Ruan, Y. Hu, J. Hankinson, M. Rubio-Roy, B. Zhang, X. Wu, C. Berger, and W. A. de Heer, “Scalable templated growth of graphene nanoribbons on sic”, *Nature Nanotechnology* **5**, 727–731 (2010).
- ¹⁴¹X. Lu, W. Yang, S. Wang, S. Wu, P. Chen, J. Zhang, J. Zhao, J. Meng, G. Xie, D. Wang, G. Wang, T. T. Zhang, K. Watanabe, T. Taniguchi, R. Yang, D. Shi, and G. Zhang, “Graphene nanoribbons epitaxy on boron nitride”, *Applied Physics Letters* **108**, 113103 (2016).
- ¹⁴²A. Celis, M. N. Nair, A. Taleb-Ibrahimi, E. H. Conrad, C. Berger, W. A. de Heer, and A. Tejeda, “Graphene nanoribbons: fabrication, properties and devices”, *Journal of Physics D: Applied Physics* **49**, 143001 (2016).
- ¹⁴³D. Bischoff, T. Krähenmann, S. Dröscher, M. A. Gruner, C. Barraud, T. Ihn, and K. Ensslin, “Reactive-ion-etched graphene nanoribbons on a hexagonal boron nitride substrate”, *Applied Physics Letters* **101**, 203103 (2012).

- ¹⁴⁴S. Engels, A. Epping, C. Volk, S. Korte, B. Voigtländer, K. Watanabe, T. Taniguchi, S. Trellenkamp, and C. Stampfer, “Etched graphene quantum dots on hexagonal boron nitride”, [Applied Physics Letters](#) **103**, 073113 (2013).
- ¹⁴⁵Y. V. Skrypnik and V. M. Loktev, “Impurity induced dirac point smearing in graphene”, [Low Temperature Physics](#) **33**, 762–766 (2007).
- ¹⁴⁶P. Simonet, D. Bischoff, A. Moser, T. Ihn, and K. Ensslin, “Graphene nanoribbons: relevance of etching process”, [Journal of Applied Physics](#) **117**, 184303 (2015).
- ¹⁴⁷D. Bischoff, J. Güttinger, S. Dröscher, T. Ihn, K. Ensslin, and C. Stampfer, “Raman spectroscopy on etched graphene nanoribbons”, [Journal of Applied Physics](#) **109**, 073710 (2011).
- ¹⁴⁸J. B. Oostinga, B. Sacépé, M. F. Craciun, and A. F. Morpurgo, “Magnetotransport through graphene nanoribbons”, [Phys. Rev. B](#) **81**, 193408 (2010).
- ¹⁴⁹F. Molitor, A. Jacobsen, C. Stampfer, J. Güttinger, T. Ihn, and K. Ensslin, “Transport gap in side-gated graphene constrictions”, [Phys. Rev. B](#) **79**, 075426 (2009).
- ¹⁵⁰C. Neumann, C. Volk, S. Engels, and C. Stampfer, “Graphene-based charge sensors”, [Nanotechnology](#) **24**, 444001 (2013).
- ¹⁵¹J. Güttinger, C. Stampfer, S. Hellmüller, F. Molitor, T. Ihn, and K. Ensslin, “Charge detection in graphene quantum dots”, [Applied Physics Letters](#) **93**, 212102 (2008).
- ¹⁵²C. Volk, C. Neumann, S. Kazarski, S. Fringes, S. Engels, F. Haupt, A. Müller, and C. Stampfer, “Probing relaxation times in graphene quantum dots”, [Nature Communications](#) **4**, 1753 (2013).
- ¹⁵³C. Volk, S. Engels, C. Neumann, and C. Stampfer, “Back action of graphene charge detectors on graphene and carbon nanotube quantum dots”, [physica status solidi \(b\)](#) **252**, 2461–2465 (2015).
- ¹⁵⁴M. Koch, F. Ample, C. Joachim, and L. Grill, “Voltage-dependent conductance of a single graphene nanoribbon”, [Nature Nanotechnology](#) **7**, 713–717 (2012).
- ¹⁵⁵N. Pascher, D. Bischoff, T. Ihn, and K. Ensslin, “Scanning gate microscopy on a graphene nanoribbon”, [Applied Physics Letters](#) **101**, 063101 (2012).
- ¹⁵⁶B. Terrés, J. Dauber, C. Volk, S. Trellenkamp, U. Wichmann, and C. Stampfer, “Disorder induced coulomb gaps in graphene constrictions with different aspect ratios”, [Applied Physics Letters](#) **98**, 032109 (2011).
- ¹⁵⁷M. Y. Han, J. C. Brant, and P. Kim, “Electron transport in disordered graphene nanoribbons”, [Phys. Rev. Lett.](#) **104**, 056801 (2010).
- ¹⁵⁸S. Dröscher, H. Knowles, Y. Meir, K. Ensslin, and T. Ihn, “Coulomb gap in graphene nanoribbons”, [Phys. Rev. B](#) **84**, 073405 (2011).
- ¹⁵⁹K. Bolotin, K. Sikes, Z. Jiang, M. Klima, G. Fudenberg, J. Hone, P. Kim, and H. Stormer, “Ultrahigh electron mobility in suspended graphene”, [Solid State Communications](#) **146**, 351–355 (2008).
- ¹⁶⁰X. Du, I. Skachko, A. Barker, and E. Y. Andrei, “Approaching ballistic transport in suspended graphene”, [Nature Nanotechnology](#) **3**, 491–495 (2008).
- ¹⁶¹K. I. Bolotin, F. Ghahari, M. D. Shulman, H. L. Stormer, and P. Kim, “Observation of the fractional quantum hall effect in graphene”, [Nature](#) **462**, 196–199 (2009).

- ¹⁶²N. Tombros, A. Veligura, J. Junesch, J. Jasper van den Berg, P. J. Zomer, M. Wojtaszek, I. J. Vera Marun, H. T. Jonkman, and B. J. van Wees, “Large yield production of high mobility freely suspended graphene electronic devices on a polydimethylglutarimide based organic polymer”, *Journal of Applied Physics* **109**, 093702 (2011).
- ¹⁶³S. Ihnatsenka and G. Kirczenow, “Conductance quantization in graphene nanoconstrictions with mesoscopically smooth but atomically stepped boundaries”, *Phys. Rev. B* **85**, 121407 (2012).
- ¹⁶⁴D.-K. Ki and A. F. Morpurgo, “Crossover from coulomb blockade to quantum hall effect in suspended graphene nanoribbons”, *Phys. Rev. Lett.* **108**, 266601 (2012).
- ¹⁶⁵P. Rickhaus, R. Maurand, M.-H. Liu, M. Weiss, K. Richter, and C. Schönenberger, “Ballistic interferences in suspended graphene”, *Nature Communications* **4**, 2342 (2013).
- ¹⁶⁶A. L. Grushina, D.-K. Ki, and A. F. Morpurgo, “A ballistic pn junction in suspended graphene with split bottom gates”, *Applied Physics Letters* **102**, 223102 (2013).
- ¹⁶⁷J.-H. Chen, C. Jang, S. Xiao, M. Ishigami, and M. S. Fuhrer, “Intrinsic and extrinsic performance limits of graphene devices on SiO₂”, *Nature Nanotechnology* **3**, 206–209 (2008).
- ¹⁶⁸J. A. Leon, N. C. Mamani, A. Rahim, L. E. Gomez, M. A. P. da Silva, and G. M. Gusev, “Transferring Few-Layer Graphene Sheets on Hexagonal Boron Nitride Substrates for Fabrication of Graphene Devices”, *Graphene* **3**, 11 (2014).
- ¹⁶⁹J. Xue, J. Sanchez-Yamagishi, D. Bulmash, P. Jacquod, A. Deshpande, K. Watanabe, T. Taniguchi, P. Jarillo-Herrero, and B. J. LeRoy, “Scanning tunnelling microscopy and spectroscopy of ultra-flat graphene on hexagonal boron nitride”, *Nature Materials* **10**, 282–285 (2011).
- ¹⁷⁰D. Bischoff, F. Libisch, J. Burgdörfer, T. Ihn, and K. Ensslin, “Characterizing wave functions in graphene nanodevices: electronic transport through ultrashort graphene constrictions on a boron nitride substrate”, *Phys. Rev. B* **90**, 115405 (2014).
- ¹⁷¹L. Banszerus, M. Schmitz, S. Engels, M. Goldsche, K. Watanabe, T. Taniguchi, B. Beschoten, and C. Stampfer, “Ballistic transport exceeding 28 nm in cvd grown graphene”, *Nano Lett* **16**, 1387–1391 (2016).
- ¹⁷²L. Wang, I. Meric, P. Y. Huang, Q. Gao, Y. Gao, H. Tran, T. Taniguchi, K. Watanabe, L. M. Campos, D. A. Muller, J. Guo, P. Kim, J. Hone, K. L. Shepard, and C. R. Dean, “One-dimensional electrical contact to a two-dimensional material”, *Science* **342**, 614–617 (2013).
- ¹⁷³A. V. Kretinin, Y. Cao, J. S. Tu, G. L. Yu, R. Jalil, K. S. Novoselov, S. J. Haigh, A. Gholinia, A. Mishchenko, M. Lozada, T. Georgiou, C. R. Woods, F. Withers, P. Blake, G. Eda, A. Wirsig, C. Hucho, K. Watanabe, T. Taniguchi, A. K. Geim, and R. V. Gorbachev, “Electronic properties of graphene encapsulated with different two-dimensional atomic crystals”, *Nano Lett* **14**, 3270–3276 (2014).
- ¹⁷⁴L. Banszerus, M. Schmitz, S. Engels, J. Dauber, M. Oellers, F. Haupt, K. Watanabe, T. Taniguchi, B. Beschoten, and C. Stampfer, “Ultrahigh-mobility graphene devices from chemical vapor deposition on reusable copper”, *Science Advances* **1**, e1500222 (2015).
- ¹⁷⁵E. Sustini, Khairurrijal, F. A. Noor, and R. Syariati, “Band gap calculations of bilayer graphene and bilayer armchair graphene nanoribbon”, *IOP Conference Series: Materials Science and Engineering* **367**, 012013 (2018).

- ¹⁷⁶L. M. Zhang, Z. Q. Li, D. N. Basov, M. M. Fogler, Z. Hao, and M. C. Martin, “Determination of the electronic structure of bilayer graphene from infrared spectroscopy”, [Phys. Rev. B **78**, 235408 \(2008\)](#).
- ¹⁷⁷S. Das Sarma, E. H. Hwang, and E. Rossi, “Theory of carrier transport in bilayer graphene”, [Phys. Rev. B **81**, 161407 \(2010\)](#).
- ¹⁷⁸E. McCann and V. I. Fal’ko, “Landau-level degeneracy and quantum hall effect in a graphite bilayer”, [Phys. Rev. Lett. **96**, 086805 \(2006\)](#).
- ¹⁷⁹E. McCann, D. S. Abergel, and V. I. Fal’ko, “The low energy electronic band structure of bilayer graphene”, [The European Physical Journal Special Topics **148**, 91–103 \(2007\)](#).
- ¹⁸⁰H. Min, B. Sahu, S. K. Banerjee, and A. H. MacDonald, “Ab initio theory of gate induced gaps in graphene bilayers”, [Phys. Rev. B **75**, 155115 \(2007\)](#).
- ¹⁸¹E. McCann and M. Koshino, “The electronic properties of bilayer graphene”, [Reports on Progress in Physics **76**, 056503 \(2013\)](#).
- ¹⁸²T. Ohta, A. Bostwick, T. Seyller, K. Horn, and E. Rotenberg, “Controlling the electronic structure of bilayer graphene”, [Science **313**, 951–954 \(2006\)](#).
- ¹⁸³G. Fiori and G. Iannaccone, “On the possibility of tunable-gap bilayer graphene fet”, [IEEE Electron Device Letters **30**, 261–264 \(2009\)](#).
- ¹⁸⁴M. LLC, “MS Windows NT kernel description”, (1999).
- ¹⁸⁵F. Schwierz, “Graphene transistors”, [Nature Nanotechnology **5**, 487–496 \(2010\)](#).
- ¹⁸⁶G. Fiori and G. Iannaccone, “Ultralow-voltage bilayer graphene tunnel fet”, [IEEE Electron Device Letters **30**, 1096–1098 \(2009\)](#).
- ¹⁸⁷M. Tian, X. Li, T. Li, Q. Gao, X. Xiong, Q. Hu, M. Wang, X. Wang, and Y. Wu, “High-performance cvd bernal-stacked bilayer graphene transistors for amplifying and mixing signals at high frequencies”, [ACS Applied Materials & Interfaces **10**, 20219–20224 \(2018\)](#).
- ¹⁸⁸S. Dröscher, C. Barraud, K. Watanabe, T. Taniguchi, T. Ihn, and K. Ensslin, “Electron flow in split-gated bilayer graphene”, [New Journal of Physics **14**, 103007 \(2012\)](#).
- ¹⁸⁹A. Goossens, “Confinement of charge carriers in bilayer graphene”, PhD thesis (TU Delft, 2013).
- ¹⁹⁰M. T. Allen, J. Martin, and A. Yacoby, “Gate-defined quantum confinement in suspended bilayer graphene”, [Nature Communications **3**, 934 \(2012\)](#).
- ¹⁹¹A. S. M. Goossens, S. C. M. Driessen, T. A. Baart, K. Watanabe, T. Taniguchi, and L. M. K. Vandersypen, “Gate-defined confinement in bilayer graphene-hexagonal boron nitride hybrid devices”, [Nano Lett **12**, 4656–4660 \(2012\)](#).
- ¹⁹²H. Overweg, H. Eggimann, X. Chen, S. Slizovskiy, M. Eich, R. Pisoni, Y. Lee, P. Rickhaus, K. Watanabe, T. Taniguchi, V. Fal’ko, T. Ihn, and K. Ensslin, “Electrostatically induced quantum point contacts in bilayer graphene”, [Nano Lett **18**, 553–559 \(2018\)](#).
- ¹⁹³K. Zou and J. Zhu, “Transport in gapped bilayer graphene: the role of potential fluctuations”, [Phys. Rev. B **82**, 081407 \(2010\)](#).
- ¹⁹⁴J. Yan and M. S. Fuhrer, “Charge transport in dual gated bilayer graphene with corbino geometry”, [Nano Lett **10**, 4521–4525 \(2010\)](#).

- ¹⁹⁵M. J. Zhu, A. V. Kretinin, M. D. Thompson, D. A. Bandurin, S. Hu, G. L. Yu, J. Birkbeck, A. Mishchenko, I. J. Vera-Marun, K. Watanabe, T. Taniguchi, M. Polini, J. R. Prance, K. S. Novoselov, A. K. Geim, and M. Ben Shalom, “Edge currents shunt the insulating bulk in gapped graphene”, *Nature Communications* **8**, 14552 (2017).
- ¹⁹⁶A. A. Zibrov, C. Kometter, H. Zhou, E. M. Spanton, T. Taniguchi, K. Watanabe, M. P. Zaletel, and A. F. Young, “Tunable interacting composite fermion phases in a half-filled bilayer-graphene landau level”, *Nature* **549**, 360–364 (2017).
- ¹⁹⁷R. Kraft, I. V. Krainov, V. Gall, A. P. Dmitriev, R. Krupke, I. V. Gornyi, and R. Danneau, “Valley subband splitting in bilayer graphene quantum point contacts”, *Phys. Rev. Lett.* **121**, 257703 (2018).
- ¹⁹⁸H. Overweg, A. Knothe, T. Fabian, L. Linhart, P. Rickhaus, L. Wernli, K. Watanabe, T. Taniguchi, D. Sánchez, J. Burgdörfer, F. Libisch, V. I. Fal’ko, K. Ensslin, and T. Ihn, “Topologically nontrivial valley states in bilayer graphene quantum point contacts”, *Phys. Rev. Lett.* **121**, 257702 (2018).
- ¹⁹⁹M. Eich, R. Pisoni, H. Overweg, A. Kurzmann, Y. Lee, P. Rickhaus, T. Ihn, K. Ensslin, F. c. v. Herman, M. Sigrist, K. Watanabe, and T. Taniguchi, “Spin and valley states in gate-defined bilayer graphene quantum dots”, *Phys. Rev. X* **8**, 031023 (2018).
- ²⁰⁰L. Banszerus, B. Frohn, A. Epping, D. Neumaier, K. Watanabe, T. Taniguchi, and C. Stampfer, “Gate-defined electron-hole double dots in bilayer graphene”, *Nano Lett* **18**, 4785–4790 (2018).
- ²⁰¹K. S. Novoselov, A. K. Geim, S. V. Morozov, D. Jiang, Y. Zhang, S. V. Dubonos, I. V. Grigorieva, and A. A. Firsov, “Electric field effect in atomically thin carbon films”, *Science* **306**, 666–669 (2004).
- ²⁰²M. S. A. Bhuyan, M. N. Uddin, M. M. Islam, F. A. Bipasha, and S. S. Hossain, “Synthesis of graphene”, *International Nano Letters* **6**, 65–83 (2016).
- ²⁰³L. Malard, M. Pimenta, G. Dresselhaus, and M. Dresselhaus, “Raman spectroscopy in graphene”, *Physics Reports* **473**, 51–87 (2009).
- ²⁰⁴M. Bayle, N. Reckinger, A. Felten, P. Landois, O. Lancry, B. Dutertre, J.-F. Colomer, A.-A. Zahab, L. Henrard, J.-L. Sauvajol, and M. Paillet, “Determining the number of layers in few-layer graphene by combining raman spectroscopy and optical contrast”, *Journal of Raman Spectroscopy* **49**, 36–45 (2018).
- ²⁰⁵C. Stampfer, F. Molitor, D. Graf, K. Ensslin, A. Jungen, C. Hierold, and L. Wirtz, “Raman imaging of doping domains in graphene on sio₂”, *Applied Physics Letters* **91**, 241907 (2007).
- ²⁰⁶A. C. Ferrari, “Raman spectroscopy of graphene and graphite: disorder, electron-phonon coupling, doping and nonadiabatic effects”, *Solid State Communications* **143**, 47–57 (2007).
- ²⁰⁷M. Huang, H. Yan, T. F. Heinz, and J. Hone, “Probing strain-induced electronic structure change in graphene by raman spectroscopy”, *Nano Lett* **10**, 4074–4079 (2010).
- ²⁰⁸M. Mohr, J. Maultzsch, and C. Thomsen, “Splitting of the raman 2D band of graphene subjected to strain”, *Phys. Rev. B* **82**, 201409 (2010).
- ²⁰⁹D. Graf, F. Molitor, K. Ensslin, C. Stampfer, A. Jungen, C. Hierold, and L. Wirtz, “Spatially resolved raman spectroscopy of single- and few-layer graphene”, *Nano Lett* **7**, 238–242 (2007).
- ²¹⁰P. Venezuela, M. Lazzeri, and F. Mauri, “Theory of double-resonant raman spectra in graphene: intensity and line shape of defect-induced and two-phonon bands”, *Phys. Rev. B* **84**, 035433 (2011).

- ²¹¹A. C. Ferrari and D. M. Basko, “Raman spectroscopy as a versatile tool for studying the properties of graphene”, *Nature Nanotechnology* **8**, 235–246 (2013).
- ²¹²C. Neumann, L. Banszerus, M. Schmitz, S. Reichardt, J. Sonntag, T. Taniguchi, K. Watanabe, B. Beschoten, and C. Stampfer, “Line shape of the raman 2d peak of graphene in van der waals heterostructures”, *physica status solidi (b)* **253**, 2326–2330 (2016).
- ²¹³F. Herziger, M. Calandra, P. Gava, P. May, M. Lazzeri, F. Mauri, and J. Maultzsch, “Two-dimensional analysis of the double-resonant 2d raman mode in bilayer graphene”, *Phys. Rev. Lett.* **113**, 187401 (2014).
- ²¹⁴S. Engels, “Limitations to charge carrier transport in high quality single- and bi-layer graphene”, PhD thesis (RWTH Aachen, 2015).
- ²¹⁵P. J. Zomer, M. H. D. Guimarães, J. C. Brant, N. Tombros, and B. J. van Wees, “Fast pick up technique for high quality heterostructures of bilayer graphene and hexagonal boron nitride”, *Applied Physics Letters* **105**, 013101 (2014).
- ²¹⁶S. J. Haigh, A. Gholinia, R. Jalil, S. Romani, L. Britnell, D. C. Elias, K. S. Novoselov, L. A. Ponomarenko, A. K. Geim, and R. Gorbachev, “Cross-sectional imaging of individual layers and buried interfaces of graphene-based heterostructures and superlattices”, *Nature Materials* **11**, 764–767 (2012).
- ²¹⁷K. K. Kim, A. Hsu, X. Jia, S. M. Kim, Y. Shi, M. Dresselhaus, T. Palacios, and J. Kong, “Synthesis and characterization of hexagonal boron nitride film as a dielectric layer for graphene devices”, *ACS Nano* **6**, 8583–8590 (2012).
- ²¹⁸I. Meric, C. R. Dean, N. Petrone, L. Wang, J. Hone, P. Kim, and K. L. Shepard, “Graphene field-effect transistors based on boron-nitride dielectrics”, *Proceedings of the IEEE* **101**, 1609–1619 (2013).
- ²¹⁹M. Evaldsson, I. V. Zozoulenko, H. Xu, and T. Heinzel, “Edge-disorder-induced anderson localization and conduction gap in graphene nanoribbons”, *Phys. Rev. B* **78**, 161407 (2008).
- ²²⁰J. Dauber, B. Terrés, C. Volk, S. Trellenkamp, and C. Stampfer, “Reducing disorder in graphene nanoribbons by chemical edge modification”, *Applied Physics Letters* **104**, 083105 (2014).
- ²²¹C. Chen, T. Low, H. Chiu, and W. Zhu, “Graphene-side-gate engineering”, *IEEE Electron Device Letters* **33**, 330–332 (2012).
- ²²²J. Güttinger, C. Stampfer, F. Libisch, T. Frey, J. Burgdörfer, T. Ihn, and K. Ensslin, “Electron-hole crossover in graphene quantum dots”, *Phys. Rev. Lett.* **103**, 046810 (2009).
- ²²³Lab Control Software Scandinavia AB, *Labber*, version V1.5.1, <http://labber.org>.
- ²²⁴S. R. F. Libisch and J. Burgdörfer, “Coherent transport through graphene nanoribbons in the presence of edge disorder”, *New Journal of Physics* **14**, 123006 (2012).
- ²²⁵M. Acik and Y. J. Chabal, “Nature of graphene edges: a review”, *Japanese Journal of Applied Physics* **50**, 070101 (2011).
- ²²⁶H. Zheng and W. Duley, “First-principles study of edge chemical modifications in graphene nanodots”, *Phys. Rev. B* **78**, 045421 (2008).
- ²²⁷S. Bala Kumar, T. Fujita, and G. Liang, “Conductance modulation in graphene nanoribbon under transverse asymmetric electric potential”, *Journal of Applied Physics* **109**, 073704 (2011).

- ²²⁸R. Landauer, “Spatial variation of currents and fields due to localized scatterers in metallic conduction”, *IBM Journal of Research and Development* **1**, 223–231 (1957).
- ²²⁹M. Büttiker, “Absence of backscattering in the quantum hall effect in multiprobe conductors”, *Phys. Rev. B* **38**, 9375–9389 (1988).
- ²³⁰S. Bhandari, G.-H. Lee, A. Klales, K. Watanabe, T. Taniguchi, E. Heller, P. Kim, and R. M. Westervelt, “Imaging cyclotron orbits of electrons in graphene”, *Nano Lett* **16**, 1690–1694 (2016).
- ²³¹S. Bhandari, G.-H. Lee, P. Kim, and R. M. Westervelt, “Analysis of scanned probe images for magnetic focusing in graphene”, *Journal of Electronic Materials* **46**, 3837–3841 (2017).
- ²³²A. Peña, A. Girschik, F. Libisch, S. Rotter, and A. A. Chabanov, “The single-channel regime of transport through random media”, *Nat. Commun* **5**, 3488 (2014).
- ²³³F. Libisch, S. Rotter, J. Güttinger, C. Stampfer, and J. Burgdörfer, “Transition to Landau levels in graphene quantum dots”, *Phys. Rev. B* **81**, 245411 (2010).
- ²³⁴T.-Y. Yang, J. Balakrishnan, F. Volmer, A. Avsar, M. Jaiswal, J. Samm, S. R. Ali, A. Pachoud, M. Zeng, M. Popinciuc, G. Güntherodt, B. Beschoten, and B. Özyilmaz, “Observation of long spin-relaxation times in bilayer graphene at room temperature”, *Phys. Rev. Lett.* **107**, 047206 (2011).
- ²³⁵S. Konschuh, M. Gmitra, D. Kochan, and J. Fabian, “Theory of spin-orbit coupling in bilayer graphene”, *Phys. Rev. B* **85**, 115423 (2012).
- ²³⁶D. Kochan, M. Gmitra, and J. Fabian, “Spin-orbit coupling in graphene structures”, *Spintronics V* **8461**, 84610L (2012).
- ²³⁷Y. Yao, F. Ye, X.-L. Qi, S.-C. Zhang, and Z. Fang, “Spin-orbit gap of graphene: first-principles calculations”, *Phys. Rev. B* **75**, 041401 (2007).
- ²³⁸C. L. Kane and E. J. Mele, “Quantum Spin Hall Effect in Graphene”, *Phys. Rev. Lett.* **95**, 226801 (2005).
- ²³⁹B. S. Kandemir, “Pseudo-spin-orbit coupling in graphene within hydrogenic impurity context”, *J. Phys. Soc. Japan* **82**, 094706 (2013).
- ²⁴⁰D. Huertas-Hernando, F. Guinea, and A. Brataas, “Spin-orbit-mediated spin relaxation in graphene”, *Phys. Rev. Lett.* **103**, 146801 (2009).
- ²⁴¹H. Min, J. E. Hill, N. A. Sinitsyn, B. R. Sahu, L. Kleinman, and A. H. MacDonald, “Intrinsic and Rashba spin-orbit interactions in graphene sheets”, *Phys. Rev. B* **74**, 165310 (2006).
- ²⁴²I. I. Klimovskikh, M. M. Otrokov, V. Y. Voroshnin, D. Sostina, L. Petaccia, G. Di Santo, S. Thakur, E. V. Chulkov, and A. M. Shikin, “Spin-orbit coupling induced gap in graphene on Pt(111) with intercalated pb monolayer”, *ACS Nano* **11**, 368–374 (2017).
- ²⁴³M. Gmitra and J. Fabian, “Graphene on transition-metal dichalcogenides: a platform for proximity spin-orbit physics and optospintronics”, *Phys. Rev. B* **92**, 155403 (2015).
- ²⁴⁴B. Fülöp, A. Márfy, S. Zihlmann, M. Gmitra, E. Tóvári, B. Szentpéteri, M. Kedves, K. Watanabe, T. Taniguchi, J. Fabian, C. Schönenberger, P. Makk, and S. Csonka, “Boosting proximity spin-orbit coupling in graphene/WSe₂ heterostructures via hydrostatic pressure”, *NPJ 2D Mater. Appl.* **5**, 82 (2021).
- ²⁴⁵A. Avsar, J. Y. Tan, T. Taychatanapat, J. Balakrishnan, G. K. W. Koon, Y. Yeo, J. Lahiri, A. Carvalho, A. S. Rodin, E. C. T. O’Farrell, G. Eda, A. H. Castro Neto, and B. Özyilmaz, “Spin-orbit proximity effect in graphene”, *Nat. Commun* **5**, 4875 (2014).

- ²⁴⁶K. Zollner, M. Gmitra, and J. Fabian, “Heterostructures of graphene and hbn: electronic, spin-orbit, and spin relaxation properties from first principles”, *Phys. Rev. B* **99**, 125151 (2019).
- ²⁴⁷L. Banszerus, S. Möller, C. Steiner, E. Icking, S. Trellenkamp, F. Lentz, K. Watanabe, T. Taniguchi, C. Volk, and C. Stampfer, “Spin-valley coupling in single-electron bilayer graphene quantum dots”, *Nat. Commun* **12**, 5250 (2021).
- ²⁴⁸J. Xu, T. Zhu, Y. K. Luo, Y.-M. Lu, and R. K. Kawakami, “Strong and tunable spin-lifetime anisotropy in dual-gated bilayer graphene”, *Phys. Rev. Lett.* **121**, 127703 (2018).
- ²⁴⁹J. C. Leutenantsmeyer, J. Ingla-Aynés, J. Fabian, and B. J. van Wees, “Observation of spin-valley-coupling-induced large spin-lifetime anisotropy in bilayer graphene”, *Phys. Rev. Lett.* **121**, 127702 (2018).
- ²⁵⁰J. Sichau, M. Prada, T. Anlauf, T. J. Lyon, B. Bosnjak, L. Tiemann, and R. H. Blick, “Resonance microwave measurements of an intrinsic spin-orbit coupling gap in graphene: a possible indication of a topological state”, *Phys. Rev. Lett.* **122**, 046403 (2019).
- ²⁵¹K. J. Thomas, J. T. Nicholls, M. Y. Simmons, M. Pepper, D. R. Mace, and D. A. Ritchie, “Possible spin polarization in a one-dimensional electron gas”, *Phys. Rev. Lett.* **77**, 135–138 (1996).
- ²⁵²A. Kristensen, H. Bruus, A. E. Hansen, J. B. Jensen, P. E. Lindelof, C. J. Marckmann, J. Nygård, C. B. Sørensen, F. Beuscher, A. Forchel, and M. Michel, “Bias and temperature dependence of the 0.7 conductance anomaly in quantum point contacts”, *Phys. Rev. B* **62**, 10950–10957 (2000).
- ²⁵³K. J. Thomas, J. T. Nicholls, M. Pepper, W. R. Tribe, M. Y. Simmons, and D. A. Ritchie, “Spin properties of low-density one-dimensional wires”, *Phys. Rev. B* **61**, R13365–R13368 (2000).
- ²⁵⁴A. C. Graham, K. J. Thomas, M. Pepper, N. R. Cooper, M. Y. Simmons, and D. A. Ritchie, “Interaction Effects at Crossings of Spin-Polarized One-Dimensional Subbands”, *Phys. Rev. Lett.* **91**, 136404 (2003).
- ²⁵⁵UNC, <https://physics.unc.edu/files/2012/10/uncertainty.pdf>.
- ²⁵⁶Natan, *Fast 2d peak finder*, <https://www.mathworks.com/matlabcentral/fileexchange/37388-fast-2d-peak-finder>.
- ²⁵⁷MATLAB, *Smooth response data*, <https://www.mathworks.com/help/curvefit/smooth.html>.
- ²⁵⁸D. Huertas-Hernando, F. Guinea, and A. Brataas, “Spin-orbit coupling in curved graphene, fullerenes, nanotubes, and nanotube caps”, *Phys. Rev. B* **74**, 155426 (2006).
- ²⁵⁹I. Shapir, A. Hamo, S. Pecker, C. P. Moca, Ö. Legeza, G. Zarand, and S. Ilani, “Imaging the electronic Wigner crystal in one dimension”, *Science* **364**, 870–875 (2019).
- ²⁶⁰M. Gmitra and J. Fabian, “Proximity Effects in Bilayer Graphene on Monolayer WSe₂: Field-Effect Spin Valley Locking, Spin-Orbit Valve, and Spin Transistor”, *Phys. Rev. Lett.* **119**, 146401 (2017).
- ²⁶¹K.-F. Berggren, P. Jaksch, and I. Yakimenko, “Effects of electron interactions at crossings of Zeeman-split subbands in quantum wires”, *Phys. Rev. B* **71**, 115303 (2005).
- ²⁶²L. Weidinger, C. Schmauder, D. H. Schimmel, and J. von Delft, “Functional renormalization group treatment of the 0.7 analog in quantum point contacts”, *Phys. Rev. B* **98**, 115112 (2018).
- ²⁶³S. Datta and B. Das, “Electronic analog of the electrooptic modulator”, *Applied Physics Letters* **56**, 665–667 (1990).

- ²⁶⁴J. O. Island, X. Cui, C. Lewandowski, J. Y. Khoo, E. M. Spanton, H. Zhou, D. Rhodes, J. C. Hone, T. Taniguchi, K. Watanabe, L. S. Levitov, M. P. Zaletel, and A. F. Young, “Spin–orbit-driven band inversion in bilayer graphene by the van der Waals proximity effect”, *Nature* **571**, 85–89 (2019).
- ²⁶⁵M. Vila, J. H. Garcia, A. W. Cummings, S. R. Power, C. W. Groth, X. Waintal, and S. Roche, “Nonlocal spin dynamics in the crossover from diffusive to ballistic transport”, *Phys. Rev. Lett.* **124**, 196602 (2020).
- ²⁶⁶B. Brun, N. Moreau, S. Somanchi, V.-H. Nguyen, K. Watanabe, T. Taniguchi, J.-C. Charlier, C. Stampfer, and B. Hackens, “Imaging dirac fermions flow through a circular veselago lens”, *Phys. Rev. B* **100**, 041401 (2019).
- ²⁶⁷A. Mreńca-Kolasińska and B. Szafran, “Imaging backscattering in graphene quantum point contacts”, *Phys. Rev. B* **96**, 165310 (2017).
- ²⁶⁸S. Schnez, J. Güttinger, M. Huefner, C. Stampfer, K. Ensslin, and T. Ihn, “Imaging localized states in graphene nanostructures”, *Phys. Rev. B* **82**, 165445 (2010).
- ²⁶⁹M. R. Connolly, K. L. Chiu, A. Lombardo, A. Fasoli, A. C. Ferrari, D. Anderson, G. A. C. Jones, and C. G. Smith, “Tilted potential induced coupling of localized states in a graphene nanoconstriction”, *Phys. Rev. B* **83**, 115441 (2011).
- ²⁷⁰A. G. F. Garcia, M. König, D. Goldhaber-Gordon, and K. Todd, “Scanning gate microscopy of localized states in wide graphene constrictions”, *Phys. Rev. B* **87**, 085446 (2013).
- ²⁷¹K. Zimmermann, A. Jordan, F. Gay, K. Watanabe, T. Taniguchi, Z. Han, V. Bouchiat, H. Sellier, and B. Sacépé, “Tunable transmission of quantum hall edge channels with full degeneracy lifting in split-gated graphene devices”, *Nature Communications* **8**, Article, 14983 (2017).
- ²⁷²L. Veyrat, A. Jordan, K. Zimmermann, F. Gay, K. Watanabe, T. Taniguchi, H. Sellier, and B. Sacépé, “Low-magnetic-field regime of a gate-defined constriction in high-mobility graphene”, *Nano Lett* **19**, 635–642 (2019).
- ²⁷³N. F. Ahmad, K. Komatsu, T. Iwasaki, K. Watanabe, T. Taniguchi, H. Mizuta, Y. Wakayama, A. M. Hashim, Y. Morita, S. Moriyama, and S. Nakaharai, “Fabry-pérot resonances and a crossover to the quantum hall regime in ballistic graphene quantum point contacts”, *Scientific Reports* **9**, 3031 (2019).
- ²⁷⁴S. Xiang, A. Mreńca-Kolasińska, V. Miseikis, S. Guiducci, K. Kolasiński, C. Coletti, B. Szafran, F. Beltram, S. Roddaro, and S. Heun, “Interedge backscattering in buried split-gate-defined graphene quantum point contacts”, *Phys. Rev. B* **94**, 155446 (2016).
- ²⁷⁵S. Nakaharai, J. R. Williams, and C. M. Marcus, “Gate-defined graphene quantum point contact in the quantum hall regime”, *Phys. Rev. Lett.* **107**, 036602 (2011).
- ²⁷⁶T. Werkmeister, Y. Ronen, S. Y. Lee, Y. J. Shin, D. Najafabadi, K. Watanabe, T. Taniguchi, and P. Kim, “Graphene quantum point contact for quantum hall interferometry”, *APS Meeting Abstracts* **1**, H14.009 (2019).
- ²⁷⁷M. Eich, R. Pisoni, A. Pally, H. Overweg, A. Kurzmann, Y. Lee, P. Rickhaus, K. Watanabe, T. Taniguchi, K. Ensslin, and T. Ihn, “Coupled quantum dots in bilayer graphene”, *Nano Lett* **18**, 5042–5048 (2018).
- ²⁷⁸A. Kurzmann, H. Overweg, M. Eich, A. Pally, P. Rickhaus, R. Pisoni, Y. Lee, K. Watanabe, T. Taniguchi, T. Ihn, and K. Ensslin, “Charge detection in gate-defined bilayer graphene quantum dots”, *Nano Lett* **19**, 5216–5221 (2019).

- ²⁷⁹B Brun, N Moreau, S Somanchi, V.-H. Nguyen, A MreÅca-KolasiÅska, K Watanabe, T Taniguchi, J.-C. Charlier, C Stampfer, and B Hackens, “Optimizing dirac fermions quasi-confinement by potential smoothness engineering”, [2D Materials](#) **7**, 025037 (2020).
- ²⁸⁰B. Brun, V.-H. Nguyen, N. Moreau, S. Somanchi, K. Watanabe, T. Taniguchi, J.-C. Charlier, C. Stampfer, and B. Hackens, “Graphene whisperitronics: transducing whispering gallery modes into electronic transport”, [Nano Letters](#) **22**, PMID: 34898223, 128–134 (2022).
- ²⁸¹N. Moreau, B. Brun, S. Somanchi, K. Watanabe, T. Taniguchi, C. Stampfer, and B. Hackens, “Upstream modes and antidots poison graphene quantum hall effect”, [Nature Communications](#) **12**, 4265 (2021).
- ²⁸²N. Moreau, B. Brun, S. Somanchi, K. Watanabe, T. Taniguchi, C. Stampfer, and B. Hackens, “Contacts and upstream modes explain the electron-hole asymmetry in the graphene quantum hall regime”, [Phys. Rev. B](#) **104**, L201406 (2021).
- ²⁸³N. Moreau, B. Brun, S. Somanchi, K. Watanabe, T. Taniguchi, C. Stampfer, and B. Hackens, “Quantum hall nano-interferometer in graphene”, [arXiv:2110.07979](#), [10.48550/arXiv.2110.07979](#) (2021).

Curriculum Vitae

Sowmya Spandana Somanchi

Born	4 th September, 1991, India
Since 07/2014	Ph.D. candidate in the group of Prof. Christoph Stampfer II. Institute of Physics A RWTH Aachen University, Germany Title: Transport through graphene quantum point contacts
01/2014 - 05/2014	Master thesis in the group of Prof. Rajanikanth Department of Physics University of Hyderabad, India Title: Synthesis and characterization of graphene using electro-chemical exfoliation of high purity graphite electrodes
07/2009 - 05/2014	Integrated Master of Science, Physics University of Hyderabad, India

Acknowledgements

Firstly, I would like to thank Prof. Dr. Christoph Stampfer for supervising my thesis and for giving me an opportunity to work on graphene quantum point contacts at RWTH Aachen. Next, I would like to thank Prof. Dr. Markus Morgenstern for being the co-examiner of my thesis.

This list would not be complete without acknowledging the opportunity provided by Joaquín Fernández-Rossier for taking me in as a part of the Marie Curie ITN project Spinograph. I thank all my fellow researchers in this project who have turned out to be not just great scientists but also good friends. Special thanks to Julian Peiro from Spinograph for being my co-author and spending numerous hours in the clean-room alongside. My deepest appreciation to all my other collaborators as well, particularly Thomas Fabian and Prof. Dr. Florian Libisch from TU Wien and Boris Brun, Nicolas Moreau and Dr. Benoît Hackens from UC Louvain for playing a major role in investigating and publishing the research mentioned in this thesis.

I am extremely grateful to our secretaries, Beatrix Dangela and Beate Nagel for not only taking care of all the bureaucracy but also making me feel welcomed at the Institute right from day one. I would also like to thank our staff including Uwe Wichmann, Guido Guelen and Lars van Hove for technical support and Sascha Mohr and Joerg Schirra for arranging Helium on short notice. I am forever grateful to Frank Volmer who provided me with immense support in the form of scientific discussions, kind words and encouragement during my preparation for the defense. Thanks are also due to Luca Banszerus and Christian Volk for taking the time for fruitful Q & A sessions. I am thankful to all the other students and colleagues in the group for interesting scientific discussions.

Last but not the least, I would like to appreciate my family and friends who supported me throughout my journey.